DOI numeris (suteikiamas atsiuntus disertaciją spausdinti)
https://orcid.org/0000-0001-7713-4347

VILNIUS UNIVERSITY

Skomantas Serapinas

The Development of Electrochemical Genosensors Based on Nucleic Acid Affinity

DOCTORAL DISSERTATION

Natural Sciences,
Biochemistry (N 004)

VILNIUS 2026

The dissertation was prepared between 2020 and 2026 at the Institute of Biochemistry, Life Sciences Center, Vilnius University. The research was supported by the Research Council of Lithuania via doctoral students support program.

Academic Supervisor – Dr. Marius Dagys (Vilnius University, Natural Sciences, Biochemistry – N 004).

Academic Consultant – Dr. Dalius Ratautas (Vilnius University, Natural Sciences, Biochemistry – N 004).

This doctoral dissertation will be defended in a public meeting of the Dissertation Defence Panel:

Chairman – Dr. Rima Budvytytė (Vilnius University, Natural Sciences, Biochemistry – N 004).
Members:
Dr. Edita Kriukienė (Vilnius University, Natural Sciences, Biochemistry – N 004),
Dr. Edita Voitechovič (Center for Physical Sciences and Technology, Natural Sciences, Biochemistry – N 004),
Dr. Rasa Petraitytė-Burneikienė (Vilnius University, Natural Sciences, Biochemistry – N 004),
Prof. Dr. Sergey Shleev (Malmö University, Natural Sciences, Biochemistry – N 004).

The dissertation shall be defended at a public meeting of the Dissertation Defence Panel at 13:00 on the 17th of September 2026 in Room R401 of the Vilnius University Life Sciences Centre.
Address: R401, Life Sciences Centre, Saulėtekio al. 7., Vilnius, Lithuania
Tel. +370 5 223 4419; e-mail: info@gmc.vu.lt;

DOI numeris (suteikiamas atsiuntus disertaciją spausdinti)
https://orcid.org/0000-0001-7713-4347

VILNIAUS UNIVERSITETAS

Skomantas Serapinas

Elektrocheminių genojutiklių paremtų nukleorūgščių afiniškumu kūrimas

DAKTARO DISERTACIJA

Gamtos mokslai,
Biochemija (N 004)

VILNIUS 2026

Disertacija rengta 2020–2026 metais Vilniaus Universitete, Gyvybės mokslų centre, Biochemijos Institute.
Mokslinius tyrimus rėmė Lietuvos mokslo taryba.

Mokslinis vadovas – dr. Marius Dagys **(**Vilniaus universitetas, gamtos mokslai, biochemija – N 004).

Mokslinis konsultantas – Dr. Dalius Ratautas (Vilniaus universitetas, gamtos mokslai, biochemija – N 004).

Gynimo taryba:
Pirmininkė – dr. Rima Budvytytė (Vilniaus universitetas, gamtos mokslai, biochemija – N 004).
Nariai:
Dr. Edita Kriukienė (Vilniaus universitetas, gamtos mokslai, biochemija – N 004)
Dr. Edita Voitechovič (Fizinių ir technologijos mokslų centras, gamtos mokslai, biochemija – N 004)
Dr. Rasa Petraitytė-Burneikienė (Vilniaus universitetas, gamtos mokslai, biochemija – N 004)
Prof. dr. Sergey Shleev (Malmö universitetas, gamtos mokslai, biochemija – N 004)

Disertacija ginama viešame Gynimo tarybos posėdyje 2026 m. rugsėjo mėn. 17 d. 13 val. Vilniaus universiteto Gyvybės mokslų centro R401 auditorijoje. Adresas: Gyvybės mokslų centras, Saulėtekio al. 7., Vilnius, Lietuva, tel. +370 5 223 4419; el. paštas: info@gmc.vu.lt

Medicinal chemists would rather have a method that proceeds in 10% yield on 90% of the substrates, than one that proceeds in 90% yield but on only 10% of the substrates.

Phil Baran, 2023 (paraphrased)

INDEX

LIST OF PUBLICATIONS

Publication 1:

Serapinas, S.; Gineitytė, J.; Butkevičius, M.; Danilevičius, R.; Dagys, M.; Ratautas, D.

Biosensor Prototype for Rapid Detection and Quantification of DNase Activity. *Biosensors and Bioelectronics* **2022**, *213*, 114475. https://doi.org/10.1016/j.bios.2022.114475.

Author contributions: Conceptualization: **S.S.**, J.G., M.B., R.D., M.D. and D.R.; Software: **S.S.**, J.G., M.B., M.D. and D.R. Investigation: **S.S.**, J.G., M.B.; Methodology: **S.S.**, J.G., M.B., M.D. and D.R.; Data curation: **S.S.**, J.G.; Formal analysis: **S.S.**, M.B., J.G., and D.R.; Validation: **S.S.**, J.G.; Writing (original draft): D.R.; Resources: R.D., M.D., and D.R.; Writing – review & editing: **S.S.**, M.B., J.G., R.D., M.D. and D.R.; Visualization: D.R.; Supervision: D.R.

Publication 2:

Gineitytė, J.; **Serapinas, S**.; Ratautas, D.

Electrochemical DNA Hybridization Signal Amplification System Using Methylene Blue and Ascorbic Acid. *Electrochimica Acta* **2024**, *507*, 145146. https://doi.org/10.1016/j.electacta.2024.145146.

Author contributions: Conceptualization: **S.S.**, J.G. and D.R.; Data curation and investigation: **S.S.**, J.G., and D.R.; Formal analysis: **S.S.**, J.G. and D.R.; Writing (original draft): J.G. and D.R.; Funding acquisition and supervision: D.R.; Writing (review, editing and graphics): **S.S.**, J.G., and D.R.

Publication 3:

Žalnėravičius, R.; Talaikis, M.; Klimas, V.; **Serapinas, S.**; Butkevičius, M.; Vaičiūnienė, J.; Morkvėnas, A.; Karabanovas, V.; Niaura, G.; Jagminas, A.; Dagys, M.

Fabrication of Porous Black Gold Films by One-Step Anodic Treatment: Towards the Development of SERS-Active Nanosensors. *Materials Today Chemistry* **2025**, *47*, 102849.

https://doi.org/10.1016/j.mtchem.2025.102849.

Author contributions: Writing – original draft: R.Z., Validation: R.Z., Methodology: R.Z., Writing – review & editing: R.Z., M.T., V.K., **S.S.**, M.B., J.V., V.K., G.N., A.J. and M.D.; Visualization: R.Z., **S.S.** and M.B., Supervision: R.Z. and M.T., Conceptualization: R.Z., V.K., V.K., G.N., A.J. and M.D.; Investigation: M.T., Data curation: M.T., Formal analysis: M.T., **S.S.**, M.B., J.V. and A.M., Resources: A.J. and M.D.; Funding acquisition: M.D.

Publication 4:

Serapinas, S.; Stakelytė, D.; Tučinskytė, K.; Tomkuvienė, M.; Dagys, M.; Ratautas, D.

Constant Temperature Electrochemical Biosensor for SNP Detection in Human Genomic DNA Based on DNA Melting Analysis. *ACS Sens.* **2025**, *10* (9), 6819–6827. https://doi.org/10.1021/acssensors.5c01577.

Author contributions: Conceptualization: **S.S.** and D.R.; Data curation and investigation: **S.S.** and D.R.; Formal analysis: **S.S.**, D.S. and K.T.; Writing (original draft): **S.S.** and D.R.; Funding acquisition and supervision: D.R.; Writing (review, editing and graphics): **S.S.**, D.S., M.T., M.D. and D.R.

LIST OF ABBREVIATIONS

AFM	Atomic force microscopy
ALP	Alkaline Phosphatase
AuNP	Gold nanoparticles
cfDNA	Cell free DNA
CV	Cyclic voltammetry
DMAP	4-Dimethylaminopyridine
DPV	Differential pulse voltammetry
ECD	Electrochemical detection
FET	Field-effect transistor
FRET	Förster resonance energy transfer
FTIR	Fourier transform infrared spectroscopy
HPLC	High performance liquid chromatography
LSV	Linear sweep voltammetry
MOSFET	Metal-Oxide Semiconductor Field-Effect Transistor
PCR	Polymerase chain reaction
PEDOT	Poly-(ethylenedioxythiophene)
PM-IRRAS	Polarization-modulation infrared reflection absorption spectroscopy
RCA	Rolling circle amplification
RNA-pol	RNA polymerase
RPA	Recombinase polymerase amplification
SAM	Self-assembled monolayer
SCE	Standard calomel electrode
SERS	Surface-enhanced Raman spectroscopy
SPE	Screen printed electrode
SPR	Surface plasmon resonance
SWV	Square wave voltammetry
TMA	Transcription-mediated amplification
TMB	3,3′,5,5′-Tetramethylbenzidine
WGA	Whole genome amplification
XPS/ESCA	X-ray photoelectron spectroscopy / Electron spectroscopy for chemical analysis

Abbv.	Reference electrode	V vs. NHE/SHE[1,2]
SCE	Standard calomel electrode	0.242 V (4.7 V*)
$Ag/AgNO_3$	Silver-Silver nitrate (10 mM $AgNO_3$ in acetonitrile)	0.54 V
Ag/AgCl	Silver-silver chloride (3M KCl)	0.197 V
SHE	Standard hydrogen electrode	0 V

* *Estimated potential in absolute terms (vs. vacuum). In electroanalytical chemistry the convention is using relative potentials.*

Note: Substrate – this term (depending on context) is used to describe both an enzymatic/biomolecular target (a chemical species) and a solid material on which a process is occurring (a solid phase).

Note: Amplification – this term (depending on context) is used to describe both sample amplification (e.g., DNA synthesis) and signal amplification (e.g., a catalytic reaction, an accumulation reaction or an electronic approach).

Note: A probe generally means a chemical species.

Note: Label-free terminology is used to mean the absence of a labeling step, and not purely the absence of a label.

THESIS LAYOUT

This thesis is composed of four publications and a discussion of their interplay in the field of biochemical assay and sensor design.

The four publications are included at the end. The related supplementary material was not included but is available at the publisher website.

This Thesis also includes appendices with additional unpublished experimental data to further expand on the practicality and the relevance of the publications provided.

INTRODUCTION AND SCIENTIFIC NOVELTY

DNA detection has very broad importance in screening for various pathogens as well as identifying and monitoring other (micro- and macro-) organisms. Some of the most important cases of DNA detection can be found in various healthcare applications for instance, diagnosing a specific tumor type or patient pharmacogenetic marker before prescribing a medical intervention.

Nucleic acid biosensors are devices capable of recognizing and detecting a target nucleic acid and can be referred to as genosensors. These devices are promising in their highly accessible nature with the potential benefits of sensor and data ownership, privacy and the convenience of low-power, miniaturized sensors, thus enabling distributed use of diagnostic tools.

The first intended users of these sensors would be analysts (professionals) with the vision of a broader acceptance by the public.

The opening quote from Dr. Baran offers wonderful insights into the critical aspect of medicinal (electro)chemistry end-user preferences. I feel this sentiment is directly translatable to the analysis field, where an assay with excellent cross-compatibility is generally more desirable and reliable than one with narrow application scope even if such an assay were to have greater sensitivity.

One exciting target for a genosensor would be pharmacogenes. It is only through extraordinarily good design or luck that pharmaceuticals are broadly safe and effective despite a massive quantity of variants of receptors, hydrolases, oxidases, ligases and transport proteins in the human population. While some medicines have pharmacogenomics–based guidelines[3–5], screening is yet to become commonplace. Some of the challenges in broader adoption include the cost and other difficulties in testing, a lack of clinical expertise or guidance, ethical concerns and the lack of clear cost–benefit evidence. [6,7] Looking ahead, broad integration of pharmacogenetic screening may improve outcomes and additionally facilitate the highly important processes of drug design and clinical trials and introduce a larger variety of precision pharmaceuticals.[8]

Microbial contamination of food, water and other samples is also a highly relevant target for a genosensor, as often a portable solution may be preferable. Notable environmental examples include *Legionella pneumophila*,[9] *Escherichia coli*[10] and *Enterococcus* spp.[11] **in water**, various mould species[12] **in air**, with *Campylobacter jejuni*[13] and *Cyclospora cayetanensis*[14] being some of the **food–borne** cases.

Diagnosis of infection in humans and animals is also an excellent application for genetic detection. Identification of infectious agents and of resistance genes like SARS-CoV-2, Ebola, HIV, Hepatitis C as well as *C. difficile* strains, MRSA *Staphylococci*, *Mycobacterium tuberculosis*, VanA *Enterococci* and others is used in practice in the form of dedicated clinical devices and highly valuable.[15,16]

The development of electrochemical DNA detection offers certain unique advantages, such as miniaturization, low power modules and thus portability and modularity. Electrochemical biosensors are also quite amenable to motion and positioning.

The goal of this dissertation is the advancement of genetic assays towards highly approachable and accessible genosensor devices. This is to be approached through the development of biosensors for specific DNA sequence recognition. Some small progress has been made in DNA sample preparation and DNA modified electrode array synthesis, however these areas are outside the scope of the thesis. The core focus of the dissertation is to assess the analytical performance and workflow design of genosensors and gain insight into their advantages and limitations, before committing to a specific design or application.

1. Objectives

To achieve this goal 3 objectives were set:

1. The detection of the presence of a specific DNA sequence with biosensors.

2. The differentiation between single-point mutations and between the two homozygous alleles of a DNA target and the heterozygous variant based on nucleic acid affinity.

3. An overarching theme of this work is achieving these tasks in a manner that is easily translatable into a portable and inexpensive device – a sensor.

The workflow of achieving these goals can be broadly described as nucleic acid target selection and recognition system design; the formation of DNA monolayers and solid-phase hybridization research; electrochemical measurements and signal analysis; supporting characterization, manufacturing and design tasks.

2. Defense statements

1. Specific detection of oligonucleotides, including the quantitation of the target nucleic acid (detectable at 3.5 nM) and its digestion by nucleases in complex biological samples can be achieved via simple electrochemical methods.
2. A novel single-surface isothermal melting approach has been developed and precalibrated genotyping of important pharmacogenes from non-invasive saliva samples was performed at 5/5 concordance with sequencing.
3. One or multiple base mutations were electrochemically measured in the target DNA sequence via their dissociation rate constants and expressed as shifts in binding affinity (with propagated standard deviations of 0.2 kcal mol^{-1}), correlating well with computed values.

3. Publications

The results of this work were published as four articles. Some further supporting data was added as thesis appendices.

The first publication "**Biosensor prototype for rapid detection and quantification of DNase activity**" and its supplement Appendix I cover the development of a sensor for the detection and quantification of nucleases.

The biosensor was able to detect DNase I – an important target in biotechnology at 0.34 mU ml^{-1} via dsDNA probe lysis – providing a convenient method for quantifying the nuclease activity of a sample. The target was first digested with a sample by mixing it into a liquid sample or an extract from a solid and allowing the reaction to occur at an elevated temperature. Afterwards the hybridization rate was monitored *in situ*, i.e., the read-off was being performed in a diluted digestion solution. Notably the digestion sample was diluted with a very high salinity electrochemical solution intended to stop the hydrolysis reaction.

Interestingly, when the system was tested with an ssRNA probe for RNase A, the sensitivity was quite good – 1×10^{-6} Kunitz U ml^{-1}, due to high intrinsic RNase stability and activity.

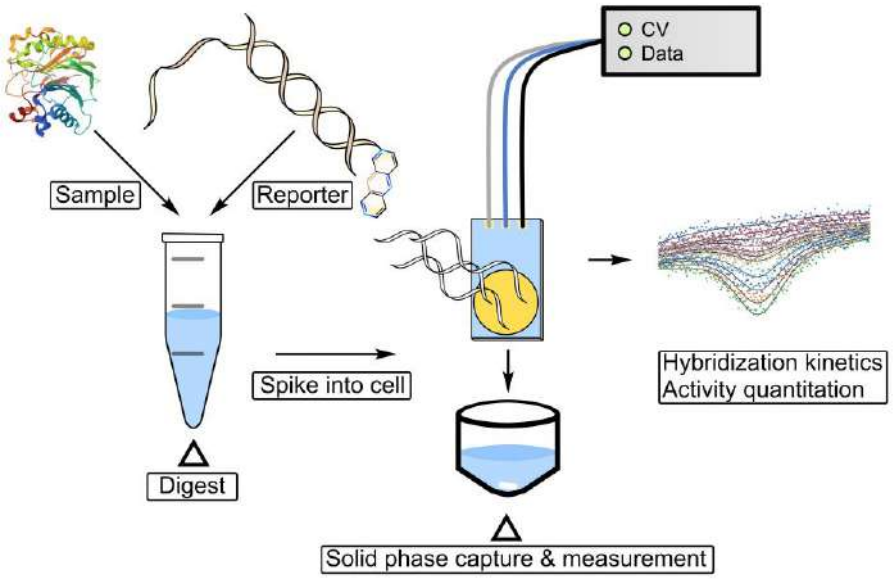

Figure 1. A representation of the workflow of the nuclease quantitation assay. CV - cyclic voltammetry.[17]

The device prototype design includes a measurement container with a Peltier thermostated cell, magnetic stirring and an electrode holder. In this case a fluidic system was not developed as the sample preparation may vary significantly. An Arduino Due based potentiostat which had been developed in–house was applied to the prototype with a custom python program to collect and fit and output the data.

Based on these results, it was concluded that MB-labeled oligo capture on gold to be suitable for further genosensor development, with hybridization rate as a viable parameter for nucleic acid quantitation.

The second publication "**Electrochemical DNA Hybridization Signal Amplification System Using Methylene Blue and Ascorbic Acid**" and its supplement Appendix II cover the development of a method for amplifying DNA hybridization signal and observing the hybridization to solid phase at temporal resolution on the order of seconds.

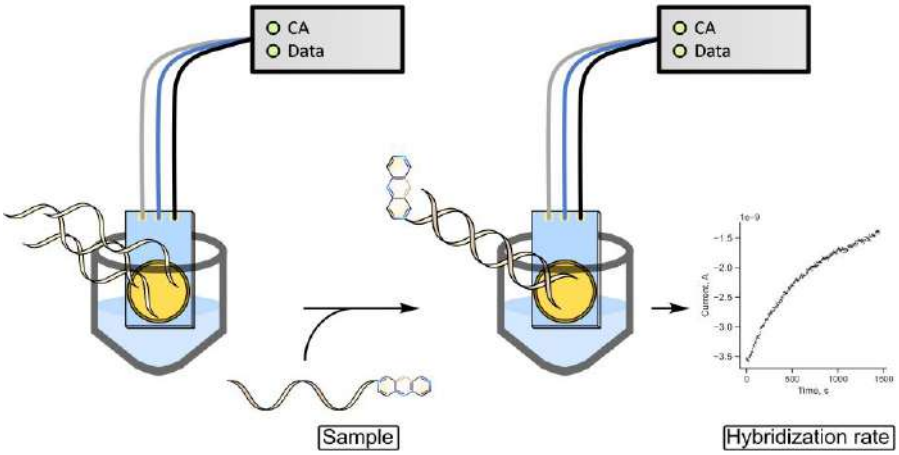

Figure 2. A representation of the workflow of the ascorbate mediated real-time hybridization monitoring assay. CA – chronoamperometry.

This was achieved via labeling the target strand with an oxidizer (MB^+) and introduction of a reducer into the solution (ascorbic acid) thus allowing for amperometric signal monitoring. The assay showed response in the 5-100 nM range producing signal on the order of 0.5-2.5 nA. The oligo association rate constants were measurable at different conditions and were in the range of 1000-8000 M^{-1} s^{-1} for varying [NaCl].

Based on these results I would expect a genosensor workflow to be in the range of 1-2 hours and predict the need to employ nucleic acid amplification for the measurement of real samples.

The third publication "**Fabrication of porous black gold films by one-step anodic treatment: towards the development of SERS-active nanosensors**" and its supplement Appendix III cover the development of a method for manufacturing SERS active electrode surfaces.

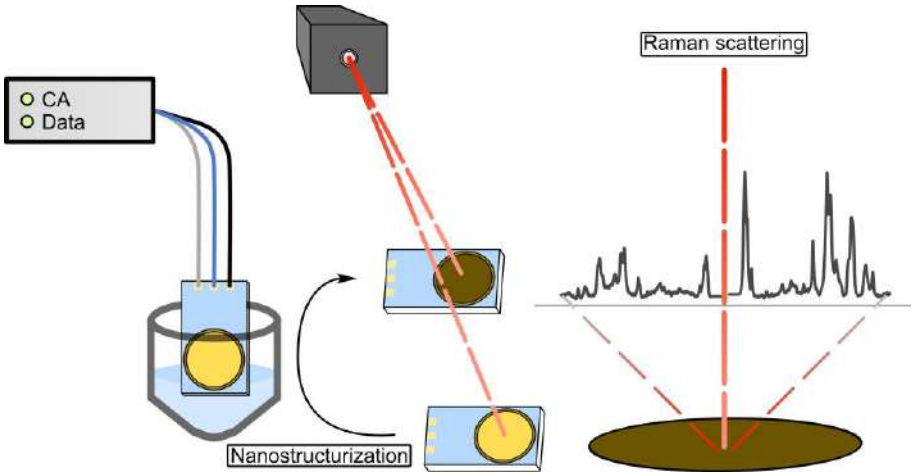

Figure 3. A representation of the workflow for generating SERS-active gold electrode surfaces. CA – chronoamperometry.

The electrodes prepared by our team show the promise of facile manufacturing and powerful Raman enhancement of 1.4×10^7. An enhancement factor of 10^5-10^6 is generally considered reasonable.[18] Clear SERS spectra of (Au-bound) 4-mercaptobenzoic acid and (SAM-adsorbed) doxorubicin were observed. Interestingly, the electrodes could be used to verify covalent surface modification and distinguish between adsorbed and bonded species.

While novel synthesis of solid phase DNA surfaces was not completed in this thesis, I am in the process of developing novel coupling reactions with varying degrees of success. Highly sensitive structural characterization is a key step towards developing such chemistries.

The fourth publication "**Constant Temperature Electrochemical Biosensor for SNP Detection in Human Genomic DNA Based on DNA Melting Analysis**" and its supplements Appendix IV and V cover the development of an assay for detecting the CYP2C19*17 (NG_008384.3:g.4220C>T) allele. 4220C>T is an interesting pharmacogene in that it is located in the non-coding region of the genome. The CYP2C19 enzyme contributes to the oxidative metabolism of many pharmaceuticals. We have successfully detected the *1 (normal), *1/*17 (rapid) and *17/*17 (ultrarapid) diplotypes in synthetic and PCR amplified biological samples. The sensor was melting kinetics-based, showing a >2σ signal difference between the diplotypes. The signal measured was the dissociation rate constant ratio or in other words, relative affinity for two reporter sequences.

The two reporter sequences were read over a 20-minute interval each at 0.05 Hz providing two 60 datapoint decay curves. Significant improvements over previous publications were achieved by performing *ex situ* hybridization by adding a small amount of buffer directly to the PCR amplicon and immersing the electrode in a small volume of concentrated sample for target capture. Additionally, polycationic ZNA probes were used on the electrode to allow the DNA duplex to collapse and transduce the signal even with longer DNA targets. Of the 6 tested saliva samples 5 were identified correctly with 1 QC fail. Additional sequence data can be obtained from the melting kinetics.

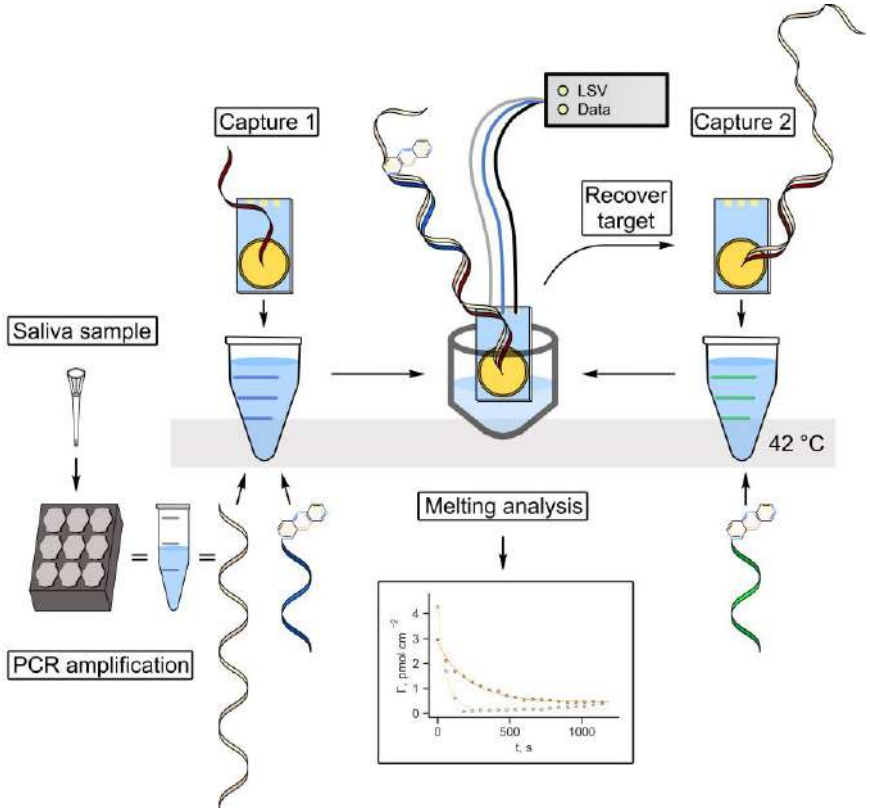

Figure 4. A representation of the workflow of the isothermal genotyping assay. LSV – linear sweep voltammetry.

While a device prototype was not constructed the design does not require many additional parts relative to our nuclease detection prototype device, where the measurement comprises potential sweeps under stirring and constant temperature. In fact, if the hybridization and the isothermal DNA amplification were to be conducted at the 42 °C measurement temperature, the devices would almost be cross-compatible.

Scientific novelty

A novel device for nuclease detection was produced. The device was able to measure DNase I concentration using screen-printed electrodes.

A novel biosensor for cytochrome P450 2C19 promoter region variants was designed. The biosensor utilizes a novel approach to detection via isothermal electrochemical dissociation rate monitoring. I believe I have developed the first isothermal dissociation kinetics-based DNA biosensor. A somewhat similar single molecule, polarization-based approach has been previously described. [19] While not completely novel, the design also grants a rare capability of differentiating between the homozygous and heterozygous samples on a single electrode. I believe this research was also the first to describe an electrochemical measurement of a single stranded nucleic acid base stacking energy.

A novel approach to gain additional sequence information from electrochemically measured melting rates via lookup of computed sequence–based properties was developed.

A novel method for manufacturing SERS–active electrodes was also developed.

Relevance

Publication I – DNase detection was mainly intended as an environmental test, but it may have various applications in diagnostics. Nucleolytic activity in saliva was measured. For further example application in RNase detection, see Appendix I.

Publication II – DNA hybridization signal amplification and real time hybridization monitoring are mostly relevant to research. For additional data on the applicability of the system to a sandwich configuration and one-pot multiplexing, see Appendix II. Amperometric multipotentiostat measurements at steady temperature may be feasible as a DNA quantitation platform.

Publication III – SERS-electrochemistry cross-compatible electrodes are mainly relevant in research at the moment. The flexibility of two detection methods may prove very powerful either in analyzing captured molecules or for electrode quality control (QC). In terms of QC, this method does allow for a facile surface chemistry standardization. For additional data on the application of SERS in characterizing surface conjugation see Appendix III.

Publication IV – Highly specific DNA detection with SNP discrimination has broad relevance, however the target is a pharmacogene,

therefore, it is mainly relevant in diagnostics, however the system could be adapted to any short desired sequence.

For further data on signal transduction, see Appendix IV.

For further sequencing calculations, see Appendix V.

LITERATURE REVIEW

1. Genotyping methods and pharmacogenetic assays

For genetic diagnostics and research, sequencing methods are generally considered the best option due to the amount of information they provide and how powerful these methods are in terms of indels and short tandem repeats. There are special cases like OGM (optical genome mapping) for aneuploidies[20], imaging methods like ChIPSEQ for DNA-protein interaction[21] and MassARRAY for methylation.[22]

DNA microarrays have improved considerably since they began seeing widespread use and have continued to improve even recently.[23] They typically range from 200 000 to 4 000 000 features (e.g., SNPs) and can accommodate on the order of 1-24 samples. Typically, these assays require relatively clean, fragmented whole genome amplicon which is usually prepared in large amounts due to the number of targets. The whole assay may take on the order of 3-4 days (Thermo Fisher Scientific Axiom, Illumina Infinium)[24,25] and usually has a large footprint (e.g., a dedicated laboratory) due to the number of steps and equipment involved in amplifying, extraction, hybridization and scanning. However, the end result provides a large amount of highly valuable data and this approach is still generally cheaper than sequencing. Multiplex ligation-dependent probe amplification (MLPA) is a powerful approach with a feature number closer to 60.[26,27] Another electrophoretic method named Shifted termination assay (STA) while lower in feature number (~20) is much more rapid than MLPA (~3 h vs. ~18 h) and has reasonable mutant allele fraction sensitivity of ~ 1-2%.[28,29]

For detecting a smaller number of features (e.g., 6), ddPCR and qPCR methods dominate. These methods are generally quite fast and require very little sample. TaqMan StepOnePlus and SpartanRX have been used as on-site assay and point of care approaches for pharmacogenetic testing in a clinical trial with reported measurement time of 2-3 h.[30] ddPCR solutions currently are bulkier than what would be considered point of care, however they are used for high sensitivity applications such as cfDNA and have high throughput.[31,32]

In terms of point of care or "point of use" devices for so-called "molecular diagnostics" bacterial and mycobacterial tests are of note. For instance, in water system applications, relatively recently LuminUltra launched a GeneCount® Cube qPCR device for *Legionella* spp.[33] Genomadix's PCR-based pharmacogenetic Cube CYP2C19 System has been

approved in 2023, for genotyping buccal swab samples in ~1 hour.[34] For application in food, a *cyclospora* targeting device/assay was recently developed by Rheonix.[14]

For infectious disease, Cepheid provides a GeneXpert POC device dedicated for mostly infectious disease such as Influenza, Streptococcus, Chlamydia, SARS-CoV-2 and a number of others.[15]

2. Nucleic acid preparation

Nucleic acid extraction

As a common step prior to DNA analysis, DNA isolation can be extremely important. As a more universal approach, DNA is traditionally extracted by homogenizing the cells via proteinase K and surfactants with or without a chaotropic agent such as urea or guanidine.[35] The sample is usually further treated with ~5 M NaCl, optionally washed with a non-polar solvent and precipitated with EtOH or i-PrOH followed by centrifugation.

For small samples, guanidinium SCN-phenol-chloroform extraction is a highly practical approach, considering that the method is amenable to DNA or RNA extraction.[36,37]

Another popular approach is affinity chromatography, sometimes referred to as "spin column chromatography" where lysed samples are passed through a stationary phase in a centrifuge tube.[38] This approach conveniently allows for DNase pretreatment on solid phase before elution.

Pipette-tip affinity chromatography has emerged as an appealing next step for oligonucleotide isolation. TruTip offers an approach where a lysed sample is bound, washed and eluted inside a pipette tip for RNA or DNA extraction.[39] It has incorporated a monolithic stationary phase – a great approach for minimizing pressure difference and allowing for high flow, while the affinity methodology negates any monolithic column drawbacks – such as manufacturing repeatability or inferior resolution. Chromatography-based approaches are amenable to automation. An alternative automatable approach entails nucleic acid binding on magnetic beads – following a very similar protocol, except with the solid phase dispersed in the sample and magnetically retained.[40]

Another proposed approach is the ePrep system wherein a disposable electrophoresis chamber is used to isolate nucleic acids rapidly and with high throughput. [41] Currently, magnetic bead-electrowetting combined systems are considered state of the art.[42]

Nucleic acid amplification – targeted

Regular PCR amplification is very commonly used for amplifying a specific sequence. With regards to solid-phase capture, an advantage of PCR lies in performing an asymmetric amplification – adding an overabundance of the desired primer. This removes the need for denaturing the product – which has a tendency to renature – leaving only a limited amount of ssDNA available for binding. Isothermal sample amplifications are especially attractive –recombinase polymerase amplification (RPA) has been applied successfully in point of care applications.[43] What's even more exciting is that asymmetric RPA has been performed in a point of care prototype electrochemical platform and combined with the phosphorylated primer exonuclease digest, where it was found that asymmetric amplicon was not further improved by exonuclease treatment.[44]

Nucleic acid amplification – WGA

WGA (whole genome amplification) methods are currently exclusively or almost exclusively intended for DNA production. MSD (multiple strand displacement) is a highly appealing method as it is isothermal and provides reasonable yields of DNA.[45] Another method for unbiased single–cell amplification is MALBAC[46] (multiple annealing and looping–based amplification cycles), additionally providing "labeled" amplification products – which may be important for designing assays. This method, however is not isothermal.

Notably, RNA polymerase-mediated nucleic acid amplification methods like TMA[47] (Transcription-mediated amplification) and Self–sustained sequence replication[48] exist since the 1990s. There, a RNA-pol promoter is introduced into a DNA amplicon and then transcribed into many RNA copies (to be reverse-transcribed by RT or detected otherwise). This would seem like an appealing technology for WGA – rapidly and isothermally generating a single stranded, easily fragmentable RNA amplicon. Yet to the best of my knowledge, no such product or suitable (i.e., promoter–free) novel RNA polymerase has come to market since the inception of this idea. In spite of all that could have been, TMA–like *targeted* amplification has been incorporated into genosensors.[49]

Nucleic acid fragmentation

If WGA is performed – often the fragments are far too long to hybridize to a sensor or difficult maintain in a denatured state. Commonly used fragmentation methods include uracil glycosylase (if the amplification was performed with uracil), restriction endonuclease digestion and ultrasound.[50]

Covaris ultrasound based fragmentation has been used with genome sequencing.[51]

A unique non-enzymatic, approach involves guanine alkylation and opening of the ribose by piperidine, to the best of my knowledge, it appears this chemistry has been completely abandoned.[52] Non-specific exo/endonucleases have been used.[53,54]

Statistically, we can calculate, that when fragmenting (assuming completely random cuts) to ~100 bp fragments, a hydrolytic approach is expected to produce reasonable amounts of ~ 35 % guaranteed intact 100 bp "target" fragments (1 cut/100 bp ~ 35 % yield; 2 cuts/100 bp ~ 12 % yield) regardless of starting fragment size: (20 Mbp - 2 kbp):

$$P(\textit{Non-sequence bonds}) = \frac{\textit{Non-sequence bonds}}{\textit{Total bonds}} * \frac{\textit{Non-sequence bonds-1}}{\textit{Total bonds - 1}} * \dots * \frac{\textit{Non-sequence bonds - n cuts}}{\textit{Total bonds - n cuts}}$$

$$n\ cuts = DNA\ size\ /\ 100 - 1$$

The complete fragmentation of the complementary strand is an equally important approach to allow and to speed up hybridization. Digestion with lambda exonuclease (λ Exo) after amplification with phosphorylated primers is a common approach.[55]

3. Nucleic acid capture and detection

Hybridization

For high selectivity the probe-target duplex length must be relatively short. We can see an example of a 7 bp-mismatch target showing a high affinity at 55 °C when the probe is quite long (70 bp).[56] While high resolution melting is able to distinguish between 300 bp sequences[57], realistically, a probe above 30 bp may already be less-suitable for detecting SNPs.[58] For recognition at "low" temperature toehold hybridization has been developed.[59] Toehold probes allow for excellent tuning of affinity[60] and have been used for high sensitivity genotyping.[61] We must however acknowledge that they may suffer from the fact that a liable blocking strand is required – therefore hybridization cannot be carried out at elevated or cycling temperatures. On the other hand, in sandwich hybridization at elevated temperature it is quite viable for two shorter *synthetic* strands (in stoichiometric excess) to displace one longer *native* complementary strand

thus securing the target strand. This however only applies if a simultaneous sandwich hybridization is performed.

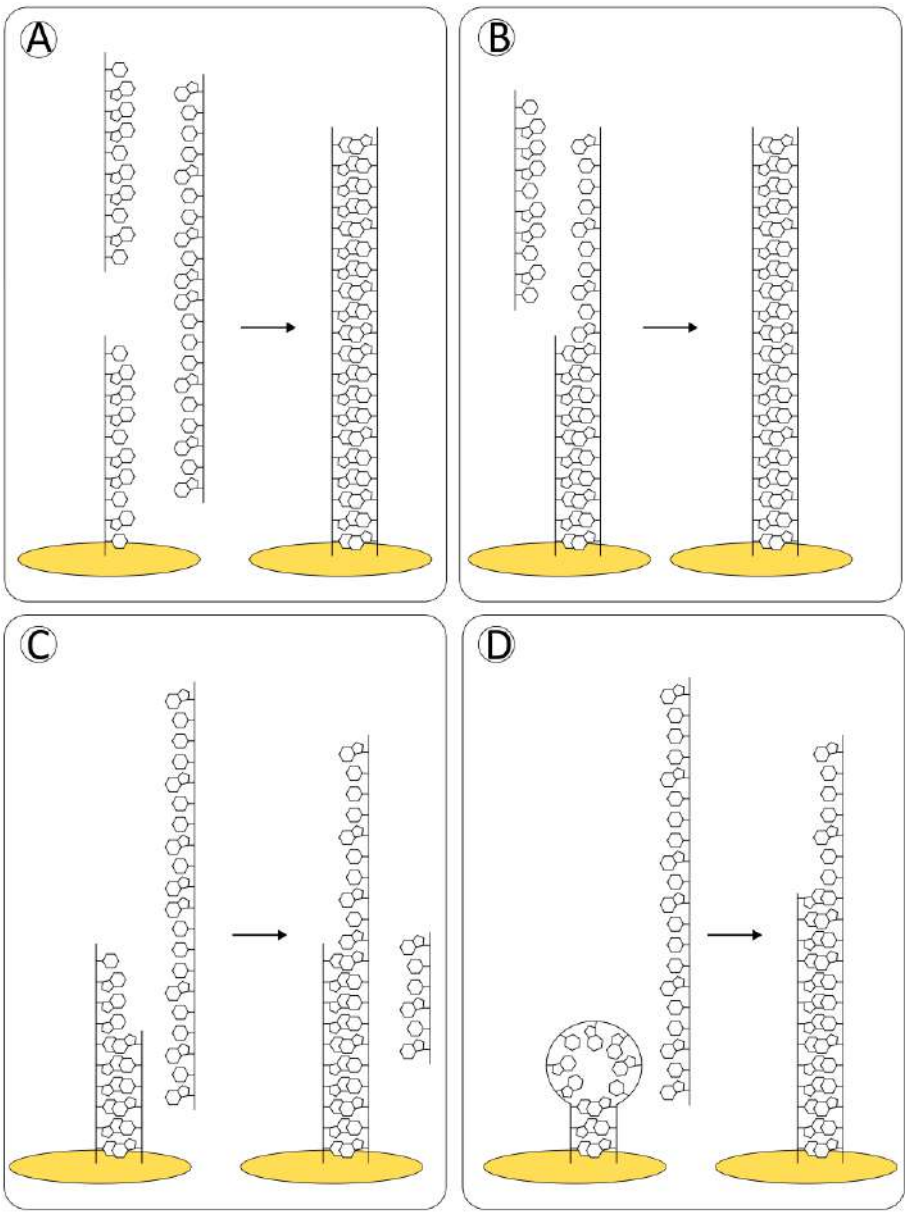

Figure 5. Possible solid phase hybridization approaches. A – simultaneous sandwich, B – stepwise sandwich, C – distal toehold probe, D – hairpin probe

When it comes to hybridizing to a solid substrate, the probe density plays an important part in the possibility and the density of hybridization. It is generally thought that ~4×10^{12} molecules cm^{-2} is a viable density with ~1×10^{13} being excessive.[62–64] Conceptually reminiscent of molecular beacon FRET quencher systems, liquid phase hybridization detection (i.e., without DNA on solid phase) via electrochemical and HPLC has been proposed.[65,66]

Electroanalytical methods

Generally, potentiostatic (and potentiodynamic) methods (i.e., electrolytic mechanisms driven by the potentiostat as opposed to galvanic mechanisms) will be used in this work in order to induce the desired electrochemical reactions by applying a voltage, leading to a measurement of an analytical signal as an amperage.

Linear sweep voltammetry (LSV), where a linear increase in potential at the working electrode (Volts) up to a desired point produces a current response (Amperes) and cyclic voltammetry (CV), where the potential scan is additionally reversed are classic electroanalytical techniques. In a voltammogram we typically look for current-potential peaks. They provide the potential at which a species reacts, the number of electrons involved in the reaction and offer insight into the species' diffusion behavior and electron transfer rate. In regards to the methods used herein, the direct quantitation of a surface-adsorbed species can be achieved, via the quantity of electrons transferred (over a surface area) by fitting an electrochemical peak using the following equation:

$$i(E) = -\frac{n^2F^2v\,[Olig]\,exp\left[\frac{nF}{RT}\,(E - E_0)\right]}{RT\left(1 + exp\left[\frac{nF}{RT}\,(E - E_0)\right]\right)^2} + a_0 + a_1(E - E_0) + a_2(E - E_0)^2$$

Equation 1. The monolayer voltammetric current–potential curve fitting equation with background compensation for the quantitation of a redox-active species.[1,67] The left side of the equation is in the shape of a peak and the right side is a polynomial background:

i – current (A, the y-axis),

n – the number of electrons participating in the reaction (for methylene blue (MB) – 2 electrons),

F – Faraday constant (96 485 C mol^{-1}),

ν – the chosen potential scan rate (e.g., 0.05 V s^{-1}, while for surface adsorbed species high scan rates – in V s^{-1} are often desirable, labeled DNA performed poorly under high scan rates),

R – the gas constant (8.3145 J K^{-1} mol^{-1}),

T – the chosen temperature (in K),

E – electrode electrochemical potential (the x-axis),

E_0 – standard redox potential of the electroactive species (i.e., MB) (~0.255 V vs. Ag/AgCl; this value is fitted within a narrow range as it depends on the DNA-MB layer behavior; although not extensively applied in this work, the obtained E_0 is a useful metric for bound DNA construct characterization),

a_0:a_2 – the background current coefficients (although not extensively applied in this work, the obtained coefficients may be useful for the detection of abnormal/faulty electrodes in an automated device),

[Olig] – the amount of the surface adsorbed species (i.e., MB modified DNA (mol),

Note: in this case the electrode area is not considered; in my experience it is more convenient to calculate the absolute moles and to normalize the surface area afterwards if needed. It is assumed that the MB reduction reaction does not change the labeled DNA reporter strand hybridization affinity in any impactful way.

For sharp, well background–subtracted peaks, the maximal current at the voltammetric peak could be used to extract the surface–bound reporter quantity (*symbols as previously defined; A – area in cm^2; [Olig] in mol cm^{-2}*). [68]

$$i_p = [n^2 F^2/4RT]\,[Olig]\,A\,v$$

Equation 2. Peak current – surface coverage and scan rate relationship.

This approach may be beneficial for a more rapid, facile computation avoiding the need for non-linear least squares, especially if an assay is intrinsically ratiometric.

Figure A5 3.1 is presented as an LSV example sweeping from 0 mV (relative to Ag/AgCl 3M KCl) towards -450 mV. The downward–facing peak is caused by electron transfer from the electrode to a DNA–tethered redox species (MB) – inducing a reduction reaction. LSV does not reverse the scan, providing less information, but for quantitation purposes, it enables a faster scan and minimizes the time the electrode is passing current. Kinetics can be monitored by running voltammograms sequentially on the order of every few seconds to minutes depending on the scan rate (mV s^{-1} – V s^{-1}).

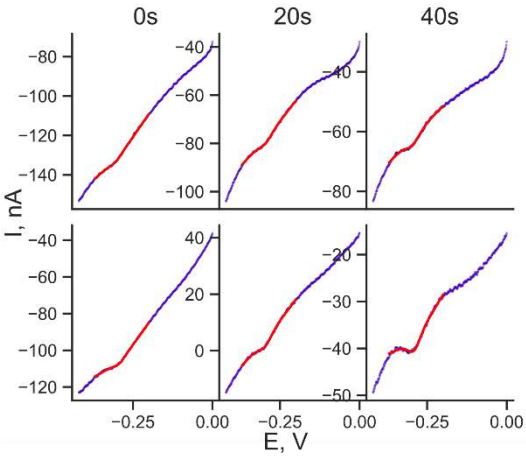

Figure A5 3.1. LSV peaks of surface-adsorbed MB label with fitting (red trace, Equation 1), under non-melting conditions (these LSVs are averaged to produce the 20 nM target DNA datapoints in **Figure A5 3 (A)**). Top: 0.5 mm, bottom: 1.6 mm electrodes.

Amperometry is a simple electrochemical technique where a static potential is applied and not varied and the current is monitored over time, producing a current vs. time curve. With fast current sampling this technique is effectively a real-time measurement.

For context, while (electrosynthetic) electrolysis may be performed at multiple (tens) of volts (albeit this is usually relative voltage), in sensors amperometry is often performed at hundreds of milivolts. This method practically eliminates all capacitive current and the measured faradaic current is proportional to the concentration of the electroactive species. The measured faradaic current is typically continuously decaying as the electroactive species is consumed, however this effect can be quite small at small electrodes. [69,70]

$$i(t) = i_{(t=0)}\, exp\, -\frac{D\,A}{\delta\,V}\, t$$

Equation 3. The function of the current decay over time under stirred conditions in constant potential amperometry.

i – current (A, the y-axis),
D – the diffusion coefficient ($\mu m^2\ s^{-1}$)
A – the electrode area (μm^2)
δ – the diffusion layer thickness (μm)
V – the solution volume (μm^3)
t – time (s)

Notably, sometimes an exhaustive electrolysis method can be desirable, and a membrane or a frit may be employed to prevent the migration to and regeneration of an electroactive species at the counter electrode.

Grafting and monolayer formation

To create a heterogeneous phase suitable for DNA recognition the DNA probe (or another recognition molecule) must be affixed to the surface. Preferably, the spaces in between the DNA probes are to be backfilled in a way that does not interfere with hybridization but eliminates non-specific signal.

The coupling of gold to thiols is a classic approach where a sulfhydryl or a disulfide generates an Au-S bond on a gold surface.[71] This reaction is rapid (a few minutes for initial coverage) and forms high density, highly repeatable self-assembled monolayers (SAMs).[72] The Au-S bond has significant stability issues at reductive voltages and elevated temperatures.[73] Trithiolated layers have been used at relatively high (80° C) temperatures.[74]

Gold-alkyne bonding is a novel approach showing somewhat improved stability over thiols.[75] Gold-phosphine monolayer bonding has been described in literature[76–78] but is very uncommon in practice.

Grafting of highly stable aromatic layers can be achieved in mild reductive conditions via *in situ* formed aryldiazonium compounds – this conjugation can yield well-controlled relatively thin layers.[79] The aryldiazonium salts can be prepared *in situ* via a traditional cold acidic $NaNO_2$ solution or in organic solvents via organic nitrites.[80,81] The electrochemically generated radicals seemingly did not destroy a linked antibody during grafting.[82] It must be emphasized that it is easy to deposit a very thick polymer-like layer especially if the diazonium solution is formed *in situ* and the concentration may be unknown. Diazotization of aliphatic amines is almost never performed due to poor stability.

Non-diazotized aromatic and importantly – aliphatic amines can be grafted directly via electrochemical oxidation, providing a convenient way of highly stable *directed* aliphatic modification.[83–85]

It is important to be aware of potential driven decarboxylation[86] which occurs at similar potentials (around ~950-1000 mV vs. SCE). From personal experience in grafting Ω-amino acids, this can make later functionalization via amidation impossible, however carboxyls can be preserved by carefully controlling the potentials (I would recommend up to ~600 mV vs. $Ag/AgNO_3$ in acetonitrile). The decarboxylation is *in and of itself* an another approach to graft (oxidation-stable or protected) functional groups. Notably,

an entire research field of carbon-carbon bond formation via (electrochemical) decarboxylation has recently come to the foreground[87], despite being proposed in the 1890s.[88]

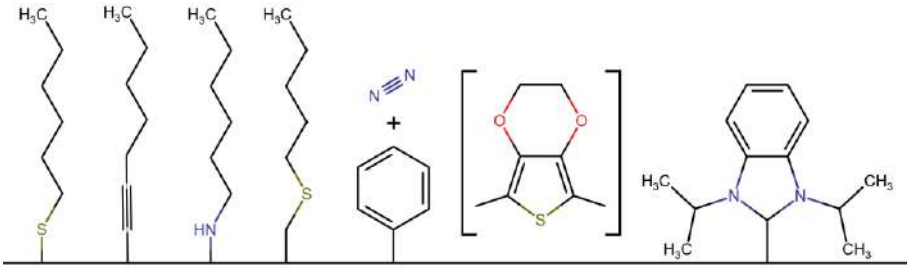

Figure 6. From left to right: Thiol SAM, Alkyne SAM, Grafted aliphatic amine, Thiol-ene grafting, Aryldiazonium grafting, PEDOT polymer, N-heterocyclic carbene SAM (see text for details).

A functionalization-ready surface can be prepared by electrochemical polymerization – such as the formation of an azido-PEDOT layer.[89]

A classic approach common in immunoassays has also been used where target DNA is adsorbed on polystyrene-polybutadiene copolymer from solution.[90] Electrochemically triggered grafted group deprotection is possible.[91,92] An elegant photocatalyzed thiol-ene approach has been put forth for both directed conjugation and patterning, but we must be aware that the generation of a sulfhydryl covered surface is not an easy task.[93] An approach with wonderful acid/base, thermal, oxidative and organic solvent stability based on N-heterocyclic carbene (NHC) films has come to the fore recently. These SAMs are created on gold via a carbene – a (shelf-stable) neutral diradical–like compound derived from a deprotonated heavily substituted imidazolium salt.[94] Unfortunately, despite otherwise superb layer stability, NHC layer degradation is observed upon electrochemical reduction. Commercial applications like CombiMatrix[95] protect their platinum surfaces with a polymer, presumably to i) allow reliable covalent bonding, ii) prevent metal-catalyzed side reactions.

A notable outlier in generating monolayers is the non-covalent pyrenebutyric acid (and derivative) stacking onto graphene and related substrates.[96]

Conjugation

The DNA probe may be introduced via grafting or chemically linked to the grafted molecular layer as a separate step.

Crosslinking may have originally become highly relevant as a method of gluing cellulose with the classical agents such as glutaraldehyde, polyepoxides and divinylsulfone now having been used for around a century.[97] Shortly after the introduction of "one carbon bridge" and "zero-length" crosslinkers[98] via formaldehyde activation and EDC crossreaction respectively, the concept of "two step zero-length crosslinking" in the form of activated esters was proposed via R-CO-NHS for amides in 1990.[99] Notably, the concept of an activated carboxylic acid in the form of R-CO-$DMAP^+$ cation for ester synthesis emerged much earlier in 1979.[100] This procedure was a massive leap forward and is still commonly used, with powerful new acylation agents still emerging.[101–106] Emphasis on longer heterobifunctionalized crosslinkers came soon after.[107]

The notable Sharpless Lab changed the landscape of conjugation chemistry with their selective aqueous azide-alkyne addition.[108,109] An amino-yne reaction with terminal or non-terminal electron withdrawing group containing alkynes has been shown.[110] Similarly, the thiol-ene click reaction is another useful approach.[111] DNA is traditionally linked via the azide-alkyne addition, maleimide coupling or via amide bonds.[112]

Unlabeled DNA signal transduction

One of the simplest ways to transduce a hybridization signal is via an intercalating agent. Intercalation can usually occur via:

- Outside edge binding – more phosphate specific (e.g., $[Ru(bpy)_3]^{+2}$)
- Intercalation – usually flat aromatic compounds (e.g., ethidium bromide)
- Groove binding – usually larger molecules than intercalation (e.g., Hoechst dyes) [113,114]

Intercalators besides fluorescence and redox signals can also produce a catalytic signal.[115] Unfortunately, this chemistry can be unreliable – for instance binding to ssDNA[116] as well as adsorbing to proteins, lipids or a solid substrate.

Intercalation of agents like methylene blue to detect DNA is still used as an alternative to covalent modifications or for binding structures like G-quadruplexes.[117]

Labeled DNA signal transduction

Covalently bound labels are available via: a complementary reporter strand via sandwich hybridization[118], distance-dependent signal via opening of a hairpin[119], modified dNTP incorporation via a polymerase[120] and (indirectly) via covalently modified Cas9.[121]

In electrochemical analysis, it can be very difficult to eliminate the signal from soluble redox-active molecules and DNA labeling is by far the more reliable approach for specificity.

Although electron transfer via the DNA duplex in a fashion similar to a highly conjugated molecular wire has been proposed[118,122,123] (usually under very strict conditions), it is difficult to account for and rule out the effects of geometry changes when solubilized dsDNA is interrogated on a surface.

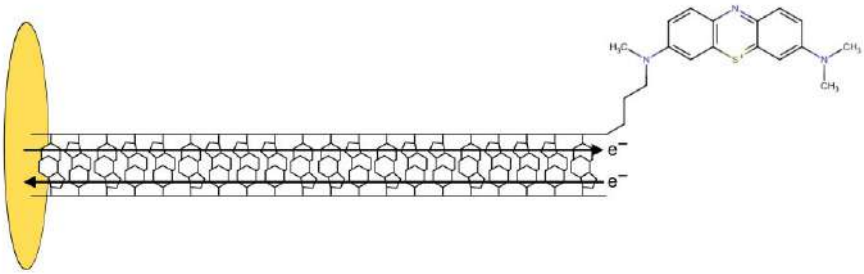

Figure 7. A representation of charge transport through a DNA molecule.

For instance, a case of reported rapid, low voltage, long-distance dsDNA charge-transfer[118] could be explained by the presence of spermidine, which is now known to collapse the DNA strands on surfaces.[124,125] If such relatively flat DNA duplexes were produced by DNA collapse, they would likely result in behavioural similarities between long and short redox-labeled oligomers (appearing as intantaneous, through-DNA conduction). Further support of contact-mediated charge transfer is expressed in literature from observations where both duplex formation and increasing monolayer densities result in lowered charge-transfer rate.[126] Since 2000s-2010s DNA seemingly has achieved limited application as a molecular wire at mild votages and highly conjugated modifications yield vast improvements in its conductivity.[127] Generally, an electroactive label proximal to the electrode produces a powerful signal and the label distal to the electrode produces a weak signal (i.e., minimal dsDNA conductivity is observed). These effects have been demonstrated via SWV to occur simultaneously as the DNA hybridization process “quenches” an existing distal label signal and introduces an increasing proximal label signal. The authors note that

proximal reporter signal is still diminished due to ion screening and should be higher.[128] In a similar fashion, many assays utilize the dsDNA signal quenching as a means to detect hybridization via a labeled hairpin probe.[129] The restraining of a dsDNA molecule has also been attempted via increasing viscosity through addition of glycerol.[128] I suspect that the changes in the screening ability of the solution by glycerol were quite marked, recognizing the difficulty to increase the matrix viscosity without affecting the matrix in other ways.

Similar behavior has been demonstrated via CV also reporting the electron transfer rate constant via SWV to be 0.7:140 s^{-1} for distal and proximal MB labels respectively.[130]

Signal amplification

Note: The categories are arbitrary. There may be large overlaps between the concepts.

Oligomerization

By forming large clusters of a signaling molecule the signal can be significantly amplified. In electrochemical assays by conjugating a large amount of MB onto gold nanoparticles detection in the 50fM range has been reported.[131] As biotin-steptavidin can form dendritic structures via anti-strepatvidin-biotin and the reagents are commercially available, this approach is common. Commercially available large beacons such as FluoSpheres (Thermo Fisher Scientific) or DiagNano™ Streptavidin Quantum Dot Beads (CD Bioparticles) are also available.

Catalytic

Catalytic signal amplification entails connecting an enzyme or another catalytic subunit as a signal transducer. Often the difference between a catalytic and a cumulative signal is arbitrary and I make these distinctions to create a theme for the reader. Conjugates such as streptavidin-HRP or ALP are a common and powerful approach. One of the mainstay methods is the HRP-H_2O_2-TMB reaction in ELISA[132]. For electrochemical genosensors sensitivity with HRP detection down to 60fM has been reported.[133]

Cumulative

Cumulative signal amplification approaches typically rely on deposition or growth of a product on the signal transducer. This category includes one of the original signal amplification approaches: silver staining in microbiological and medical imaging.[134] Biometallization approaches can be regarded as cumulative and very high sensitivities have been achieved.[135,136]

Resistive signal amplification

Resistive signal amplification is again, almost identical to cumulative approaches as some analyte or product must be deposited onto a conductive surface. However, in this case the focus is on generating a very large signal on the "naked" sensor which subsequently is quenched by analyte recognition. For electrochemical genosensors HRP mediated precipitation of benzo-4-chlorohexadienone with reported sensitivities in the 600fM range.[137] Polymer and dendrimer[138] substrates are used for obtaining high resistive signals.

Charge accumulation

It is less common to accumulate a large potential bias or like-polarity ion concentration. Such processes are highly unfavorable and are more frequently encountered in biofuel cells. Minute charge accumulation can be detected by tuning to a specific gate voltage in a MOSFET. If a charged molecule (such as DNA with counter ions) is captured this small change in gate voltage produces a large source to drain current.[121]

Captured sample amplification

Additional sample amplification can be performed after hybridization. RCA has been applied to massively increase the size of DNA reporters.[139] Solid phase RPA utilizing modified dNTPs as ferrocene labels has been applied for simultaneous signal amplification and sequence recognition.[120]

Electrochemical genosensors

To date some excellent electrochemical genosensor designs have been proposed. A highly accurate device for measuring a genotype has been reported by Yang et al. (2014).[74] In this case a synthetic unlabeled ssDNA target is used. The sensor captures the target onto solid phase via a distally labeled trithiolated probe. These probes are remarkably thermally stable up to ~80 °C. After the hybridization the device can be filled with fresh electrolyte and a stepwise temperature ramp is performed. The melting is monitored via alternating current voltammetry. The device consists of a Peltier element with a gold electrode containing PDMS microfluidics requiring sample volumes on the order of 10 µl.

Yenice et. al. (2023) has demonstrated a wonderful melting temperature-based device. The sample is prepared from a capillary blood sample which undergoes in-solution hybridization with a ferrocenylated primer and is amplified isothermally via asymmetric RPA.[44] This yields a sample solution with proximal-side ferrocenylated ssDNA targets which bind to solid phase probes. As targets are synthesized with a preexisting label, sandwich hybridization or probe labeling methods are not needed. The

electrode array is then placed into a solid phase thermal block and the temperature is scanned stepwise with a DPV recording at each temperature. This creates a thermal melting curve, allowing to discern between alleles including heterozygous samples.

The device consists of an Arduino-based syringe pump and Peltier element with a 64 gold electrode array containing PMMA microfluidics. A really meaningful design change reported therein is the use of an Au pseudoreference, which greatly simplifies array manufacturing and makes the method highly scalable.

A highly innovative approach to accelerate the k_d of a dsDNA strand via an electrostatic bias was proposed by Vernick et al. (2017).[19] In contrast to potentiostat where a bias is measured versus the reference and an unknown bias exists versus the counter electrode, the study used FET electrodes where the bias is recorded versus the gate (V_g) which represents the surrounding solution. The DNA probe is grafted to a carbon nanotube via aryldiazonium followed by amide condensation and is hybridized to the target. The team found that melting curves can be recorded at a constant temperature by changing the V_g and these melting curves differentiate a SNP target. As the device records source-drain current, and not a voltammetric measurement, the bias can be applied constantly.

Realistically such FET devices are very powerful but extremely difficult to manufacture. As the grafting is electrically switchable there is great potential for miniaturization. While on paper nucleic acid amplification may not be needed using FET electrodes, realistically capturing unamplified neat genomic or viral DNA is not an easy task.

A different mode of recognition in a FET device has been shown by Hajian et al. (2019).[121] In this case the DNA recognition event modulates the V_g-V_s potential which causes a change in current. In this approach the DNA recognition occurs via a dCas9 which is complexed with a target-specific RNA sequence.

The most pressing issues in genosensors

Some excellent prototype devices have been proposed to date, such as MEQ-LAMP and others.[44,120,140] While some signal amplification methods are justifiable, polymerase-based amplification clearly serves as the foremost, multi-purpose tool. Generally, it would be desirable to have fewer plausible points of failure and limit the amount of enzymes, nanomaterials, master-mixes, etc.

Label-free methods are very popular but as they are intrinsically capable of producing a signal without any secondary labeling, it may be

difficult to maintain full confidence under variable test conditions without a full suite of controls.

One of the biggest issues in genosensors is the sample automation. Generally, sample-to-answer platforms are the most convenient and desirable. While some simple tasks are soluble via capillary action or vacuum-chambers, the complex sample preparation for genetic measurements has typically been done by a pipetting robot. Currently, various microfluidic, electrowetting on dielectric (EWOD), magnetic beads or centrifugation options are encountered commercially for more complicated tasks.

Another very important challenge in genosensors is miniaturization. This means removal of the pumps, heat control, as well as power supply potentiostat and electrode size diminution by clever design. These two latter areas (sampling and miniaturization) are generally difficult to approach as doing so requires complete commitment to the current (electro)chemistry.

Genotyping is an important function that does not always get directly addressed in genosensors. The approaches of adding genotyping capability are often via multiplexing electrodes[120], temperature sweep melting[74,141] and using two allele-specific reporters on one surface.[61]

Generally, it is difficult to avoid readout multiplexing which poses assay and device design implications – intermittent versus constant electrochemistry, one-pot versus separate cells, shared microfluidics versus EWOD chips, analog signal conditioning and conversion and other important parameters.

In a broader context, electrochemical genosensor development to commercial products may be stifled by intrinsically low throughput. As compared to e.g., fluorescence where no direct chemical interaction is required (i.e., touching the solution), and 50-100 samples may be plausible in a minute with a single sensor. Highly intricate mechanochemical (QCM) or semiconductor (gFET) electrodes are at a further disadvantage from this perspective.

What about sequencing?

There are many applications where DNA sequencing simply cannot be replaced by genotyping or target detection, such as haplotype determination (e.g., identifying the interplay and assigning all present variations to one specific protein). Impressively, such subtle differences have been mechanistically verified *in vitro*.[142]

Electrochemical and electronic methods have been prolific in the rapidly evolving field of DNA sequencing and they will be briefly covered to contrast the technologies better.

In the early days of Sanger sequencing the only electrochemical application was gel, capillary[143] and later multi-capillary electrophoresis (Applied Biosystems 3100).[144–146]

Despite capillary analyzer improvements to 384-formats [147–149] electrophoretic methods had a general throughput limitation and the optical array-based Roche 454 analyzer brought a start to the NGS revolution in the mid-2000s.[150]

Despite the dominance of the chemiluminescence driven Roche 454 analyzer in the late 2000s and the latter overwhelmingly fluorescence-based systems (such as Illumina MiSeq, NovaSeq; PacBio RS; Thermo Fisher Scientific SOLiD; MGI DNBSEQ), electronic analysis methods have continuously brought innovations in the genetic assay field.

Sequencing by synthesis (SBS) was elegantly translated into electrical detection bringing about the Ion torrent analyzer soon after its commercial breakout via ion-sensitive field-effect transistor (ISFET) based detection.[151]

A very exciting approach to electrical sequencing readout followed with Oxford Nanopore MinION. [152–154] The device uses a transposase and sequencing adapters ligated onto a long genomic DNA strand. The readout is at 400 bases s^{-1} and over 4Mb length. The basecalling is processed via measuring current passed through the nanopore at a bias voltage. The company followed up with PromethION in 2017 massively expanding the throughput with 24 flow cells.

Prayoga Life Sciences GenapSys Sequencing Platform added to the list with their novel electrically detected SBS approach. It uses solid phase one nucleotide at a time addition which produces continuously increasing electrical impedance in steps corresponding to the added nucleotide.[155]

LiDia-SEQ, an ISFET-based device with sample-to-answer onboard processing is being developed by DNAe.[156]

Further innovation has been demonstrated by the recently announced Roche Axelios 1 sequencer. The device will measure current through a nanopore by using a chemically labelled DNA sequence. The target sequence is converted to Xpandomer sequence by coupling expandable nucleoside triphosphate bases containing polyamine, polyphosphate and polyether moieties. As the Xpandomer surrogate passes through a nanopore, the current for each base is much more identifiable than for a corresponding DNA polymer. [157]

Structural variations (such as alterations in gene copy numbers or translocations) are detected at larger scales of the genome (100s to 100 000s of base pairs) than DNA sequence mutations. OhmX, a solid-state resistance-based electronic nanochannel commercial solution (single-molecule) has been developed by Nabsys and released in 2023. [158]

Overall, electronic or electrochemical DNA sequencing readout has seen numerous applications. While sequencing workflows are generally significantly more expensive than a genetic ("molecular diagnostics") assay, they can provide invaluable insights.

DISCUSSION

The relevance of DNase and RNase in environmental and diagnostic fields.

Both RNase and DNase monitoring are important and effective tools in biobank, calibration and testing laboratories.[159] This is especially noteworthy for laboratories where nuclease digestion takes place as a step in nuclear material isolation or fragmentation. At the same time, bacterial DNA/RNA in environmental or food samples may undergo rapid degradation in presence of nucleases, making genetic environmental tests unreliable. Therefore, detecting the nuclease activity in samples may be a viable precaution. Extraneous DNase seemingly did not impact DNA detection in intact *C. jejuni* cells (20 °C and 55 °C pretreatment), but for cells lysed at high temperatures, external DNase significantly decreased the nuclear material.[13] Extraneous RNase I has been shown to degrade environmental RNA with a strong impact on 16S rRNA, which is generally a good target for determining species.[160] Considering that environmental tests for known sequences are strong candidates for affinity based detection, the ability to screen samples for nucleases is a powerful feature for future genosensors. Our sensor (**Publication 1**, workflow: **Figure 1**, mechanism: **Figure 8**) measured DNases recovered in environmental samples (swabs) ranging between 0.05 U ml^{-1} (a breakroom table) and 0.0013 U ml^{-1} (a computer keyboard) DNase I equivalents.

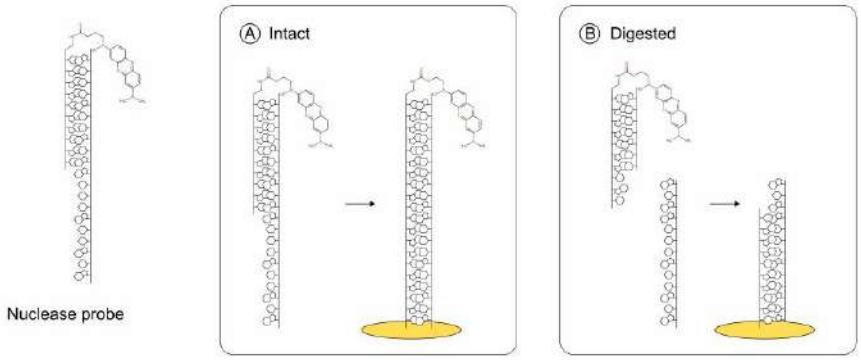

Figure 8. A representation of the nuclease detection mechanism used.

Similarly, discernible activity was detected in commercial protein preparations >0.05 U ml^{-1} (Glucose oxidase) and 0.0058 U ml^{-1} (Papain),[161] indicating a widespread and unpredictable, nuclease contamination. Overall

performance was comparable to commercial assays (**Figure A1 1**, **Appendix I**)

Both human endonucleases[162] and exonucleases[163] have been reported to have significance in cancer diagnosis.

In short, our nuclease biosensor can be used in biotechnological and diagnostic fields. Both RNase and DNase detection sensitivities were comparable to commercial kits but had lower dynamic range.

The relevance of signal amplification in genosensors.

The sensitivity in affinity based detection is twofold: there are the equilibrium association and dissociation constants and there is the signal to noise. Increasing the signal therefore entails producing a *stronger response* at, say 0.1% surface saturation and/or increasing the *target density* on the surface.

We can see that the 1–10 nM limit of detection in our genosensors could perhaps be attributed to the fact that a substantial fraction (a few %) of the target is captured and concentrated on the surface. At 0.8 nM [Target] there are more *available* probes on the surface than there is sample in the entire bulk of the solution (100-120 µl), (**Table 1**).

Target, nM	Target, nmol	Target captured, nmol 0.031 cm^{-2}	Target captured, %	Molecules, cm^{-2} (Reporter)	Probe molecules, cm^{-2} (RuHex)	Surface saturation, %
0.8	9.6×10^{-5}	$1.42\pm0.2\times10^{-6}$	1.5%	2.7×10^{10}	3.5×10^{12}	0.8%
3	3.6×10^{-4}	$1.19\pm0.4\times10^{-6}$	0.3%	2.3×10^{10}	3.5×10^{12}	0.7%
12.5	1.5×10^{-3}	$6.7\pm4.6\times10^{-5}$	4.5%	1.3×10^{12}	3.5×10^{12}	37.3%
50	6×10^{-3}	$1.5\pm0.08\times10^{-4}$	2.4%	2.8×10^{12}	3.5×10^{12}	81.1%

Table 1. 5×SSC solution hybridization (20 minutes, one-pot, 37°C) efficiency, of a flush DNA target on regular DNA probes (data from **Appendix V, Figure A5 2)**. At 0.8 and 3 nM, detection is not observed (*Note: with density-controlled ZNA electrodes, 3.2 nM [Target] is readily visible*).

Indeed, an increase in target density via probe density seems unproductive. An improvement of 3–6× was achieved in our system by controlling the probe density (see **Figure A5 3B**) and this likely cannot be improved any further. Packing more DNA onto the surface will decrease the

hybridization efficiency, where "high density" surfaces ($>5\times10^{12}$ molecules cm^{-2}) trend towards 10–20% efficiency.[64] In our case, the area just above the gold (12.5 nm) should have on the order of 4 mM DNA.

Target hybridization efficiency improvement at low DNA concentrations was attempted by "forcing" the hybridization through different hybridization buffers as improvements have been noted in literature.[164] The differences between the 5×SSC and the 30% EtOH HEPES buffers were minimal (See **Appendix V, Figure A5 2**). Some other buffers (such as 20% MeCN HEPES or regular PBS with a large amount of blocking oligonucleotides – to check for target depletion via adsorption onto plastics or degradation) have been briefly tested and showed no signal at low (a few nM or lower) DNA concentrations and such experiments were not further pursued. As an article by Vanderhoeven et. al. succinctly states: "… *spot intensity and the final detection limit are purely equilibrium-dominated quantities, and can hence not be improved by hybridization enhancement methods*…"[165] and arrives to the conclusion that only changing the dimensionality or reducing the feature size may improve the LOD. Notably the authors state that the LOD is improved via the sample **concentration** increase through volume contraction. Our experiments led us in a similar direction arriving at low volume *ex situ* hybridization in a dedicated low volume vessel which is not used for any measurements. Another team has found that smaller feature size improves the hybridization efficiency and that the feature edges show much improved hybridization efficiency.[166] An improvement in efficiency was also observed through glycol spacers – where a longer spacer (up to a certain point) results in higher DNA capture.[167] Others report that a 5 µm feature microarray behaves as well as a 30 µm one. The study shows that the median fluorescence intensity follows the trend 5 µm > 8 µm > 30 µm, but it is difficult to tell if the arrays are directly comparable. [168] My preliminary results (See **Appendix V**) indicate that no real improvement in sensitivity was had by lowering the feature size (K_D: 2 mm = 3.8 nM, 1.6 mm = 3.7 nM, 0.5 mm = 3.5 nM) (**Figure A5 1**). At 0.5 mm diameter, it is notable that the overall current and the signal to background become quite poor (i.e., any electrical noise or system capacitance will have a larger impact).

Ø	K_D
0.5 mm (ds-SAM)	3.5 nM
1.6 mm (ds-SAM)	3.7 nM
2.0 mm (ds-SAM)	3.8 nM
2.0 mm (ss-SAM)	28.5 nM

Figure A5 1. The hybridization sensitivities of different electrode disc sizes.

Albeit these were not true microelectrodes, a decrement of 2 mm → 0.5 mm, represents an area reduction of around 15×, therefore a change in the sensitivity on this scale would be clearly distinguishable, bringing the K_D to 0.2 nM range. This mechanistically represents the total probe molecule impact, ruling out the target depletion mechanism.

In these electrodes, the concentration gradient is maintained at around 3 nM → 4 mM solution to surface (4 mM is an arbitrarily calculated "concentration" of the DNA monolayer). These results strongly imply that the mass transport (I typically used a 20-minute solid phase capture interval for practicality) is the main limitation.

At the same time, (assuming 5 nm DNA molecule diameter), the fraction of the "outer layer" probes (circumference probes at the electrode edge, having few neighbors and thus very easily accessible) to total probes on the electrode increases around 4 times. However, the outer layer fraction is meaninglessly small, on the scale of 1 in 10^6; therefore, this size reduction does not realistically test the impact of the probe accessibility mechanism. This mechanism was not further explored as very small electrodes would mandate very low current measurement, which brings its own hardware and non-diffusing molecule LSV signal transduction problems.

The bottleneck of low currents when measuring very small electrodes with slow charge transfer via potential-sweep methods emphasizes the appeal of constant-potential methods with a diffusing molecule as a signal carrier, therefore, amperometry may be a viable choice for miniaturization.

In terms of an amperometric detection we have published a method for chemical reduction-mediated signal amplification (**Publication 2**, workflow: **Figure 2,** mechanism: **Figure 9**).[169]

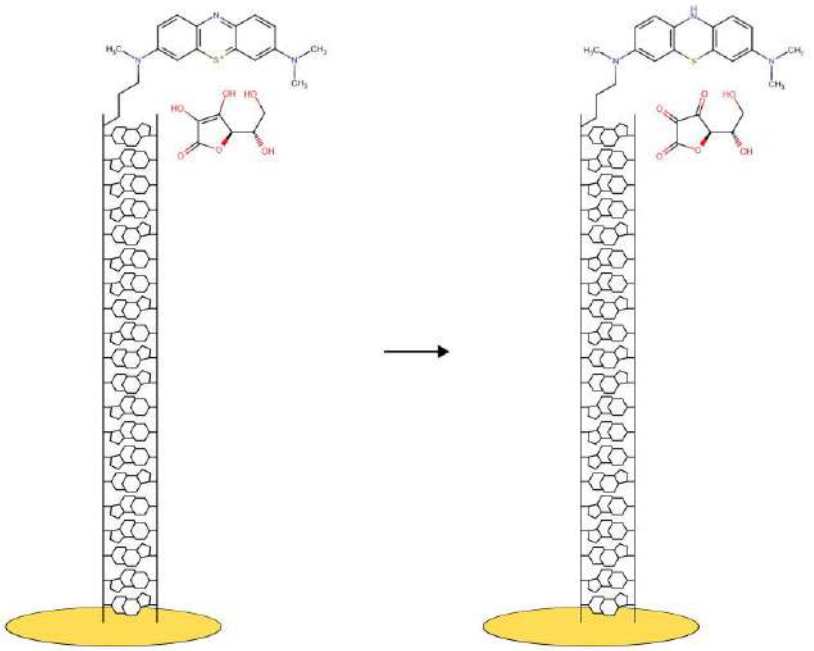

Figure 9. Chemical MB label reduction at the electrode.

While relatively small signal amplification was achieved (a few nanoamperes at saturation) this method remains intriguing for microelectrode use. It is possible that drastically lowering the surface area will allow for extremely low sample volumes. At the same time, ascorbic acid diffusion would be improved. An amperometric approach may perform better at very low currents than a potential sweep as it eliminates the capacitive component. Thus, this approach remains interesting. I have demonstrated for clarity that the reaction still works in a sandwich configuration and in multiplex readout, but was unable to improve the reaction rate via label positioning (see **Appendix II**). Reaction rate loss has been reported in a similar system upon chemically modifying nucleobases, indicating that the oligo construct clearly impacts the reaction.[170] In my experiments, positioning the MB label in the middle of the DNA chain completely destroyed the detection with DNA probes, but not with ZNA probes (see **Appendix II, Figure A2 2**).

In short, sample size contraction and DNA probe density control produce viable but limited improvements in sensitivity. Altering hybridization buffer composition or electrode size reduction down

to 0.5 mm did not notably improve sensitivity. Further feature size reduction is desirable but will likely present very low currents. A reaction monitoring approach for real-time measurement of hybridization is presented.

The relevance of conjugation in biosensors:

Broadly speaking in chemical and biochemical assay **methods** and standalone **components** (e.g., magnetic beads, affinity resin, solid phase peptide synthesis, batteries etc.) solid phase (bio)molecule grafting is a process of the highest importance. However, it is in my personal experience and observed by some others that verifying *the nature* of the coupling chemistry is difficult.[171,172] In fact even differentiating between adsorption/ agglomeration/ precipitation and grafting presents extreme difficulties. This is due to i) minute chemical differences between a ligated and an adsorbed molecule and ii) a single molecular layer represents a small quantity thus requiring a high sensitivity method. Therefore, it is common for a grafted molecule to be confirmed via i) function or ii) presence but not often via iii) chemical bonding. Often the various ligation chemistries (e.g., comparing the assay using two completely different surfaces, solvents or antibodies, etc.) are compared as "apples to oranges". This is somewhat unavoidable because the reagents, the biomolecules and the surfaces have drastically different behavior (due to size, charge, intermolecular interactions etc.), which cannot be easily compensated for. Unfortunately, "non-ligation controls" (e.g., minus carbodiimide) are not standard especially in more complex assays.[172–174]

The inability to confirm coupling with high confidence can become a serious problem when designing new grafting chemistries and manufacturing processes.

The widespread use of blocking agents (often containing naturally occurring proteins, oligosaccharides or synthetic polymers[175]) in bioassays further emphasizes the pervasive problem of unexpected adsorption events. If a low solubility compound forms a strong non-polar interaction, it can be surprisingly difficult to remove.

For nucleic acid detection, solution phase recognition is the extremely scalable in terms of price and volume, e.g., for primer-polymerase methods you could manufacture a million reactions worth of master mix. Unfortunately, it becomes impossible to manage a library of >1000s of primers, unless they are adhered onto a substrate. Currently, it is desirable to attach DNA probes via various linkers to change their behavior (e.g.,

flexibility, charge) and to selectively bind specific sequences to multielectrodes.

The main methods to study grafting or chemical modification of a surface at the moment are XPS/ESCA for **composition** and oblique reflection FTIR/PM-IRRAS or AFM-IR for **bonding**.[176,177] All three are highly specialized methods. Other methods like AFM,[178] SEM,[179] liquid scintillation,[180] antibody staining[95] or SPR[181] are capable of confirming the presence of a modification but are not usually able to indicate bonding.

Through this discussion I wish to bring attention to an important bottleneck in sensor array development (research and optimization) and manufacturing (quality control). When developing a novel directed ligation chemistry (*I wish to keep the methods outside of the scope of this dissertation as these processes are still in development*) I have run into a case of interfering non-directed ligation or adsorption problems which serve as a good example of SERS-active electrode application. (**Figure A3 6**).

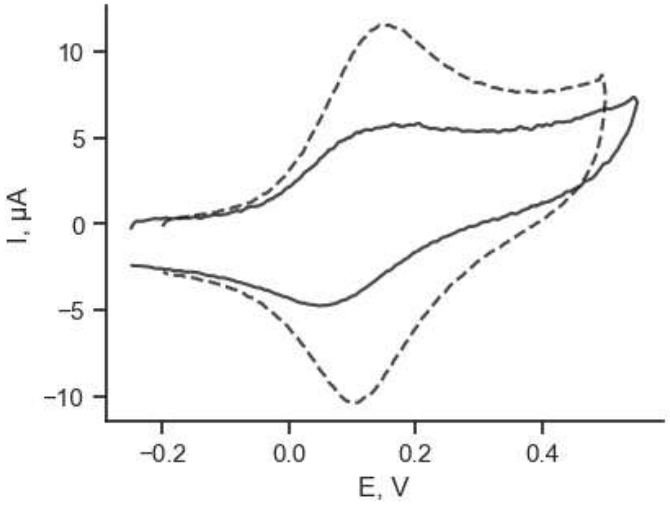

Figure A3 6. A directed ligation chemistry currently in development. **Dashed line:** directed ligation, **solid line:** simultaneous non-directed coupling side-reaction onto a nearby electrode.

In other words, a neighboring electrode in an array (intended for a subsequent modification for a separate target) may parasitically couple to a biomolecule during the first step, and perhaps, show an electrochemical signal (i.e., presence detected, without revealing the mechanism). Such non-directed cross-reaction may well occur in photo/electrochemical, fluidic, thermal, dropcasting or other means of directed array modification,

underscoring the importance of a rapid, inexpensive, sensitive and spatially-addressable auxiliary surface structural analysis method.

An interesting prospect arose during our SERS-active electrode testing (**Publication 3**, workflow: **Figure 3**), where various surface modifications could be structurally detected. Turns out, the adsorption and ligation of 4-aminobenzonitrile (used as a proxy for a biomolecule) can be differentiated based on the relevant functional group bands (see **Appendix III, Figure A3 4**).

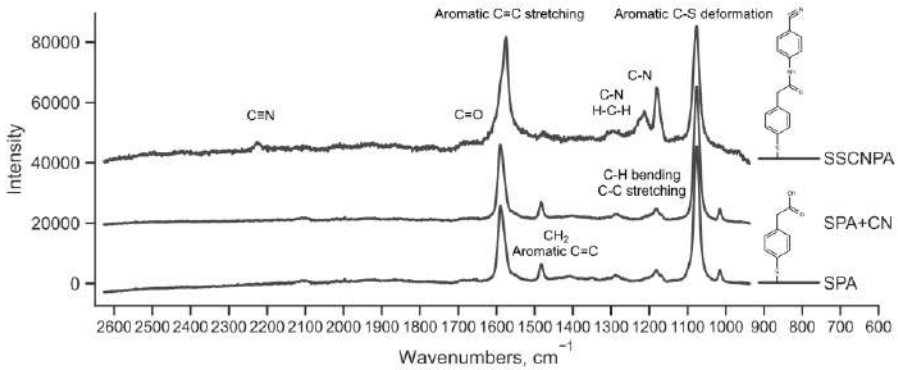

Figure A3 4. SERS spectra of SSCNPA, SPA + CN and SPA (clean) with tentative peak assignments.[182]

While limited to a gold substrate this is a facile and rapid means to measure bonding. Such an application clearly elevates the research and manufacturing relevance of these electrodes. Most interestingly, the preliminary SERS experiments indicate that nanostructured gold enhances the proximal (nearby) functional groups much better than the more distant ones. Therefore, in principle there is selectivity for nearby bonds while far-away bonds may perhaps be selectively enhanced separately afterward.

Aside from one or two-step couplings/graftings, conductive polymers and MIPs (molecularly imprinted polymers) are some of the very few commonly encountered solid phase synthesis products in electrochemical analytical methods.

On the other hand, "piece-wise" receptor construction on the electrode is almost never used (i.e., solid phase synthesis of peptides[95] and proteins to capture small molecules, oligonucleotides to capture DNA or, for instance, oligosaccharides to be used as antigens).

Fundamentally, step-wise solid phase synthesis is a perfectly viable and powerful approach, especially for highly diverse molecules. If a deprotection

or a coupling reaction can be easily confirmed via a SERS measurement, these step-wise methods may become more approachable.

Another plausible application yet to be explored is confirming directed (oriented) antibody linking.

In short, if solid phase synthesis or directed conjugation methods on electrode surface do gain traction in the future, SERS will be a good option for verifying the reactions. Verifying one-step coupling is currently viable on SERS-active electrodes.

The importance of signal transduction in affinity genosensors:

A major signal transduction problem was encountered with larger DNA target molecules where the distal DNA overhang produced significant interference (**Publication 4**, workflow: **Figure 4**, signal transduction: **Figure 10**). It was suspected that the MB label was encapsulated by the overhanging strand's negative charges or lost mobility through the increased hydrodynamic radius and thus, the MB label was unable to approach the electrode.

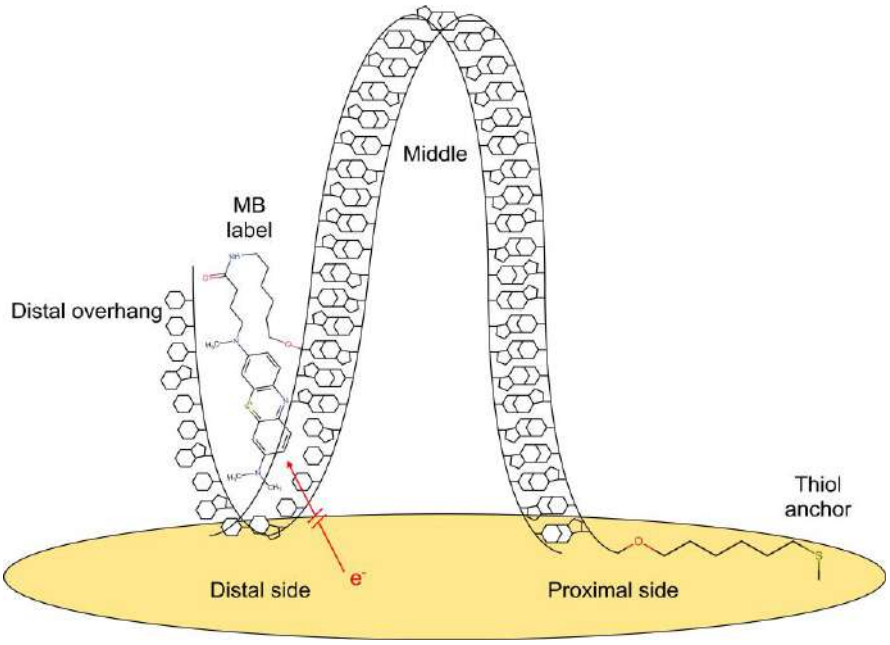

Figure 10. Sandwich representation containing the **DNA probe** and **R*1** which has a distal MB label. Only the distal **T*1** overhang is shown. The sandwich is likely in a more "upright" conformation than shown. This is an

attempt to represent a macromolecular structure. The "average" conformation is not known. Elements are not to scale.

As the label is on an upper reporter strand it was impossible to get the MB labels proximal to the surface. An attempt was made to chain the electron transfer through:

ReporterMB → ProbeMB → Probe|Target → Electrode

This approach would dramatically increase the remaining MB background post melting but I expected to account for it via data fitting. Unfortunately, this approach was also unsuccessful (see **Appendix IV, Figure A4 2.2.**).

Our results were comparable to other sources. Silva et. al.[183] show findings where if we assume perfect hybridization, as the probe density is quite low, we can extrapolate an MB label position to signal relationship as such:

ssDNA: Distal > Almost proximal ~ Almost distal ~ Proximal

dsDNA: Proximal > Almost proximal ~ Distal > Almost distal

This "Almost distal" middle position proves highly unfavorable for a label as it is electronically (due to encapsulation by negative charges) blocked from approaching the surface. Similarly, rather than affixing the label towards the middle, keeping the label proximal and lifting the whole duplex upwards via a spacer (where the probe effectively has a proximal overhang) produces increasingly lowered signal.[184] *Note: if we were measuring say, some phenoxazine derivative at +0.8 V vs. Ag/AgCl, these observations may no longer apply.*

If the mechanism of conduction through dsDNA stacked nucleobases is assumed this behavior becomes very difficult to explain. To further this point, a distally MB-labeled ssRNA target performed perfectly well in an RNase sensing application in **Appendix I**.

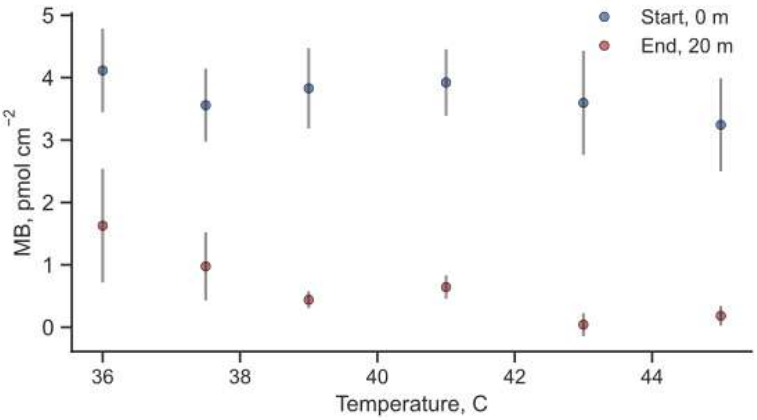

Figure A4 1.3. (from Appendix IV) shows the starting and end MB signal at various temperatures.

Unexpected dsDNA bending has been observed in solution at frequencies of up to a hundred thousand times higher than predicted.[185] One of the proposed mechanisms is the melted-bubble model where DNA spontaneously forms melted sites at ambient conditions.

Figure A4 1.3 shines additional light on the matter of *through-DNA* versus *DNA-mobility* mediated signal transfer. Through-DNA transfer relies on the idea of a fully pi-stacked chain, but we know this is not the case in nature where DNA is constantly partially melting and reannealing. If ds-DNA were the conductor, we would expect a temperature-dependent loss of signal, rendering all melting-based sensors impractical.

An important observation regarding ssDNA came from Uzawa et al.[186] where no impact on charge transfer was noted from probe packing density. This implies that DNA crowding is an unlikely explanation to poor signal transduction.

In our case, the PCR amplicon has distal overhangs which impede the voltammetric signal significantly (see **Appendix IV, Fig. A4 1.2**). To fix the signal transduction, it would have been reasonable to attempt inverting the probe and reporter strands so that the target molecule hangs "downwards" toward the surface, but I was concerned about the impacts this would have on hybridization. With on the order of 3.5×10^{12} probes/cm^2 we suspected our electrodes to be near 10% of the maximum theoretical ssDNA packing[187] and in practical terms at maximal density for dsDNA.[62] The inversion of sandwich geometry therefore raised valid concerns. The DNA probe molecules in the immediate vicinity of the inverted target may repel the oncoming reporter molecules.

A safer approach seemed to collapse the sandwich structure, thus eliminating the signal transduction problems. This was attempted via polyamine containing ZNA–4 probes lowering the net charge of the probe molecules from –21 to –10. This approach was very successful, eliminating the signal transduction problems and granting tolerance for overhanging PCR-produced targets.

Note: at the probe charge of –10, a very small amount non-specific reporter adsorption could be observed if the electrode is interrogated immediately after hybridization and without reaching 42 °C. This is acceptable in our system, however, at complete neutrality we would expect unwanted DNA adsorption.

In contrast to probe-linked polyamines, adding free polyamines into solution would possibly result in uncontrollable polyamine accumulation and possibly lead to non-specific DNA adsorption.

Another successful approach to fixing the charge transfer problems was also attempted. By attaching MB via a flexible polyethylene glycol sidearm rather than directly to DNA, the MB mobility is improved. This approach now works in both DNA– and ZNA–probe sandwiches, with a longer distal (3') sidearm being the most preferable (**Figure A4 4.2**).

In short, while it is believed that charge transduction through dsDNA occurs, I was unable to force electrochemical transformations of DNA-tethered methylene blue in many configurations. It appears that under the experimental conditions used, the charge transfer is occurring via DNA label mobility.

The importance of SNP assays

Distinguishing between two single base-mismatched sequences and their combination can give information about slight differences in proteins between individuals which is highly applicable to diagnostics.

In **Publication 4**, a PCR amplicon is captured onto a solid phase probe, and interrogated with 2 different allele-specific reporters. In addition, an approach similar to gene sequencing allows us to gain extra sequence information during the screening of a specific target (see **Appendix V, Figure A5 5.**).

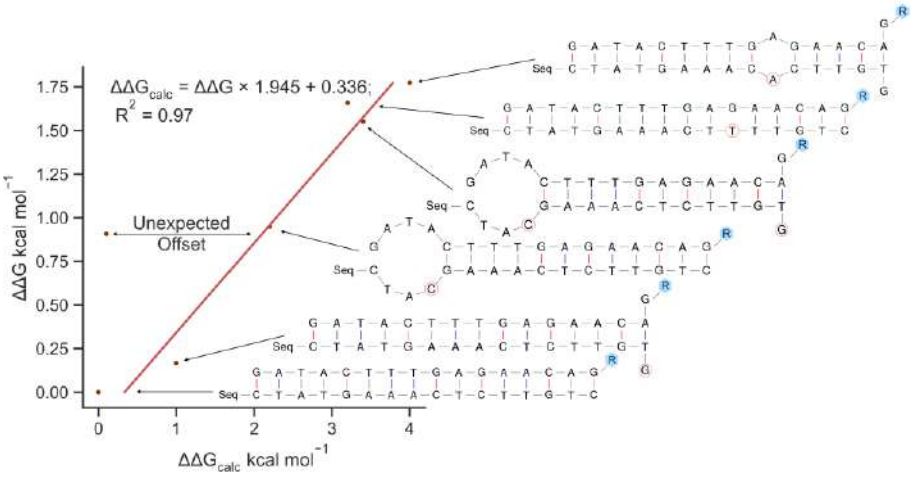

Figure 11. Sequence-dependent changes in hybridization energy. Data from **Publication 4**. Unexpected offset denotes a digitally unaccounted for nicked site heterocyclic base stacking interaction (and is equal to the stacking affinity) (see **Publication 4**).

Albeit the genosensor was designed for multiplexing, in terms of true scalability, the use of a specific reporter sequence is a major challenge. Objectively speaking, the use of **target-specific reporters** after a certain point is not scalable. Once you are trying to measure up to 200 million sequences it becomes to the best of my knowledge, impossible to manage the fluid handling. While various innovative liquid handling approaches have been proposed such as voltage-mediated dispensing from droplets,[188] or electrowetting on dielectric[189] this is likely an insurmountable obstacle. For instance, Ion Torrent uses on the order of 8-14 solutions in total for any DNA target.[190,191] Therefore, the scope of applications of the proposed assay falls more into the characterization of a handful of genetic targets.

The genosensor was not only able to detect different genotypes in real, non-invasive saliva samples, but also characterize various other mutations by how destabilizing they are. This was also translated into the units of kcal mol^{-1}, allowing for measured vs. calculated energy comparison (**Fig. 11**).

Solution phase Gibbs free energy has been recently used in assay design to predict crosshybridization; with a recommended difference of $\geq -9 + 7.5$ kcal mol^{-1} ΔG which results in around $\geq$1.5 kcal mol^{-1} $\Delta\Delta G$ under given conditions.[192] This is not too dissimilar from the sequences we selected for our study, comprising around 2.2 kcal mol^{-1} (solution phase $\Delta\Delta G$) in the case of homozygotes and half that in the heterozygous allele (see

Publication 4). The strength of the DNA base stacking interaction was found to be on a similar magnitude. I calculate the A|G base stacking energy to be on the order of **2.0 ± 0.3 kcal mol^{-1}** (literature ~2.1 kcal mol^{-1}).[193]

The obtained equilibrium constants (**Appendix V**, **Figure A5 1**) are quite reasonable as they suggest the binding to be on the order of 10.9–12.2 kcal mol^{-1} depending on the probe density (in agreement with DinaMelt provided sequence-based hybridization ΔG of 12.1 kcal mol^{-1}). Interestingly, when compared to DNA hybridization, antibody-antigen and aptamer-ligand equilibrium dissociation constants are not significantly better.[194,195]

In DNA affinity sensors a fundamental limitation is reached where a sample solution containing a similar quantity of DNA to the amount of the interrogating probe (or size and density of an interrogating surface) will likely give poor signal. At 0.17 pmol/surface (0.0314 cm^2) that is 1.7 nM for a 0.1 ml sample. In practice (see **Appendix IV**, **Figure A5 3**) the signal becomes clear in the range of 3-20 nM. However, a 1.7 nM solution of the human genome (if amplified and processed) when translated into 30 bp oligos equals a solution with ~350 mM oligos. In practice a DNA oligo solution of 5 mM (on the order of 100 mg/ml), is already highly concentrated and can show marked changes in viscosity. For a more general sequencing application a dramatic reduction in electrode size would be necessary.

In short, a novel genotyping platform has been developed, capable of genotyping heterozygous samples at ~ 10 nM of DNA. This suggests that the current sensitivity of the genosensor is perhaps three to four orders of magnitude too low to perform "sequence fishing" in a fragmented whole genome amplicon of a sample, yet, if tergeted amplification is used, it is possible to extract some sequence information.

A summary of the broader insights

Generally, these genosensors are suitable for the analysis of any nucleic acid sequence, indeed we have observed good signal transduction form an RNA reporter. Besides recognizing a specific oligonucleotide, these assays can be implemented to: glean additional sequence information, quantify relative and absolute abundance, observe nucleolytic reactions and likely others, like ligation, extension, etc.

Significant improvements were introduced to lower the required amount of DNA from the first iteration (~195 pmol) such as *in situ* hybridization signal amplification via a redox reaction (~25 pmol) and *ex situ* hybridization (~0.5 pmol). Attempts of hybridization acceleration, surface miniaturization, attempting to route the redox signal transfer, chemical signal amplification generally provided only marginal improvements in sensitivity. DNA probe density and sample contraction provided only linear improvements, but were impactful in ensuring good sensitivity. MB-labeled DNA appears to perform the redox charge transfer though a chain mobility or other physical proximity mechanism.

Applying this system to real samples research has led to an innovative incorporation of charge-altering ZNA probes enabling the use of targets with larger overhangs. This is yet to be published, but non-charge altering ethylene glycol spacers between the DNA and the MB molecule performed equally well (in combination with both DNA and ZNA probes).

While the DNA concentration inference from the hybridization rate is accurate and also sufficient to detect DNase and RNase with good sensitivities, fundamentally, the dynamic range for nuclease measurement is quite low, as the concentrations needed for rapid hybridization are moderate.

While the chemically (ascorbate) amplified hybridization rate measurement can be performed in real time, the obtained currents were quite small, requiring a considerable amount of time (~ 1 h) to reach saturation. With constant temperature and electrode potential, this approach could provide the benefit of inexpensive and simple electronics.

While the decay curve of DNA melting contains its sequence information, the resolution we currently have is much too small to perform a *de-novo* sequencing of a 16-bp region. Low salt concentration and the addition of formamide allowed us to measure relatively rapid (15-20 min) melting reactions at moderate temperatures (42 °C). This sensor ignores by design any need to carefully control the reporter strand crosshybridization to a mismatched target and exploits this behavior.

CONCLUSIONS

Overall, three nucleotide affinity based biosensor types were produced. The results are as follows:

1. DNA and RNA sequences were detectable voltammetrically (hybridization), amperometrically (hybridization) and voltammetrically (dehybridization) in “synthetic” and real samples.

2. Point mutations were detected in homo- and heterozygous diploid samples, isothermally. 5 human saliva samples were genotyped for CYP2C19 *1 and *17 alleles correctly.

3. Sensor-relevant design features were explored and incorporated.
   3.1. SPE use for nuclease detection.
   3.2. A prototype analyzer was produced for Nucleases.
   3.3. Nanostructured porous gold electrodes were developed allowing to observe spatial and molecular properties via SERS.
   3.4. Electrode chemical functionalization assessment via SERS was demonstrated as a proof of concept.
   3.5. A direct PCR amplification followed by direct hybridization were used without sample DNA or amplicon purification.
   3.6. Isothermal methods significantly lower the device complexity, size and energy use.
   3.7. Amperometric DNA quantification was explored as it is important for microelectrodes and would simplify the potentiostat design.
   3.8. Analysis of diploid samples achieved on a single surface.
   3.9. One-pot melting analysis with solid phase hybridization was achieved, thus removing pumping, heating and waste removal steps.
   3.10. *Ex situ* hybridization allows for sample pooling, amplification multiplexing and sample reuse.

Genetinio kodo sekų detekcija yra ypatingai plati sritis turinti didžiulę įvairovę taikinių. Tokie metodai leidžia identifikuoti ir apibrėžti mikro- bei makro-organizmus bei jų savybes. Sveikatos apsaugos sritys remiasi ypatingai svarbiais DNR paremtais diagnostiniais metodais kaip navikų arba sveikų ląstelių žmogaus genomo charakterizavimas. Šie metodai dažnai naudojami parinkti tinkamiausiai gydymo krypčiai. Pavyzdžiui, farmakogenetinis žymuo gali būti nustatytas vieną kartą prieš farmakoterapiją, tuo tarpu vėžinės ligos progreso stebėjimas gali būti naudojamas ir terapijos metu.

Geneojutikliai yra biologiniais procesais paremti prietaisai galintys specifiškai aptikti DNR arba RNR grandis. Genojutikliai pasižymi prieinamumu, tiek savo kaina, tiek savo paprastumu, ir jų naudotojai turi tiek asmeninių duomenų, tiek analitinio instrumento fizinę kontrolę.

Žinoma, žmogaus genomas nėra vienintelis taikinys, mikrobinės taršos nustatymas maisto, vandens ir kitose terpėse taip pat yra svarbi užduotis, tinkama genetinės analizės metodams. Mikrobiologiniai organizmai kaip *Legionella pneumophila*,[9] *Escherichia coli*[10] ir *Enterococcus*[11] gali būti matuojami **vandens mėginiuose**, įvairūs pelėsiai[12] – **oro mėginiuose**, bei *Campylobacter jejuni*[13] ir *Cyclospora cayetanensis*[14] – **maisto mėginiuose**.

Dar viena taikymo kryptis yra infekcijos sukėlėjų identifikacija bei, dažnai tuo pačiu metu atliekami, antibiotikų atsparumo matavimai. Įvairių mikroorganizmų kaip SARS-CoV-2, Ebola, ŽIV, Hepatitas C, *Clostridium difficile*, meticilinui atsparių *Staphylococci*, VanA turičių *Enterococci* bei kitų organizmų aptikimas yra dažnai taikomas.[15,16]

Problematika

Biojutiklių kontekste, nors įvairūs signalo stiprinimo metodai suteikia didelius jautrius, DNR sekos replikacija polimerazėmis atlieka tiek signalo stiprinimą, tiek mėginio apdorojimą vienu metu. Taigi, DNR (arba RNR) amplifikacija yra turbūt dažniausiai naudojama fermentinė reakcija genojutiklių dizaine. Atveijais kai metodas atsiremia į fermentinę (arba kitais baltymais, pvz., antikūnais paremtą) amplifikaciją, tipiškai, metodo veikimas yra apribotas baltymo stabilumo ir tokie metodai gali būti mažiau tinkami komerciniam analizatoriui kurti. Dizaino atžvilgiu, norima signalo pernašą paremti paprastesniais zondais. Žinoma, norint tyrinėti baltymų-DNR sąveiką, tokie metodai yra nepakeičiami.

Metodai nenaudojantys žymėjimo (angl. label-free), yra labai patrauklūs, tačiau, išgaunant signalą tiesiai iš mėginio reikalinga didelė imtis

kontrolinių matavimų, kad įsitikinti ar antriniai mechanizmai negali sukelti nespecifinės detekcijos.

Viena iš didžiausių kliūčių genojutiklių kūrime yra automatizuotas mėginio paruošimas. Paprasti skysčio transporto uždaviniai yra sprendžiami kapiliarinės jėgos arba vakuumo pagalba, tačiau sudėtingesni – reikalauja mikrofluidikos, dielektrinės membranos elektrodrėkinimo technologijų (angl. *electrowetting on dielectric*) arba pipetavimo robotų. Modernūs mėginių apdirbimo instrumentai taip pat dažnai naudoja magnetines nanodaleles, elektroforetinius mėginio apdorojimus bei centrifūgavimą. Kitas svarbus žingsnis yra miniatiūrizacija, t.y. pompų bei kaitinimo sistemų pašalinimas ir elektrodų bei potenciostatų (ir jų maitinimo šaltinių) sumažinimas.

Genotipavimas (DNR atpažinimas organizmo kontekste) yra kitas svarbus iššūkis sprendžiamas daugybiniais elektrodais[120], kintamos temperatūros lydymu[74,141] ir naudojant du aleliams specifiškus zondus kartu ant vieno paviršiaus.[61]

Bendrame kontekste, elektrocheminė detekcija reikalauja skystinio kontakto su analizuojamu mėginiu ir ši mechanika fundamentaliai riboja mėginių nuskaitymo spartą lyginant su pvz. fluorescencija, kur vienas fotodetektorius gali pamatuoti 50-100 mėginių per minutę. Šis trūkumas ženkliai didėja su elektromechaniniais (angl. „QCM“) ir puslaidininkiniais (angl. „gFET“) prietaisais, naudojančiais daug sudėtingesnius paviršius.

Šia disertacija siekiama sukurti biojutiklius tinkamus specifinėms DNR sekoms nustatyti, kurie palengvintų genetinių matavimų atlikimą ir prieinamumą. Šiam tikslui pasiekti buvo apibrėžti 3 uždaviniai:

1. Specifinės DNR sekos aptikimas elektrocheminiais biojutikliais.
2. Taškinės mutacijos aptikimas biojutikliais bei atskyrimas homozigotinių ir heterozigotinių mėginių.
3. Šių uždavinių atlikimo metu, metodo dizainas turi supaprastinti arba palengvinti diagnostinio/analitinio prietaiso kūrimą. Technologiškai priartėjama prie realistiško prietaiso.

Šių uždavinių įgyvendinimą galime plačiai apibrėžti tikslinių nukleino rūgščių specifinio atpažinimo sistemų kūrimu, DNR molekulinių monosluoksnių bei hibridizacijos procesų optimizavimu, elektrocheminių signalų matavimu, bei duomenų analize. Atliekamos papildomos dizaino, charakterizavimo ir gamybinės užduotys.

Gauti rezultatai buvo paskelbti keturiuose straipsniuose. Tolimesni papildantys darbai buvo pridėti kaip disertacijos priedai.

Pirmajame straipsnyje buvo pademonstruotas elektrocheminis metodas bei naujas prietaisas skirtas nukleazių aptikimui. Šis prietaisas gali atlikti kiekybinius deoksiribonukleazės I matavimus ant vienkartinių elektrodų.

Nukleolitiniai fermentai yra svarbūs pramonėje bei diagnostikoje. Šis metodas naudoja dgDNR zondą, kurio skilimas (suvartojimas), sumaišius su kieto paviršiaus tepinėliu arba skystu mėginiu, gali būti pamatuotas pagal hibridizacijos greitį. Kadangi zondo hibridizacija ant komplementarios elektrodo sekos tiesiogiai priklauso nuo zondo koncentracijos, gaunamas hidrolitinės reakcijos našumas ir nukleazės koncentracija gali būti apskaičiuota. DNazės I aptikimo riba – 0,34 mvnt. ml^{-1}; Pirmame disertacijos priede sistema taip pat buvo patikrinta naudojant RNR zondą, kur RNazės A aptikimo riba – 1×10^{-6} Kunitz vnt. ml^{-1}. Šie rezultatai gerai prilygsta komerciškai prieinamiems (chromogeniniams / fluorogeniniams) rinkiniams.

Antrajame straipsnyje aprašomas befermentine redukcija paremtas DNR hibridizacijos signalo (nanoamperų lygio elektros srovės) stiprinimo metodas. Šis metodas paremtas imobilizuotos ant elektrodo paviršiaus, taikiniui komplementarios DNR grandies, ir metileno mėliu žymėtos taikinio DNR grandies hibridizacija matavimo celėje. Atliekant šį taikinio prijungimą su aksorbo rūgštimi tirpale, hibridizacijai ir cheminei metileno mėlio redukcijai palankiomis sąlygomis, išgaunamas amperometrinis signalas realiu laiku. Metodas leido aptikti specifines DNR molekules 5-100 nM koncentracijų intervale. Sistemos veikimas naudojant nežymėtą DNR taikinį papildomai parodytas antrame disertacijos priede.

Trečiame straipsnyje aprašomas vienkartinių bei daugkartinių aukso elektrodų paviršių oksidacinio nanostruktūrizavimo metodas. Šiuo metodu pagaminti elektrodų paviršiai pasižymi reikšmingu paviršiaus sustiprintos Raman sklaidos (SERS) stiprinimo faktoriumi – 1.4×10^{7}. Taigi, šie elektrodai yra tinkami (fiziniai) substratai tiek elektrocheminiams matavimams tiek spektroskopijai. SERS spektrai buvo tinkami identifikuoti tiek prijungtą 4-merkapto benzoinės rūgšties monosluoksnį, tiek nespecifiškai adsorbuotas doksorubicino molekules. Trečiame disertacijos priede yra aptariamas SERS pritaikymas įvertinti kovalentinėms paviršiaus modifikacijoms. Toks struktūrinis monosluoksnio charakterizavimas yra labai svarbus žingsnis kietos fazės DNR sintezei ir jungimo reakcijoms vystyti.

Ketvirtame straipsnyje aprašoma CYP2C19*17 alelio genotipavimo sistema. Citochromo P450 2C19 izoforma yra atsakinga už įvairių mažų molekulių oksidcinę apykaitą. *17 alelis yra nekoduojančioje genomo dalyje ir įtakoja fermento ekspresiją, kuri yra aktuali vaistų metabolizmui.

Ši sistema sėkmingai identifikavo įprasto (*1), greito (*1/*17) bei itin greito (*17) metabolizmo diplotipus, tiek švariuose sintetinės DNR mėginiuose, tiek seilių mėginių amplikonuose (specifiškumas >2σ). Sistema yra paremta DNR duplekso lydymosi kinetika ir mano žiniomis, tai yra pirmas izotermine disociacijos kinetika paremtas genojutiklis. Taip pat, ši sistema pasižymi reta savybe – diploidinis mėginys gali būti analizuojamas ant vieno elektrodo. Vieno paviršiaus santykinis signalas ženkliai supaprastina elektrodų gamybinio atkartojamumo problematiką.

Metodas buvo sustiprintas zip-nukleino rūgščių (ZNR) pritaikymu DNR atpažinimui ant kietos fazės bei asimetrine skystos fazės PGR – tokiu būdu sistema yra tinkama ilgesniems DNR taikiniams ir taikinių fiksavimas ant elektrodo gali būti įvykdytas iškart po amplifikavimo, be jokių gryninimo, fragmentacijos ar denatūracijos žingsnių.

Metodas taip pat buvo jautrus papildomoms taškinėms mutacijoms ir mano žiniomis, tai yra pirmas elektrocheminis jutiklis pamatavęs nukleobazių stekingo sąveikos stiprį (išraiška vienetais – kcal mol^{-1}).

Apibendrinantys pastebėjimai

Apibendrinant, šie genojutikliai yra platformos, fundamentaliai tinkamos bet kokios (santykinai trumpos) DNR sekos aptikimui ir net RNR yra pritaikoma analitė. Šių matavimų metu taip pat galima išgauti informaciją apie DNR sekos pokyčius, reliatyvų bei absoliutų kiekį, vykstančias nukleolitines reakcijas bei DNR ilgį.

Keičiant genojutiklių dizainą, DNR jautris buvo ženkliai sustiprintas nuo pirmo jutiklio naudojančio *in situ* hibridizaciją elektrocheminėje celėje (~195 pmol), iki *in situ* hibridizacijos redokso stiprinimo (~25 pmol) ir *ex situ* hibridizacijos (~0,5 pmol). Bandyti hibridizacijos greitinimo, elektrodo paviršiaus ploto miniatiūrizacijos, signalo pernašos mechanizmo bei redokso amplifikacijos krūvio pernašos patobulinimai nesuteikė ženklaus (pvz., >3×) DNR jautrio pagerinimo. DNR zondo tankis ant paviršiaus ir mėginio tūrio dydis keičia jautrį tiesiškai, tačiau leidžia reikšmingai ir nesunkiai pagerinti genojutiklio veikimą. Redokso molekule žymėtos, ant kieto paviršiaus esančios DNR krūvio pernašos elgesys sutampa su DNR mobilumo ar kitokiu fizinio suartėjimo mechanizmu. Nors signalo pernašos pagerinimui pritaikėme poliaminais modifikuotą krūvinį ZNR zondą (krūvio

kompensacija paremta pernaša), elektrocheminiai žymenys prijungti per lanksčius, nekrūvinius etilenglikolio intarpus taip pat davė puikų signalą (žymens mobilumu paremta pernaša). Abi pernašos pagerinimo strategijos suteikia galimybę matuoti DNR taikinius besitęsiančius virš atpažinimo zondų, tokiu būdu jutiklis nereikalauja apibrėžto ilgio taikinio.

Nors DNR (bei RNR) koncentracijos apskaičiavimas pagal hibridizacijos greitį yra patikimas ir tinkamas nukleolitinių fermentų reakcijų matavimams, šio metodo dinaminis diapazonas yra palygintinai siauras, kadangi vis mažinant DNR koncentraciją, hibridizacijos laikas ženkliai ilgėja.

Nors MB^+ redukcija askorbo rūgštimi leido matuoti hibridizaciją realiu laiku ir naudojo labai paprastas pastovaus potencialo bei temperatūros sąlygas, išgautos srovės buvo nedidelės, tuo tarpu hibridizacijos reakcija ir srovės prisotinimas gali užtrukti ilgai (kelias valandas).

Nors lydymosi kinetika savyje turi visos DNR sekos informaciją, lydymosi greičio (bei lydymosi energijos) rezoliucija yra ženkliai per maža atliki *de-novo* 16 bazių porų DNR mėginio sekoskaitai. Šis metodas yra labiau tinkamas aptikti vienai ar keletui mutacijų. Formamido pridėjimas kartu su žema [NaCl] leido matuoti greitą (~15-20 min) lydymąsi pakankamai žemose temperatūrose (42 °C). Šis matavimas išsaugo DNR taikinį ant kietos fazės ir automatiškai paruošia elektrodą antro žymens hibridizacijai.

Išvados

1. DNR ir RNR sekų atpažinimas buvo įvykdytas voltamperometriškai (hibridizacija), amperometriškai (hibridizacija), bei voltamperometriškai (dehibridizacija), „sintetiniuose“ ir biologiniuose mėginiuose.

2. Taškinės mutacijos buvo atpažintos homo- ir heterozigotiniuose diploidiniuose mėginiuose izoterminiu metodu. 5 žmogaus seilių mėginių CYP2C19 *1 ir *17 aleliai buvo teisingai genotipuoti.

3. Įgyvendintos automatizavimui ir miniatiūrizacijai svarbios dizaino ypatybės:
   3.1. Vienkartinių elektrodų pritaikymas nukleazių detekcijai.
   3.2. Sukurtas prototipinis nukleazių analizatorius.
   3.3. Sukurti nanostruktūrizuoti vienkartiniai elektrodai tinkami erdviniams ir molekuliniams SERS matavimams.

3.4. Pademonstruotas paviršiaus cheminio modifikavimo molekulinis kokybės kontrolės pavyzdys, paviršių sintezei.
3.5. Atlikta tiesioginė mėginių PGR amplifikacija ir tiesioginė amplikono hibridizacija, be gryninimo ar kitų žingsnių (atliktas skiedimas dėl mažo tūrio).
3.6. Izoterminiai metodai ženkliai supaprastina prietaiso energijos sąnaudas, kompleksiškumą ir dydį.
3.7. Panaudota amperometrinė detekcija, kuri supaprastina potenciostato dizainą.
3.8. Pademonstruotas amperometrinis dviejų elektrodų hibridizacijos matavimas vienu metu.
3.9. Įgyvendintas vieno elektrodo (su prihibridizuotu taikiniu) matavimas dvejais zondais diploidiniams mėginiams.
3.10. Įgyvendintas vienos talpos (angl. *„one-pot“*) lydymo matavimas – panaikina pumpavimą, elektrodų plovimą, skystas atliekas ir skystos fazės kaitinimo laiko sąnaudas.
3.11. *Ex situ* hibridizacija leidžia kartoti analizes ir išsaugo mėginį.

Taikomumas

Pirmas straipsnis – DNazės detekcija yra labiausiai susijusi su aplinkos monitoringu, tačiau taip pat gali būti pritaikyta diagnostikoje.

Antras straipsnis – DNR hibridizacijos cheminė signalo amplifikacija ir hibridizacijos matavimas realiu laiku yra artimiausi mokslinių tyrimų sričiai. Tačiau šis metodas yra tinkamas multipotenciostatiniams, pastovios temperatūros ir potencialo matavimams ir gali būti pritaikytas gardelinei DNR kiekybinei analizei.

Trečias straipsnis – Dvigubo taikymo SERS-elektrocheminiai paviršiai šiuo metu yra artimiausi moksliniams tyrimams. Dviejų detekcijų taikymas gali ženkliai sustiprinti duomenų patikimumą. Metodas taip pat ženkliai sustiprintų chemiškai modifikuotų elektrodų gamybą, kokybės kontrolę ir leistų lengvai standartizuoti paviršius.

Ketvirtas straipsnis – specifiška DNR analizė gali būti taikoma labai plačiai, pademonstruotas farmakogenetinis taikinys, kas yra svarbu diagnostikai.

CONFERENCES

2024-10-04; Oral communication
S. Serapinas, D. Stakelytė, K. Tučinskytė, M. Tomkuvienė, D. Ratautas
Detection of single nucleotide polymorphisms in human genomic DNA using electrochemical biosensor based on melting analysis
Eleventh International Workshop on Biosensors, Marrakech, Morroco (2024)

2022-03-01; Poster
S. Serapinas, J. Gineitytė, M. Butkevičius, M. Dagys, R. Danilevičius, D. Ratautas.
Electrochemical biosensor for deoxyribonuclease detection and measurement
International Life Sciences Conference The COINS, Vilnius, Lithuania (2022)

CURRICULUM VITAE

Name	Skomantas Serapinas
Education	**2020-2026** PhD studies in Biochemistry Institute of Biochemistry, Life Sciences Centre, Vilnius University, Saulėtekio al. 7, Vilnius, Lithuania 2012-2016 Master's of Pharmacy (Upper Second-Class Honours) University of Brighton, Moulsecoomb Place, Lewes Road, BN2 4HQ
Employment	**2021-2026** Junior Scientist Institute of Biochemistry, Life Sciences Centre, Vilnius University, Saulėtekio al. 7, Vilnius, Lithuania
Project collaborator	• Development of an electrochemical biosensor for detecting single nucleotide polymorphisms 2023 – 2025; Project funded by Research Council of Lithuania under Researcher Group projects framework, project No. S-MIP-23-127. • Development of a bioelectrochemical L-amino acid-urea analyzer for monitoring of intensive care patients 2023 – 2024; Project funded by Research Council of Lithuania under Technology Development Projects framework, project No. P-TPP-23-047. • Development of the electrochemical device for nuclease detection and determination 2021-2022; The project is funded by the Agency for Science, Innovation and Technology of Lithuania, grant number BIOTECH-02-005
Publications not included in the thesis	1. Ratautas, D.; **Serapinas, S**.; Gineityte, J.; Butkevicius, M.; Danilevicius, R.; Dagys, M. Electrochemical System for the Rapid and Sensitive Detection and Quantification of Nuclease-like Activity Exhibiting Enzymes. EP4209596A1, July 12, 2023. https://patents.google.com/patent/EP4209596A1/en (accessed 2025-05-13).

	2. Ratautas, D.; **Serapinas, S.**; Stakelytė, D.; Guobužaitė, S.; Danytė, A.; Dagys, M. Quo Vadis, Electrochemical DNA Biosensor? Lessons from Three Decades of SNP Sensing. ACS Sens. 2026, 11 (7), 5296–5314. https://doi.org/10.1021/acssensors.6c01221.

SOFTWARE USED

The text was compiled in Microsoft Office and Libre Office.

The Figures were generated using PDF XChange editor (10.3.1), Marvin JS (Chemaxon, 22.19.0), Paint.net (4.3.8), Inkscape (1.2), and Python 3 libraries Matplotlib (3.8.4) and Seaborn (0.13.2).

References were managed via Zotero (6.0.36).

REFERENCES

(1) Bard, A. J.; Faulkner, L. R. *Electrochemical Methods: Fundamentals and Applications*, 2nd ed.; Wiley: New York, 2001.

(2) Chowdhury, D. R.; Spiccia, L.; Amritphale, S. S.; Paul, A.; Singh, A. A Robust Iron Oxyhydroxide Water Oxidation Catalyst Operating under near Neutral and Alkaline Conditions. *J. Mater. Chem. A* **2016**, *4* (10), 3655–3660. https://doi.org/10.1039/C6TA00313C.

(3) Amstutz, U.; Henricks, L. M.; Offer, S. M.; Barbarino, J.; Schellens, J. H. M.; Swen, J. J.; Klein, T. E.; McLeod, H. L.; Caudle, K. E.; Diasio, R. B.; Schwab, M. Clinical Pharmacogenetics Implementation Consortium (CPIC) Guideline for Dihydropyrimidine Dehydrogenase Genotype and Fluoropyrimidine Dosing: 2017 Update. *Clinical Pharmacology & Therapeutics* **2018**, *103* (2), 210–216. https://doi.org/10.1002/cpt.911.

(4) Maillard, M.; Schwab, M.; Whirl-Carrillo, M.; Moyer, A. M.; Suarez-Kurtz, G.; Pui, C.-H.; Stein, C. M.; Klein, T. E.; Spahn, C.; Kwon, S.; Hartono, J. L.; de Boer, N. K.; Ahmad, T.; Antillon-Klussmann, F. G.; Caudle, K. E.; Kato, M.; Yeoh, A. E. J.; Schmiegelow, K.; Yang, J. J. Clinical Pharmacogenetics Implementation Consortium (CPIC) Guideline for Thiopurine Dosing Based on TPMT and NUDT15 Genotypes: 2025 Update. *Clinical Pharmacology & Therapeutics* **2026**, *119* (4), 916–927. https://doi.org/10.1002/cpt.70209.

(5) *CYP2C19 genotype testing to guide clopidogrel use after ischaemic stroke or transient ischaemic attack | Guidance | NICE*. https://www.nice.org.uk/guidance/htg724 (accessed 2026-04-12).

(6) Medwid, S.; Kim, R. B. Implementation of Pharmacogenomics: Where Are We Now? *British Journal of Clinical Pharmacology* **2024**, *90* (8), 1763–1781. https://doi.org/10.1111/bcp.15591.

(7) Abou Diwan, E.; Zeitoun, R. I.; Abou Haidar, L.; Cascorbi, I.; Khoueiry Zgheib, N. Implementation and Obstacles of Pharmacogenetics in Clinical Practice: An International Survey. *British Journal of Clinical Pharmacology* **2019**, *85* (9), 2076–2088. https://doi.org/10.1111/bcp.13999.

(8) Ginsburg, G. S. Implications of Pharmacogenomics for Drug Development and Clinical Practice. *Arch Intern Med* **2005**, *165* (20), 2331. https://doi.org/10.1001/archinte.165.20.2331.

(9) Donohue, M. J. Quantification of *Legionella Pneumophila* by qPCR and Culture in Tap Water with Different Concentrations of Residual Disinfectants and Heterotrophic Bacteria. *Science of The Total Environment* **2021**, *774*, 145142. https://doi.org/10.1016/j.scitotenv.2021.145142.

(10) Sivaganesan, M.; Aw, T. G.; Briggs, S.; Dreelin, E.; Aslan, A.; Dorevitch, S.; Shrestha, A.; Isaacs, N.; Kinzelman, J.; Kleinheinz, G.; Noble, R.; Rediske, R.; Scull, B.; Rosenberg, S.; Weberman, B.; Sivy,

T.; Southwell, B.; Siefring, S.; Oshima, K.; Haugland, R. Standardized Data Quality Acceptance Criteria for a Rapid *Escherichia Coli* qPCR Method (Draft Method C) for Water Quality Monitoring at Recreational Beaches. *Water Research* **2019**, *156*, 456–464. https://doi.org/10.1016/j.watres.2019.03.011.

(11) Sivaganesan, M.; Dean, S. A.; Willis, J. R.; Friedman, S. D.; Haugland, R.; Shanks, O. C. A Streamlined qPCR Method for Characterization of *Enterococcus* Spp. Levels in Ambient Surface Water Samples. *Water Research* **2025**, *284*, 123936. https://doi.org/10.1016/j.watres.2025.123936.

(12) Vesper, S. j.; Wymer, L. j.; Meklin, T.; Varma, M.; Stott, R.; Richardson, M.; Haugland, R. a. Comparison of Populations of Mould Species in Homes in the UK and USA Using Mould-Specific Quantitative PCR. *Letters in Applied Microbiology* **2005**, *41* (4), 367–373. https://doi.org/10.1111/j.1472-765X.2005.01764.x.

(13) Nogva, H. K.; Bergh, A.; Holck, A.; Rudi, K. Application of the 5′-Nuclease PCR Assay in Evaluation and Development of Methods for Quantitative Detection of Campylobacter Jejuni. *Appl Environ Microbiol* **2000**, *66* (9), 4029–4036. https://doi.org/10.1128/aem.66.9.4029-4036.2000.

(14) Zhu, H.; Kim, B. J.; Spizz, G.; Rothrock, D.; Yasmin, R.; Arida, J.; Grocholl, J.; Montagna, R.; Schwartz, B.; Trujillo, S.; Almeria, S. Development and Evaluation/Verification of a Fully Automated Test Platform for the Rapid Detection of Cyclospora Cayetanensis in Produce Matrices. *Microorganisms* **2023**, *11* (11), 2805. https://doi.org/10.3390/microorganisms11112805.

(15) *GeneXpert Family of Systems*. https://www.cepheid.com/en-US/systems/genexpert-family-of-systems/genexpert-system.html (accessed 2025-05-30).

(16) *Cepheid-Corporate-Menu-Flyer-US-IVD-0323-English*. https://cepheid.widen.net/content/6rod6rervw/pdf/Cepheid-Corporate-Menu-Flyer-US-IVD-0323-English.pdf?u=bk12mm (accessed 2025-09-04).

(17) Chereau, D.; Kerff, F.; Graceffa, P.; Grabarek, Z.; Langsetmo, K.; Dominguez, R. Actin-Bound Structures of Wiskott–Aldrich Syndrome Protein (WASP)-Homology Domain 2 and the Implications for Filament Assembly. *Proceedings of the National Academy of Sciences* **2005**, *102* (46), 16644–16649. https://doi.org/10.1073/pnas.0507021102.

(18) Langer, J.; Jimenez de Aberasturi, D.; Aizpurua, J.; Alvarez-Puebla, R. A.; Auguié, B.; Baumberg, J. J.; Bazan, G. C.; Bell, S. E. J.; Boisen, A.; Brolo, A. G.; Choo, J.; Cialla-May, D.; Deckert, V.; Fabris, L.; Faulds, K.; García de Abajo, F. J.; Goodacre, R.; Graham, D.; Haes, A. J.; Haynes, C. L.; Huck, C.; Itoh, T.; Käll, M.; Kneipp, J.; Kotov, N. A.; Kuang, H.; Le Ru, E. C.; Lee, H. K.; Li, J.-F.; Ling, X. Y.; Maier, S. A.; Mayerhöfer, T.; Moskovits, M.; Murakoshi, K.; Nam, J.-M.; Nie, S.;

Ozaki, Y.; Pastoriza-Santos, I.; Perez-Juste, J.; Popp, J.; Pucci, A.; Reich, S.; Ren, B.; Schatz, G. C.; Shegai, T.; Schlücker, S.; Tay, L.-L.; Thomas, K. G.; Tian, Z.-Q.; Van Duyne, R. P.; Vo-Dinh, T.; Wang, Y.; Willets, K. A.; Xu, C.; Xu, H.; Xu, Y.; Yamamoto, Y. S.; Zhao, B.; Liz-Marzán, L. M. Present and Future of Surface-Enhanced Raman Scattering. *ACS Nano* **2020**, *14* (1), 28–117. https://doi.org/10.1021/acsnano.9b04224.

(19) Vernick, S.; Trocchia, S. M.; Warren, S. B.; Young, E. F.; Bouilly, D.; Gonzalez, R. L.; Nuckolls, C.; Shepard, K. L. Electrostatic Melting in a Single-Molecule Field-Effect Transistor with Applications in Genomic Identification. *Nat Commun* **2017**, *8* (1), 15450. https://doi.org/10.1038/ncomms15450.

(20) Levy, B.; Baughn, L. B.; Chartrand, S.; LaBarge, B.; Claxton, D.; Lennon, A.; Akkari, Y.; Cujar, C.; Kolhe, R.; Kroeger, K.; Pitel, B.; Sahajpal, N.; Sathanoori, M.; Vlad, G.; Zhang, L.; Fang, M.; Kanagal-Shamanna, R.; Broach, J. A National Multicenter Evaluation of the Clinical Utility of Optical Genome Mapping for Assessment of Genomic Aberrations in Acute Myeloid Leukemia. medRxiv November 10, 2020, p 2020.11.07.20227728. https://doi.org/10.1101/2020.11.07.20227728.

(21) Schmidt, D.; Wilson, M. D.; Spyrou, C.; Brown, G. D.; Hadfield, J.; Odom, D. T. ChIP-Seq: Using High-Throughput Sequencing to Discover Protein-DNA Interactions. *Methods* **2009**, *48* (3), 240–248. https://doi.org/10.1016/j.ymeth.2009.03.001.

(22) Sequenom MassARRAY Technology for the Analysis of DNA Methylation: Clinical Applications. In *Epigenetic Biomarkers and Diagnostics*; Academic Press, 2016; pp 137–153. https://doi.org/10.1016/B978-0-12-801899-6.00007-3.

(23) Verlouw, J. A. M.; Clemens, E.; de Vries, J. H.; Zolk, O.; Verkerk, A. J. M. H.; am Zehnhoff-Dinnesen, A.; Medina-Gomez, C.; Lanvers-Kaminsky, C.; Rivadeneira, F.; Langer, T.; van Meurs, J. B. J.; van den Heuvel-Eibrink, M. M.; Uitterlinden, A. G.; Broer, L. A Comparison of Genotyping Arrays. *Eur J Hum Genet* **2021**, *29* (11), 1611–1624. https://doi.org/10.1038/s41431-021-00917-7.

(24) *Axiom Genotyping Assay User Manual.pdf*. https://assets.thermofisher.com/TFS-Assets/LSG/brochures/axiom_genotyping_assay_user_manual.pdf (accessed 2025-05-29).

(25) *Illumina Infinium LCG Quad Assay, Manual Protocol.pdf*. https://support.illumina.com/content/dam/illumina-support/documents/documentation/chemistry_documentation/infinium_assays/infinium_lcg_quad_assay/inf_lcg_quad_manual_euc_15025909_reva.pdf (accessed 2025-05-29).

(26) Bergval, I.; Sengstake, S.; Brankova, N.; Levterova, V.; Abadía, E.; Tadumaze, N.; Bablishvili, N.; Akhalaia, M.; Tuin, K.; Schuitema, A.;

Panaiotov, S.; Bachiyska, E.; Kantardjiev, T.; Zwaan, R. de; Schürch, A.; Soolingen, D. van; Hoog, A. van 't; Cobelens, F.; Aspindzelashvili, R.; Sola, C.; Klatser, P.; Anthony, R. Combined Species Identification, Genotyping, and Drug Resistance Detection of Mycobacterium Tuberculosis Cultures by MLPA on a Bead-Based Array. *PLOS ONE* **2012**, *7* (8), e43240. https://doi.org/10.1371/journal.pone.0043240.

(27) MRC Holland. *MLPA General Protocol*. https://support.mrcholland.com/file.php/10426MWJTMDBNWJ104254647B954DPD/MLPA-General-Protocol-MDP-v010.pdf (accessed 2025-08-08).

(28) Shackelford, W.; Deng, S.; Murayama, K.; Wang, J. A New Technology for Mutation Detection. *Annals of the New York Academy of Sciences* **2004**, *1022* (1), 257–262. https://doi.org/10.1196/annals.1318.040.

(29) Trimgen. *KRAS Codon 61 Mutation Analysis Reagents User Manual V1.4*. https://www.trimgen.com/sites/default/files/upload/GP06%20KRAS%2061%20Manual%20V1.4.pdf (accessed 2025-08-08).

(30) Claassens, D. M. F.; Vos, G. J. A.; Bergmeijer, T. O.; Hermanides, R. S.; Hof, A. W. J. van 't; Harst, P. van der; Barbato, E.; Morisco, C.; Gin, R. M. T. J.; Asselbergs, F. W.; Mosterd, A.; Herrman, J.-P. R.; Dewilde, W. J. M.; Janssen, P. W. A.; Kelder, J. C.; Postma, M. J.; Boer, A. de; Boersma, C.; Deneer, V. H. M.; Berg, J. M. ten. A Genotype-Guided Strategy for Oral P2Y12 Inhibitors in Primary PCI. *New England Journal of Medicine* **2019**, *381* (17), 1621–1631. https://doi.org/10.1056/NEJMoa1907096.

(31) *QX600 Droplet Digital PCR System – Bio-Rad*. https://www.bio-rad.com/en-lt/product/qx600-droplet-digital-pcr-system?ID=b07d12ac-0585-fc4c-a586-3ddf20d5c4a0 (accessed 2025-05-29).

(32) *Nio®: 7-color digital PCR solution | Stilla*. Stilla Technologies. https://www.stillatechnologies.com/ (accessed 2025-05-29).

(33) LuminUltra. *LuminUltra Acquires Legionella Testing Business from Genomadix and Inks Strategic License to Commercialize Additional Tests for Ultra-portable Molecular Diagnostic Platform*. LuminUltra. https://www.luminultra.com/blog/luminultra-acquires-genomadix-cube/ (accessed 2025-05-30).

(34) *K220026 510(k) Premarket Notification*. https://www.accessdata.fda.gov/scripts/cdrh/cfdocs/cfpmn/pmn.cfm?ID=K220026 (accessed 2026-04-12).

(35) Cawthorn, D.-M.; Steinman, H. A.; Witthuhn, R. C. Comparative Study of Different Methods for the Extraction of DNA from Fish Species Commercially Available in South Africa. *Food Control* **2011**, *22* (2), 231–244. https://doi.org/10.1016/j.foodcont.2010.07.003.

(36) Wehmeier, U. F.; Hilberg, T. Capillary Earlobe Blood May Be Used for RNA Isolation, Gene Expression Assays and microRNA Quantification.

Molecular Medicine Reports **2014**, *9* (1), 211–216. https://doi.org/10.3892/mmr.2013.1779.

(37) Hlazunova, O. D.; Melnichuk, N. S. Aspects of Gene Expression Analysis in Small–Volume Blood Samples Using the Real–Time PCR. *Biopolym. Cell* **2025**, *41* (1), 3–12. https://doi.org/10.7124/bc.000B11.

(38) Sigma-Aldrich. *GenElute™ Total RNA Purification Kit RNB100 - Product Information*. https://www.sigmaaldrich.com/deepweb/assets/sigmaaldrich/product/documents/365/400/rnb100bul-ms.pdf.

(39) Holmberg, R. C.; Gindlesperger, A.; Stokes, T.; Brady, D.; Thakore, N.; Belgrader, P.; Cooney, C. G.; Chandler, D. P. High-Throughput, Automated Extraction of DNA and RNA from Clinical Samples Using TruTip Technology on Common Liquid Handling Robots. *Journal of Visualized Experiments (JoVE)* **2013**, No. 76, e50356. https://doi.org/10.3791/50356.

(40) *Dynabeads™ DNA DIRECT™ Universal Kit*. https://www.thermofisher.com/order/catalog/product/63006 (accessed 2025-06-23).

(41) Kueppers, C.; Schlappa, S.; Bogdoll, A.; Breitkopf, L.; Seip, N.; Singer, T. The ePrep-System: A New Electrophoretic Approach for DNA Isolation from Biological Samples. *ELECTROPHORESIS* **2017**, *38* (17), 2200–2209. https://doi.org/10.1002/elps.201600546.

(42) Hung, P.-Y.; Jiang, P.-S.; Lee, E.-F.; Fan, S.-K.; Lu, Y.-W. Genomic DNA Extraction from Whole Blood Using a Digital Microfluidic (DMF) Platform with Magnetic Beads. *Microsyst Technol* **2017**, *23* (2), 313–320. https://doi.org/10.1007/s00542-015-2512-9.

(43) Martorell, S.; Maquieira, Á.; Tortajada-Genaro, L. A. A Genosensor for Detecting Single-Point Mutations in Dendron Chips after Blocked Recombinase Polymerase Amplification. *Analyst* **2022**, *147* (10), 2180–2188. https://doi.org/10.1039/D2AN00160H.

(44) Yenice, C. P.; Chahin, N.; Jauset-Rubio, M.; Hall, M.; Biggs, P.; Dimai, H.-P.; Obermayer-Pietsch, B.; Ortiz, M.; O'Sullivan, C. K. Semiautomated Electrochemical Melting Curve Analysis Device for the Detection of an Osteoporosis Associated Single Nucleotide Polymorphism in Blood. *Anal. Chem.* **2023**, *95* (38), 14192–14202. https://doi.org/10.1021/acs.analchem.3c01668.

(45) Arriola, E.; Lambros, M. B. K.; Jones, C.; Dexter, T.; Mackay, A.; Tan, D. S. P.; Tamber, N.; Fenwick, K.; Ashworth, A.; Dowsett, M.; Reis-Filho, J. S. Evaluation of Phi29-Based Whole-Genome Amplification for Microarray-Based Comparative Genomic Hybridisation. *Laboratory Investigation* **2007**, *87* (1), 75–83. https://doi.org/10.1038/labinvest.3700495.

(46) Chapman, A. R.; He, Z.; Lu, S.; Yong, J.; Tan, L.; Tang, F.; Xie, X. S. Single Cell Transcriptome Amplification with MALBAC. *PLOS ONE* **2015**, *10* (3), e0120889. https://doi.org/10.1371/journal.pone.0120889.

(47) *Nucleic Acid Amplification Technologies: Application to Disease Diagnosis*; Lee, H. H., Morse, S. A., Olsvik, Ø., Eds.; BioTechniques books; Birkhäuser Boston: Cambridge, MA, 1997.
(48) Fahy, E.; Kwoh, D. Y.; Gingeras, T. R. Self-Sustained Sequence Replication (3SR): An Isothermal Transcription-Based Amplification System Alternative to PCR. *Genome Res.* **1991**, *1* (1), 25–33. https://doi.org/10.1101/gr.1.1.25.
(49) Yan, Y.; Ding, S.; Zhao, D.; Yuan, R.; Zhang, Y.; Cheng, W. Direct Ultrasensitive Electrochemical Biosensing of Pathogenic DNA Using Homogeneous Target-Initiated Transcription Amplification. *Sci Rep* **2016**, *6* (1), 18810. https://doi.org/10.1038/srep18810.
(50) Dunn, P.; Albury, C. L.; Maksemous, N.; Benton, M. C.; Sutherland, H. G.; Smith, R. A.; Haupt, L. M.; Griffiths, L. R. Next Generation Sequencing Methods for Diagnosis of Epilepsy Syndromes. *Front. Genet.* **2018**, *9*. https://doi.org/10.3389/fgene.2018.00020.
(51) Aird, D.; Ross, M. G.; Chen, W.-S.; Danielsson, M.; Fennell, T.; Russ, C.; Jaffe, D. B.; Nusbaum, C.; Gnirke, A. Analyzing and Minimizing PCR Amplification Bias in Illumina Sequencing Libraries. *Genome Biology* **2011**, *12* (2), R18. https://doi.org/10.1186/gb-2011-12-2-r18.
(52) Mattes, W. B.; Hartley, J. A.; Kohn, K. W. Mechanism of DNA Strand Breakage by Piperidine at Sites of *N*7-Alkylguanines. *Biochimica et Biophysica Acta (BBA) - Gene Structure and Expression* **1986**, *868* (1), 71–76. https://doi.org/10.1016/0167-4781(86)90088-6.
(53) Gangl, E. T.; Turesky, R. J.; Vouros, P. Detection of in Vivo Formed DNA Adducts at the Part-per-Billion Level by Capillary Liquid Chromatography/Microelectrospray Mass Spectrometry. *Anal. Chem.* **2001**, *73* (11), 2397–2404. https://doi.org/10.1021/ac0100401.
(54) Liao, Q.; Chiu, N. H. L.; Shen, C.; Chen, Y.; Vouros, P. Investigation of Enzymatic Behavior of Benzonase/Alkaline Phosphatase in the Digestion of Oligonucleotides and DNA by ESI-LC/MS. *Anal. Chem.* **2007**, *79* (5), 1907–1917. https://doi.org/10.1021/ac062249q.
(55) Ferguson, B. S.; Buchsbaum, S. F.; Wu, T.-T.; Hsieh, K.; Xiao, Y.; Sun, R.; Soh, H. T. Genetic Analysis of H1N1 Influenza Virus from Throat Swab Samples in a Microfluidic System for Point-of-Care Diagnostics. *J. Am. Chem. Soc.* **2011**, *133* (23), 9129–9135. https://doi.org/10.1021/ja203981w.
(56) Öhrmalm, C.; Jobs, M.; Eriksson, R.; Golbob, S.; Elfaitouri, A.; Benachenhou, F.; Strømme, M.; Blomberg, J. Hybridization Properties of Long Nucleic Acid Probes for Detection of Variable Target Sequences, and Development of a Hybridization Prediction Algorithm. *Nucleic Acids Research* **2010**, *38* (21), e195. https://doi.org/10.1093/nar/gkq777.
(57) Applied Biosystems. A Guide to High Resolution Melting (HRM) Analysis, 2010. https://documents.thermofisher.com/TFS-Assets/LSG/manuals/cms_070283.pdf (accessed 2026-03-29).

(58) Relógio, A.; Schwager, C.; Richter, A.; Ansorge, W.; Valcárcel, J. Optimization of Oligonucleotide-Based DNA Microarrays. *Nucleic Acids Research* **2002**, *30* (11), e51. https://doi.org/10.1093/nar/30.11.e51.
(59) Wang, X.; Zou, M.; Huang, H.; Ren, Y.; Li, L.; Yang, X.; Li, N. Gold Nanoparticle Enhanced Fluorescence Anisotropy for the Assay of Single Nucleotide Polymorphisms (SNPs) Based on Toehold-Mediated Strand-Displacement Reaction. *Biosensors and Bioelectronics* **2013**, *41*, 569–575. https://doi.org/10.1016/j.bios.2012.09.023.
(60) Haley, N. E. C.; Ouldridge, T. E.; Mullor Ruiz, I.; Geraldini, A.; Louis, A. A.; Bath, J.; Turberfield, A. J. Design of Hidden Thermodynamic Driving for Non-Equilibrium Systems via Mismatch Elimination during DNA Strand Displacement. *Nat Commun* **2020**, *11* (1), 2562. https://doi.org/10.1038/s41467-020-16353-y.
(61) Lu, H.; Ding, B.; Tong, L.; Wu, F.; Yi, X.; Wang, J. Toehold-Mediated Strand Displacement Reaction for Dual-Signal Electrochemical Assay of Apolipoprotein E Genotyping. *ACS Sens.* **2020**, *5* (9), 2959–2965. https://doi.org/10.1021/acssensors.0c01511.
(62) Steel, A. B.; Herne, T. M.; Tarlov, M. J. Electrochemical Quantitation of DNA Immobilized on Gold. *Anal. Chem.* **1998**, *70* (22), 4670–4677. https://doi.org/10.1021/ac980037q.
(63) Simon, L.; Gyurcsányi, R. E. Multiplexed Assessment of the Surface Density of DNA Probes on DNA Microarrays by Surface Plasmon Resonance Imaging. *Analytica Chimica Acta* **2019**, *1047*, 131–138. https://doi.org/10.1016/j.aca.2018.09.048.
(64) Peterson, A. W.; Heaton, R. J.; Georgiadis, R. M. The Effect of Surface Probe Density on DNA Hybridization. *Nucleic Acids Research* **2001**, *29* (24), 5163. https://doi.org/10.1093/nar/29.24.5163.
(65) Aoki, H.; Kitajima ,Akiko; and Tao, H. Label-Free and 'Signal-on' DNA Detection Using a Probe DNA Terminated with Ferrocene and β-Cyclodextrin. *Supramolecular Chemistry* **2010**, *22* (7–8), 455–460. https://doi.org/10.1080/10610278.2010.486034.
(66) Kitamura, Y.; Mishio, K.; Arslan, P.; Ikeda, B.; Imoto, C.; Katsuda, Y.; Ihara, T. Electrochemical Molecular Beacon for Nucleic Acid Sensing in a Homogeneous Solution. *ANAL. SCI.* **2020**, *36* (8), 959–964. https://doi.org/10.2116/analsci.19P456.
(67) Serapinas, S.; Gineitytė, J.; Butkevičius, M.; Danilevičius, R.; Dagys, M.; Ratautas, D. Biosensor Prototype for Rapid Detection and Quantification of DNase Activity. *Biosensors and Bioelectronics* **2022**, *213*, 114475. https://doi.org/10.1016/j.bios.2022.114475.
(68) Persson, B. A Chemically Modified Graphite Electrode for Electrocatalytic Oxidation of Reduced Nicotinamide Adenine Dinucleotide Based on a Phenothiazine Derivative, 3-β-Naphthoyl-Toluidine Blue O. *Journal of Electroanalytical Chemistry and*

Interfacial Electrochemistry **1990**, *287* (1), 61–80. https://doi.org/10.1016/0022-0728(90)87160-L.
(69) *Electroanalytical Methods: Guide to Experiments and Applications*, 2nd, rev.extended ed ed.; Scholz, F., Bond, A. M., Eds.; Springer: Heidelberg ; New York, 2010.
(70) Bard, A. J.; Inzelt, G.; Scholz, F. *Electrochemical Dictionary*, 2nd ed.; Springer: Heidelberg, 2012.
(71) Nuzzo, R. G.; Allara, D. L. Adsorption of Bifunctional Organic Disulfides on Gold Surfaces. *J. Am. Chem. Soc.* **1983**, *105* (13), 4481–4483. https://doi.org/10.1021/ja00351a063.
(72) Ulman, A. Formation and Structure of Self-Assembled Monolayers. *Chem. Rev.* **1996**, *96* (4), 1533–1554. https://doi.org/10.1021/cr9502357.
(73) Civit, L.; Fragoso, A.; O'Sullivan, C. K. Thermal Stability of Diazonium Derived and Thiol-Derived Layers on Gold for Application in Genosensors. *Electrochemistry Communications* **2010**, *12* (8), 1045–1048. https://doi.org/10.1016/j.elecom.2010.05.020.
(74) Yang, A. H. J.; Hsieh, K.; Patterson, A. S.; Ferguson, B. S.; Eisenstein, M.; Plaxco, K. W.; Soh, H. T. Accurate Zygote-Specific Discrimination of Single-Nucleotide Polymorphisms Using Microfluidic Electrochemical DNA Melting Curves. *Angewandte Chemie International Edition* **2014**, *53* (12), 3163–3167. https://doi.org/10.1002/anie.201310059.
(75) Olivan, L. A.; Hand, K.; White, R. J. Utilization of Spontaneous Alkyne–Gold Self-Assembly Chemistry as an Alternative Method for Fabricating Electrochemical Aptamer-Based Sensors. *Langmuir* **2024**, *40* (23), 12117–12123. https://doi.org/10.1021/acs.langmuir.4c00972.
(76) Taton, T. A. Preparation of Gold Nanoparticle–DNA Conjugates. *CP Nucleic Acid Chemistry* **2002**, *9* (1). https://doi.org/10.1002/0471142700.nc1202s09.
(77) Westermark, G.; Kariis, H.; Persson, I.; Liedberg, B. An Infrared Study on the Chemisorption of Tertiary Phosphines on Coinage and Platinum Group Metal Surfaces. *Colloids and Surfaces A: Physicochemical and Engineering Aspects* **1999**, *150* (1), 31–43. https://doi.org/10.1016/S0927-7757(98)00536-6.
(78) Jewell, A. D.; Tierney, H. L.; Sykes, E. C. H. Gently Lifting Gold's Herringbone Reconstruction: Trimethylphosphine on Au(111). *Phys. Rev. B* **2010**, *82* (20), 205401. https://doi.org/10.1103/PhysRevB.82.205401.
(79) Brooksby, P. A.; Downard, A. J. Electrochemical and Atomic Force Microscopy Study of Carbon Surface Modification via Diazonium Reduction in Aqueous and Acetonitrile Solutions. *Langmuir* **2004**, *20* (12), 5038–5045. https://doi.org/10.1021/la049616i.
(80) Baranton, S.; Bélanger, D. In Situ Generation of Diazonium Cations in Organic Electrolyte for Electrochemical Modification of Electrode

Surface. *Electrochimica Acta* **2008**, *53* (23), 6961–6967. https://doi.org/10.1016/j.electacta.2008.02.105.
(81) Corgier, B. P.; Marquette, C. A.; Blum, L. J. Diazonium−Protein Adducts for Graphite Electrode Microarrays Modification: Direct and Addressed Electrochemical Immobilization. *J. Am. Chem. Soc.* **2005**, *127* (51), 18328–18332. https://doi.org/10.1021/ja056946w.
(82) Harper, J. C.; Polsky, R.; Wheeler, D. R.; Dirk, S. M.; Brozik, S. M. Selective Immobilization of DNA and Antibody Probes on Electrode Arrays: Simultaneous Electrochemical Detection of DNA and Protein on a Single Platform. *Langmuir* **2007**, *23* (16), 8285–8287. https://doi.org/10.1021/la701775g.
(83) Chrétien, J.-M.; Ghanem, M. A.; Bartlett, P. N.; Kilburn, J. D. Covalent Tethering of Organic Functionality to the Surface of Glassy Carbon Electrodes by Using Electrochemical and Solid-Phase Synthesis Methodologies. *Chemistry – A European Journal* **2008**, *14* (8), 2548–2556. https://doi.org/10.1002/chem.200701559.
(84) Liu, J.; Cheng, L.; Liu, B.; Dong, S. Covalent Modification of a Glassy Carbon Surface by 4-Aminobenzoic Acid and Its Application in Fabrication of a Polyoxometalates-Consisting Monolayer and Multilayer Films. *Langmuir* **2000**, *16* (19), 7471–7476. https://doi.org/10.1021/la9913506.
(85) Barbier, B.; Pinson, J.; Desarmot, G.; Sanchez, M. Electrochemical Bonding of Amines to Carbon Fiber Surfaces Toward Improved Carbon-Epoxy Composites. *J. Electrochem. Soc.* **1990**, *137* (6), 1757–1764. https://doi.org/10.1149/1.2086794.
(86) Morales-Martínez, D.; Ramírez-Chan, D. E.; Palacios-Ramírez, J. I.; Galicia, M.; González, F. J. Covalent Modification of Carbon Surfaces by Direct and Redox Catalysed Oxidation of Carboxylates in Acetonitrile – Concepts and Mechanisms. *ChemCatChem* **2023**, *15* (12), e202300470. https://doi.org/10.1002/cctc.202300470.
(87) Harwood, S. J.; Palkowitz, M. D.; Gannett, C. N.; Perez, P.; Yao, Z.; Sun, L.; Abruña, H. D.; Anderson, S. L.; Baran, P. S. Modular Terpene Synthesis Enabled by Mild Electrochemical Couplings. *Science* **2022**, *375* (6582), 745–752. https://doi.org/10.1126/science.abn1395.
(88) Brown, Alex. C.; Walker, J. Elektrolytische Synthese Zweibasischer Säuren. *Justus Liebigs Annalen der Chemie* **1891**, *261* (1), 107–128. https://doi.org/10.1002/jlac.18912610106.
(89) Galán, T.; Prieto-Simón, B.; Alvira, M.; Eritja, R.; Götz, G.; Bäuerle, P.; Samitier, J. Label-Free Electrochemical DNA Sensor Using "Click"-Functionalized PEDOT Electrodes. *Biosensors and Bioelectronics* **2015**, *74*, 751–756. https://doi.org/10.1016/j.bios.2015.07.037.
(90) Authier, L.; Grossiord, C.; Brossier, P.; Limoges, B. Gold Nanoparticle-Based Quantitative Electrochemical Detection of Amplified Human Cytomegalovirus DNA Using Disposable Microband Electrodes. *Anal. Chem.* **2001**, *73* (18), 4450–4456. https://doi.org/10.1021/ac0103221.

(91) Maurer, K.; McShea, A.; Strathmann, M.; Dill, K. The Removal of the T-BOC Group by Electrochemically Generated Acid and Use of an Addressable Electrode Array for Peptide Synthesis. *J. Comb. Chem.* **2005**, *7* (5), 637–640. https://doi.org/10.1021/cc0498175.

(92) Maurer, K.; Cooper, J.; Caraballo, M.; Crye, J.; Suciu, D.; Ghindilis, A.; Leonetti, J. A.; Wang, W.; Rossi, F. M.; Stöver, A. G.; Larson, C.; Gao, H.; Dill, K.; McShea, A. Electrochemically Generated Acid and Its Containment to 100 Micron Reaction Areas for the Production of DNA Microarrays. *PLoS One* **2006**, *1* (1), e34. https://doi.org/10.1371/journal.pone.0000034.

(93) McKenas, C. G.; Fehr, J. M.; Donley, C. L.; Lockett, M. R. Thiol–Ene Modified Amorphous Carbon Substrates: Surface Patterning and Chemically Modified Electrode Preparation. *Langmuir* **2016**, *32* (41), 10529–10536. https://doi.org/10.1021/acs.langmuir.6b02961.

(94) Crudden, C. M.; Horton, J. H.; Ebralidze, I. I.; Zenkina, O. V.; McLean, A. B.; Drevniok, B.; She, Z.; Kraatz, H.-B.; Mosey, N. J.; Seki, T.; Keske, E. C.; Leake, J. D.; Rousina-Webb, A.; Wu, G. Ultra Stable Self-Assembled Monolayers of N-Heterocyclic Carbenes on Gold. *Nature Chem* **2014**, *6* (5), 409–414. https://doi.org/10.1038/nchem.1891.

(95) Maurer, K.; McShea, A.; Strathmann, M.; Dill, K. The Removal of the T-BOC Group by Electrochemically Generated Acid and Use of an Addressable Electrode Array for Peptide Synthesis. *J. Comb. Chem.* **2005**, *7* (5), 637–640. https://doi.org/10.1021/cc0498175.

(96) Mishyn, V.; Hugo, A.; Rodrigues, T.; Aspermair, P.; Happy, H.; Marques, L.; Hurot, C.; Othmen, R.; Bouchiat, V.; Boukherroub, R.; Knoll, W.; Szunerits, S. The Holy Grail of Pyrene-Based Surface Ligands on the Sensitivity of Graphene-Based Field Effect Transistors. *Sensors & Diagnostics* **2022**, *1* (2), 235–244. https://doi.org/10.1039/D1SD00036E.

(97) Faudi, F. Kugelgelenk. CH131172A, January 31, 1929. https://patents.google.com/patent/CH131172A/en (accessed 2025-07-30).

(98) Kunkel, G. R.; Mehrabian, M.; Martinson, H. G. Contact-Site Cross-Linking Agents. *Mol Cell Biochem* **1981**, *34* (1), 3–13. https://doi.org/10.1007/BF02354846.

(99) Grabarek, Z.; Gergely, J. Zero-Length Crosslinking Procedure with the Use of Active Esters. *Analytical Biochemistry* **1990**, *185* (1), 131–135. https://doi.org/10.1016/0003-2697(90)90267-D.

(100) Ziegler, F. E.; Berger, G. D. A Mild Method for the Esterification of Fatty Acids. *Synthetic Communications* **1979**, *9* (6), 539–543. https://doi.org/10.1080/00397917908060958.

(101) Umehara, A.; Shimizu, S.; Sasaki, M. Synthesis of Bulky N-Acyl Heterocycles by DMAPO/Boc2O-Mediated One-Pot Direct N-Acylation of Less Nucleophilic N-Heterocycles with α-Fully Substituted

Carboxylic Acids. *Advanced Synthesis & Catalysis* **2023**, *365* (14), 2367–2376. https://doi.org/10.1002/adsc.202300487.

(102) Adler, P.; Gras, M.; Smietana, M. Catalytic and Sustainable Amide Bond Formation Using a DABCO/Dichlorotriazine System. *ChemCatChem* **2023**, *15* (10), e202300264. https://doi.org/10.1002/cctc.202300264.

(103) Liu, J.; Fujita, H.; Kitamura, M.; Shimada, D.; Kunishima, M. Development of a Triazinedione-Based Dehydrative Condensing Reagent Containing 4-(Dimethylamino)Pyridine as an Acyl Transfer Catalyst. *Org. Biomol. Chem.* **2021**, *19* (21), 4712–4719. https://doi.org/10.1039/D1OB00450F.

(104) Lagueux-Tremblay, P.-L.; Fabrikant, A.; Arndtsen, B. A. Palladium-Catalyzed Carbonylation of Aryl Chlorides to Electrophilic Aroyl-DMAP Salts. *ACS Catal.* **2018**, *8* (6), 5350–5354. https://doi.org/10.1021/acscatal.8b00757.

(105) Hutchby, M.; Houlden, C. E.; Haddow, M. F.; Tyler, S. N. G.; Lloyd-Jones, G. C.; Booker-Milburn, K. I. Switching Pathways: Room-Temperature Neutral Solvolysis and Substitution of Amides. *Angewandte Chemie International Edition* **2012**, *51* (2), 548–551. https://doi.org/10.1002/anie.201107117.

(106) El-Faham, A.; Funosas, R. S.; Prohens, R.; Albericio, F. COMU: A Safer and More Effective Replacement for Benzotriazole-Based Uronium Coupling Reagents. *Chemistry – A European Journal* **2009**, *15* (37), 9404–9416. https://doi.org/10.1002/chem.200900615.

(107) Mattson, G.; Conklin, E.; Desai, S.; Nielander, G.; Savage, M. D.; Morgensen, S. A Practical Approach to Crosslinking. *Mol Biol Rep* **1993**, *17* (3), 167–183. https://doi.org/10.1007/BF00986726.

(108) Rostovtsev, V. V.; Green, L. G.; Fokin, V. V.; Sharpless, K. B. A Stepwise Huisgen Cycloaddition Process: Copper(I)-Catalyzed Regioselective "Ligation" of Azides and Terminal Alkynes. *Angewandte Chemie International Edition* **2002**, *41* (14), 2596–2599. https://doi.org/10.1002/1521-3773(20020715)41:14%3C2596::AID-ANIE2596%3E3.0.CO;2-4.

(109) Lewis, W. G.; Green, L. G.; Grynszpan, F.; Radić, Z.; Carlier, P. R.; Taylor, P.; Finn, M. G.; Sharpless, K. B. Click Chemistry In Situ: Acetylcholinesterase as a Reaction Vessel for the Selective Assembly of a Femtomolar Inhibitor from an Array of Building Blocks. *Angewandte Chemie International Edition* **2002**, *41* (6), 1053–1057. https://doi.org/10.1002/1521-3773(20020315)41:6%3C1053::AID-ANIE1053%3E3.0.CO;2-4.

(110) Akar, E.; Luleburgaz, S.; Gunay, U. S.; Kumbaraci, V.; Tunca, U.; Durmaz, H. Amino-Yne Reaction: An Exquisite Method for Polymer-Polymer Conjugation and Post-Polymerization Modification. *European Polymer Journal* **2023**, *199*, 112470. https://doi.org/10.1016/j.eurpolymj.2023.112470.

(111) Chan, J. W.; Hoyle, C. E.; Lowe, A. B. Sequential Phosphine-Catalyzed, Nucleophilic Thiol−Ene/Radical-Mediated Thiol−Yne Reactions and the Facile Orthogonal Synthesis of Polyfunctional Materials. *J. Am. Chem. Soc.* **2009**, *131* (16), 5751–5753. https://doi.org/10.1021/ja8099135.

(112) Gautier, C.; López, I.; Breton, T. A Post-Functionalization Toolbox for Diazonium (Electro)-Grafted Surfaces: Review of the Coupling Methods. *Mater. Adv.* **2021**, *2* (9), 2773–2810. https://doi.org/10.1039/D1MA00077B.

(113) Sirajuddin, M.; Ali, S.; Badshah, A. Drug–DNA Interactions and Their Study by UV–Visible, Fluorescence Spectroscopies and Cyclic Voltametry. *Journal of Photochemistry and Photobiology B: Biology* **2013**, *124*, 1–19. https://doi.org/10.1016/j.jphotobiol.2013.03.013.

(114) *Nucleic Acids in Chemistry and Biology*, 3. ed.; Blackburn, G. M., Gait, M., Loakes, D., Williams, D., Eds.; Royal Society of Chemistry: Cambridge, 2006.

(115) Nassi, A.; Guillon, F.-X.; Amar, A.; Hainque, B.; Amriche, S.; Maugé, D.; Markova, E.; Tsé, C.; Bigey, P.; Lazerges, M.; Bedioui, F. Electrochemical DNA-Biosensors Based on Long-Range Electron Transfer: Optimization of the Amperometric Detection in the Femtomolar Range Using Two-Electrode Setup and Ultramicroelectrode. *Electrochimica Acta* **2016**, *209*, 269–277. https://doi.org/10.1016/j.electacta.2016.04.144.

(116) Wong, E. L. S.; Erohkin, P.; Gooding, J. J. A Comparison of Cationic and Anionic Intercalators for the Electrochemical Transduction of DNA Hybridization via Long Range Electron Transfer. *Electrochemistry Communications* **2004**, *6* (7), 648–654. https://doi.org/10.1016/j.elecom.2004.05.002.

(117) Kékedy-Nagy, L.; Kotlyar, A. B.; Ferapontova, E. E. Long-Range Electron Transfer Mediated by G-Quadruplex Wires Attached to Gold Electrodes via Phosphorothioated dA Tags. *Electrochimica Acta* **2024**, *476*, 143761. https://doi.org/10.1016/j.electacta.2024.143761.

(118) Slinker, J. D.; Muren, N. B.; Renfrew, S. E.; Barton, J. K. DNA Charge Transport over 34 Nm. *Nature Chem* **2011**, *3* (3), 228–233. https://doi.org/10.1038/nchem.982.

(119) Sykes, K. S.; White, R. J. Effects of Nucleic Acid Structural Heterogeneity on the Electrochemistry of Tethered Redox Molecules. *Langmuir* **2022**, *38* (23), 7322–7330. https://doi.org/10.1021/acs.langmuir.2c00840.

(120) Ortiz, M.; Jauset-Rubio, M.; Kodr, D.; Simonova, A.; Hocek, M.; O'Sullivan, C. K. Solid-Phase Recombinase Polymerase Amplification Using Ferrocene-Labelled dNTPs for Electrochemical Detection of Single Nucleotide Polymorphisms. *Biosensors and Bioelectronics* **2022**, *198*, 113825. https://doi.org/10.1016/j.bios.2021.113825.

(121) Hajian, R.; Balderston, S.; Tran, T.; deBoer, T.; Etienne, J.; Sandhu, M.; Wauford, N. A.; Chung, J.-Y.; Nokes, J.; Athaiya, M.; Paredes, J.; Peytavi, R.; Goldsmith, B.; Murthy, N.; Conboy, I. M.; Aran, K. Detection of Unamplified Target Genes via CRISPR–Cas9 Immobilized on a Graphene Field-Effect Transistor. *Nat Biomed Eng* **2019**, *3* (6), 427–437. https://doi.org/10.1038/s41551-019-0371-x.

(122) Jiménez-Monroy, K. L.; Renaud, N.; Drijkoningen, J.; Cortens, D.; Schouteden, K.; van Haesendonck, C.; Guedens, W. J.; Manca, J. V.; Siebbeles, L. D. A.; Grozema, F. C.; Wagner, P. H. High Electronic Conductance through Double-Helix DNA Molecules with Fullerene Anchoring Groups. *J. Phys. Chem. A* **2017**, *121* (6), 1182–1188. https://doi.org/10.1021/acs.jpca.7b00348.

(123) Genereux, J. C.; Barton, J. K. Mechanisms for DNA Charge Transport. *Chem. Rev.* **2010**, *110* (3), 1642–1662. https://doi.org/10.1021/cr900228f.

(124) Göeken, K. L.; Schasfoort, R. B. M.; Subramaniam, V.; Gill, R. Spermine Induced Reversible Collapse of Deoxyribonucleic Acid-Bridged Nanoparticle-Based Assemblies. *Nano Res.* **2018**, *11* (1), 383–396. https://doi.org/10.1007/s12274-017-1641-0.

(125) Sykes, K. S.; White, R. J. Nucleic Acid Identity, Structure, and Flexibility Affect the Electrochemical Signal of Tethered Redox Molecules upon Biopolymer Collapse. *Langmuir* **2021**, *37* (42), 12466–12475. https://doi.org/10.1021/acs.langmuir.1c02161.

(126) Ma, T.; Baker, D. V.; Martinez-Blanco, G.; Bizzotto, D. An EIS Study of the Heterogeneity of Redox Labeled DNA SAMs on Gold before and after Hybridization. *Electrochimica Acta* **2025**, *517*, 145747. https://doi.org/10.1016/j.electacta.2025.145747.

(127) Lin, K.-Y.; Burke, A.; King, N. B.; Kahanda, D.; Mazaheripour, A.; Bartlett, A.; Dibble, D. J.; McWilliams, M. A.; Taylor, D. W.; Jocson, J.-M.; Minary-Jolandan, M.; Gorodetsky, A. A.; Slinker, J. D. Enhancement of the Electrical Properties of DNA Molecular Wires through Incorporation of Perylenediimide DNA Base Surrogates. *ChemPlusChem* **2019**, *84* (4), 416–419. https://doi.org/10.1002/cplu.201800661.

(128) Silva, S. M.; Tavallaie, R.; Gonçales, V. R.; Utama, R. H.; Kashi, M. B.; Hibbert, D. B.; Tilley, R. D.; Gooding, J. J. Dual Signaling DNA Electrochemistry: An Approach To Understand DNA Interfaces. *Langmuir* **2018**, *34* (4), 1249–1255. https://doi.org/10.1021/acs.langmuir.7b02787.

(129) Gu, Q.; Nanney, W.; Cao, H. H.; Wang, H.; Ye, T. Single Molecule Profiling of Molecular Recognition at a Model Electrochemical Biosensor. *J. Am. Chem. Soc.* **2018**, *140* (43), 14134–14143. https://doi.org/10.1021/jacs.8b07325.

(130) Abi, A.; Safavi, A. Determination of the Binding Site Size of Hexaammineruthenium(III) inside Monolayers of DNA on Gold. *Analyst* **2021**, *146* (2), 547–557. https://doi.org/10.1039/D0AN01685C.
(131) Wang, Z.; Zhang, J.; Zhu, C.; Wu, S.; Mandler, D.; Marks, R. S.; Zhang, H. Amplified Detection of Femtomolar DNA Based on a One-to-Few Recognition Reaction between DNA–Au Conjugate and Target DNA. *Nanoscale* **2014**, *6* (6), 3110–3115. https://doi.org/10.1039/C3NR05625B.
(132) Bos, E. S.; van der Doelen ,A. A.; Rooy ,N. van; and Schuurs, A. H. W. M. 3,3′,5,5′-Tetramethylbenzidine as an Ames Test Negative Chromogen for Horse-Radish Peroxidase in Enzyme-Immunoassay. *Journal of Immunoassay* **1981**, *2* (3–4), 187–204. https://doi.org/10.1080/15321818108056977.
(133) Yin, H.; Zhou, Y.; Zhang, H.; Meng, X.; Ai, S. Electrochemical Determination of microRNA-21 Based on Graphene, LNA Integrated Molecular Beacon, AuNPs and Biotin Multifunctional Bio Bar Codes and Enzymatic Assay System. *Biosensors and Bioelectronics* **2012**, *33* (1), 247–253. https://doi.org/10.1016/j.bios.2012.01.014.
(134) Golgi, C. *Untersuchungen über den feineren Bau des centralen und peripherischen Nervensystems*; Jena : G. Fischer, 1894.
(135) Hwang, S.; Kim, E.; Kwak, J. Electrochemical Detection of DNA Hybridization Using Biometallization. *Anal. Chem.* **2005**, *77* (2), 579–584. https://doi.org/10.1021/ac048778g.
(136) Si, Y.; Sun, Z.; Zhang, N.; Qi, W.; Li, S.; Chen, L.; Wang, H. Ultrasensitive Electroanalysis of Low-Level Free MicroRNAs in Blood by Maximum Signal Amplification of Catalytic Silver Deposition Using Alkaline Phosphatase-Incorporated Gold Nanoclusters. *Anal. Chem.* **2014**, *86* (20), 10406–10414. https://doi.org/10.1021/ac5028885.
(137) Alfonta, L.; Singh, A. K.; Willner, I. Liposomes Labeled with Biotin and Horseradish Peroxidase: A Probe for the Enhanced Amplification of Antigen−Antibody or Oligonucleotide−DNA Sensing Processes by the Precipitation of an Insoluble Product on Electrodes. *Anal. Chem.* **2001**, *73* (1), 91–102. https://doi.org/10.1021/ac000819v.
(138) Chandra, S.; Gäbler, C.; Schliebe, C.; Lang, H.; Bahadur, D. Fabrication of a Label-Free Electrochemical Immunosensor Using a Redox Active Ferrocenyl Dendrimer. *New J. Chem.* **2016**, *40* (11), 9046–9053. https://doi.org/10.1039/C6NJ00830E.
(139) Yao, B.; Liu, Y.; Tabata, M.; Zhu, H.; Miyahara, Y. Sensitive Detection of microRNA by Chronocoulometry and Rolling Circle Amplification on a Gold Electrode. *Chem. Commun.* **2014**, *50* (68), 9704–9706. https://doi.org/10.1039/C4CC03330B.
(140) Hsieh, K.; Patterson, A. S.; Ferguson, B. S.; Plaxco, K. W.; Soh, H. T. Rapid, Sensitive, and Quantitative Detection of Pathogenic DNA at the Point of Care through Microfluidic Electrochemical Quantitative Loop-Mediated Isothermal Amplification. *Angewandte Chemie*

International Edition **2012**, *51* (20), 4896–4900. https://doi.org/10.1002/anie.201109115.

(141) Chahin, N.; Escobar-Nassar, S.; Osma, J.; Bashammakh, A. S.; AlYoubi, A. O.; Ortiz, M.; O'Sullivan, C. K. Low-Cost Platform for Multiplexed Electrochemical Melting Curve Analysis. *ACS Meas. Sci. Au* **2022**, *2* (2), 147–156. https://doi.org/10.1021/acsmeasuresciau.1c00044.

(142) Fukunaga, K.; Hishinuma, E.; Hiratsuka, M.; Kato, K.; Okusaka, T.; Saito, T.; Ikeda, M.; Yoshida, T.; Zembutsu, H.; Iwata, N.; Mushiroda, T. Determination of Novel CYP2D6 Haplotype Using the Targeted Sequencing Followed by the Long-Read Sequencing and the Functional Characterization in the Japanese Population. *J Hum Genet* **2021**, *66* (2), 139–149. https://doi.org/10.1038/s10038-020-0815-x.

(143) Smith, L. M.; Sanders, J. Z.; Kaiser, R. J.; Hughes, P.; Dodd, C.; Connell, C. R.; Heiner, C.; Kent, S. B. H.; Hood, L. E. Fluorescence Detection in Automated DNA Sequence Analysis. *Nature* **1986**, *321* (6071), 674–679. https://doi.org/10.1038/321674a0.

(144) Huang, X. C.; Quesada, M. A.; Mathies, R. A. DNA Sequencing Using Capillary Array Electrophoresis. *Anal. Chem.* **1992**, *64* (18), 2149–2154. https://doi.org/10.1021/ac00042a021.

(145) Woolley, A. T.; Mathies, R. A. Ultra-High-Speed DNA Fragment Separations Using Microfabricated Capillary Array Electrophoresis Chips. *Proceedings of the National Academy of Sciences* **1994**, *91* (24), 11348–11352. https://doi.org/10.1073/pnas.91.24.11348.

(146) *US6143152A - Microfabricated capillary array electrophoresis device and method - Google Patents*. https://patents.google.com/patent/US6143152A (accessed 2026-02-26).

(147) Alaverdian, L.; Alaverdian, S.; Bilenko, O.; Bogdanov, I.; Filippova, E.; Gavrilov, D.; Gorbovitski, B.; Gouzman, M.; Gudkov, G.; Domratchev, S.; Kosobokova, O.; Lifshitz, N.; Luryi, S.; Ruskovoloshin, V.; Stepoukhovitch, A.; Tcherevishnick, M.; Tyshko, G.; Gorfinkel, V. A Family of Novel DNA Sequencing Instruments Based on Single-Photon Detection. *ELECTROPHORESIS* **2002**, *23* (16), 2804–2817. https://doi.org/10.1002/1522-2683(200208)23:16%3C2804::AID-ELPS2804%3E3.0.CO;2-9.

(148) Emrich, C. A.; Tian, H.; Medintz, I. L.; Mathies, R. A. Microfabricated 384-Lane Capillary Array Electrophoresis Bioanalyzer for Ultrahigh-Throughput Genetic Analysis. *Anal. Chem.* **2002**, *74* (19), 5076–5083. https://doi.org/10.1021/ac020236g.

(149) Shibata, K.; Itoh, M.; Aizawa, K.; Nagaoka, S.; Sasaki, N.; Carninci, P.; Konno, H.; Akiyama, J.; Nishi, K.; Kitsunai, T.; Tashiro, H.; Itoh, M.; Sumi, N.; Ishii, Y.; Nakamura, S.; Hazama, M.; Nishine, T.; Harada, A.; Yamamoto, R.; Matsumoto, H.; Sakaguchi, S.; Ikegami, T.; Kashiwagi, K.; Fujiwake, S.; Inoue, K.; Togawa, Y.; Izawa, M.; Ohara, E.; Watahiki, M.; Yoneda, Y.; Ishikawa, T.; Ozawa, K.; Tanaka, T.;

Matsuura, S.; Kawai, J.; Okazaki, Y.; Muramatsu, M.; Inoue, Y.; Kira, A.; Hayashizaki, Y. RIKEN Integrated Sequence Analysis (RISA) System—384-Format Sequencing Pipeline with 384 Multicapillary Sequencer. *Genome Res.* **2000**, *10* (11), 1757–1771. https://doi.org/10.1101/gr.152600.

(150) Margulies, M.; Egholm, M.; Altman, W. E.; Attiya, S.; Bader, J. S.; Bemben, L. A.; Berka, J.; Braverman, M. S.; Chen, Y.-J.; Chen, Z.; Dewell, S. B.; Du, L.; Fierro, J. M.; Gomes, X. V.; Godwin, B. C.; He, W.; Helgesen, S.; Ho, C. H.; Irzyk, G. P.; Jando, S. C.; Alenquer, M. L. I.; Jarvie, T. P.; Jirage, K. B.; Kim, J.-B.; Knight, J. R.; Lanza, J. R.; Leamon, J. H.; Lefkowitz, S. M.; Lei, M.; Li, J.; Lohman, K. L.; Lu, H.; Makhijani, V. B.; McDade, K. E.; McKenna, M. P.; Myers, E. W.; Nickerson, E.; Nobile, J. R.; Plant, R.; Puc, B. P.; Ronan, M. T.; Roth, G. T.; Sarkis, G. J.; Simons, J. F.; Simpson, J. W.; Srinivasan, M.; Tartaro, K. R.; Tomasz, A.; Vogt, K. A.; Volkmer, G. A.; Wang, S. H.; Wang, Y.; Weiner, M. P.; Yu, P.; Begley, R. F.; Rothberg, J. M. Genome Sequencing in Microfabricated High-Density Picolitre Reactors. *Nature* **2005**, *437* (7057), 376–380. https://doi.org/10.1038/nature03959.

(151) Rothberg, J. M.; Hinz, W.; Rearick, T. M.; Schultz, J.; Mileski, W.; Davey, M.; Leamon, J. H.; Johnson, K.; Milgrew, M. J.; Edwards, M.; Hoon, J.; Simons, J. F.; Marran, D.; Myers, J. W.; Davidson, J. F.; Branting, A.; Nobile, J. R.; Puc, B. P.; Light, D.; Clark, T. A.; Huber, M.; Branciforte, J. T.; Stoner, I. B.; Cawley, S. E.; Lyons, M.; Fu, Y.; Homer, N.; Sedova, M.; Miao, X.; Reed, B.; Sabina, J.; Feierstein, E.; Schorn, M.; Alanjary, M.; Dimalanta, E.; Dressman, D.; Kasinskas, R.; Sokolsky, T.; Fidanza, J. A.; Namsaraev, E.; McKernan, K. J.; Williams, A.; Roth, G. T.; Bustillo, J. An Integrated Semiconductor Device Enabling Non-Optical Genome Sequencing. *Nature* **2011**, *475* (7356), 348–352. https://doi.org/10.1038/nature10242.

(152) Jain, M.; Fiddes, I. T.; Miga, K. H.; Olsen, H. E.; Paten, B.; Akeson, M. Improved Data Analysis for the MinION Nanopore Sequencer. *Nat Methods* **2015**, *12* (4), 351–356. https://doi.org/10.1038/nmeth.3290.

(153) Loman, N. J.; Quick, J.; Simpson, J. T. A Complete Bacterial Genome Assembled de Novo Using Only Nanopore Sequencing Data. *Nat Methods* **2015**, *12* (8), 733–735. https://doi.org/10.1038/nmeth.3444.

(154) Wang, Y.; Yang, Q.; Wang, Z. The Evolution of Nanopore Sequencing. *Front. Genet.* **2015**, *5*. https://doi.org/10.3389/fgene.2014.00449.

(155) *Genapsys sequencer*. Prayoga Lifesciences Inc. https://www.prayogalifesciences.com/genapsys-sequencer-new/ (accessed 2026-03-26).

(156) Killpack, J.; Galova, K.; Christova, R.; Palmer, E.; Barratt, G.; Greenwood, C.; Fraccari, R.; Acquah, J.; Reed, S.; Wisniewski, M.

Innovative Technology to Automate and Improve the Detection Sensitivity of Ultra-Low Frequency Mutations Directly from Blood Liquid Biopsies; DNAe, 2025. https://www.dnae.com/wp-content/uploads/2025/11/DNAe_AMP_Oncology_Poster_print.pdf (accessed 2026-03-26).

(157) Kokoris, M.; McRuer, R.; Nabavi, M.; Jacobs, A.; Prindle, M.; Cech, C.; Berg, K.; Lehmann, T.; Machacek, C.; Tabone, J.; Chandrasekar, J.; McGee, L.; Lopez, M.; Reid, T.; Williams, C.; Barrett, S.; Lehmann, A.; Kovarik, M.; Busam, R.; Miller, S.; Banasik, B.; Kesic, B.; Arryman, A.; Rogers-Peckham, M.; Kimura, A.; LeProwse, M.; Wolfin, M.; Kritzer, S.; Leadbetter, J.; Babazadeh, M.; Chase, J.; Thiessen, G.; Lint, W.; Goodman, D.; O'Connell, D.; Lumanpauw, N.; Hoffman, J.; Vellucci, S.; Collins, K.; Vellucci, J.; Taylor, A.; Murphy, M.; Lee, M.; Corning, M. Sequencing by Expansion (SBX) – a Novel, High-Throughput Single-Molecule Sequencing Technology. bioRxiv March 15, 2025, p 2025.02.19.639056. https://doi.org/10.1101/2025.02.19.639056.

(158) Nabsys. The OhmX™ Platform: Electronic Genome Mapping. https://cdn.prod.website-files.com/67608f2c14ae5d4abe8a107c/68edd0b6b99c19707839d5b6_OhmX%20White%20Paper.pdf (accessed 2026-03-26).

(159) Henry, E.; Charalambous, E.; Betsou, F.; Mathieson, W. Implementing Routine Monitoring for Nuclease Contamination of Equipment and Consumables into the Quality Management System of a Laboratory. *Heliyon* **2024**, *10* (2), e24603. https://doi.org/10.1016/j.heliyon.2024.e24603.

(160) Cholet, F.; Ijaz, U. Z.; Smith, C. J. Differential Ratio Amplicons (Ramp) for the Evaluation of RNA Integrity Extracted from Complex Environmental Samples. *Environmental Microbiology* **2019**, *21* (2), 827–844. https://doi.org/10.1111/1462-2920.14516.

(161) Ratautas, D.; Serapinas, S.; Gineityte, J.; Butkevicius, M.; Danilevicius, R.; Dagys, M. Electrochemical System for the Rapid and Sensitive Detection and Quantification of Nuclease-like Activity Exhibiting Enzymes. EP4209596A1, July 12, 2023. https://patents.google.com/patent/EP4209596A1/en (accessed 2025-09-05).

(162) Wang, Y.-Y.; Hung, A. C.; Lo, S.; Hsieh, Y.-C.; Yuan, S.-S. F. MRE11 as a Molecular Signature and Therapeutic Target for Cancer Treatment with Radiotherapy. *Cancer Letters* **2021**, *514*, 1–11. https://doi.org/10.1016/j.canlet.2021.05.013.

(163) Zhou, C.; Feng, M.; Chen, X.; Gao, Y.; Chen, L.; Li, L.; Li, D.; Cao, Y. Exonuclease 1 (EXO1) Is a Potential Prognostic Biomarker and Correlates with Immune Infiltrates in Lung Adenocarcinoma. *Onco Targets Ther* **2021**, *14*, 1033–1048. https://doi.org/10.2147/OTT.S286274.

(164) Dave, N.; Liu, J. Fast Molecular Beacon Hybridization in Organic Solvents with Improved Target Specificity. *J. Phys. Chem. B* **2010**, *114* (47), 15694–15699. https://doi.org/10.1021/jp106754k.
(165) Vanderhoeven, J.; Pappaert, K.; Dutta, B.; Vanhummelen, P.; Baron, G. V.; Desmet, G. Exploiting the Benefits of Miniaturization for the Enhancement of DNA Microarrays. *ELECTROPHORESIS* **2004**, *25* (21–22), 3677–3686. https://doi.org/10.1002/elps.200406116.
(166) Dandy, D. S.; Wu, P.; Grainger, D. W. Array Feature Size Influences Nucleic Acid Surface Capture in DNA Microarrays. *Proceedings of the National Academy of Sciences* **2007**, *104* (20), 8223–8228. https://doi.org/10.1073/pnas.0606054104.
(167) Shchepinov, M. S.; Case-Green, S. C.; Southern, E. M. Steric Factors Influencing Hybridisation Of Nucleic Acids To Oligonucleotide Arrays. *Nucleic Acids Research* **1997**, *25* (6), 1155–1161. https://doi.org/10.1093/nar/25.6.1155.
(168) Ammar, R.; Smith, A. M.; Heisler, L. E.; Giaever, G.; Nislow, C. A Comparative Analysis of DNA Barcode Microarray Feature Size. *BMC Genomics* **2009**, *10* (1), 471. https://doi.org/10.1186/1471-2164-10-471.
(169) Gineitytė, J.; Serapinas, S.; Ratautas, D. Electrochemical DNA Hybridization Signal Amplification System Using Methylene Blue and Ascorbic Acid. *Electrochimica Acta* **2024**, *507*, 145146. https://doi.org/10.1016/j.electacta.2024.145146.
(170) Boal, A. K.; Barton, J. K. Electrochemical Detection of Lesions in DNA. *Bioconjugate Chem.* **2005**, *16* (2), 312–321. https://doi.org/10.1021/bc0497362.
(171) Kasprzak, A.; Zuchowska, A.; Poplawska, M. Functionalization of Graphene: Does the Organic Chemistry Matter? *Beilstein J. Org. Chem.* **2018**, *14*, 2018–2026. https://doi.org/10.3762/bjoc.14.177.
(172) Lim, C. Y.; Owens, N. A.; Wampler, R. D.; Ying, Y.; Granger, J. H.; Porter, M. D.; Takahashi, M.; Shimazu, K. Succinimidyl Ester Surface Chemistry: Implications of the Competition between Aminolysis and Hydrolysis on Covalent Protein Immobilization. *Langmuir* **2014**, *30* (43), 12868–12878. https://doi.org/10.1021/la503439g.
(173) Lozano-Chamizo, L.; Márquez, C.; Marciello, M.; Galdon, J. C.; de la Fuente-Zapico, E.; Martinez-Mazón, P.; Gonzalez-Rumayor, V.; Filice, M.; Gamiz, F. High Enhancement of Sensitivity and Reproducibility in Label-Free SARS-CoV-2 Detection with Graphene Field-Effect Transistor Sensors through Precise Surface Biofunctionalization Control. *Biosensors and Bioelectronics* **2024**, *250*, 116040. https://doi.org/10.1016/j.bios.2024.116040.
(174) Brustoloni, C. J.-M.; Soltan Khamsi, P.; Kammarchedu, V.; Ebrahimi, A. Systematic Study of Various Functionalization Steps for Ultrasensitive Detection of SARS-CoV-2 with Direct Laser-Functionalized Au-LIG Electrochemical Sensors. *ACS Appl. Mater.*

Interfaces **2024**, *16* (37), 49041–49052. https://doi.org/10.1021/acsami.4c09571.
(175) Fujimoto, N.; Bade, S.; Röckendorf, N.; Ramaker, K.; Frey, A. Polyethylene Glycol-Conjugated Alkylamines - A Novel Class of Surfactants for the Saturation of Immunoassay Solid Phase Surfaces. *Talanta* **2020**, *211*, 120741. https://doi.org/10.1016/j.talanta.2020.120741.
(176) Ricci, A. M.; Méndez De Leo, L. P.; Williams, F. J.; Calvo, E. J. Some Evidence for the Formation of an Azo Bond during the Electroreduction of Diazonium Salts on Au Substrates. *ChemPhysChem* **2012**, *13* (8), 2119–2127. https://doi.org/10.1002/cphc.201100882.
(177) Kenkel, S.; Mittal, S.; Bhargava, R. Closed-Loop Atomic Force Microscopy-Infrared Spectroscopic Imaging for Nanoscale Molecular Characterization. *Nat Commun* **2020**, *11* (1), 3225. https://doi.org/10.1038/s41467-020-17043-5.
(178) Muzyka, K.; Rico, F.; Xu, G.; Casuso, I. DNA at Conductive Interfaces: What Can Atomic Force Microscopy Offer? *Journal of Electroanalytical Chemistry* **2023**, *938*, 117448. https://doi.org/10.1016/j.jelechem.2023.117448.
(179) Muller, D. A. Structure and Bonding at the Atomic Scale by Scanning Transmission Electron Microscopy. *Nature Mater* **2009**, *8* (4), 263–270. https://doi.org/10.1038/nmat2380.
(180) Gong, P.; Lee, C.-Y.; Gamble, L. J.; Castner, D. G.; Grainger, D. W. Hybridization Behavior of Mixed DNA/Alkylthiol Monolayers on Gold: Characterization by Surface Plasmon Resonance and 32P Radiometric Assay. *Anal. Chem.* **2006**, *78* (10), 3326–3334. https://doi.org/10.1021/ac052138b.
(181) Špringer, T.; Šípová, H.; Vaisocherová, H.; Štěpánek, J.; Homola, J. Shielding Effect of Monovalent and Divalent Cations on Solid-Phase DNA Hybridization: Surface Plasmon Resonance Biosensor Study. *Nucleic Acids Research* **2010**, *38* (20), 7343–7351. https://doi.org/10.1093/nar/gkq577.
(182) Colthup, N. B.; Daly, L. H.; Wiberley, S. E. *Introduction to Infrared and Raman Spectroscopy*, 3rd ed.; Academic Press: Boston, 1990.
(183) Silva, S. M.; Hoque, S.; Gonçales, V. R.; Gooding, J. J. The Impact of the Position of the Redox Label on Charge Transfer and Hybridization Efficiency at DNA Interfaces. *Electroanalysis* **2018**, *30* (7), 1529–1535. https://doi.org/10.1002/elan.201800197.
(184) Khuda, N.; Somasundaram, S.; Urgunde, A. B.; Easley, C. J. Ionic Strength and Hybridization Position near Gold Electrodes Can Significantly Improve Kinetics in DNA-Based Electrochemical Sensors. *ACS Appl. Mater. Interfaces* **2023**, *15* (4), 5019–5027. https://doi.org/10.1021/acsami.2c22741.
(185) Cloutier, T. E.; Widom, J. DNA Twisting Flexibility and the Formation of Sharply Looped Protein–DNA Complexes. *Proceedings of*

the National Academy of Sciences **2005**, *102* (10), 3645–3650. https://doi.org/10.1073/pnas.0409059102.

(186) Uzawa, T.; Cheng, R. R.; White, R. J.; Makarov, D. E.; Plaxco, K. W. A Mechanistic Study of Electron Transfer from the Distal Termini of Electrode-Bound, Single-Stranded DNAs. *J. Am. Chem. Soc.* **2010**, *132* (45), 16120–16126. https://doi.org/10.1021/ja106345d.

(187) Steel, A. B.; Levicky, R. L.; Herne, T. M.; Tarlov, M. J. Immobilization of Nucleic Acids at Solid Surfaces: Effect of Oligonucleotide Length on Layer Assembly. *Biophys J* **2000**, *79* (2), 975–981.

(188) Jia, Y.; Sobolev, Y. I.; Cybulski, O.; Klucznik, T.; Quintana, C.; Ahumada, J. C.; Grzybowski, B. A. Aerodynamically Levitated Droplets as Small-Scale Chemical Reactors and Liquid Microprinters. *Angewandte Chemie International Edition* **2024**, *63* (39), e202318038. https://doi.org/10.1002/anie.202318038.

(189) Barman, S. R.; Khan, I.; Chatterjee, S.; Saha, S.; Choi, D.; Lee, S.; Lin, Z.-H. Electrowetting-on-Dielectric (EWOD): Current Perspectives and Applications in Ensuring Food Safety. *J Food Drug Anal 28* (4), 595–621. https://doi.org/10.38212/2224-6614.1239.

(190) *Ion 550™ Kit—Chef 8 reactions | Contact Us | Ion Torrent™ | thermofisher.com*. https://www.thermofisher.com/order/catalog/product/A34541 (accessed 2025-07-30).

(191) Rothberg, J. M.; Hinz, W.; Rearick, T. M.; Schultz, J.; Mileski, W.; Davey, M.; Leamon, J. H.; Johnson, K.; Milgrew, M. J.; Edwards, M.; Hoon, J.; Simons, J. F.; Marran, D.; Myers, J. W.; Davidson, J. F.; Branting, A.; Nobile, J. R.; Puc, B. P.; Light, D.; Clark, T. A.; Huber, M.; Branciforte, J. T.; Stoner, I. B.; Cawley, S. E.; Lyons, M.; Fu, Y.; Homer, N.; Sedova, M.; Miao, X.; Reed, B.; Sabina, J.; Feierstein, E.; Schorn, M.; Alanjary, M.; Dimalanta, E.; Dressman, D.; Kasinskas, R.; Sokolsky, T.; Fidanza, J. A.; Namsaraev, E.; McKernan, K. J.; Williams, A.; Roth, G. T.; Bustillo, J. An Integrated Semiconductor Device Enabling Non-Optical Genome Sequencing. *Nature* **2011**, *475* (7356), 348–352. https://doi.org/10.1038/nature10242.

(192) Kim, S.; Im, J.; Wang, S. X.; Lee, J.-R. Design and Validation of Specific Oligonucleotide Probes on Planar Magnetic Biosensors. *Anal. Chem.* **2024**, *96* (49), 19447–19455. https://doi.org/10.1021/acs.analchem.4c03973.

(193) Abraham Punnoose, J.; Thomas, K. J.; Chandrasekaran, A. R.; Vilcapoma, J.; Hayden, A.; Kilpatrick, K.; Vangaveti, S.; Chen, A.; Banco, T.; Halvorsen, K. High-Throughput Single-Molecule Quantification of Individual Base Stacking Energies in Nucleic Acids. *Nat Commun* **2023**, *14* (1), 631. https://doi.org/10.1038/s41467-023-36373-8.

(194) Hock, B.; Seifert, M.; Kramer, K. Engineering Receptors and Antibodies for Biosensors. *Biosensors and Bioelectronics* **2002**, *17* (3), 239–249. https://doi.org/10.1016/S0956-5663(01)00267-6.
(195) Strehlitz, B.; Nikolaus, N.; Stoltenburg, R. Protein Detection with Aptamer Biosensors. *Sensors* **2008**, *8* (7), 4296–4307. https://doi.org/10.3390/s8074296.
(196) *RNaseAlert™ Lab Test Kit 25 reactions | Contact Us | Invitrogen™ | thermofisher.com*. https://www.thermofisher.com/order/catalog/product/AM1964 (accessed 2025-01-21).
(197) Stein, J. A. C.; Ianeselli, A.; Braun, D. Kinetic Microscale Thermophoresis for Simultaneous Measurement of Binding Affinity and Kinetics. *Angewandte Chemie International Edition* **2021**, *60* (25), 13988–13995. https://doi.org/10.1002/anie.202101261.
(198) Immoos, C. E.; Lee, S. J.; Grinstaff, M. W. DNA-PEG-DNA Triblock Macromolecules for Reagentless DNA Detection. *J. Am. Chem. Soc.* **2004**, *126* (35), 10814–10815. https://doi.org/10.1021/ja046634d.
(199) Alagic, A.; Koprianiuk, A.; Kluger, R. Hemoglobin−Superoxide DismutaseChemical Linkages That Create a Dual-Function Protein. *J. Am. Chem. Soc.* **2005**, *127* (22), 8036–8043. https://doi.org/10.1021/ja050339r.
(200) Žalnėravičius, R.; Talaikis, M.; Klimas, V.; Serapinas, S.; Butkevičius, M.; Vaičiūnienė, J.; Morkvėnas, A.; Karabanovas, V.; Niaura, G.; Jagminas, A.; Dagys, M. Fabrication of Porous Black Gold Films by One-Step Anodic Treatment: Towards the Development of SERS-Active Nanosensors. *Materials Today Chemistry* **2025**, *47*, 102849. https://doi.org/10.1016/j.mtchem.2025.102849.
(201) *About dbSNP (Updated March 11, 2025)*. https://www.ncbi.nlm.nih.gov/snp/docs/about/ (accessed 2025-07-17).
(202) *rs12248560 RefSNP Report - dbSNP - NCBI*. https://www.ncbi.nlm.nih.gov/snp/rs12248560 (accessed 2025-07-16).

APPENDICES

Appendix I: Further application – The application of the DNase biosensor for RNase detection.

Appendix II: The mechanistic implications for live DNA hybridization monitoring: Exploration of the signal transduction mechanism of the methylene blue – ascorbic acid couple.

Appendix III: The application of the prepared SERS-active electrodes for quality control of chemical surface modifications.

Appendix IV: The mechanistic implications for melting-based DNA mismatch detection: Exploration of the signal transduction mechanism from the methylene blue-labeled DNA reporter strand and the hybridization impacts of solid-phase DNA probe density.

Appendix V: Application – the detection of double SNPs, miniaturization and sequencing.

1. Appendix I

The application of the DNase biosensor for RNase detection

Materials and Methods

Detection of RNases is typically performed at lower concentration than DNases, as RNases are more stable, difficult to inhibit and are generally more problematic due to low RNA stability.

Name	Composition (Sequence 5'-3')
Ribonuclease working buffer solution	20mM PBS, 20mM NaCl, pH 6
RNase stock solution	1000 Kunitz unit ml^{-1} RNAse A, 50mM Tris, 50% glycerol, pH 7
RNase sensor target stock solution	40 µM Oligonucleotide target, 20mM Tris, pH 7.00
RNase sensor probe sequence	Thiol-C6- AAT TAT CAA ACA CAA ACA GAC TTA A
RNase sensor target sequence	Atto MB2-g gca ggg cag ggc agu cgu uaa guc ugu uug ugu uug aua auu

Lyophilized Ribonuclease A was from bovine pancreas and glycerol were purchased from Sigma-Aldrich. DNase Alert kit was purchased from Sigma. All solutions were prepared in nuclease-free water. The working PBS buffer solution was heated to boiling in a household microwave and aliquoted into sterile test tubes and stored at ~4 °C.

RNA nucleic acid sequence (oligonucleotide target) was purchased from Metabion and used as received without additional purification procedures. Samples were prepared to measure the nuclease-like activity in laboratory water (nuclease-free) 0 KU ml^{-1}, 1×10^{-7} KU ml^{-1}, 1×10^{-6} KU ml^{-1}, 5×10^{-6} KU ml^{-1}, 1×10^{-5} KU ml^{-1}.

The oligonucleotide target was introduced into the samples and kept for 30 min at 37 ºC. The digested solution hybridization was monitored for 30 min.

Results

The DNase sensor when measured in parallel was comparable to a commercial kit (DNase Alert) (Fig. A1 1).

In samples with higher activity of RNase A (e.g., 1×10^{-5} KU ml^{-1}), the hybridization rate was negligible, since the enzyme cleaved the

overwhelming majority target present in the solution. It was impossible to quantify the RNase from 1×10^{-5} KU ml^{-1} onward. The LOD can be comfortably set at 1×10^{-6} KU ml^{-1} as these datapoints are over 3×SD away from control. (**Fig. A1 2**) At the activity given by the manufacturer of RNase Alert of 82 KU mg^{-1}, we can estimate a lower limit of detection of 12.2 pg ml^{-1} of sample. Using a commercial assay RNase Alert we would expect a detection limit of 2.5-5 pg/ml, (manufacturer also states this value as 3.5×10^{-7} units per 0.1 ml of sample[196]), meaning a very similar sensitivity is achieved.

One shortcoming of this iteration of assay design is the use of 3.5 ml of sample, because the hybridization is ultimately measured in a relatively large volume. The hybridization cell can be reasonably miniaturized to ~1 ml requiring an estimated 0.5 ml of sample for such assay. However, in the future the methods of external hybridization may be applied to avoid such problems. External hybridization can be easily performed in a 0.1 ml volume.

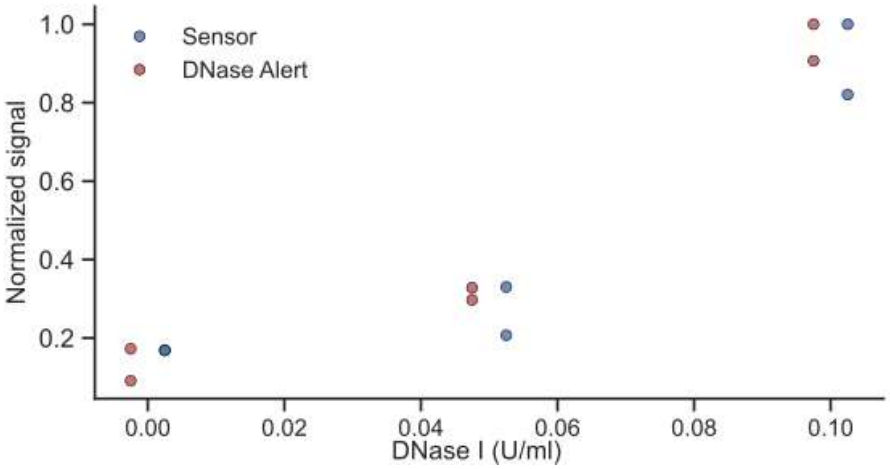

Figure A1 1. A comparison of the DNase sensor versus a commercial kit (signal normalized to 1 at the maximal value for simplicity, unitless).

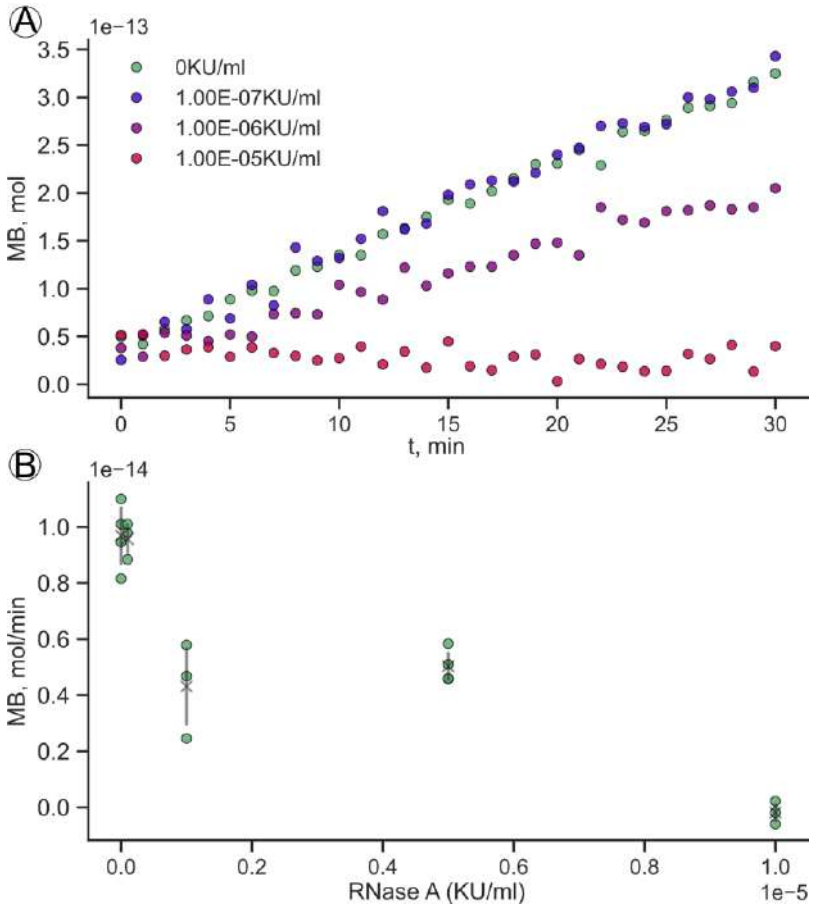

Figure A1 2. A: An example of hybridization kinetics using RNase A pretreated target; B: RNase concentration measurements (Mean ± SD).

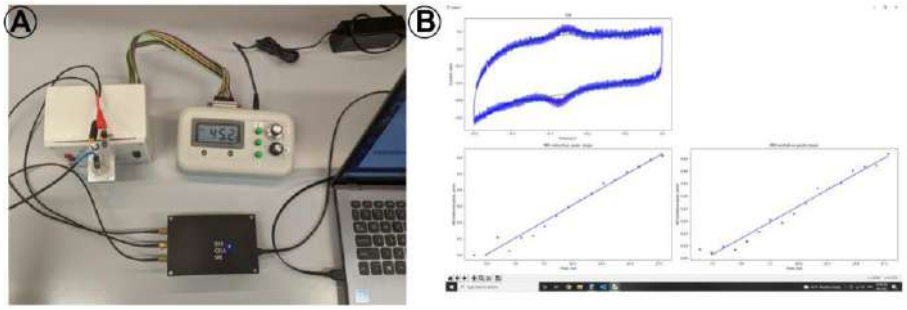

Figure A1 3. A representation of A) a prototype device and B) prototype software (from **Publication 1 SI**).

2. Appendix II

The mechanistic implications for live DNA hybridization monitoring: Exploration of the signal transduction mechanism of the methylene blue – ascorbic acid couple

Name	Sequence 5'-3'
DNA Probe (DNAP)	Thiol-C6-CGC ATT ATC TCT TAC ATC AGA
ZNA Probe (ZNAP)	Thiol-C6-CGC ATT ATC TCT TAC ATC AGA-(ZNA-4)
Reporter *1 HEG5	Atto MB2-(HEG-spacer)×2-GAT GCT TTG AGA ACA
Reporter *1 HEG3	GAT GCT TTG AGA ACA-(HEG-spacer)×4-Atto MB2
Reporter *1 5	Atto MB2-GAT GCT TTG AGA ACA
Reporter *1 3	GAT GCT TTG AGA ACA-Atto MB2
Target *1s	C TGT TCT CAA AGC ATC TCT GAT GTA AGA GAT AAT GCG

Methods

The experiments were carried out according to Gineitytė et. al.,[169] using 3 M NaCl, 30 mM Ascorbate, pH 7, 25 °C, 1500 rpm stirring with -100 mV vs. Ag/AgCl (3 M KCl) at 0.5 Hz. The reporter sequences were introduced at 150 s (no visible signal was observed) and the target sequence **Target *1s** was introduced at 400 s. The DNA and the ZNA electrodes were measured simultaneously with PalmSens4 bipotentiostat.

$$I_t = A(1\text{-}e^{-Bt}) + C \qquad \text{Equation (A1)}$$

$$I_t = k\ n\ F\ [AA]\ ptMB_{max}(1\text{-}e^{-k_{on}[Targ]t}) \qquad \text{Equation (A2)}$$

The current was zeroed and the baseline was fitted according to Eq. A1 and the hybridization was fitted according to Eq. A2, where:

- n = 2 (electrons participating in a process),
- F = 96485 C mol^{-1} (Faraday's constant),
- [AA] = 0.03 M (ascorbic acid concentration),
- [Targ] = 20 × 10^{-9} M (+ 4× excess of the reporters was used),
- $ptMB_{max}$ = 0.0205 × 10^{-12} M – this value was not fitted as per publication but rather is a reasonable estimate from previous CV experiments [Appendix IV],
- The parameters k and k_{on} were fitted

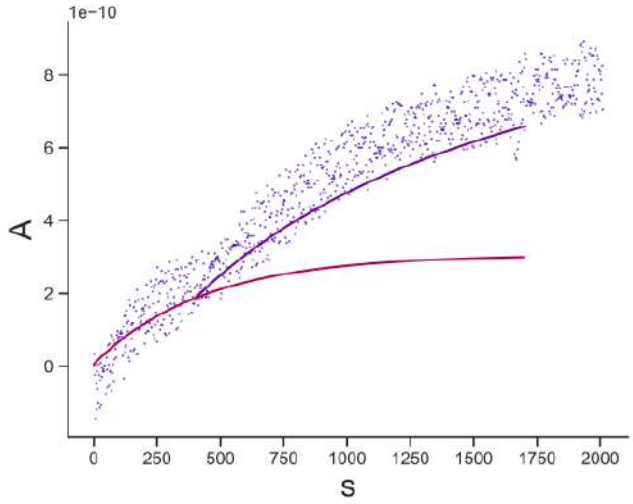

Figure A2 1. Typical experimental data with baseline and hybridization fits shown.

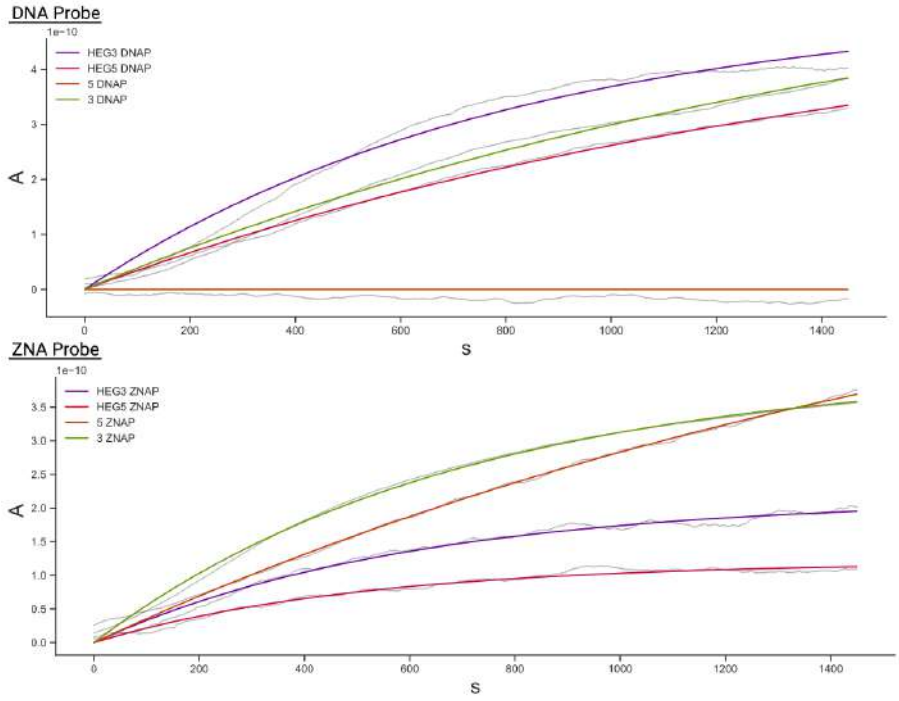

Figure A2 2. Hybridization currents after zeroing, smoothing and baselining (the dots represent processed data, average of 2 electrodes and the lines represent the fitted curves).

While these results successfully demonstrate the hybridization kinetics in sandwich format, the previously obtained (8 M^{-1} s^{-1})[169] bimolecular constant was not improved and the signal is generally poor (~0.3 nA/20 nM Target).

These experiments were predominantly exploratory in nature as an improvement in electron transfer rate constant of ~100× is reported in literature via MB position change.[130] The observed changes in the signal are not noteworthy and further optimization was not pursued. Modifying the solid phase for probes containing a distal ZNA-4 modification similarly shows no large improvement.

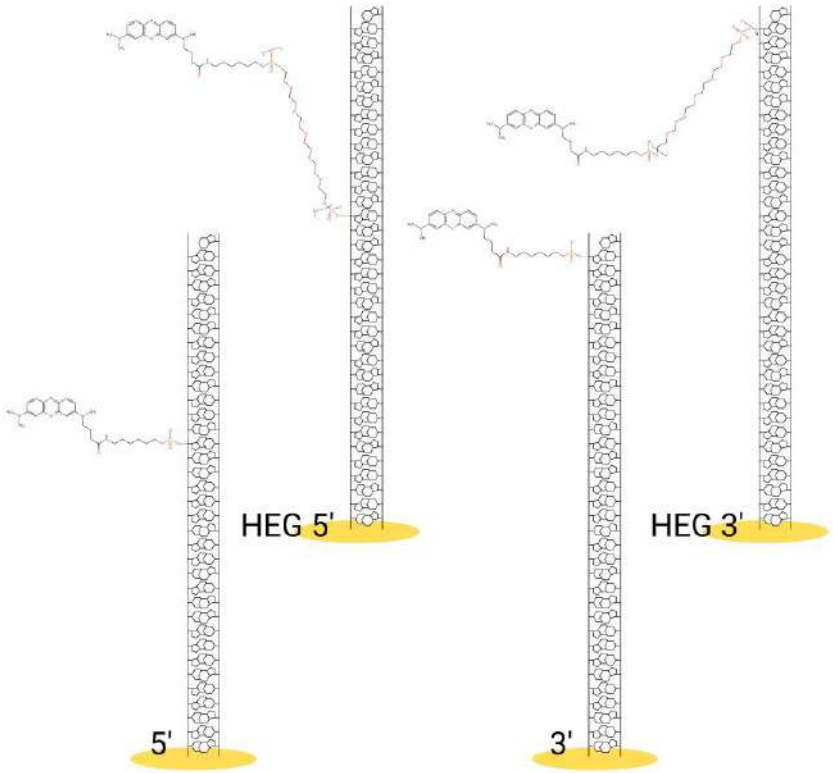

Figure A2 3. Label position on distal and proximal sides of the reporter and via an ethylene glycol bridge.

The k_{on} constant is reported in literature in the range of 500 [63]–1 500 000 [197] M^{-1} s^{-1} and is [NaCl] and probe coverage dependent. In these experiments the k_{on} was much higher than in our publication.

Name	k (M^{-1} s^{-1})	k_{on} (M^{-1} s^{-1})	Name	k (M^{-1} s^{-1})	k_{on} (M^{-1} s^{-1})
HEG3 DNAP	4.35	62150	HEG3 ZNAP	1.80	83869
HEG5 DNAP	4.63	32239	HEG5 ZNAP	1.00	99203
5 DNAP	0.00	0	5 ZNAP	5.81	26286
3 DNAP	5.49	30570	3 ZNAP	3.42	72877

Table A2 1. The measured constants of various duplex-ascorbic acid reaction.

Interestingly the 5 DNAP sandwich – a sandwich with expected low MB mobility due to DNA duplex repulsion – (to move the label, the entire DNA chain with a large negative charge must bend sharply) shows an abysmal response. HEG extension has lowered the reaction rate constant (k) in all cases as it likely increases the label travel distance. This is indicative of a mobility-driven charge transfer. Internal PEG bridges have been previously used to lower the rate of label-surface collisions.[198]

Another interesting observation is that the hybridization rates were overall improved using the ZNA probes, suggesting a potential application for more rapid measurements.

3. Appendix III

The application of the prepared SERS-active electrodes for quality control of chemical surface modifications

Materials and Methods

Electrode manufacturing

Methrohm C220AT SPE gold electrodes were prepared in 300 mM aqueous oxalic acid at 5 °C, +3 V vs. $Hg/HgSO_4$.

Synthetic methods (adapted from[199]) (Fig. A3 1)

4,4'-Dithiobisphenylacetic acid (**I**)

I_2 (88 mg; 0.35 mmol) was dissolved in ~3ml of anhydrous ethanol and triethylamine (300 µl) was added, then 4-mercaptophenylacetic acid (106mg; 0.63mmol) in a minimal amount of EtOH was added and the solution instantly discolored. The reaction was left overnight in a capped vial. 300 µl of 10% aq. Na_2SSO_3 was added for quenching followed by ~30 ml of 50 mM aq. HCl, the precipitate was collected by filtration and washed with water, dried; yield: 62 mg (59 %).

4,4'-Dithiobisphenylacetyl chloride (**II**)

(62 mg; 0.185 mmol) of **I** was dissolved in 3 ml dichloromethane and 1 ml $SOCl_2$ in a flask and agitated with ultrasound for ~5 min. The solution was left to stir overnight at room temperature, volatiles removed by vacuum distillation leaving ~ 60 mg of a yellow residue which was flushed with argon to remove any trace of $SOCl_2$ and processed as-is immediately.

4,4'-Dithiobis-N-(4-**C**ya**n**ophenyl)-**P**henyl**A**cetamide (SSCNPA)

Into the flask containing (~60 mg; ~0.161 mmol) of **II**, 2 ml of DMAc was added, followed by catalytic dimethylaminopyridine (~2 mg) and 4-aminobenzonitrile (42 mg; 0.356 mmol). The solution was left to stir overnight. Water and 50 mM HCl were added until no more precipitate was formed. The suspension was centrifuged under 1800 g, mixed with another 30 ml of 50 mM HCl which was decanted after centrifugation and then with water which was processed likewise. The resulting light yellow powder was recrystallized from $CHCl_3$ and checked with TLC-UV with EtOAc-hexanes 1:1 (a single spot separate from the starting materials). Yield: 26 mg (30 %) of lightweight white-parchment color powder which is highly insoluble.

Thin-layer chromatography (TLC) was performed on Macherey-Nagel silica gel 60 aluminium plates containing UV indicator.

Spectroscopic methods

The Raman spectra were recorded employing inVia (Renishaw, UK) spectrometer equipped with a thermoelectrically cooled CCD camera (−70 °C) with a confocal LEICA microscope. A 785 nm laser beam was used as an excitation source. 1200 lines/mm gratings were used to record the Raman spectra. The laser power at the sample surface was restricted to 8 mW (10%). The 50x/NA 0.75 objective was used during all the measurements. The laser was focused to ~ 1,3 μm diameter spot on the sample. The total integration time for each spectrum was 100 s. The measurements were performed on Metrohm C220AT screen printed gold electrodes with electrochemical structurization[200] and chemical modification.

4-mercaptophenylacetic acid was grafted from a 3 mM methanolic solution at room temperature overnight. Adsorbed 4-aminobenzonitrile was dropcast as a 10 μl volume of 12 μM methanolic solution (practically, a small amount, but on the order of 1000× excess relative to monolayer). SSCNPA was grafted from a 200 μM acetone solution overnight. All electrodes were washed with a large amount of methanol.

The spectra were flattened via asymmetric least squares, the regions 937-1859 and 1860-2627 cm^{-1} were trimmed, additively offset to align and joined, the intensity was normalized to the common 1076 cm^{-1} peak and then the complete spectra were offset from each other in Python.

NMR experiments were performed on a Bruker Avance Neo NMR console equipped with Bruker Ascend 14.1 T superconducting magnet and 5 mm high-resolution probe. 1H NMR spectra were collected at 25 ppm width with 64 k point density after excitation with a 10 μs rectangular pulse.

ATR-FTIR was performed on a Bruker LUMOS II FTIR microscope running OPUS 8.5 software. A MIR source, ZnSe beamsplitter, room temperature TE-MCT detector and a germanium crystal at medium contact pressure were used. Spectra were recorded on household aluminium foil in the range 4000-600 cm^{-1}, at 4 cm^{-1} resolution, averaged from 64 spectra.

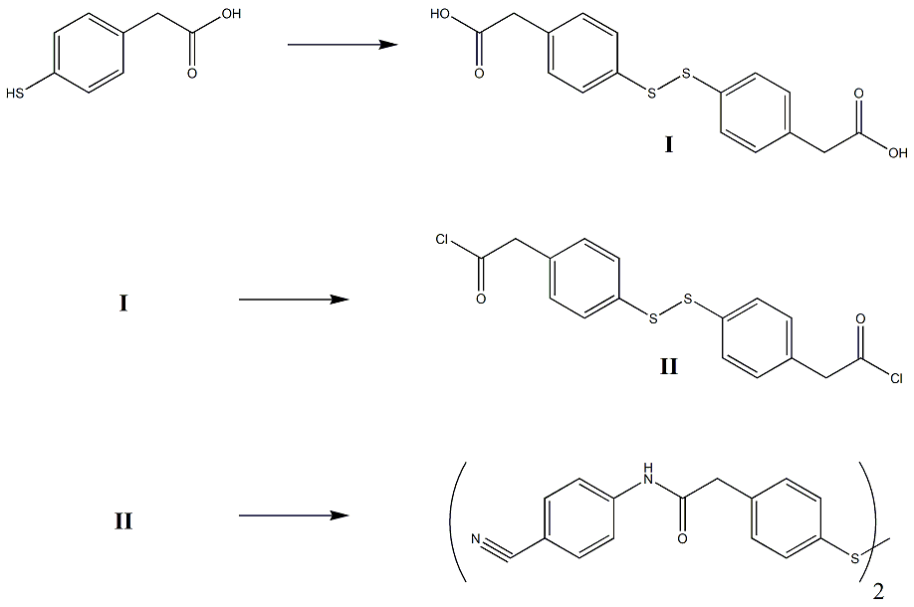

Figure A3 1. SSCNPA synthesis: **I**: $EtOH/I_2$, rt; **II**: $SOCl_2/MeCl_2$, rt; **SSCNPA**: DMAc/4-aminobenzonitrile, rt.

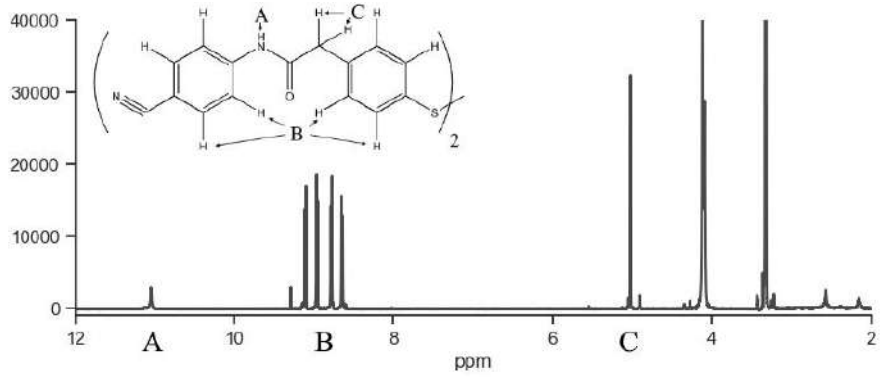

Figure A3 2. SSCNPA ^1H NMR (600 MHz) in Acetone-d6.

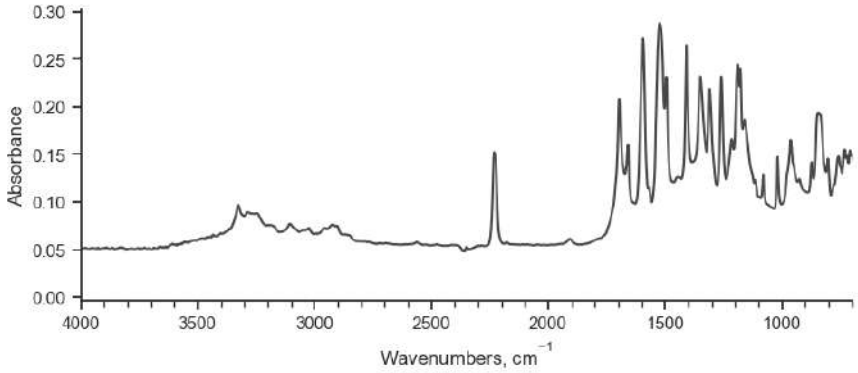

Figure A3 3. An ATR-FTIR spectrum of SSCNPA as a thin film (~1-10 μg) cast from acetone onto aluminium foil. The triple bond frequency is very clear at ~2230 cm^{-1}, with N-H stretching at 3325 cm^{-1} and the carbonyl at 1700 cm^{-1}.

Results

Raman spectroscopy is one of the very few (perhaps the only) methods for rapid and approachable structural characterization of solid phase molecular monolayers.

First, a diisocyanate surface activation (somewhat analogous to the ubiquitous glutaral) was investigated as it is exceptionally rarely employed in biosensors. The coupling of hexyl diisocyanate (often referred to as HMDI) was attempted onto mixed terminal -OH of mercaptohexanol/mercaptoethanol layers in THF, MeCN and in DMF under various concentrations, temperatures and organic base catalysts. Unfortunately, perhaps due to layer thickness or the crosslinker reactivity to air or to itself, the SCN vibration was never observed in a SERS spectrum. These measurements already inform us that the attempted Au-S-Hex-O-C(=O)-N-Hex-N=C=O reactive layer formation was likely unsuccessful, possibly explaining the sparse literature reporting.

SERS application for verifying amide (specifically, anilide) formation on a surface adsorbed monolayer was investigated.

SSCNPA spectra were recorded (**Figure A3 4**) as a:

- preassembled unit bound as a monolayer (simulated “perfect” solid phase coupling; **SSCNPA**)
- a surface with a free carboxyl monolayer and the nitrile dropcast (10 nM solution in MeOH) on top (simulated unsuccessful solid phase coupling + adsorption; **SPA + CN**)

- and the acid alone (simulated unsuccessful solid phase coupling, clean surface; **SPA**).

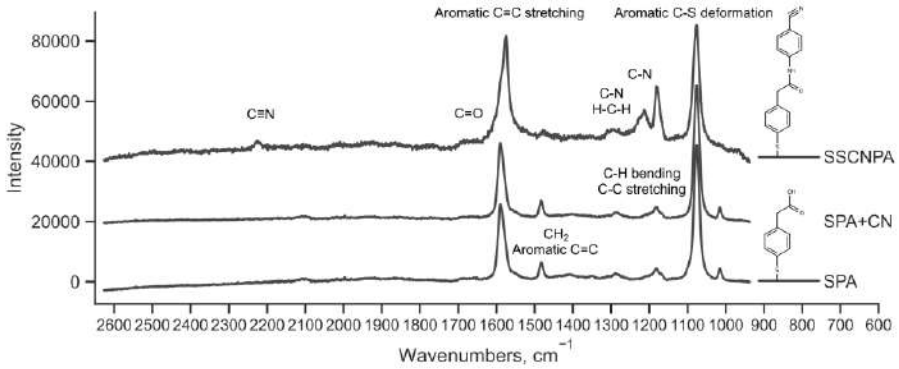

Figure A3 4. SERS spectra of SSCNPA (coupled), SPA + CN (adsorbed) and SPA (clean) with tentative peak assignments.[182]

Interestingly, the cyanide group enhancement (~2230 cm^{-1}) was very mild (unlike in FTIR, where a very sharp and distinct peak was observed, albeit from a significantly larger (~microgram) quantity of material), and the ~1200 cm^{-1} C-N vibrations (common in nitrile and amine) were a much better indicator of coupling. Other features that were clear indicators of coupling include the 1590 cm^{-1} region aromatic bands.

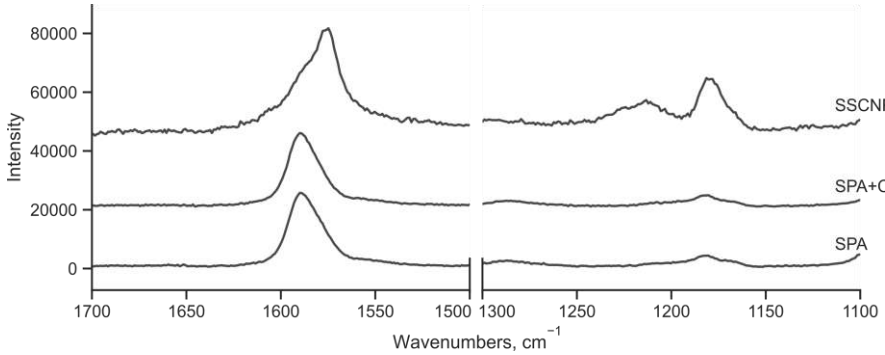

Figure A3 5. SERS spectra of SSCNPA (coupled), SPA + CN (adsorbed) and SPA (clean) 1590 cm^{-1} and 1200 cm^{-1} regions.

Interestingly the dropcast aminobenzonitrile contamination was not observable, despite a relatively large amount (~0.12 nmol) applied. The results, however are encouraging as ultimately we can observe a tremendous difference between coupling test and control groups and clearly identify non-coupled electrodes and gain insight whether any crossreaction was adsorptive or covalent. Thus, solid phase synthesis/coupling optimization

and success for novel reactions could be monitored via SERS moving forward.

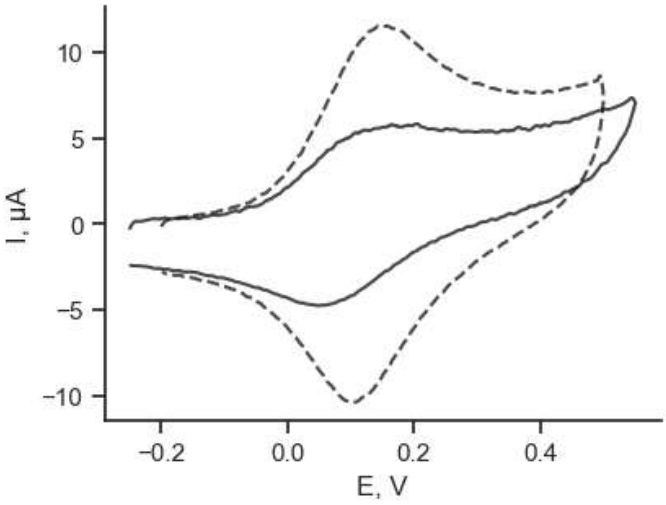

Figure A3 6. A directed ligation chemistry currently in development. **Dashed line:** directed ligation, **solid line:** simultaneous non-directed coupling side-reaction onto a nearby electrode.

4. Appendix IV

The mechanistic implications for melting-based DNA mismatch detection: Exploration of the signal transduction mechanism from the methylene blue-labeled DNA reporter strand and the hybridization impacts of solid-phase DNA probe density

Materials and Methods

DNA Probe density was measured according to Steel.[62]

Name	Sequence 5'-3'
DNA Probe	Thiol-C6-CGC ATT ATC TCT TAC ATC AGA
Probe 3MB	Thiol-C6-CGC ATT ATC TCT TAC ATC AGA-Atto MB2
ZNA Probe	Thiol-C6-CGC ATT ATC TCT TAC ATC AGA-(ZNA-4)
R*1 HEG5	Atto MB2-(HEG-spacer)×2-GAT GCT TTG AGA ACA
R*1 HEG3	GAT GCT TTG AGA ACA-(HEG-spacer)×4-Atto MB2
R*1 5MB	Atto MB2-GAT GCT TTG AGA ACA
R*17 5MB	Atto MB2-GAT ACT TTG AGA ACA G
R*1	GAT GCT TTG AGA ACA-Atto MB2
R*17	GAT ACT TTG AGA ACA G-Atto MB2
T*1	**CAA ATT TGT GTC TT** CTG TTC TCA AAG CAT C TCT GAT GTA AGA GAT AAT GCG **CCA C**
T*1m	**CAA ATT TGT GTC TT** CTG TTC TCA AAG CAT C TCT GAT GTA AGA GAT AAT GCG
T*1s	CTG TTC TCA AAG CAT C TCT GAT GTA AGA GAT AAT GCG
T*17	**CAA ATT TGT GTC TT** CTG TTC TCA AAG TAT C TCT GAT GTA AGA GAT AAT GCG **CCA C**

Results

When using a target with 5'-overhangs we encountered a very large loss of signal and peak overpotential (**Fig. A4 1.2**). It is suspected that as the label is now (due to the overhangs at the top) located towards the middle of the duplex it is fairly well insulated from approaching the electrode surface. The MB label is in other words, surrounded by negative charges from both sides.

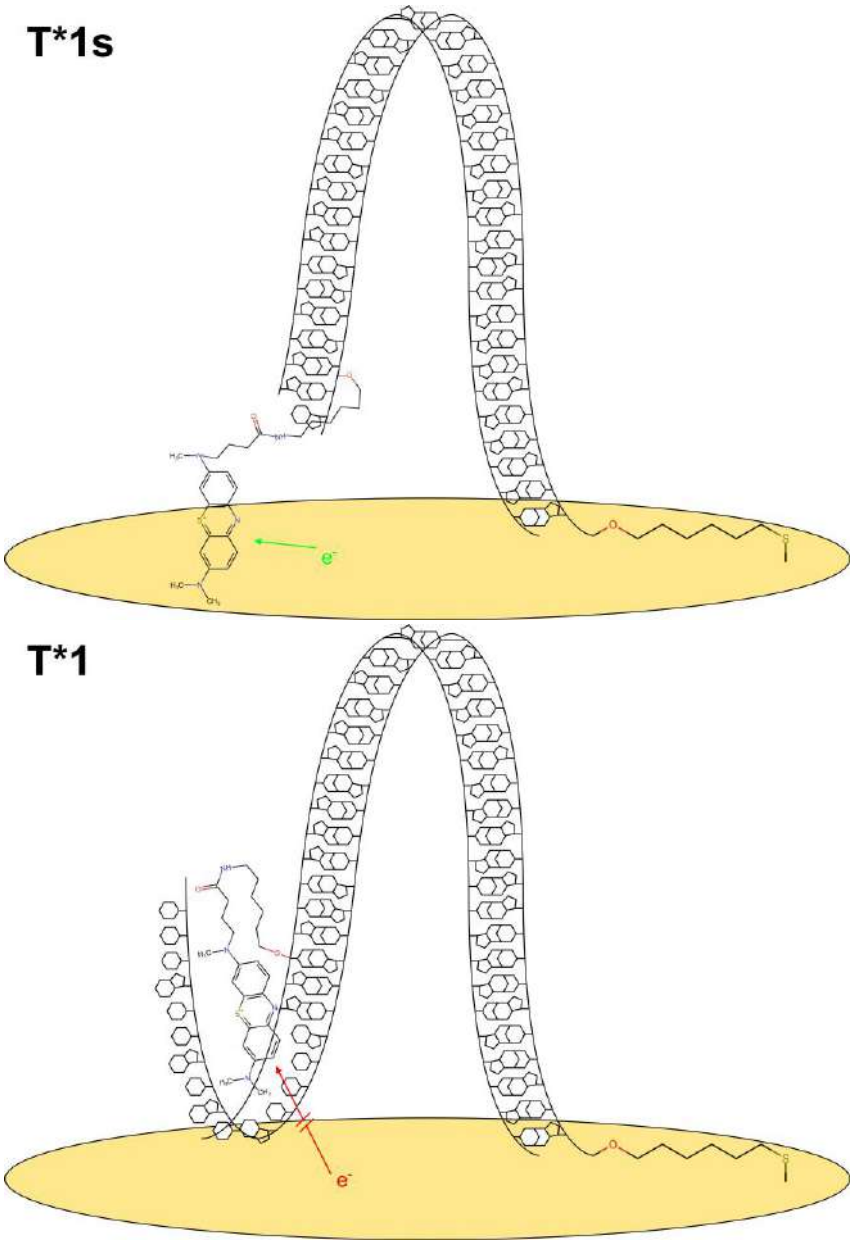

Figure A4 1.1 Sandwich representation containing the **DNA probe** and **R*1**. With a 1-bp overhang (**T*1s**), the signal is clear. With a 15-bp overhang (**T*1**), the signal becomes becomes very poor. Only the upper overhang is shown. The sandwich is likely in a more "upright" conformation than shown. This is an attempt to represent a macromolecular structure. The average conformation is not known. Elements are not to scale.

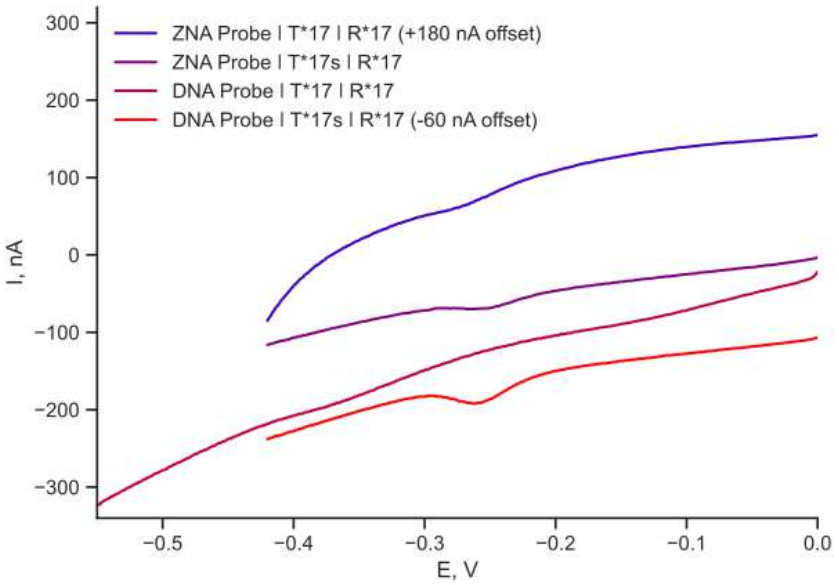

Figure A4 1.2. Linear sweep voltammograms of various sandwich duplexes. Average of 2 electrodes each. We can see that the DNA probe works well with T*17s ("short") but very poorly with T*17 (overhanging). The introduced ZNA-4-modified probe works well with both targets. *The DNA and ZNA probe densities are not physically standardized relative to each other.*

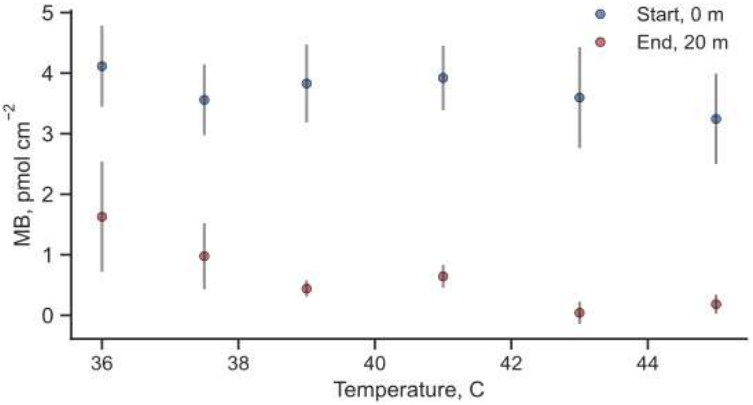

Figure A4 1.3. T*1s construct on DNA Probe at various temperatures. We can see that the starting signal is mostly stable over the 9 °C range, and the full melting is achieved at around 41 °C (at 20 minutes).

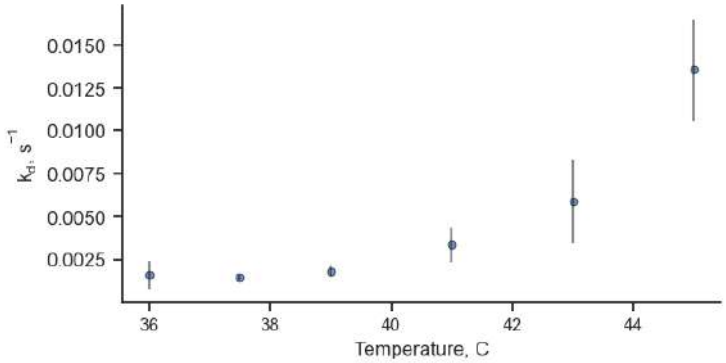

Figure A4 1.4. T*1s construct on DNA Probe at various temperatures. The relationship between the dissociation rate constant and the temperature appears exponential.

An attempt was made to "plug in" the label via a labeled probe, so that the path MB(target)→MB(probe)→Probe chain→electrode is made very direct if the signal transduction were occurring via the DNA duplex (**Figure A4 2.2**). Since from the MB(probe) molecule everything is covalently linked to the electrode and the target ǀ probe duplex should display π–π stacking – better signal transduction was expected. However, no powerful signals were ever observed.

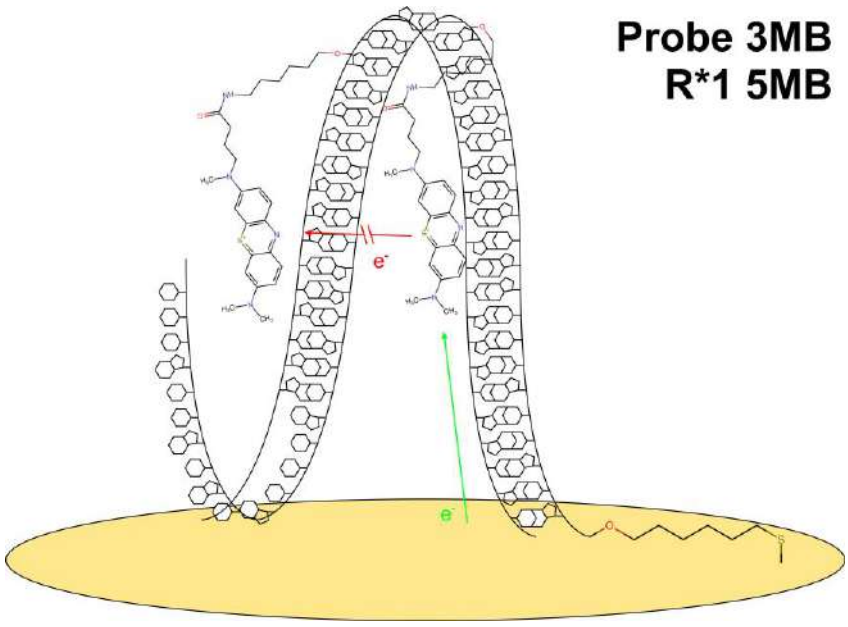

Figure A4 2.1. Sandwich representation containing the labeled DNA probe **Probe 3MB** and the inverted reporter **R*1 5MB**. Only the upper

overhang is shown. The sandwich is likely in a more “upright” conformation than shown. This is an attempt to represent a macromolecular structure. The average conformation is not known. Elements are not to scale.

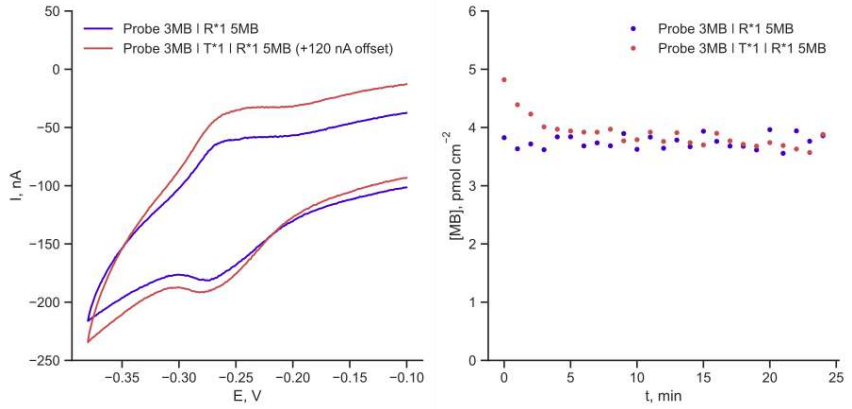

Figure A4 2.2. Inverted reporter | labeled probe sandwich (Probe 3MB | R*1 5MB). The results displayed are of 1 replicate, but were performed subsequently on the same electrode, therefore are directly comparable. We can see that the signal increase from the reporter is very small, generally a hybridization efficiency of 80% and therefore a signal of 180% would not be unreasonable. It is unclear as to why the melting appears to be so rapid, simultaneous gain of MB and mobility-loss-mediated quenching may offer some explanation.

Plugging in the reporter label was unsuccessful and gave weak and inconsistent results every time. The probe density appears to be reasonable from the MB density. The existing MB label could change intensity due to other reasons such as probe mobility or screening and presented a risk of false results. This system was not pursued further.

A ZNA probe was introduced to screen the DNA duplexes and allow greater mobility (DNA collapse) and higher stability. The ZNA-4 chain ideally should change the probe charge from -21 to -10, approximately halving it. Introducing free polycations in solution may, for instance, cause uneven screening and a minuscule change in the concentration (e.g., 100 nM) of a dissolved polycation could result in a change from partial (-10) to complete (-0) screening. Complete screening would likely allow other DNA oligomers to adsorb negating any specificity of the sensor. The measurement of the **ZNA** probe surface density with RuHex was unsuccessful ($\sim 2\times10^{12} \pm 2\times10^{12}$ molecules cm^{-2}) and the optimal density is unknown, but

as the charge was halved, the concentration of the probe was thus also halved producing practically functional electrodes. The **DNA** probe density achieved was $4.6\times10^{12} \pm 3\times10^{11}$ molecules cm^{-2}, which is generally considered to be excellent. The ZNA probes were later optimized further via easy-to-manufacture physical blocking [**Appendix V**] producing improvements in hybridization of almost an order of magnitude with excellent repeatability.

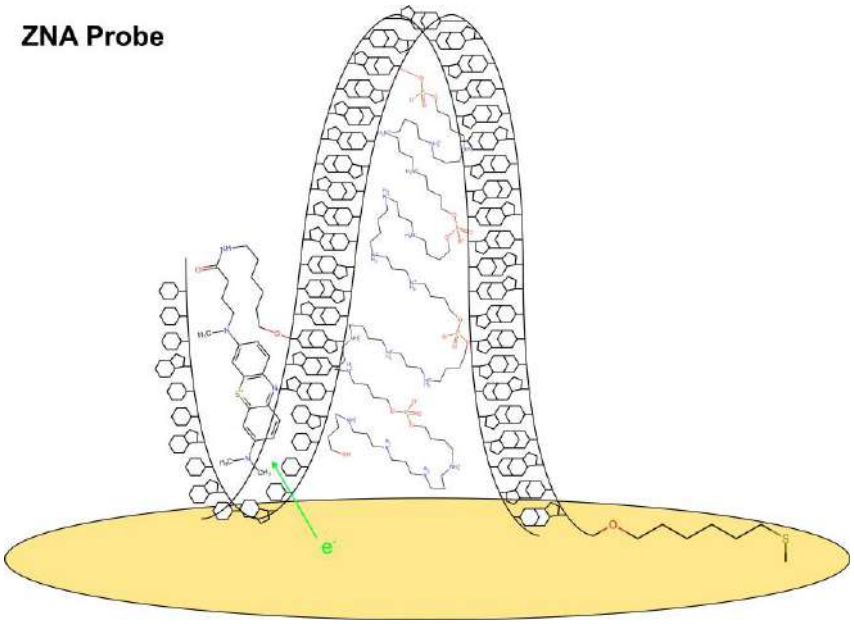

Figure A4 3. A sandwich representation containing the **ZNA probe** and **R*1**. Only the upper overhang is shown. The sandwich is likely collapsed, releasing the MB bringing it closer to the surface. This is an attempt to represent a macromolecular structure. The average conformation is not known. Elements are not to scale.

To further interrogate the signal transduction, "freely moving" labels were tested. A PEG chain from the sandwich middle and from the top – minus the overhang was extended to approximately reach the electrode surface – these were the HEG inserted reporters.

The HEG reporters both showed excellent signal transduction with both DNA and ZNA probes and any target overhangs. This reinforces the idea that the label mobility is greatly important in the signal transduction. Perhaps the MB is still able to intercalate somewhere near the electrode and

transduce some of its signal via π–π stacking or perhaps it overwhelmingly occurs via relocation to the surface. This finding does not completely rule out small dsDNA conductivity, but it does convincingly show that removing the MB from entrapment inside negative charges is very important, either via mobility (PEG) or via charge screening (ZNA). The fourth publication was carried out with ZNA probes and regular DNA reporters as this combination showed good results, however the HEG reporters show promise for future applications. *Note: the HEG reporter melting may occur in a completely different manner. I would like to also add an anecdotal report of a HEG reporter showing large reductive (but not oxidative – asymmetric) peak broadening under different voltammetric conditions and electrolytes than discussed here.*

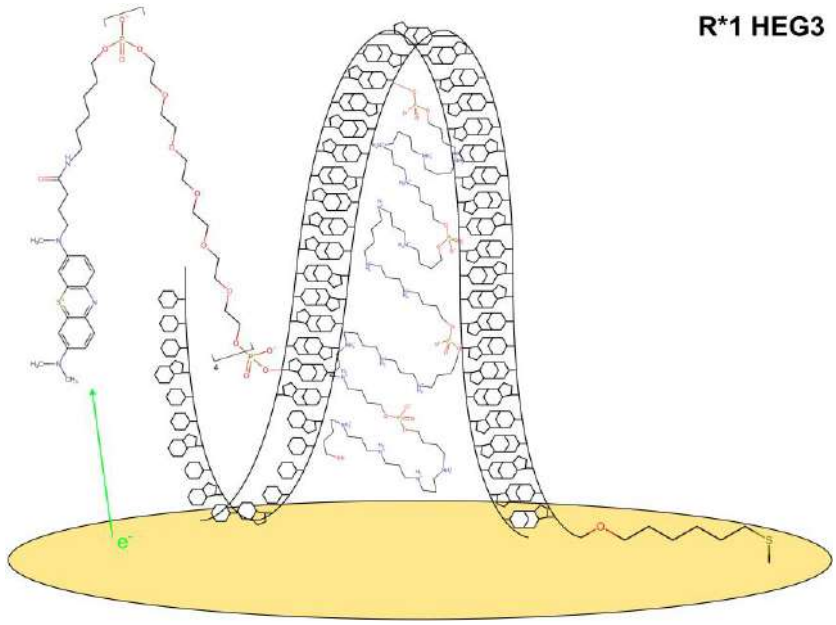

Figure A4 4.1. A sandwich representation containing the **ZNA probe** and **R*1 HEG3**. Only the upper overhang is shown. The sandwich is likely collapsed, and the "long" distal (6×4 ethylene moieties) PEG chain allows for extensive mobility of the MB. The PEG-MB chain was chosen to be long enough to reach the electrode in an "upright" configuration from the very top. This is an attempt to represent a macromolecular structure. The average conformation is not known. The elements are not to scale.

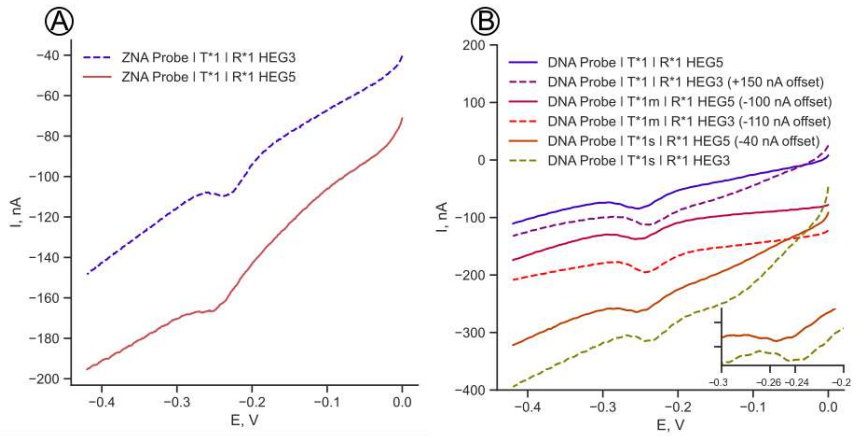

Figure A4 4.2. Linear sweep voltammograms of the HEG reporters. A) **ZNA probes** (2 electrode averages); B) **DNA probes** (1 electrode each). T*1m and T*1s are overhang-removed target sequences. Broadly in all cases R*1 HEG3 (the "long" distal PEG chain) reporter has a lower overpotential (inset) at ~-240mV vs. ~-250mV with DNA and even lower with ZNA.

5. Appendix V

Application – the detection of double SNPs, miniaturization and sequencing

Name	Sequence 5'-3'
DNA Probe	Thiol-C6-CGC ATT ATC TCT TAC ATC AGA
ZNA Probe	Thiol-C6-CGC ATT ATC TCT TAC ATC AGA-(ZNA-4)
R*1	GAT GCT TTG AGA ACA-Atto MB2
R*17	GAT ACT TTG AGA ACA G-Atto MB2
T*1	**CAA ATT TGT GTC TT** CTG TTC TCA AAG CAT C TCT GAT GTA AGA GAT AAT GCG **CCA C**
T*1s	CTG TTC TCA AAG CAT C TCT GAT GTA AGA GAT AAT GCG
T*17	**CAA ATT TGT GTC TT** CTG TTC TCA AAG TAT C TCT GAT GTA AGA GAT AAT GCG **CCA C**

Methods

Electrode preparation:

The 0.5 mm electrodes were manufactured in house from 0.5 mm 99.99 % gold wire (Sigma Aldrich). A 0.6 mm hole was drilled into a 2 mm copper cylinder serving as an electrical and mechanical contact, wherein ~10 mm length of gold wire was inserted and a short section crimped. Two gold-tip copper rods were inserted side-by-side into an upright brass tube with a PTFE spacer disc to keep the wires from drifting and cast in polypropylene at 140-200 °C in a commercial oven under air. While these electrodes are excellent mechanically and chemically, I must note that polypropylene has notable thermal expansion and is not an ideal material choice for encasing metals.

The electrodes were prepared and measured as per **Publication 4**. The dsZNA condition entails physical blocking – preparing a ZNA Probe|T*1 duplex prior to gold modification (i.e., using sacrificial DNA target as a "spacer" during solid phase modification), thus physically blocking excess probe adsorption. The electrodes prepared with dsZNA probe were washed in pure water at 37 °C overnight to ensure target removal prior to measurement.

30% EtOH hybridization buffer: 10 mM HEPES, 300 mM NaCl, 30% EtOH, salmon testes DNA 50 µg/ml, pH 7.6

20X SSC hybridization buffer: 300 mM monosodium citrate, 3 M NaCl, pH 7 (diluted to 5X and SDS added to 0.1%)

Melting buffer: 20 mM PBS, 280 mM NaCl, 10% Formamide, 0.05% Tween-20, pH 7. *Note: melting is not appreciably occurring at room temperature; only non-specific adsorption is being removed.*

In **Figure A5 2:** 3 cyclic voltammograms (0.1 V → –0.38 V, 50 mVs^{-1}) with intermittent stirring at 37° C were recorded and averaged to obtain 1 datapoint. The DNA probe and the short target (T*1s) are used with at least 4× excess of R*1. Hybridization is carried out in one-pot at 37° C. A melting buffer with 200 mM NaCl is used.

In **Figure A5 3:** 4 linear sweep voltammograms (0 V → –0.42 V, 50 mVs^{-1}) with constant stirring at 25° C were recorded and averaged to obtain 1 datapoint. The ZNA probe and the full target (T*1) are used with at least 2× excess of R*1 or at least 80 nM R*1. Both strands are hybridized in one-pot at 37° C for 20 min.

The following equation was used to fit the Langmuir constant with the MB cm^{-2}_{max} taken as 1.5 pmol for ssZNA and 2.3 pmol for dsZNA, Olig being the target concentration and K_L being the Langmuir constant (nM^{-1}).

$$MB\ cm^{-2} = \frac{MB\ cm^{-2}{}_{max} \times K_L \times Olig}{1 + K_L \times Olig}$$

Total hybridization ΔG was calculated from:

$$\Delta G = -RT ln K_L$$

Results

Controlling the SAM density experimentally via a sacrificial DNA target was very simple and produced reasonably good sensitivity of a few nM compared to tens of nM from previous design. Changing the hybridization buffer did not meaningfully improve the signal (**Figure A5 2**). Changing the electrode size did not meaningfully improve the sensitivity (**Figure A5 3A**). If the Langmuir adsorption model is fitted, the following reciprocal Langmuir constants (i.e., equilibrium constants) are obtained:

Ø	K_D
0.5 mm (ds–SAM)	3.5 nM
1.6 mm (ds–SAM)	3.7 nM
2.0 mm (ds–SAM)	3.8 nM
2.0 mm (ss–SAM)	28.5 nM

Figure A5 1. The hybridization sensitivities of different electrode disc sizes.

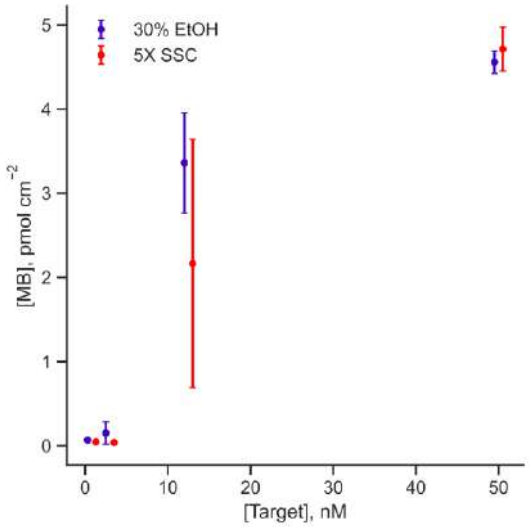

Figure A5 2. The comparison of hybridization buffers. DNA probe: T*1s | R*1 sandwich with varying T*1s concentration. Mean and SD. [Target], nM staggered, n = 3.

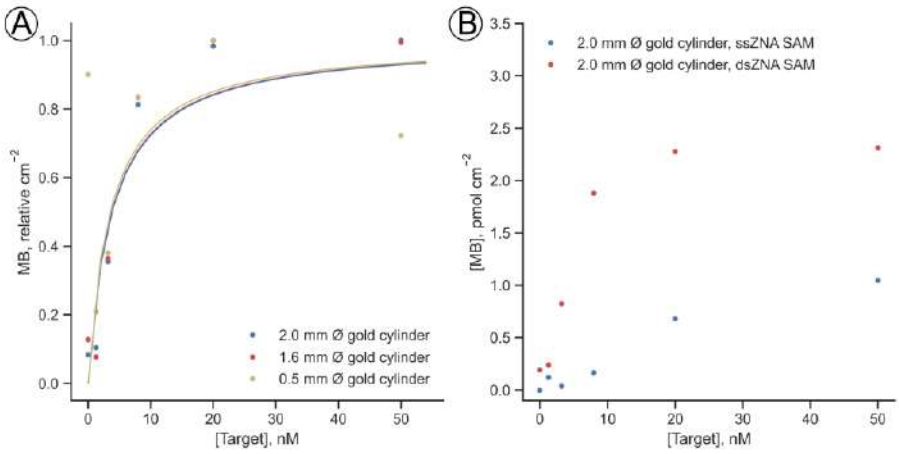

Figure A5 3. The measurement of low DNA target concentrations.

A – A comparison of electrode sizes. (ds)ZNA probe ǀ T*1 ǀ R*1 sandwich with varying T*1 concentration. Fit represents the Langmuir adsorption model. *Mean normalized to surface area and to 1. Ø 2.0 mm and 1.6 mm n = 2 as the replicates were almost overlapping; Ø 0.5 mm n = 5 as there was noise due to low currents. The dsZNA-SAM was a necessary experimental consideration to ensure the electrodes had very similar surfaces and were comparable.*

B – A comparison of probe density. ZNA probe ǀ T*1 ǀ R*1 sandwich with varying T*1 concentration, n=2.

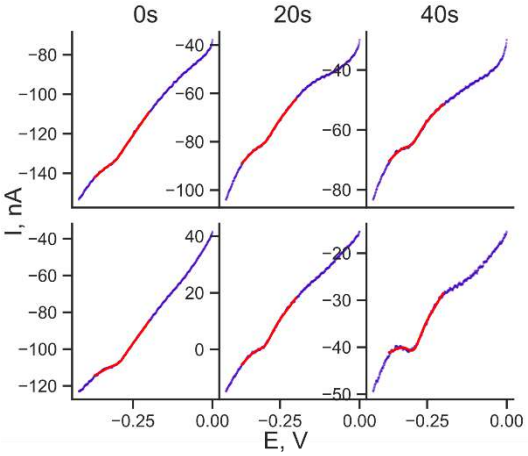

Figure A5 3.1. LSV peaks with fitting under non-melting conditions (these LSVs are averaged to produce the 20 nM datapoints in Figure A5 3A). Top: 0.5 mm, bottom: 1.6 mm electrode.

Sequencing calculations

A library of sequences was generated by checking every base in every position in the T*17s reporter complementary fragment C TGT TCT CAA AGT ATC; and if a base is not found in the position a new sequence is generated with a new substituted base:

C TGT TCT CAA AGT ATC → **C**==A? → False → **A** TGT TCT CAA AGT ATC

For each new base the process was repeated to generate every possible secondary mismatch:

A TGT TCT CAA AGT ATC → **T**==A? → False → **A A**GT TCT CAA AGT ATC

Note: tertiary mismatches were not generated as there is a very large number of them and our system likely will not be able to measure them – most triple mismatches will melt too fast.

Thus a library of 1129 sequences was rapidly generated and (together with the experimentally used R*17 sequence) was fed to the DINAMelt Two state hybridization model. The DINAMelt parameters were DNA at 42°C, 0.01 mM, 0.28 M Na^+, 0 M Mg^{++}, oligo mode. The model provided the ΔG values in a matter of a few seconds and the $\Delta\Delta G$ values were calculated by subtracting the perfect match. The energies range from 0 to 8.2 kcal mol^{-1} and at 1 decimal point precision and a library with only *79 energy levels* is obtained. This means that the range 0-8.2 kcal mol^{-1} at intervals of 0.1 is much too narrow to map 1129 sequences. The provided Gibbs free energy resolution is however, sensible as measuring at 0.01 kcal mol^{-1} intervals may be practically unachievable. The obtained propagated standard deviations were on the order of 0.2 kcal mol^{-1}.

The goal is to measure the $\Delta\Delta G$ value of an unknown sequence and to reference it to our library of values, thus predicting the unknown DNA sequence. Unfortunately, in practice this leaves us with on the order of 20-70 hits per experimental result.

To demonstrate the workflow, I will remove the wild-type target **"S2"** from our dataset and treat it as an unknown sample.

First, a relationship between the calculated energies and the experimental values is established (**Figure A5 5, 1**). From the linear regression, the **S2** (excluded from **Figure A5 5, 1**) measurement is converted into the corresponding "calculated" value, which can then be used to look up sequences from the library. In our case a value of 2.194 kcal mol^{-1} was obtained and this value at ±0.15 kcal mol^{-1} or closer (arbitrary author's choice – a large, but fair window) was considered a match. The true $\Delta\Delta G_{calc}$ should be 2.2 kcal mol^{-1}, however we presume this is an unknown sequence for the sake of demonstration. If searching for a single nucleobase difference (**Figure A5 2, 2**), we can see 3 matching sequences:

G1	CTGTTC**G**CAAAGTATC
G2	CTGTTCTC**G**AAGTATC
G3	CTGTTCTCAAAG**C**ATC

With G3 being the correct match.

When searching through the entire library (Fig. 2, 3A-3D), a total of **39 matches** was found.

In our study another limitation is present: the PCR amplification forces most of the positions in the sequence, leaving only the positions 9-16. This still outputs **13/276 hits**: 10 various relaxed permutations of **S2** and 3 unrelated sequences.

CTGTTCTC**G**AAGTATC	Complete miss
CTGTTCTC**G**AAGTAT**A**	
CTGTTCTC**G**AAGTAT**G**	
CTGTTCTCAAAG**C**ATC	Hit/patrial hit
CTGTTCTCAAAG**CC**TC	
CTGTTCTCAAAG**CG**TC	
CTGTTCTCAAAG**CT**TC	
CTGTTCTCAAAG**C**A**A**C	
CTGTTCTCAAAG**C**A**C**C	
CTGTTCTCAAAG**C**A**G**C	
CTGTTCTCAAAG**C**AT**A**	
CTGTTCTCAAAG**C**AT**G**	
CTGTTCTCAAAG**C**AT**T**	

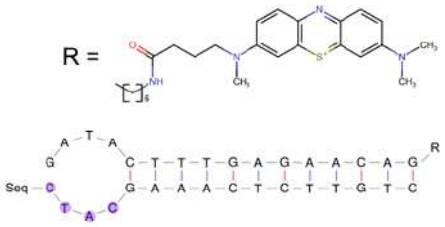

Figure A5 4. Exemplary search results of a known (blinded) sequence S2.

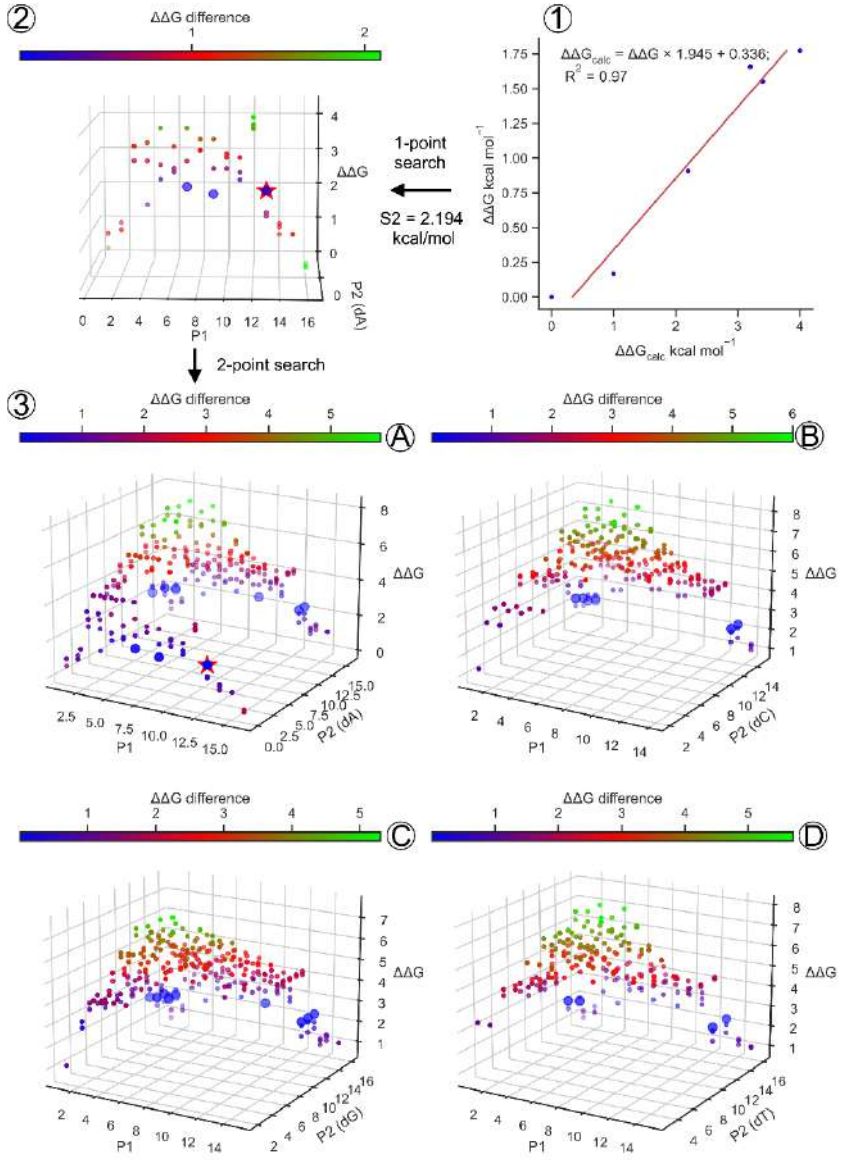

Figure A5 5. The isothermal dissociation library

1: The measured sequence energies compared to their calculated values. S2 is deliberately removed and used as an unknown sample.

2: Screening in the 1 mismatch library. *ΔΔG* represents kcal mol^{-1}. The bottom axes represent the positions in the target sequence. While the term "*ΔΔG* difference" sounds redundant the color scale represents the distance of the library entry from the searched datapoint.

3: Each P1 location has 3 nucleobase datapoints (e.g., dA, dG, dT) plus the original sequence (P1 = 0; P2 = 0; *not shown*). The mutations do not go backwards, e.g., **P1 : 1A, P2 : 2A** but no **P1 : 2A, P2 : 1A** as this just duplicates the sequence. Each P2 location represents only 1 nucleobase to reduce graph complexity (e.g., only dA). The large spheres ● represent the hits and the star ★ represents the true sequence.

We can see that:

a) The **electrochemical sequencing by isothermal dissociation** approach actually guesses both the *position* and the variant *nucleobase* well, e.g., 13T→C and variants were correctly guessed, while 13T→G was correctly **not** guessed, even though the middle positions are clearly "highly" destabilizing and the terminal ones are "mildly" destabilizing.

b) Both our measurement and the library need a significant increase in the precision of the $\Delta\Delta G$ values to narrow down the number of hits to a usable number (e.g., from 39 hits to 1). This may be practically unachievable.

c) While this approach seems unsuitable for an exhaustive profiling of a segment (any position, any base ± any other base), for any practical application the human genome is far more conservative than:
$9 \times (3\,080\,000\,000 + 3\,079\,999\,999 + ...) + (3 \times 3\,080\,000\,000) =$
4.27×10^{19} variants. Only around 5×10^{9} are listed in dbSNP.[201]
In our region of interest, of the given 1129 sequences only ~9 are listed in dbSNP.[202]

Calculations used for the conclusions section (data from **Publication 4**)

ΔΔG, kcal mol^{-1}	(Dinamelt) Solution phase *ΔΔG* calc., kcal mol^{-1}	Slope	Intercept	S6 *ΔΔG* measured, kcal mol^{-1}	Extrapolated total S6 *ΔΔG* solution phase kcal mol^{-1}	S6 solution phase mismatch *ΔΔG* calc., kcal mol^{-1}	Solution phase G|A stack, kcal mol^{-1}
0.00	0.00	1.948	0.317	0.907	2.085	0.1	1.985
0.17	1.00						
0.96	2.20						
1.66	3.20						
1.55	3.40						
1.77	4.00						

Allele 2 (heterozygous sample)	Expected solid phase *ΔΔG*, kcal mol^{-1}	Allele 1 (homozygous sample)	Expected solid phase *ΔΔG*, kcal mol^{-1}	Difference, kcal mol^{-1}	2×SD, kcal mol^{-1}
1 + 0	955	0 + 1	0	955	320
1 + 1	478	0 + 2	0	478	320
1 + 2	318	0 + 3	0	318	320
1 + 3	239	0 + 4	0	239	320

For instance, 1+3 heterozygosity (a tetraploid sample with 1 fraction of wild type allele and 3 fractions of the different one) would produce <2×SD change in signal and be sometimes mistaken as having (0+4) no Allele 2.

COPIES OF PUBLICATIONS

1. Publication I

Serapinas, S.; Gineitytė, J.; Butkevičius, M.; Danilevičius, R.; Dagys, M.; Ratautas, D.
Biosensor Prototype for Rapid Detection and Quantification of DNase Activity. *Biosensors and Bioelectronics* **2022**, *213*, 114475. https://doi.org/10.1016/j.bios.2022.114475.

Biosensors and Bioelectronics 213 (2022) 114475

Contents lists available at ScienceDirect

Biosensors and Bioelectronics

journal homepage: www.elsevier.com/locate/bios

Biosensor prototype for rapid detection and quantification of DNase activity

Skomantas Serapinas [a,b,1], Justina Gineitytė [a,c,1], Marius Butkevičius [a,b], Rapolas Danilevičius [b], Marius Dagys [a,c], Dalius Ratautas [a,c,*]

[a] Life Sciences Center, Vilnius University, Saulėtekio al. 7, LT-10257, Vilnius, Lithuania
[b] UAB "Laboratorija 1", Pamėrkalnio g. 36, LT-01114, Vilnius, Lithuania
[c] UAB "Bioanalizės sistemos", Saulėtekio al. 15, LT-10224, Vilnius, Lithuania

ARTICLE INFO

Keywords:
Nuclease
Biosensor
DNA immobilization
DNA hybridization
DNase I

ABSTRACT

DNases are enzymes that cleave phosphodiesteric bonds of deoxyribonucleic acid molecules and are found everywhere in nature, especially in bodily fluids, i.e., saliva, blood, or sweat. Rapid and sensitive detection of DNase activity is highly important for quality control in the pharmaceutical and biotechnology industries. For clinical diagnostics, recent reports indicate that increased DNase activity could be related to various diseases, such as cancers. In this paper, we report a new bioelectronic device for the determination of nuclease activity in various fluids. The system consists of a sensor electrode, a custom design DNA target to maximize the DNase cleavage rate, a signal analysis algorithm, and supporting electronics. The developed sensor enables the determination of DNase activity in the range of $3.4 \times 10^{-4} - 3.0 \times 10^{-2}$ U mL^{-1} with a limit of detection of up to 3.4×10^{-4} U mL^{-1}. The sensor was tested by measuring nuclease activity in real human saliva samples and found to demonstrate high accuracy and reproducibility compared to the industry standard DNaseAlert™ . Finally, the entire detection system was implemented as a prototype device system utilizing single-use electrodes, custom-made cells, and electronics. The developed technology can improve nuclease quality control processes in the pharmaceutical/biotechnology industry and provide new insights into the importance of nucleases for medical applications.

1. Introduction

Nucleases are a family of hydrolytic enzymes that cleave phosphodiesteric bonds between nucleotides, producing 3′-phospho or 5′-phospho end products. These enzymes can be classified as endo- and exonucleases, cleaving at the inside of a polynucleotide chain or at the ends, respectively; however, some enzymes can show both activities (Yang, 2011). Typically, some nucleases prefer double-stranded nucleic acids (e.g., DNase I) (Suck, 1994), while others cleave single-stranded (e.g., nuclease P1) (Fujimoto et al., 1974) or RNA–DNA hybrid (RNase H) (Nakamura et al., 1991) polynucleotides. Deoxyribonucleases (DNases) are important targets in biotechnology and are used as tools for DNA manipulation (Pan et al., 2013) and appear as contaminants where nuclease-like activity is undesired (Senavirathne et al., 2015; Lopez et al., 2017). Furthermore, data have emerged indicating the importance of DNase activity detection for medical applications, i.e., DNases may be related to various diseases and could be used to monitor the progress of various cancers (Patel et al., 2000; Balian and Hernandez, 2021) and inflammatory diseases (Pedersen et al., 2018) as well as biomarkers for bacterial infections (Flenker et al., 2017). In a recent review by Balian and Hernandez it was shown that increased DNase I activity is related to gastric and colorectal carcinomas, and elevated activities of many other nucleases and cancers were demonstrated (Balian and Hernandez, 2021). Typically, DNases are being detected and quantified using a classical approach: fluorescence detection (Youemura and Maeda, 1982; Choi and Szoka, 2000) or gel electrophoresis (Blank et al., 1982) techniques. Although these methods are highly sensitive and reliable, they are costly, time-consuming, and require toxic markers such as ethidium bromide or radiolabeled molecules (Vogel and Frantz, 2015; Boswell et al., 1989). As alternative methods, novel detection techniques for DNase detection have been reported, mainly based on fluorescence or chemiluminescence detection incorporating nanomaterials for signal enhancement (Mozioglu et al., 2016; Gu et al., 2019; He et al., 2013). Electrochemical biosensors provide a simple and inexpensive platform

* Corresponding author. Life Sciences Center, Vilnius University, Saulėtekio al. 7, LT-10257 Vilnius, Lithuania.
E-mail address: Dalius.Ratautas@gmc.vu.lt (D. Ratautas).
[1] Both authors contributed equally.

https://doi.org/10.1016/j.bios.2022.114475
Received 14 April 2022; Received in revised form 5 June 2022; Accepted 8 June 2022
Available online 10 June 2022
0956-5663/

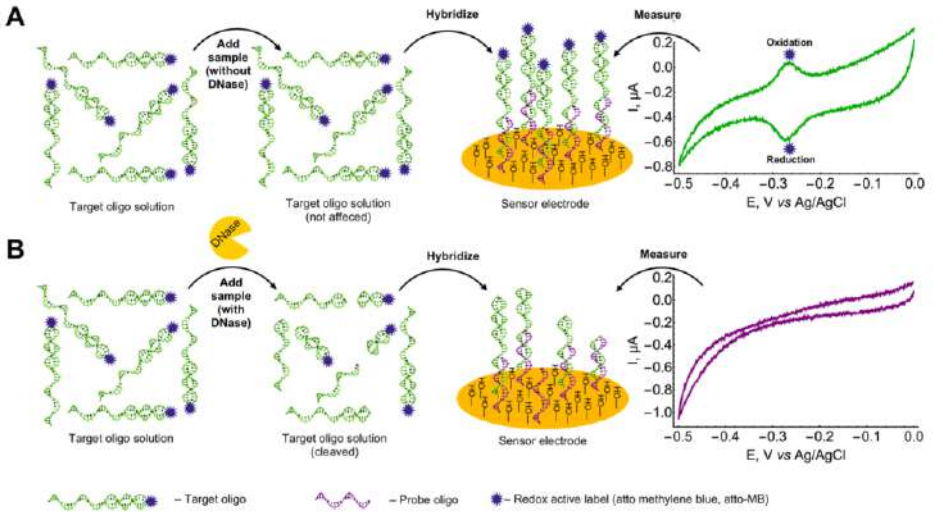

Fig. 1. The general operation scheme of the DNase biosensor. The target oligo is incubated with the sample. The hybridization rate between the target oligo and the sensor electrode is monitored. **(A)** The sample does not contain DNases. **(B)** The sample contains DNases.

for biomolecule detection while maintaining a high degree of accuracy and sensitivity. To date, the absolute majority of electrochemical biosensors have been developed for small biomolecules, e.g., glucose (Gineitytė et al., 2019; Ratautas and Dagys, 2019), glycerol (Ramonas et al., 2019), lactate (Yang et al., 1999), formaldehyde (Teišerskytė et al., 2021), and others. The targeting of large macromolecules, i.e., proteins or enzymes, is still somewhat lagging with a few exceptions (Agostini et al., 2021; Liu et al., 2022). Therefore, the development of electrochemical biosensors for these targets can produce novel sensitive assays. For the case of DNase detection, some biosensors have been reported. Sato et al. reported an electrochemical biosensor for DNase I detection based on ferrocene-modified DNA immobilized onto the electrode surface with a detection limit (LOD) of 10^{-2} U mL^{-1}. Ding and Qin reported a potentiometric biosensor for the detection of DNases based on a polycation-sensitive membrane, and for DNase I, a LOD of 0.45 U mL^{-1} was reported (Ding and Qin, 2013). Despite advances, electrochemical biosensors developed for DNase detection still lack sensitivities comparable to that of fluorescence or radiolabeling-based methods and the reliability required for the analysis of real samples.

In this work, we present a rapid and sensitive bioelectrochemical device for the determination of nuclease activity in various fluids which can significantly improve nuclease quality control processes in the pharmaceutical/biotechnology industry and provide new insights into the importance of nucleases for medical applications (Fig. 1).

2. Experimental

2.1. Materials and methods

DNase I (1000 U mL^{-1}, RNase-free), Ultra Low Range DNA Ladder (Invitrogen), TopVision Agarose Tablets, SYBR™ Gold Stain and DNAseAlert™ QC System were purchased from Thermo Fisher Scientific. Nuclease-free water, Tris(2-carboxyethyl)phosphine hydrochloride (TCEP), 6-mercapto-1-hexanol (MCH), and potassium hydroxide, and TBE buffer (89 mM Tris-borate and 2 mM EDTA, pH 8.3) were purchased from Sigma. Sodium dihydrogen phosphate and disodium hydrogen phosphate were purchased from Reachen Slovakia. Magnesium chloride hexahydrate, calcium chloride and sulfuric acid were purchased from Merck. Sodium chloride and Tris were obtained from Roth. All reagents were analytical grade. Nuclease-free water was used during the measurements.

Oligonucleotides were purchased from Metabion AG. The sequences are given in Table 1. The freeze-dried oligonucleotides obtained were dissolved in 10 mM Tris buffer solution, pH 8.00. The storage concentration of the probe sequence was 800 μM, and this solution was kept at −20 °C. The target oligo solution was prepared by heating a 10 mM Tris solution consisting of 40 μM DNA1 and 42 μM DNA2 sequences to 65 °C for 10 min and allowing the solution to cool down gradually. The probe oligo solution was prepared using TCEP solution (20 mM TCEP, 10 mM

Table 1
Oligonucleotides used in this research.

Oligonucleotide	Sequence (5′ → 3′)
Probe oligo	SH-C6-AATTATCAAACACAAACAGACTTAA
Target oligo	DNA1: GCCCGAGAGCAGTAGTCGTTAAGTCTGTTTGTGTTTGATAATT DNA2: CGACTACTGCTCTCGGGC-AttoMB
ssDNA oligo	AttoMB-GCCCGAGAGCAGTAGTCGTTAAGTCTGTTTGTGTTTGATAATT
Noncomplementary DNA oligo	AttoMB-CAGGTGGAACCTCATCAGGAGATGC

Tris, 100 mM $MgCl_2$, pH 7.2). This mixture was kept at room temperature in the dark for 1.0 h. After reduction, the oligonucleotides were diluted to a final concentration of 1.0 μM (10 mM Tris, 100 mM $MgCl_2$, pH 7.2). This solution was used to immobilize the probe oligo on the electrode surface and is referred to as the working probe solution (WPS).

2.2. Electrode preparation procedures

Gold disc (d = 2 mm) and screen-printed (d = 2 mm) electrodes for sensor preparation were purchased from BASi and Zimmer & Peacock, respectively. First, mechanical electrode cleaning was performed by rinsing the gold surface with deionized water and gently dabbing with lab tissue soaked with acetone. Subsequently, the electrodes were polished on microcloth wetted with deionized water and a 0.3 μm alumina suspension for several minutes, and mechanical cleaning was performed by sonicating the electrodes for 5 min in an ultrasound bath. Subsequently, electrochemical cleaning was performed, as described previously (Ratautas et al., 2017). Next, 2.0 μL of gold nanoparticle (AuNP) solution was placed onto the electrode surface and left to dry at room temperature. Once completely dry, the nanostructured surface was electrochemically cleaned once again. The prepared electrodes were placed into 120.0 μL WPS and kept at +4 °C overnight. Subsequently, the electrodes were thoroughly rinsed with deionized water, and submerged in 4.0 mM 6-mercapto-1-hexanol solution for 4 h at room temperature. Finally, the electrodes were stored in hybridization buffer (HBS, 20 mM PBS, 3M NaCl, pH 7.0) until measurements.

2.3. Preparation of samples

To obtain an artificial sample, 55.6 nM DNA oligonucleotide (either ssDNA, target or noncomplementary DNA oligo) was added to 3.5 mL of DNase I working buffer (DWB, 10 mM Tris-HCl, 2.5 mM $MgCl_2$, 0.5 mM $CaCl_2$, pH 7.6) solution. Afterward, a specific amount of DNase I was added. The solution was agitated at 37 °C for 30 min before being transferred to the electrochemical measurement cell.

Human saliva samples were purchased from UAB 'RDA Spot' (Lithuania). The samples were taken from volunteers under a written agreement. Saliva samples were collected from a volunteer into a sterile polypropylene tube. The collection was carried out in the morning before the volunteer ate or drank anything. The sample (800 μL) was centrifuged at 1600 rcf for 10 min and again at 16 000 rcf for 10 min. The supernatant (5.0 μL) was added to a 3.5 mL DWB solution containing 55.6 nM target oligo. The solution was gently mixed by inverting, and the reaction was carried out at 37 °C for 30 min with agitation. Finally, the resulting solution was measured using cyclic voltammetry.

2.4. Methods

Electrochemical measurements were conducted in a 7.0 mL cell using a three-electrode system (probe oligo-modified working electrode, Pt auxiliary electrode, and Ag/AgCl (3 M KCl) reference electrode) with a Gamry Reference 600™ potentiostat. The experiments were carried out in a 1:1 (V/V) mixture of HBS and sample solutions at 45 °C. The cell was constantly stirred between cyclic voltammetry (CV) measurements, but the stirring was turned off while the CVs were being recorded. CVs were run from 0 to −0.5 V at a scan rate of 0.05 V s^{-1}. CVs were recorded at intervals of 1 min, 5 min, or 10 min. Electrochemical measurements with single-use electrodes followed the same protocol, except that the stirring was not turned off even when the CVs were being recorded.

DNA electrophoresis was conducted to investigate the cleavage of double-stranded DNA (target oligo) and single-stranded DNA (ssDNA oligo) oligonucleotides. The target and ssDNA oligo solutions (26.6 μM in DWB) were incubated with DNase I at 36 °C (0 U mL^{-1} for the control and 2.6 U mL^{-1} for the test). Subsequently, the oligonucleotide solutions were diluted with an equivalent volume of DNase I inhibition solution (200 mM EDTA, 1.5 M Na_2HPO_4, pH 7) and mixed. Agarose gel (5.0%)

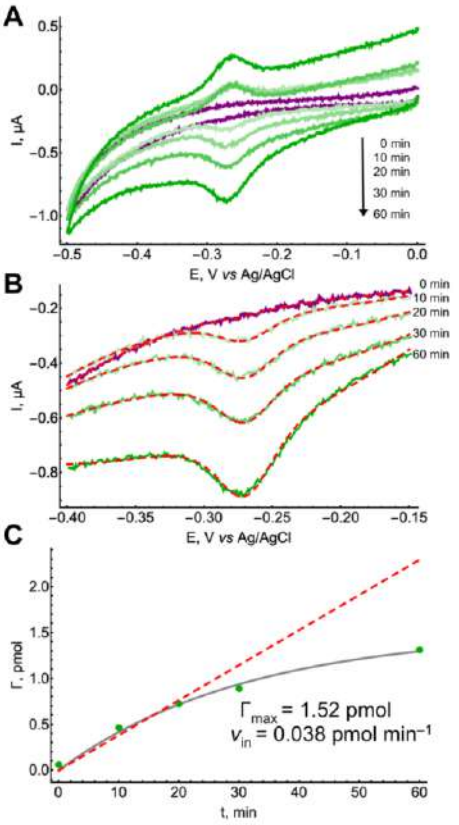

Fig. 2. Electrochemical analysis of the sensor electrode demonstrating the hybridization of ssDNA oligo with atto-MB. **(A)** CV analysis of the electrode after the addition of a 60 nM ssDNA oligo. CVs were recorded at different times after addition of ssDNA oligo in the range 0–60 min. **(B)** The fitting of cathodic current values to the model (SI, Equation S(1)). Green data points indicate the measurement data, while red dashed lines indicate fitted curves with surface coverage values. **(C)** Curve demonstrating the dependence of the hybridization of ssDNA oligo on time. Surface coverage values were fitted to a model (SI, Equation S(1)), and the hybridization parameters were extracted. The red dotted line demonstrates the fit of the initial hybridization data to a linear model.

was loaded with a ladder (3.0 μl per lane) and the electrophoresis was performed of eight samples (10.0 μl per lane) in TBE buffer at 80 V for 80 min. The gel was submerged in a water bath to prevent an increase in the buffer solution temperature. Next, the gel was stained with SYBR Gold in TBE for 1 h.

DNase Alert™ sample testing was carried out using the manufacturer's instructions with a PerkinElmer LS fluorescence spectrometer equipped with a biokinetic accessory and a thermostat. Briefly, 315 μL of nuclease-free water was mixed with 45 μL 10X NucleaseAlert buffer, 45 μL DNase Alert Substrate, and 45 μL of saliva supernatant. The solution

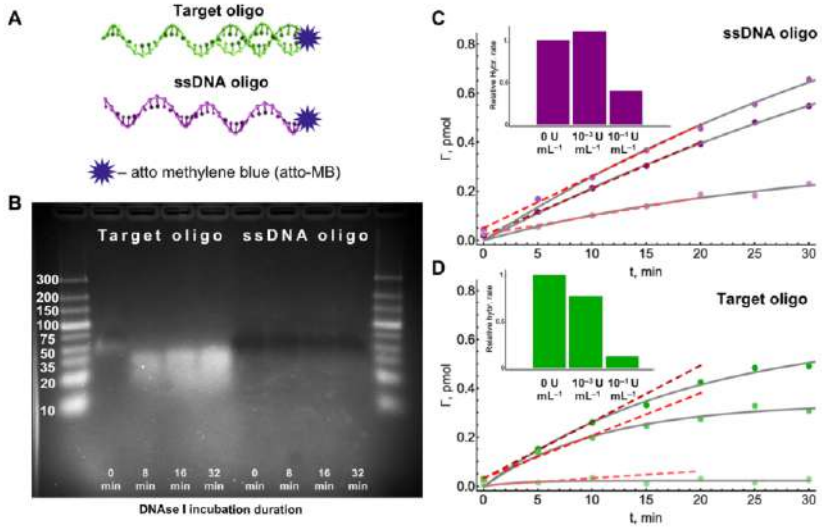

Fig. 3. Comparison of DNase I activity for single-stranded DNA (ssDNA oligo) and hybrid (containing both single- and double-stranded) DNA (target oligo). **(A)** Schematic illustration of DNA oligonucleotides used to investigate DNase I activity – ssDNA oligo (purple) and target oligo (green). **(B)** Gel electrophoresis for the target (lanes 1–4) and ssDNA oligos (lanes 5–8). The lane progresses by increasing the incubation time with DNase I (0 min, 8 min, 16 min, 32 min). **(C)** Curve demonstrating the hybridization rate of ssDNA oligos incubated with solutions of various DNase I activities. The inset shows the relative hybridization rate dependence on DNase I solution activity. **(D)** Curve demonstrating the hybridization rate of the target oligo incubated with solutions of various DNase I activities. The inset shows the relative hybridization rate dependence on DNase I solution activity.

was measured in a low volume quartz cuvette with stirring at 37 °C using real-time fluorescence measurements at 30 s intervals (Ex: 535 nm, Em: 556 nm).

3. Results and discussion

3.1. Development of DNA-modified electrodes for DNA hybridization

Designing an electrode surface capable of hybridizing DNA at high rates and specificities was critical for a functioning nuclease sensor. The final iteration electrodes, prepared using AuNPs, with immobilized probe oligo (Table 1) and self-assembled MCH monolayer, were named sensor electrodes. The representation of the sensor electrode is presented in Fig. 1. The rationale for using AuNPs is based on our previous experience indicating that AuNPs significantly increase the active surface area of the electrode and allow for the adsorption of more biomolecules (Ratautas et al., 2016). MCH was used based on previous works, which have shown that self-assembled monolayers significantly improve the efficiency and specificity of DNA immobilization on gold (Steel et al., 1998; Lao et al., 2005; Farjami et al., 2010, 2012).

The sensor electrode was used to investigate the hybridization parameters of the complementary ssDNA oligo with the redox-active marker (atto-MB) at the 3' end. After the addition of the ssDNA oligo, the CVs were recorded from 0 to −0.5 V after 0–60 min (Fig. 2A). CV analysis did not show a significant electrochemical process immediately after the addition of ssDNA oligo (t = 0 min, purple curve). After 10 min, CV was recorded again, and atto-MB reduction and oxidation peaks were observed at −0.271 V and −0.265 V, respectively. These potential values were found to be similar to that for methylene blue redox on DNA-modified electrodes, as reported previously (Kelley et al., 1997). The electrode was allowed to hybridize for up to 60 min, while the CVs were recorded at 20, 30 and 60 min. CVs demonstrate an increase in current values, but no significant changes in potentials are observed, thus providing evidence for the progression of DNA hybridization on the electrode. It is important to note that the potential difference between the cathodic and anodic peaks is only 0.006 V, showing the electrochemistry of surface-bound species (Bard and Faulkner, 2001). Control experiments were carried out to demonstrate that specific DNA–DNA hybridization is observed (SI, Figs. S2–S5). Controls were recorded using electrodes without probe oligo, without MCH and using the final sensor electrode (both MCH and probe oligo) but adding a noncomplementary DNA oligo. In all three cases, no increase in redox peaks was observed.

We investigated the kinetics of ssDNA oligo hybridization to evaluate its surface coverage and rate. First, we estimated the amount of ssDNA oligo on the electrode surface by fitting the CV data to the potential-current function for surface-adsorbed redox-active species from Bard (Bard and Faulkner, 2001) (SI, 1. Fitting). The fitting was carried out for a cathodic scan in the potential range of −0.15 to −0.4 V (Fig. 2 B; SI, Equation S(1)) and demonstrated excellent agreement with the experimental data points. From the fitted CV curves, the molar number for the ssDNA oligo was determined to vary in the range of 0–1.2 pmol. Afterward, we evaluated the hybridization rate and the surface saturation of the sensor electrode with the ssDNA oligo (Fig. 2C). Molar numbers of ssDNA oligo were plotted against time and fitted to the equation describing time-dependent DNA hybridization on the electrode (SI, Fitting, Equation S(2)). The data show excellent agreement with the experimental results, indicating that DNA hybridization on the electrode can be approximated using first-order kinetics. The maximum molar number for hybridized ssDNA oligo is approximately 1.5 pmol (or calculated to be 75 pmol cm^{-2} for a geometric electrode surface area).

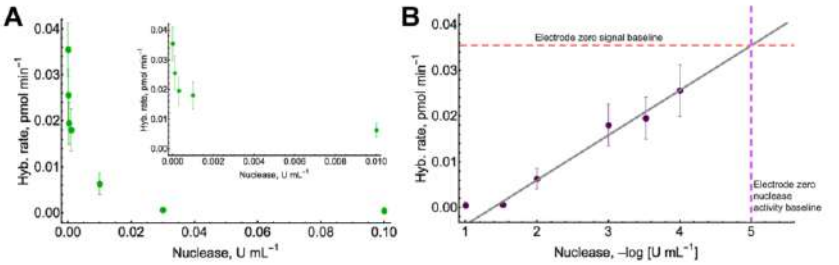

Fig. 4. The sensor electrode performance when hybridized with 55.6 nM target oligo solutions incubated with various DNase I activities (0, 10^{-4}, 3×10^{-4}, 10^{-3}, 10^{-2}, 3×10^{-2}, 10^{-1} U mL^{-1}). **(A)** Dependence of the hybridization rate on DNase activity (0–10^{-1} U mL^{-1}). The inset shows a lower DNase activity range (0–10^{-2} U mL^{-1}). **(B)** Calibration curve demonstrating a linear dependence on the negative logarithm of nuclease activity.

This number is much higher than the values reported previously (1.6–6.5 pmol cm^{-2}) (Steel et al., 1998; Zhang et al., 2007) and can be attributed to the usage of gold nanoparticles, which significantly increase the surface area and allow more complementary DNA to hybridize. To evaluate the hybridization rate, the initial data points (up to 15 min) were fitted to a linear model (Fig. 2C, red line), and the slope of the line was named v_{in}. The value of v_{in} shows the hybridization rate (pmol min^{-1}) and can be further used in the developed biosensor to evaluate the nuclease activity.

3.2. Optimization of the DNA oligonucleotide for maximum and nonspecific DNase activity

Once we have developed an electrode for fast and selective hybridization of DNA and a method to evaluate the hybridization rate, a DNA target sensitive to a broad nuclease activity is required. DNases have sequence-dependent activity, most notably significant activity differences for single- and double-stranded DNA (Suck, 1994; Dingwall et al., 1981; Desai and Shankar, 2003). Our aim was to detect total nuclease activity in a sample, thus indiscriminately detecting the activity of most nucleases. For this reason, we designed a hybrid DNA oligonucleotide composed of single- and double-stranded DNA (Fig. 3A). This oligonucleotide is composed of longer (43 nt) and shorter (18 nt) DNA chains hybridized together in a solution and was named the target oligo. Initially, electrophoresis was conducted to investigate the activity of the model enzyme DNase I toward ssDNA and target oligos (Fig. 3B). The results demonstrate that the target and ssDNA oligos are bound to the SYBR Gold dye, which emits at a wavelength of ~537 nm, while the redox-active label atto-MB absorbs light at ~668 nm. As a result, darker bands are visible on the gel with atto-MB-labeled oligos, indicating that the fragments are not affected by nucleases (t = 0 min). Significant differences between the target and ssDNA oligos appear after 8–32 min of incubation with DNase I. Broader bright bands appear as the target oligo is cleaved by DNase I, since the redox-active label atto-MB is removed from the DNA chain. In contrast, the ssDNA oligo did not show any obvious signs of a decrease in mass or band broadening, indicating that this type of DNA is not significantly affected by DNase I.

Electrochemical measurements show that both the ssDNA and target oligos are able to hybridize with the probe oligo attached to the surface and approach the surface saturation (Fig. 3CD). CV measurements were carried out using oligos treated with DNase I solution with different activities (0, 10^{-3}, 10^{-1} U mL^{-1}) (Fig. 3CD). The results demonstrate that the target oligo shows an apparent decrease in the hybridization rate (v_{in}) with an increase in DNase I activity (Fig. 3D, inset). The hybridization rate of the ssDNA oligo is only decreased at significantly higher DNase I activities. Thus, a custom-designed target oligo was chosen as a nucleotide for DNase detection.

3.3. Characterization and performance of the nuclease activity biosensor, prototype biosensor development

The sensor electrodes were calibrated using DNase I solutions with various activities. First, the target oligo was incubated with 0–10^{-1} U mL^{-1} DNase I and then hybridized with the sensor electrodes. The dependence of the hybridization rate (v_{in}) on the nuclease activity is presented in Fig. 4. The data show that v_{in} for the target oligo is related to nuclease activity. For the case when no DNase I is used, v_{in} is 0.035 ± 0.005 pmol min^{-1}. For example, when the target oligo is incubated with 10^{-1} U mL^{-1} DNase I, v_{in} is decreased to 0.00047 ± 0.0007 pmol min^{-1}. To carry out the calibration, we plotted the dependence of the hybridization rate against the negative logarithm of nuclease activity (Fig. 4B). The data were fitted to a linear model, and a calibration curve was obtained:

$$y = -\log[Nuclease]a + b \quad \text{(Equation 1)}$$

Here, a – slope (0.0098), b – intercept (0.014). It is important to determine the parameters of the biosensor, the limit of detection (LOD) and the sensitivity. Sensitivity is usually defined as the slope of the calibration curve (Bhalla et al., 2016); therefore, the sensitivity of the biosensor was determined to be 0.0098 pmol min^{-1} (–log[nuclease activity])$^{-1}$, with the biosensor showing that a 10-fold increase in nuclease activity results in a 2-fold change in signal. LOD is typically estimated using the 3 σ criterion and is defined as LOD = 3 σ of the signal blank/sensitivity corresponding to a confidence level of 99.7% (Lavín et al., 2018). Since there is no standardized method to define the LOD for a negative signal sensor, we determined the LOD using the 3 σ criterion and additionally evaluated the electrode zero-nuclease activity baseline (purple curve in Fig. 4B). Thus, LOD = electrode zero-nuclease activity baseline – 3 σ of the electrode zero signal baseline/sensitivity. The calculations gave an LOD value of 3.47, which is equal to 3.4×10^{-4} U mL^{-1}. The lowest nuclease activity point in calibration (10^{-4} U mL^{-1}) is lower than the calculated LOD; however, we emphasize that we present the LOD based on a confidence level of 99.7% (3 σ). For this reason, high reliability can only be achieved when measuring in the range 3.4×10^{-4} to 3×10^{-2} U mL^{-1}. A detailed comparison between our developed sensor and other relevant works is presented in SI, Table S1.

To demonstrate the practical application of the system, we built a biosensor prototype system. The prototype was built around a customized PTFE electrochemical cell, which was integrated into a Peltier element-based thermostatic cell system with a magnetic stirrer. The electronic system was developed using an Arduino Due electronic set linked with a laptop computer *via* a USB interface. The biosensor prototype was tested under various nuclease concentrations and found to give reproducible results (SI, 4. Biosensor prototype system).

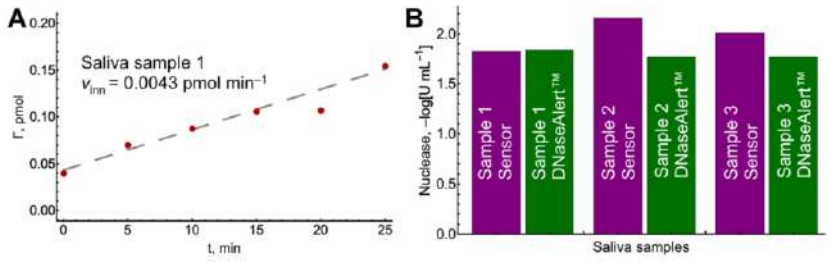

Fig. 5. DNase activity determination in human saliva samples taken from the same subject. **(A)** Time-dependent target oligo hybridization after incubation with human saliva samples. **(B)** A comparative histogram demonstrating nuclease activity in human saliva samples measured with the developed sensor and compared with the industry standard DNaseAlert™ .

3.4. DNase activity determination in human saliva samples

To show that operation with biological fluids is possible we measured nuclease activity in human saliva samples. The target oligo was incubated with saliva samples and subsequently hybridized on the sensor electrodes. The typical hybridization is presented in Fig. 5A. The hybridization line shows that the target oligo after incubation with saliva sample is capable of hybridizing but at a significantly lower rate; for example, for sample 1, v_{in} is equal to 0.00432 pmol min^{-1}. Using the calibration curve (Equation (1)), the hybridization rates were converted to DNase activity, and considering a sample dilution, the nuclease activities were calculated to vary in the range of 6.5–10.6 U mL^{-1}. Additionally, we used DNaseAlert™ to analyze the saliva samples. A comparison of the results obtained with the Sensor and DNaseAlert™ is presented in Fig. 5B. The results demonstrate that the sensor electrodes give results that are comparable with an alternative method. It can be observed that the logarithmic difference in nuclease activity between the Sensor electrodes and DNaseAlert™ varies in the range of 1–18%. The absolute difference in nuclease activity is presented in SI, Table S1 and varies in the range of 4–81%. The difference in nuclease activity measurements between our method and DNaseAlert™ most likely risen due to differences in the DNA substrate sequence resulting in somewhat different affinities towards DNases.

4. Conclusions

In this paper, we report a new bioelectrochemical device – a rapid and sensitive nuclease detection system consisting of a sensor electrode, a custom-designed DNA oligonucleotide target to maximize the nuclease cleavage rate, a signal analysis algorithm, and supporting electronics. Our designed sensor electrode is prepared by immobilizing gold nanoparticles on a gold electrode after immobilization of the DNA probe with the supporting layer (6-mercapto-1-hexanol) to form a specific DNA surface with a high DNA surface coverage of 1.5 pmol (or calculated as 75 pmol cm^{-2} for a geometric electrode surface area). The sensor electrode is capable of hybridizing a redox-labeled complementary DNA with a high rate (up to 0.04 pmol min^{-1}) and selectivity. We also designed a custom DNA oligonucleotide for the detection and monitoring of DNase activity. The DNA oligonucleotide is composed of both single- and double-stranded DNA to ensure the suitability of the oligonucleotide for various types of nucleases and is additionally labeled with atto methylene blue (atto-MB) for electrochemical detection. The hybridization of DNA oligonucleotide with atto-MB was monitored and fitted to a potential-current function to determine the rate of hybridization. The nuclease-treated DNA oligonucleotide was cleaved, thus resulting in a lower rate of hybridization, and, in turn, lower development of the signal. The designed biosensor enabled us to determine DNase activity in the range of 3.4×10^{-4} to 3×10^{-2} U mL^{-1} with a detection limit of 3.4×10^{-4} U mL^{-1}. Furthermore, the sensor was tested by measuring nuclease activity in human saliva samples and was found to demonstrate high accuracy and reproducibility compared to the industry standard DNaseAlert™. Finally, the whole system was implemented in the design of a prototype biosensor excluding the standard laboratory equipment (e.g., cells, thermostats, potentiostats). The device contained a custom polytetrafluoroethylene (PTFE) reaction cell, the electronic part, and a program written in Python language for electrochemical signal analysis and data fitting.

Funding

This research was funded by Agency for Science, Innovation and Technology (Lithuania) under the measure of "Development of biotechnology industry in Lithuania" grant no: BIOTECH-02-005.

CRediT authorship contribution statement

Skomantas Serapinas: Conceptualization, Software, Investigation, Methodology, Formal analysis, Data curation, Validation, Writing – review & editing. **Justina Gineityte:** Conceptualization, Software, Investigation, Methodology, Formal analysis, Data curation, Validation, Writing – review & editing. **Marius Butkevicius:** Conceptualization, Software, Investigation, Methodology, Formal analysis, Writing – review & editing. **Rapolas Danilevicius:** Conceptualization, Writing – review & editing, Resources. **Marius Dagys:** Conceptualization, Software, Methodology, Writing – review & editing, Resources. **Dalius Ratautas:** Conceptualization, Methodology, Software, Formal analysis, Writing – original draft, Writing – review & editing, Visualization, Resources, Supervision.

Declaration of competing interest

The authors declare that they have no known competing financial interests or personal relationships that could have appeared to influence the work reported in this paper.

Appendix A. Supplementary data

Supplementary data to this article can be found online at https://doi.org/10.1016/j.bios.2022.114475.

References

Agostini, M., Amato, F., Vieri, M.L., Greco, G., Tonazzini, I., Baroncelli, L., Caleo, M., Vannini, E., Santi, M., Signore, G., Cecchini, M., 2021. Biosens. Bioelectron. 172, 112774 https://doi.org/10.1016/j.bios.2020.112774.

Balian, A., Hernandez, F.J., 2021. Biomarker Research 9, 86. https://doi.org/10.1186/s40364-021-00342-4.
Bard, A.J., Faulkner, L.R., 2001. Electrochemical Methods: Fundamentals and Applications, second ed. Wiley, New York.
Bhalla, N., Jolly, P., Formisano, N., Estrela, P., 2016. Essays Biochem. 60, 1–8. https://doi.org/10.1042/EBC20150001.
Blank, A., Sugiyama, R.H., Dekker, C.A., 1982. Anal. Biochem. 120, 267–275. https://doi.org/10.1016/0003-2697(82)90347-5.
Boswell, G.S., Dimitrijevich, S.D., Gracy, R.W., 1989. Anal. Biochem. 182, 20–24. https://doi.org/10.1016/0003-2697(89)90711-2.
Choi, S.-J., Szoka, F.C., 2000. Anal. Biochem. 281, 95–97. https://doi.org/10.1006/abio.2000.4529.
Desai, N.A., Shankar, V., 2003. FEMS (Fed. Eur. Microbiol. Soc.) Microbiol. Rev. 26, 457–491. https://doi.org/10.1111/j.1574-6976.2003.tb00626.x.
Ding, J., Qin, W., 2013. Biosens. Bioelectron. 47, 559–565. https://doi.org/10.1016/j.bios.2013.03.066.
Dingwall, C., Lomonossoff, G.P., Laskey, R.A., 1981. Nucleic Acids Res. 9, 2659–2674. https://doi.org/10.1093/nar/9.12.2659.
Farjami, E., Campos, R., Ferapontova, E.E., 2012. Langmuir 28, 16218–16226. https://doi.org/10.1021/la3032336.
Farjami, E., Clima, L., Gothelf, K.V., Ferapontova, E.E., 2010. Analyst 135, 1443. https://doi.org/10.1039/c0an00049c.
Flenker, K.S., Burghardt, E.L., Dutta, N., Burns, W.J., Grover, J.M., Kenkel, E.J., Weaver, T.M., Mills, J., Kim, H., Huang, L., Owczarzy, R., Musselman, C.A., Behlke, M.A., Ford, B., McNamara, J.O., 2017. Mol. Ther. 25, 1353–1362. https://doi.org/10.1016/j.ymthe.2017.03.015.
Fujimoto, M., Kuninaka, A., Yoshino, H., 1974. Agric. Biol. Chem. 38, 1555–1561. https://doi.org/10.1080/00021369.1974.10861384.
Gineityte, J., Meškys, R., Dagys, M., Ratautas, D., 2019. J. Power Sources 441, 227163. https://doi.org/10.1016/j.jpowsour.2019.227163.
Gu, Z., Fu, A., Ye, L., Kuerban, K., Wang, Y., Cao, Z., 2019. ACS Sens. 4, 2922–2929. https://doi.org/10.1021/acssensors.9b01303.
He, Y., Xiong, L.-H., Xing, X.-J., Tang, H.-W., Pang, D.-W., 2013. Biosens. Bioelectron. 42, 467–473. https://doi.org/10.1016/j.bios.2012.10.045.
Kelley, S.O., Barton, J.K., Jackson, N.M., Hill, M.G., 1997. Bioconjugate Chem. 8, 31–37. https://doi.org/10.1021/bc960070o.
Lao, R., Song, S., Wu, H., Wang, L., Zhang, Z., He, L., Fan, C., 2005. Anal. Chem. 77, 6475–6480. https://doi.org/10.1021/ac050911x.
Lavín, Á., Vicente, J., Holgado, M., Laguna, M., Casquel, R., Santamaría, B., Maigler, M., Hernández, A., Ramírez, Y., 2018. Sensors 18, 2038. https://doi.org/10.3390/s18072038.
Liu, N., Liu, R., Zhang, J., 2022. Bioelectrochemistry 146, 108105. https://doi.org/10.1016/j.bioelechem.2022.108105.
Lopez, M.A., Mackler, R.M., Altman, M.P., Yoder, K.E., 2017. JoVE 130, e56605. https://doi.org/10.3791/56605.
Mozioğlu, E., Akgoz, M., Kocagöz, T., Tamerler, C., 2016. Anal. Methods 8, 4017–4021. https://doi.org/10.1039/C5AY02310F.
Nakamura, H., Oda, Y., Iwai, S., Inoue, H., Ohtsuka, E., Kanaya, S., Kimura, S., Katsuda, C., Katayanagi, K., Morikawa, K., 1991. Proc. Natl. Acad. Sci. USA 88, 11535–11539. https://doi.org/10.1073/pnas.88.24.11535.
Pan, Y., Xiao, L., Li, A.S.S., Zhang, X., Sirois, P., Zhang, J., Li, K., 2013. Mol. Biotechnol. 55, 54–62. https://doi.org/10.1007/s12033-012-9613-9.
Patel, P.S., Patel, B.P., Rawal, R.M., Raval, G.N., Patel, M.M., Patel, J.B., Jha, F.P., Patel, D.D., 2000. Tumor Biol. 21, 82–89. https://doi.org/10.1159/000030113.
Pedersen, H.L., Horvei, K.D., Thiyagarajan, D., Norby, G.E., Seredkina, N., Moroni, G., Eilertsen, G.O., Holdnæs, H., Strøm, E.H., Bokland, G., Meroni, P.-L., Rekvig, O.P., 2018. J. Pathol. Clin. Res. 4, 193–203. https://doi.org/10.1002/cjp2.99.
Ramonas, E., Ratautas, D., Dagys, M., Meškys, R., Kulys, J., 2019. Talanta 200, 333–339. https://doi.org/10.1016/j.talanta.2019.03.063.
Ratautas, D., Dagys, M., 2019. Catalysts 10, 9. https://doi.org/10.3390/catal10010009.
Ratautas, D., Laurynėnas, A., Dagys, M., Marcinkevičienė, L., Meškys, R., Kulys, J., 2016. Electrochim. Acta 199, 254–260. https://doi.org/10.1016/j.electacta.2016.03.057.
Ratautas, D., Tetianec, L., Marcinkevičienė, L., Meškys, R., Kulys, J., 2017. Biosens. Bioelectron. 98, 215–221. https://doi.org/10.1016/j.bios.2017.06.048.
Senavirathne, G., Liu, J., Lopez, M.A., Haine, J., Martin-Lopez, J., Lee, J.-B., Yoder, K.E., Fishel, R., 2015. Nat. Methods 12, 901–902. https://doi.org/10.1038/nmeth.3588.
Steel, A.B., Herne, T.M., Tarlov, M.J., 1998. Anal. Chem. 70, 4670–4677. https://doi.org/10.1021/ac9805376.
Suck, D., 1994. J. Mol. Recogn. 7, 65–70. https://doi.org/10.1002/jmr.300070203.
Teišerskyte, V., Urbonavičius, J., Ratautas, D., 2021. Talanta 234, 122657. https://doi.org/10.1016/j.talanta.2021.122657.
Vogel, B., Frantz, S., 2015. Anal. Biochem. 471, 73–79. https://doi.org/10.1016/j.ab.2014.11.013.
Yang, Q., Atanasov, P., Wilkins, E., 1999. Biosens. Bioelectron. 14, 203–210. https://doi.org/10.1016/S0956-5663(98)00109-2.
Yang, W., 2011. Q. Rev. Biophys. 44, 1–93. https://doi.org/10.1017/S0033583510000181.
Yonemura, K., Maeda, H., 1982. J. Biochem. 92, 1297–1303. https://doi.org/10.1093/oxfordjournals.jbchem.a134048.
Zhang, J., Wang, L., Pan, D., Song, S., Fan, C., 2007. Chem. Commun. 1154–1156. https://doi.org/10.1039/B615742D.

2. Publication II

Gineitytė, J.; **Serapinas, S**.; Ratautas, D.
Electrochemical DNA Hybridization Signal Amplification System Using Methylene Blue and Ascorbic Acid. *Electrochimica Acta* **2024**, *507*, 145146. https://doi.org/10.1016/j.electacta.2024.145146.

Electrochimica Acta 507 (2024) 145146

Contents lists available at ScienceDirect

Electrochimica Acta

journal homepage: www.journals.elsevier.com/electrochimica-acta

Electrochemical DNA hybridization signal amplification system using methylene blue and ascorbic acid

Justina Gineitytė, Skomantas Serapinas, Dalius Ratautas *

Life Sciences Center, Vilnius University, Saulėtekio al. 7, LT-10257 Vilnius, Lithuania

ARTICLE INFO

Keywords:
DNA hybridization
Electrochemistry
Chronoamperometry
Electrocatalytic amplification
Methylene blue, Ascorbic acid

ABSTRACT

This study presents a method for real-time monitoring of heterogeneous DNA hybridization using chronoamperometry (CA). The electrochemical assay is based on methylene blue (MB)-labeled ssDNA target (tMB) hybridization with a complementary ssDNA capture probe (p) chemisorbed to a gold electrode through the Au-S linkage. Real-time monitoring of nucleic acid binding is enabled by introducing ascorbic acid (AA) during CA measurements at oxidative potential. After hybridization, the newly formed MB-labeled double stranded DNA (ptMB) oxidized AA and, as a result, shuttled the electrons directly to the electrode. AA-ptMB electrocatalytic cycle allows amplifying the signal from hybridized MB-labeled DNA through oxidation of AA. The process consists three particular processes: hybridization of tMB to the surface probe, reaction between AA and ptMB, and (c) the electron transfer from ptMB to the electrode. We have demonstrated that system is limited by the AA-ptMB redox reaction (bimolecular constant, $k = 8 \pm 0.1\ M^{-1}\ s^{-1}$). AA-ptMB cycle is sequence-specific, thus fully developed current saturation curves can be used to calculate hybridization parameters and evaluate binding kinetics under various conditions. In addition, evaluating the initial hybridization rate allows quantifying the concentration of labeled ssDNA (tMB) in several minutes. This study provides the first report of a simple electrocatalytic cycle between MB-labeled DNA and a reducer AA for monitoring DNA hybridization in real time.

1. Introduction

Sensors for DNA hybridization are valuable for their specificity and sensitivity and have found applications in biotechnology and clinical diagnostics [1–4]. While many biosensors have been developed for end-point readout of the hybridization event with a focus on improving detection limits, there is also a need to monitor the kinetics of nucleic acid binding quantitatively in real time. Real-time hybridization monitoring can provide advantages over end-point measurements [4], especially in such applications as diagnostic testing and drug discovery. For example, real-time monitoring enables more precise evaluation of hybridization kinetics, leading to improvements in assay sensitivity and specificity, and usually allowing for reduced sample-to-answer times. As a result, one of the aims of bioanalytical chemistry should be to develop real-time hybridization monitoring devices that are simple, reusable, and low-cost.

To date, real-time hybridization signal readout techniques are mainly based on optical (SPR [5,6], fluorescence [3,4]), or acoustic (QCM [7]) methods, while more recently promising FET sensors have been introduced [8]. Since modern light detectors are sensitive, fluorometric detection usually does not require signal enhancement, but the amount of target molecules is often amplified. One recent study demonstrated the use of capture probes immobilized on polystyrene beads, complementary to fluorophore-labeled target oligonucleotides, to monitor DNA hybridization kinetics in real time and detect single nucleotide polymorphisms in amplicons of bacterial genes in 5-15 min [3]. For SPR and QCM methods, the binding of a small number of oligonucleotides is difficult to detect due to their low molar mass, so these readout methods require signal amplification. QCM measurements without signal amplification can provide nanomolar sensitivity for DNA hybridization sensors, whereas using nanoparticle conjugation or precipitation by enzymatic or chemical means has helped to reduce the limit of detection to the attomolar range [7]. With SPR, hybridization of 0.5 μM DNA oligonucleotide could be monitored with no signal amplification [5], whereas attaching the oligonucleotides of interest to silica nanoparticles aided researchers in following their hybridization and melting in real time at the functionalized bead concentration of 0.1 mg mL^{-1} [6]. FET sensors have been demonstrated to reach a 10 pM limit of

* Corresponding author.
E-mail addresses: skomantas.serapinas@gmc.vu.lt (S. Serapinas), dalius.ratautas@gmc.vu.lt (D. Ratautas).

https://doi.org/10.1016/j.electacta.2024.145146
Received 22 May 2024; Received in revised form 5 September 2024; Accepted 23 September 2024
Available online 24 September 2024

detection with no signal amplification when capture probes were immobilized on a graphene FET and the hybridization process of a 26 nt length oligonucleotide was monitored in real time as a shift in charge neutrality point voltage [8]. However, the traditional methods often require large and complicated equipment which is difficult to miniaturize and adapt for high throughput applications, while FET biosensor production procedures tend to be difficult and expensive or have issues when performing specific detection in complex matrixes. Electrochemical DNA hybridization signal readout methods [9] are known for simple sensor preparation, compatibility with microfabrication techniques, device portability, low cost, and the ability to operate in complex, turbid samples [10]. Still, current electrochemical hybridization signal readout methods have limitations in their sensitivity and temporal resolution. For monitoring of unlabeled oligonucleotide hybridization, impedance-based methods can be implemented and have achieved detection limits of 1 pM in buffer solutions, however, the detection limit in complex samples (e.g., diluted human blood plasma) was lowered to nanomolar concentration with 15 s temporal resolution [11]. It could be expected that employing faradaic reactions for electrochemically labeled oligonucleotide detection could aid in improving detection limits in complex matrixes, as these signals are easier to distinguish from noise. However, only a few attempts have been reported at monitoring the hybridization of labeled oligos in real time. For example, potential scanning methods such as square wave voltammetry [12] and cyclic voltammetry [1] have allowed achieving 5 min temporal resolution and nanomolar detection limits with no signal amplification. Electrochemical assay performance could be improved by applying signal amplification methods, such as enzymatic [13–18] or nanoparticle-based [19] approaches, both of which have drawbacks like high cost and lack of stability. Usually, these signal amplification tools allow only end-point measurements because multiple washing steps are needed. There is, therefore, a need for a simple and effective tool to electrochemically monitor heterogeneous DNA hybridization in real time with good temporal resolution, which can potentially be achieved with the aid of chemical catalysis [20–22].

This study focused on the development of an electrochemical method for real-time readout of heterogeneous DNA hybridization and fundamental understanding of the process in general by employing an electrochemical signal amplification system composed of MB-labeled DNA and ascorbic acid redox cycle. The designed cycle is similar in principle to the redox system reported by Lapierre et al. where DNA hybridization amplification was demonstrated involving redox reactions between Ru$(NH_3)_6^{3+}$ and Fe$(CN)_6^{3-}$ [23]. The signal of MB-labeled oligonucleotide heterogeneous binding was chemically amplified by ascorbic acid, thus allowing the use of chronoamperometry (CA) for hybridization monitoring. Real-time electrochemical hybridization monitoring of 25 nt length DNA in the concentration range from 5 nM to 100 nM was achieved.

2. Experimental

2.1. Materials and methods

Oligonucleotides (including atto-methylene blue 2 (MB)-modified oligonucleotides) were purchased from Metabion AG (sequences are given in Table 1). Nuclease-free water, l-ascorbic acid (AA), Tris(2-carboxyethyl) phosphine hydrochloride (TCEP), 6-mercapto-1-hexanol (MCH), sodium hydroxide (NaOH), acetic acid (CH_3COOH), hexaammineruthenium(III) (RuHex) and boric acid (H_3BO_4) were purchased from Sigma-Aldrich. Sodium dihydrogen phosphate (NaH_2PO_4) and disodium hydrogen phosphate (Na_2HPO_4) were purchased from Reachen Slovakia. Magnesium chloride hexahydrate ($MgCl_2{\cdot}6H_2O$), sulfuric acid (H_2SO_4), phosphoric acid (H_3PO_4), and methylene blue were purchased from Merck. Sodium chloride (NaCl) and Tris were obtained from Roth.

Measurements were usually performed (if not stated differently) using hybridization buffer solution (HBS) containing 50 mM phosphate-buffered saline (PBS), 3 M NaCl, pH was adjusted to 7.0.

Data fitting was performed using SciPy (1.13.1) and Wolfram Mathematica (14.0) in-built least square methods for non-linear model fitting. Curve fitting data and fitted parameters are given in Supporting Information (Fitting data).

Table 1
Oligonucleotides used in this study.

ssDNA name, length	Sequence (5'→ 3')	T_m, °C	T_m, °C (salt adjusted for HBS/AA)*
probe (p), 25 nt	Thiol-C6 GAG GTG GAA CCT CAT CAG GAG ATG C	61.0	98.6
target-MB (tMB)**, 25 nt	AttoMB2 GCA TCT CCT GAT GAG GTT CCA CCT G		
target, 25 nt	GCA TCT CCT GAT GAG GTT CCA CCT G		
MB-labeled non-complementary (noncomp-MB), 25 nt	AttoMB2 CGC CAG CTC TGT AGA ATA CTC AGC T		

* calculated using the OligoCalc online tool [24].
** The AttoMB2 label is a derivative of MB, and their electrochemical behaviors are largely identical, therefore, for the sake of simplicity, the AttoMB2 label is referred to as MB.

2.2. Oligonucleotide solution preparation

The freeze-dried oligonucleotides obtained were dissolved in 10 mM Tris buffer solution, pH 8.00. Probe oligonucleotide storage concentrations were 800 μM, while target oligonucleotide (Target-MB) storage concentrations were 400 μM. Storage solutions were kept at −20 °C. Probe oligonucleotide solution was prepared for immobilization on gold electrodes using a reducing TCEP solution (20 mM TCEP, 10 mM Tris, 100 mM $MgCl_2$, pH 7.2). The probe storage solution was mixed with TCEP solution in a 1:4 ratio and incubated at room temperature in the dark for 60 min. After reduction, Probe oligos were diluted to 1 μM using immobilization buffer (10 mM Tris, 100 mM $MgCl_2$, pH 7.2). This solution, labeled probe immobilization solution (PIS) was immediately used to prepare electrodes.

2.3. Electrode preparation

Gold disc electrodes (d = 2 mm) were purchased from BASi. Electrodes were cleaned mechanically by polishing on a microcloth wetted by alumina suspension (d = 0.3 μm) in deionized water for several minutes. Then, electrodes were ultrasonicated in deionized water for 10 min. Afterward, electrochemical cleaning was performed, as described previously [25]. Electrodes were rinsed thoroughly with deionized water after each cleaning step. Electrodes were incubated in 120 μL of PIS at +4 °C overnight. After Probe immobilization, the electrodes were rinsed with deionized water again and placed in 200 μL of 4 mM MCH for 4 h at room temperature. Finally, electrodes were submerged in 300 μL of HBS and conditioned at room temperature for no <20 h (stable for at least a month) before performing any measurements.

2.4. Electrochemical measurements

Electrochemical measurements were conducted in a 10 mL jacketed glass cell using a three-electrode system (modified Au electrode as working electrode, Pt auxiliary electrode, and Ag/AgCl (3 M KCl) reference electrode) with Gamry Reference 600+ potentiostat. Experiments were done at +25 °C temperature unless stated otherwise. CA experiments were carried out at 1 Hz frequency with constant agitation of solution by a magnetic stirrer at 1500 rpm. Cyclic voltammetry (CV)

measurements were recorded in the potential range from 0.1 to −0.4 V at 0.05 V s^{-1} scan rate unless stated otherwise. The measurement solution was not stirred during the recording of cyclic voltammograms (CVs) but was agitated (1500 rpm by a magnetic stirrer) between CVs when real-time hybridization measurements were performed. All potential values are reported vs Ag/AgCl (3 M KCl).

Real-time hybridization data from CA measurements were baseline-corrected. For all measurements, the current value at the moment of the target-MB oligonucleotide introduction was set to 0 (1500s in all hybridization measurements by CA). The ΔI vs time data was then baseline drift-corrected. To obtain the baseline current drift with each used electrode, 3 measurements at 0 nM target-MB were conducted. ΔI values of these 3 measurements were averaged and subtracted from the data obtained with their respective electrodes at other target concentrations. Baseline-corrected data was used for creating graphs and fitting to models.

Chronocoulometric DNA surface density quantification was carried out using the method by Steel et al. [26]. Briefly, the electrodes were equilibrated at 0.147 V for 5 s in 10 mM argon-saturated Tris buffer solution (pH 7.4), after which the reductive current was measured at −0.353 V for 1.5 s. The current was sampled every 0.005 s. The electrodes were measured before and after the addition of 100.0 μM RuHex.

3. Results and discussion

3.1. Electrode design for target-MB (tMB) hybridization monitoring

At first, we investigated the electrochemistry of freely diffusing methylene blue (MB) on an MCH-modified gold electrode to observe its electrochemistry and identify the potential values of its oxidation and reduction as a reference (Supplementary Information, Figure S1). Results indicated that MB had a distinctive oxidation with a standard redox potential (E_0) equal to −0.176 V. Afterward, electrodes were prepared to enable electrochemical monitoring of complimentary ssDNA (target-MB) hybridization to surface-immobilized capture Probe (p). The design was based on the one we previously used to monitor DNA-MB hybridization for DNase detection [1]. The main difference in this study was the omission of gold nanoparticles from the design, making sensing electrode preparation cheaper and simpler. The rationale for using MB-labeled DNA was based on several factors such as relatively low redox potential, good reversibility of the redox process and MB's ability to be reduced by external chemicals. Briefly, gold electrodes were covered in a self-assembled monolayer (SAM) of capture p oligonucleotides (Table 1), followed by surface blocking with MCH [27]. These modified electrodes were termed Sensing electrodes. Afterward, we conducted control experiments to demonstrate that Sensing electrodes can selectively and specifically hybridize complementary target-MB

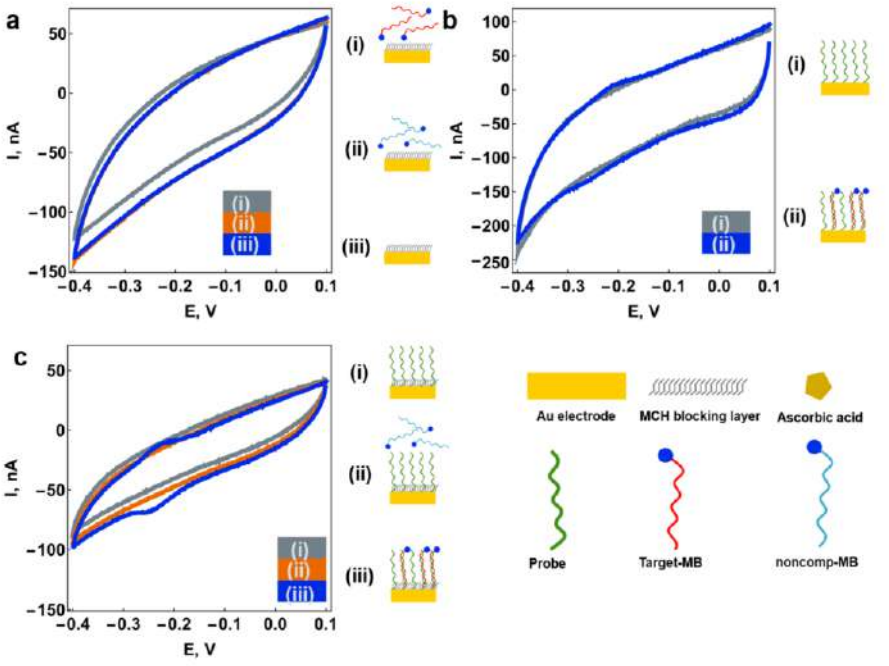

Fig. 1. Electrochemical investigation of electrodes. a. Electrode covered by a SAM of MCH before ((i), gray), after incubation with 100 nM noncomp-MB ((ii), orange), and after incubation with 100 nM target-MB ((iii), blue). b. Electrode covered by a SAM of probe before ((i), gray), and after incubation with 100 nM target-MB ((ii), blue). c. Sensing electrode covered by SAMs of probe and MCH before ((i), gray), after incubation with 100 nM noncomp-MB ((ii), orange), and after incubation with 100 nM target-MB ((iii), blue). The DNA oligonucleotides presented in schemes are for illustration purposes only and do not necessarily appear as demonstrated.

oligonucleotides (Fig. 1).

Various design electrodes were incubated with complementary and noncomplementary DNA oligonucleotides. The absence of the Probe does not result in the electrochemical signal of MB, thus the electrochemical signal of MB cannot be originated from non-specific DNA adsorption of electrode surface (Fig. 1a). Using an electrode without MCH still results in detectable MB electrochemistry, but the background signal is significantly greater indicating that is beneficial to use MCH (Fig. 1b). We can be confident that the final iteration of the Sensing electrodes is DNA-specific. MB signal is observed only in case an electrode is incubated with complimentary target-MB but not with non-complimentary oligonucleotide (Fig. 1c). Also, background currents resulting from the oxygen present in the solution were significantly reduced. We also estimated the surface coverage of the Probe present on Sensing electrodes using RuHex according to the reported method [26]. The surface coverage was found to be $6.92 \pm 1.08 \bullet 10^{12}$ molecules cm^{-2} (11.49 ± 1.79 pmol cm^{-2}). The ssDNA density on the electrode is reasonable ($<10 \bullet 10^{12}$) although somewhat higher than previously reported optimal hybridization densities ($\sim 4 \bullet 10^{12}$) [26,28]. Nevertheless, the hybridization was fair showing approximately $1.1 \bullet 10^{12}$ Target-MB molecules/cm^2 according to MB electrochemistry, indicating that hybridization effectiveness at maximum surface saturation is around 16 %.

CV was the method of choice for confirming successful target-MB hybridization to electrode surface-immobilized probe, due to signal specificity afforded by easily distinguishable MB redox peaks. After the addition of 100 nM target-MB, CVs were recorded every five minutes for an hour at 25 °C (Fig. 2). The first CV ($t = 0$) (Fig. 2a, left) does not exhibit any features expected from a significant redox process. However, with increasing incubation time in a stirred solution of target-MB, reduction and oxidation peaks of the electrochemical label became apparent (Fig. 2a, right). Peak potential values were similar to those reported previously [1,29]: −0.233 V for the reduction and −0.220 V for the oxidation peaks. The recorded peaks corresponded well with the values received using freely diffusing MB on MCH-modified electrode accounting for the expected potential shift resulting from surface immobilized vs. freely diffusing species. CV data were fitted to a model that describes the potential-current function of surface-adsorbed redox active species accounting also background current as described [30] (Supporting information, Equation S1, Fitting data). CV fitting yielded the amount of probe-target-MB (ptMB) at each time point (Fig. 2b). Hybridized ptMB amount ranged from 0 pmol at the start of the measurements to around 0.056 pmol after 1 h.

The process of hybridization is impacted by temperature, ionic strength, pH, and the number of oligonucleotide base pairs. For the implemented experimental conditions (measurement $T = 25$ °C, while T_m=98.6 °C (salt adjusted, calculated using the OligoCalc online tool [24]), 25 nt length, pH 7.0, high ionic strength buffer), it is expected that no dehybridization could occur [31]. Therefore, the observed hybridization kinetic curves can be described by the irreversible adsorption model:

$$p + [\mathrm{tMB}] \xrightarrow{k_{on}} \mathrm{ptMB} \quad (1)$$

The rate of ptMB hybrid formation is given by equation:

$$\frac{d\mathrm{ptMB}_t}{dt} = k_{on}\, p\, [\mathrm{tMB}] \quad (2)$$

Here p, $\mathrm{ptMB_t}$, [tMB] are the amounts or of free capture probe on the electrode surface (mol), the amount of probe-target-MB hybrid on the electrode surface at time point t (mol), and the concentration of target-MB in solution (M), respectively. k_{on} – second order hybridization rate constant ($M^{-1}s^{-1}$). Considering that $p = \mathrm{ptMB_{max}} - \mathrm{ptMB_t}$ ($\mathrm{ptMB_{max}}$ – the maximum amount of probe-target-MB hybrid on the electrode surface) and solving the rate equation analytically gives:

$$\mathrm{ptMB_t} = \mathrm{ptMB_{max}}\left(1 - e^{-k_{on}\,[\mathrm{tMB}]\,t}\right) \quad (3)$$

Eq. (3) was used to fit surface saturation versus time data (Fig. 2b, Supporting information, Fitting data). k_{on} was fitted $8300 \pm 660\ M^{-1}s^{-1}$ and $\mathrm{ptMB_{max}}$ was fitted 0.057 pmol, yielding a maximum coverage of 1.81 pmol cm^{-2} for the geometric surface area of the electrode, which falls in the range of previously reported values (1.6 – 6.5 pmol cm^{-2}) [26] [32].

Once Sensing electrode was fully hybridized, the electrode was further investigated using increased scan rates in range 0–300 mV s^{-1} (Supporting information, Figure S1b) to determine electrode parameters such as the electron transfer rate between the electrode and hybridized DNA (ptMB). Since the hybridization is irreversible (both oxidized and reduced forms are irreversibly adsorbed), we can use Laviron established approach to determine electron transfer constant (k_0) from the cathodic and the anodic peak separation dependence of the potential scan rate [33]. Parameters were received: $k_0 = 76 \pm 25\ s^{-1}$ and $\alpha = 0.66 \pm 0.07$. The received parameters are in range of the reported values of previous papers for electron transfer rate between DNA and electrodes [34,35]. Using k_0, it is possible to determine the limiting current (i_{ET}) of the system of the fully hybridized electrode at saturation [36,37]:

$$i_{ET} = n\, F\, k_0\, \mathrm{ptMB_{max}} \quad (4)$$

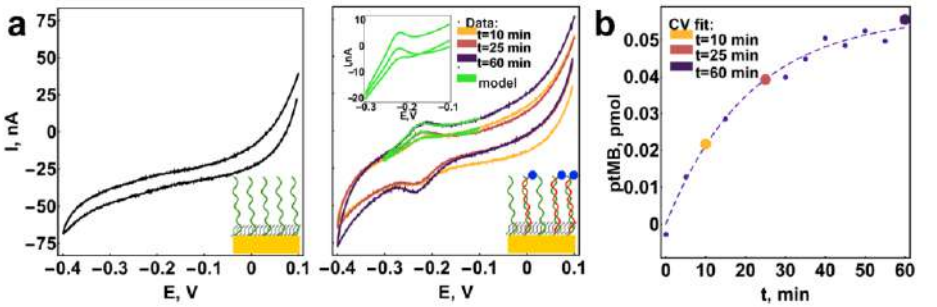

Fig. 2. Sensing electrode response to target-MB oligonucleotide. **a.** CV plot before (left) and after (right) incubation with 100 nM of target-MB at 10, 25, and 60 min. Inset illustrations show modified electrode surface. The inset graph on the right side shows the enlarged area of MB oxidative peaks. **b.** Probe-target-MB (ptMB) amount as a function of time. Dashed line shows a heterogeneous hybridization model fit (Eq. (3), Supporting information, Fitting data). The DNA oligonucleotides presented in schemes are for illustration purposes only and does not necessarily appear as demonstrated.

Here, $n = 2$ (electrons participating in a process), $F = 96{,}485$ C mol^{-1} (Faraday constant), k_0 – electron transfer constant (76±25 s^{-1}), ptMB$_{max}$ – the maximum amount of probe-target-MB hybrid on the electrode surface (0.057 pmol). Placing all the parameters into Eq. (4), the limiting current of the electrode can be calculated 830±390 nA (the detailed discussion about the limiting current is given in Section 3.3).

As evident from Fig. 2c, using CV to measure heterogeneous DNA hybridization yields results with poor temporal resolution. For the scan rate used here (50 mV s^{-1}) the highest possible temporal resolution would be 20 s. In such case, however, no time would be left for solution stirring, thus likely retarding the hybridization. Another drawback of continuous hybridization measurement using CV is the need to impose a negative potential, here up to –0.4 V. DNA SAMs, immobilized through alkanethiol linkers, are stable in the potential range from –0.6 V to +0.6 V at physiological pH [38]. In the negative potential region, reductive desorption of thiolated DNA occurs [38,39]. Therefore, approaching the reductive stability limit during measurements increases the chances of destabilizing the Sensing electrode surface. Due to these limitations, an alternative electrochemical assay for monitoring heterogeneous DNA hybridization is favorable.

3.2. Probe-target-MB (ptMB) signal amplification using ascorbic acid

We have developed a method to increase the number of electrons obtained from a single event of labeled DNA hybridization to improve the temporal resolution of binding monitoring, as well as decrease the probability of thiolated DNA desorption from the Sensing electrode. CA is a suitable electrochemical method to achieve these goals, as the typical sampling frequency is 1 s and there is a possibility to perform the measurement at potentials that do not induce electrode surface deterioration. To implement signal amplification, we used ascorbic acid (AA) – a well-known reducer of MB [40,41] which has previously been used for ascorbic acid biosensors [42–44], as well as signal amplification of nucleic acid biosensors for end-point readout [45]. However, to our best knowledge, ascorbic acid has not been demonstrated to aid in real-time hybridization monitoring.

At first, the electrocatalytic cycle of MB reduction by AA and reoxidation at the Sensing electrode surface was demonstrated using freely diffusing MB. The oxidation current of the reduced MB (MB$_{red}$) was recorded during CA measurements (Fig. 3). Increasing concentrations of AA were added to a buffer solution either containing 1 μM of MB or without MB (Fig. 3a). When MB was added to the buffer prior to introducing AA (Fig. 3a, blue curve), the current increased in proportion to the added AA concentration. Increasing AA concentration increased signal amplification (Fig. 3a inset), however, 30 mM of AA also increased noise in data. Therefore, for further measurements with freely diffusing MB, the maximum used ascorbic acid concentration was 20 mM. When AA was added to solution without MB (Fig. 3a, red curve) no signal was present. However, once at the end of such experiment 1.0 μM of MB was added to the solution, an instantaneous rise in oxidative current was observed indicating that the AA-MB redox cycle started and it could be used to amplify the signal from surface-attached ptMB oligonucleotides.

Further experiments were performed to demonstrate that the observed increase in MB oxidative current can be applied to detect electrode surface-bound MB-tagged DNA (Fig. 3b). Using the Sensing electrode, different CA measurements were performed: (1) when the electrode surface was covered by probe (Fig. 3b, dark orange curve), (2) when probe was prehybridized with target (but without MB) forming dsDNA (Fig. 3b, green curve), and (3) when probe was hybridized with target-MB forming an electrode surface covered by ptMB (Fig. 3b, purple curve). Since it has been reported by the group of J. Justin Gooding that small negative molecules could have significantly different redox properties depending on whether the electrode surface is covered by ssDNA or dsDNA [46], measurements (1) and (2) were done as a control to provide evidence that the received electrochemical signal is specific to AA-ptMB redox cycle and does not result from the changes in DNA layer ionic permeability due to a dsDNA formation. Results of

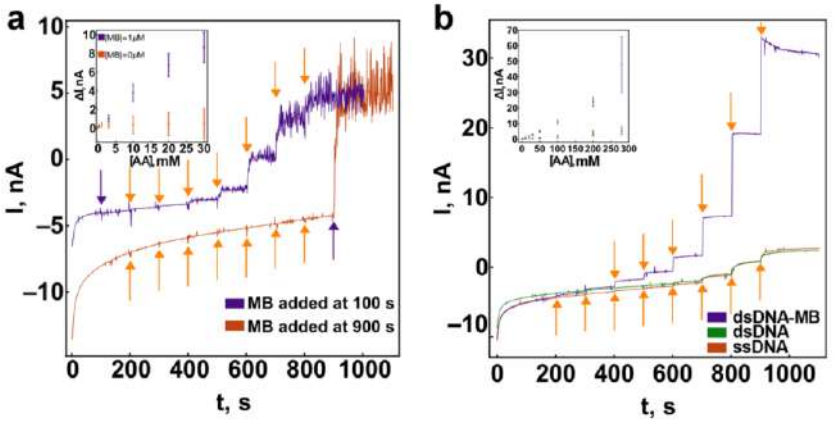

Fig. 3. CA measurements. a. Probe-modified electrode current response to additions of increasing concentrations of AA. Orange arrows mark increases in AA concentration (0.1 mM, 0.3 mM, 1 mM, 3 mM, 10 mM, 20 mM, and 30 mM). Blue arrows mark the addition of 1.0 μM MB. b. Current response to additions of an increasing concentration of AA when the working electrode is modified with ssDNA (probe) (red curve), dsDNA (probe-target without MB) (green curve), and with dsDNA-MB (ptMB) (blue curve). Orange arrows mark increases in ascorbic acid concentration (3 mM, 10 mM, 20 mM, 30 mM, 50 mM, 100 mM, 200 mM, 280 mM). For both graphs: provided here is a representative view of $n = 3$ measurements of independently prepared electrodes. The insets show the relationship between added AA concentration and change in oxidative current relative to the background. The mean ±s.d. ($n = 3$) is shown. Measurements were performed at −0.1 V in 0.2 M PBS with 10 mM of NaCl, pH 7, magnetic stirring at 1500 rpm. For these experiments, a lower NaCl concentration was used because dsDNA was formed before the measurements.

experiments indicate that AA added to either dsDNA- or ssDNA-modified electrodes did not show any significant increase in current (Fig. 3b, green and dark orange curves). A different response was observed for measurement (3) when ascorbic acid was added to the electrode containing ptMB (Fig. 3b, purple curve). With each increase in AA concentration (from 3 mM to 280 mM), oxidative current also increased; however, no apparent saturation was reached (Fig. 3b, inset). Results demonstrated that the electrochemical current originated due to specific reactions between AA and ptMB. For further measurements, AA concentration of 30 mM was chosen to avoid generating oxidative currents that are unrelated to target-MB hybridization. The effects of buffer pH and applied potential during CA measurements on the magnitude of signal amplification were also tested (Supporting information, Figure S2), confirming that pH 7.0 and –0.1 V potential ensured optimal signal enhancement.

3.3. Kinetics of the AA-ptMB cycle and real-time measurement of MB-labeled oligonucleotide hybridization

To demonstrate the applicability of AA-ptMB electrocatalytic cycle to observe the hybridization of labeled ssDNA and also to investigate the kinetics of the process, we monitored the binding of target-MB oligonucleotide in HBS buffer with 30 mM of AA added (Fig. 4). At first, we demonstrated that the signal increase was proportional to target-MB concentration in solution. From Fig. 4a, it can be observed that increasing target-MB concentration to 5 nM, 10 nM, 30 nM, and 100 nM results in the increase in the initial hybridization rates and time to saturation. Secondly, the AA-ptMB electrocatalytic cycle was used to monitor hybridization rate in various ionic strength buffer solutions (Fig. 4b). Hybridization should occur more rapidly in high ionic strength conditions [12], owing to better screening of DNA backbone negative charge. This was confirmed by real-time hybridization measurements once [NaCl] was varied from 0.01 M to 3 M. Using 0.01 M and 0.1 M [NaCl] no hybridization could be detected. Increasing [NaCl] (to 0.5 M and more) resulted in higher observed hybridization rates (Supporting information, Fitting data). Finally, to assure that the AA-ptMB electrocatalytic cycle is necessary for signal generation, CA and CV (Supporting information, Figure S3) experiments were recorded when the cycle was disrupted. No current increase was observed in either case of AA or MB exclusion (Fig. 4c). Signal generation specificity was also confirmed by recording no increase in a current after introducing a noncomplementary ssDNA.

To describe the kinetics of AA-ptMB electrocatalytic cycle, a function current vs. time model is needed. The resulting electrocatalytic current is depending on the catalytic parameters of the system, AA concentration and the amount of ptMB:

$$I_t = k\, n\, F\, [AA]\, ptMB_t \tag{5}$$

Substituting Eq. (3) into (5) gives a current vs. time function:

$$I_t = k\, n\, F\, [AA]\, ptMB_{max}\left(1 - e^{-k_{on}[tMB]t}\right) \tag{6}$$

Here $n = 2$ (electrons participating in a process), $F = 96{,}485$ C mol^{-1} (Faraday constant), [AA]=0.03 M (ascorbic acid concentration), [tMB]=100 • 10^{-9} M (target-MB concentration), while k, k_{on} and $ptMB_{max}$ are parameters were to be fitted (for detailed data fitting data see the Supporting information, Fitting data). From CA measurements given in Fig. 4b, the $ptMB_{max}$ value was fitted 0.0573±0.0007 pmol, k = 8 ± 0.1 M^{-1} s^{-1}, and k_{on} was dependent on the [NaCl]. Lowest ([NaCl]= 0.01 M) gave k_{on}=77.43 M^{-1} s^{-1}, while the highest ([NaCl]=3.0 M) gave k_{on}=8049 M^{-1} s^{-1}. It is worth noticing, that $ptMB_{max}$ and k values were independent on concentration of NaCl, since NaCl influences the rate of DNA hybridization, thus only k_{on} was affected.

The observed process could be divided into three separate components (Fig. 5): (a) hybridization of tMB to probe forming ptMB, (b) reaction between AA and ptMB, and (c) electron transfer from ptMB to the electrode.

The received constants k_{on}, k and k_0 relates to those components. For component (a), constant k_{on}=8049 M^{-1}s^{-1} ([NaCl]=3.0 M) describes the hybridization rate of tMB to the probe forming ptMB. As we have demonstrated, k_{on} value is greatly affected by ionic strength of the solution influencing the hybridization rate (Fig. 4b; Supporting information, Data fitting). Current of the electrode, is limited by either component (b) the reaction rate between AA-ptMB (constant k), or (c) electron transfer to electrode (constant k_0). It is evident, that the current is limited by the reaction rate between AA-ptMB (component (b)). Firstly, the electrode current using 30 mM AA reaches around 2.5 nA at saturation (Fig. 4). We have demonstrated using Eq. (4), that the limiting current of the electrode should be 830±390 nA. Secondly, while our received bimolecular constant (k = 8 ± 0.1 M^{-1} s^{-1}) has a greater value compared to values reported in the literature for MB reduction

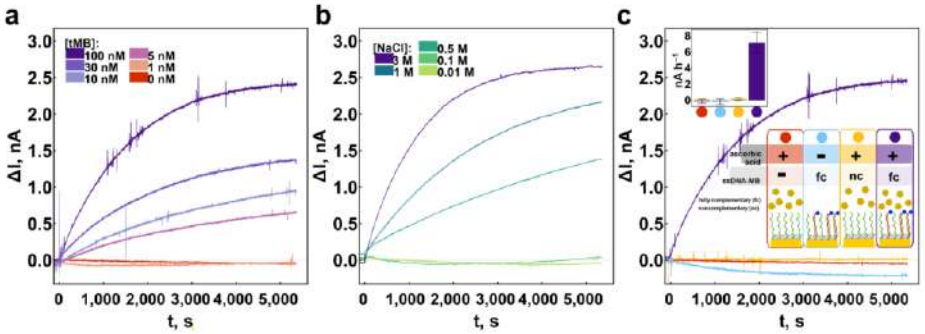

Fig. 4. Real-time CA measurement of heterogeneous MB-labeled oligonucleotide hybridization. a. Hybridization using target-MB (0 nM, 1 nM, 5 nM, 10 nM, 30 nM, and 100 nM). Measurement conditions: –0.1 V, HBS/AA, pH 7.0, magnetic stirring at 1500 rpm. b. The influence of buffer ionic strength (0.01 M, 0.1 M, 0.5 M, 1 M, or 3 M of NaCl) on hybridization kinetics. Measurement conditions:0.1 V, 50 mM PBS and 30 mM AA (pH 7.0), magnetic stirring at 1500 rpm c. CA of AA-ptMB electrocatalytic cycle and control. Red – HBS/AA; Light blue – HBS with 0 mM AA and 100 nM target-MB; Yellow – HBS/AA with 100 nM noncomp-MB; Purple – HBS/AA with 100 nM target-MB. Measurement conditions:0.1 V, pH 7.0, magnetic stirring at 1500 rpm. For all graphs: t = 0 is the time of addition of target-MB. A representative view of n = 3 experiments with independently prepared electrodes is shown. The DNA oligonucleotides presented in schemes are for illustration purposes only and do not necessarily appear as demonstrated.

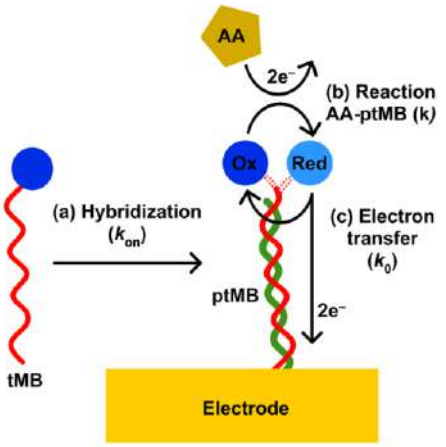

Fig. 5. A scheme demonstrating a full process: (a) hybridization of tMB (governed by a constant k_{on}) forming ptMB, (b) redox reaction between AA and ptMB (governed by a constant k), and (c) electron transfer from ptMB to the electrode (governed by a constant k_0).

using AA (approximately 1 $M^{-1}s^{-1}$) [47][41], it is low in general. Low bimolecular constant value suggests that a reaction between AA and ptMB is a rate (and current) limiting. Finally, experimental investigation using different concentrations of AA (Fig. 3b) indicated that electrode current does not reach the saturation even at greater concentrations of AA (e.g., 280 mM). Using Eq. (6) one could predict electrode currents using various concentrations of AA. Modeling shows that in order to reach the limiting current in our used experimental time range (approximately 3600 s after oligonucleotide addition), around [AA]=10 M should be used, confirming that the electrocatalytic cycle is being limited by AA-ptMB reaction.

5. Conclusions

Here, we have demonstrated a novel method for real-time monitoring of DNA hybridization using chronoamperometry. The electrochemical assay is based on the electrocatalytic cycle between ascorbic acid (AA) and methylene blue (MB) when MB-labeled ssDNA is hybridized to complementary capture probes chemisorbed to the surface of a gold electrode. The assay is specific and can be used to study the hybridization kinetics of target oligonucleotides in the concentration range of 5-100 nM with 1 s temporal resolution. The electrochemical assay consists of three processes: (a) hybridization of MB-labeled ssDNA (tMB) to surface probe forming probe-target-MB (ptMB), (b) redox reaction between AA and ptMB, and (c) electron transfer from ptMB to the electrode. We have studied in detail all the processes and demonstrated that system is limited by the AA-ptMB electrocatalytic reaction (bimolecular constant, $k = 8 \pm 0.1\ M^{-1}\ s^{-1}$), indicating a future work is needed to discover better compounds which could enable to enhance the signal further and/or to detect lower concentrations of DNA. Nevertheless, the initial hybridization rate can be evaluated after several minutes after target DNA introduction, enabling shorter sample-to-answer times. At the current state, the analytical system could be used to investigate the hybridization kinetics of specific DNA sequences of greater importance, for example, detection of SNPs. We also believe that this method can contribute to the development of more accurate and efficient systems for the investigation of heterogeneous DNA hybridization such as analytical systems using secondary target DNA structures as analytes (not labeled by methylene blue) utilizing MB-labeled DNA as a primary target, i.e., "sandwich" systems.

Declaration of competing interest

The authors declare that they have no known competing financial interests or personal relationships that could have appeared to influence the work reported in this paper.

Funding

This project has received funding from the Research Council of Lithuania (LMTLT), agreement No S-MIP-23–127.

Supplementary materials

Supplementary material associated with this article can be found, in the online version, at doi:10.1016/j.electacta.2024.145146.

References

[1] S. Serapinas, J. Gineitytė, M. Butkevičius, R. Danilevičius, M. Dagys, D. Ratautas, Biosensor prototype for rapid detection and quantification of DNase activity, Biosens. Bioelectron. 213 (2022) 114475, https://doi.org/10.1016/j.bios.2022.114475.
[2] A. Abi, A. Safavi, Targeted detection of single-nucleotide variations: progress and promise, ACS Sens. 4 (2019) 792–807, https://doi.org/10.1021/acssensors.8b01604.
[3] K. Boissinot, R. Peytavi, S. Chapdelaine, M. Geissler, M. Boissinot, E.A. Martel, D. Beliveau-Viel, J.-F. Gravel, L. Malic, T. Veres, D. Boudreau, M.G. Bergeron, Real-time monitoring of bead-based DNA hybridization in a microfluidic system: study of amplicon hybridization behavior on solid supports, Analyst 146 (2021) 4226–4234, https://doi.org/10.1039/D1AN00394A.
[4] N. Ostromohov, D. Huber, M. Bercovici, G.V. Kaigala, Real-time monitoring of fluorescence in situ hybridization kinetics, Anal. Chem. 90 (2018) 11470–11477, https://doi.org/10.1021/acs.analchem.8b02630.
[5] K.A. Peterlinz, R.M. Georgiadis, T.M. Herne, M.J. Tarlov, Observation of hybridization and dehybridization of thiol-tethered DNA using two-color surface plasmon resonance spectroscopy, J. Am. Chem. Soc. 119 (1997) 3401–3402, https://doi.org/10.1021/ja964326c.
[6] F. Delport, J. Pollet, K. Janssen, B. Verbruggen, K. Knez, D. Spasic, J. Lammertyn, Real-time monitoring of DNA hybridization and melting processes using a fiber optic sensor, Nanotechnology. 23 (2012) 065503, https://doi.org/10.1088/0957-4484/23/6/065503.
[7] L. Liu, Nucleic acid amplification strategies based on QCM, in: S. Zhang, S. Bi, X. Song (Eds.), Nucleic Acid Amplification Strategies for Biosensing, Bioimaging and Biomedicine, Springer Singapore, Singapore, 2019: pp. 197–209. https://doi.org/10.1007/978-981-13-7044-1_10.
[8] S. Xu, J. Zhan, B. Man, S. Jiang, W. Yue, S. Gao, C. Guo, H. Liu, Z. Li, J. Wang, Y. Zhou, Real-time reliable determination of binding kinetics of DNA hybridization using a multi-channel graphene biosensor, Nat. Commun. 8 (2017) 14902, https://doi.org/10.1038/ncomms14902.
[9] Y.Y. Zhang, F.-X. Guillon, S. Griveau, F. Bedioui, M. Lazerges, C. Slim, Evolution of nucleic acids biosensors detection limit III, Anal. Bioanal. Chem. 414 (2022) 943–968, https://doi.org/10.1007/s00216-021-03722-9.
[10] T. Goda, M. Tabata, Y. Miyahara, Electrical and electrochemical monitoring of nucleic acid amplification, Front. Bioeng. Biotechnol. 3 (2015), https://doi.org/10.3389/fbioe.2015.00029.
[11] P. Capaldo, S.R. Alfarano, L. Ianeselli, S.D. Zilio, A. Bosco, P. Parisse, L. Casalis, Circulating disease biomarker detection in complex matrices: real-time, in situ measurements of DNA/miRNA hybridization via electrochemical impedance spectroscopy, ACS. Sens. 1 (2016) 1003–1010, https://doi.org/10.1021/acssensors.6b00262.
[12] N. Khuda, S. Somasundaram, A.B. Ugande, C.J. Easley, Ionic strength and hybridization position near gold electrodes can significantly improve kinetics in DNA-based electrochemical sensors, ACS Appl. Mater. Interfaces 15 (2023) 5019–5027, https://doi.org/10.1021/acsami.2c22741.
[13] Y. Zhang, A. Pothukuchy, W. Shin, Y. Kim, A. Heller, Detection of ~10^3 copies of DNA by an electrochemical enzyme-amplified sandwich assay with ambient O_2 as the substrate, Anal. Chem. 76 (2004) 4093–4097, https://doi.org/10.1021/ac0495034.
[14] S. Dong, R. Zhao, J. Zhu, X. Lu, Y. Li, S. Qiu, L. Jin, X. Jiao, S. Song, C. Fan, R. Hao, H. Song, Electrochemical DNA biosensor based on a tetrahedral nanostructure probe for the detection of avian influenza A (H7N9) virus, ACS Appl. Mater. Interfaces 7 (2015) 8834–8842, https://doi.org/10.1021/acsami.5b01438.
[15] G. Liu, Y. Wan, V. Gau, J. Zhang, L. Wang, S. Song, C. Fan, An enzyme-based E-DNA sensor for sequence-specific detection of femtomolar DNA targets, J. Am. Chem. Soc. 130 (2008) 6820–6825, https://doi.org/10.1021/ja800554t.

[16] R.M. Torrente-Rodriguez, V. Ruiz-Valdepenas Montiel, S. Campuzano, M. Farchado-Dinis, R. Barderas, P. San Segundo-Acosta, J.J. Montoya, J. M. Pingarron, Fast electrochemical miRNAs determination in cancer cells and tumor tissues with antibody-functionalized magnetic microcarriers, ACS. Sens. 1 (2016) 896–903, https://doi.org/10.1021/acssensors.6b00266.
[17] J. Wu, S. Campuzano, C. Halford, D.A. Haake, J. Wang, Ternary surface monolayers for ultrasensitive (zeptomole) amperometric detection of nucleic acid hybridization without signal amplification, Anal. Chem. 82 (2010) 8830–8837, https://doi.org/10.1021/ac101474k.
[18] J. Wu, K.Y. Chumbimuni-Torres, M. Galik, C. Thammakhet, D.A. Haake, J. Wang, Potentiometric detection of DNA hybridization using enzyme-induced metallization and a silver ion selective electrode, Anal. Chem. 81 (2009) 10007–10012, https://doi.org/10.1021/ac9018507.
[19] Md.N. Islam, M.K. Masud, N.-T. Nguyen, V. Gopalan, H.R. Alamri, Z.A. Alothman, Md.S.A. Hossain, Y. Yamauchi, A.K. Lamd, M.J.A. Shiddiky, Gold-loaded nanoporous ferric oxide nanocubes for electrocatalytic detection of microRNA at attomolar level, Biosens. Bioelectron. 101 (2018) 275–281, https://doi.org/10.1016/j.bios.2017.09.027.
[20] J. Das, I. Ivanov, E.H. Sargent, S.O. Kelley, DNA clutch probes for circulating tumor DNA analysis, J. Am. Chem. Soc. 138 (2016) 11009–11016, https://doi.org/10.1021/jacs.6b05679.
[21] T.M. Alligrant, E.G. Nettleton, R.M. Crooks, Electrochemical detection of individual DNA hybridization events, Lab. Chip. 13 (2013) 349–354, https://doi.org/10.1039/C2LC40993C.
[22] E.M. Boon, D.M. Ceres, T.G. Drummond, M.G. Hill, J.K. Barton, Mutation detection by electrocatalysis at DNA-modified electrodes, Nat. Biotechnol. 18 (2000) 1096–1100, https://doi.org/10.1038/80301.
[23] M.A. Lapierre, M. O'Keefe, B.J. Taft, S.O. Kelley, Electrocatalytic detection of pathogenic DNA sequences and antibiotic resistance markers, Anal. Chem. 75 (2003) 6327–6333, https://doi.org/10.1021/ac0349429.
[24] W.A. Kibbe, OligoCalc: an online oligonucleotide properties calculator, Nucleic Acids Res. 35 (2007) W43–W46, https://doi.org/10.1093/nar/gkm234.
[25] D. Ratautas, L. Tetianec, L. Marcinkevičienė, R. Meškys, J. Kulys, Bioanode with alcohol dehydrogenase undergoing a direct electron transfer on functionalized gold nanoparticles for an application in biofuel cells for glycerol conversion, Biosens. Bioelectron. 98 (2017) 215–221, https://doi.org/10.1016/j.bios.2017.06.048.
[26] A.B. Steel, T.M. Herne, M.J. Tarlov, Electrochemical quantitation of DNA immobilized on gold, Anal. Chem. 70 (1998) 4670–4677, https://doi.org/10.1021/ac9800374.
[27] T.M. Herne, M.J. Tarlov, Characterization of DNA probes immobilized on gold surfaces, J. Am. Chem. Soc. 119 (1997) 8916–8920, https://doi.org/10.1021/ja9719586.
[28] L. Simon, R.E. Gyurcsányi, Multiplexed assessment of the surface density of DNA probes on DNA microarrays by surface plasmon resonance imaging, Anal. Chim. Acta 1047 (2019) 131–138, https://doi.org/10.1016/j.aca.2018.09.048.
[29] C.G. Pheeney, J.K. Barton, DNA electrochemistry with tethered methylene blue, Langmuir. 28 (2012) 7063–7070, https://doi.org/10.1021/la300566x.
[30] M. Jakubowska, Signal processing in electrochemistry, Electroanalysis. 23 (2011) 553–572, https://doi.org/10.1002/elan.201000465.
[31] Q. Su, S. Vogt, G. Nöll, Langmuir analysis of the binding affinity and kinetics for surface tethered duplex DNA and a ligand–apoprotein complex, Langmuir. 34 (2018) 14738–14748, https://doi.org/10.1021/acs.langmuir.7b04347.
[32] J. Zhang, L. Wang, D. Pan, S. Song, C. Fan, DNA hybridization "turns on" electrocatalysis at gold electrodes, Chem. Commun. (2007) 1154–1156, https://doi.org/10.1039/B615742D.
[33] E. Laviron, General expression of the linear potential sweep voltammogram in the case of diffusionless electrochemical systems, J. Electroanal. Chem. Interfacial. Electrochem. 101 (1979) 19–28, https://doi.org/10.1016/S0022-0728(79)80075-3.
[34] L. Kékedy-Nagy, E.E. Ferapontova, Sequence-specific electron transfer mediated by DNA duplexes attached to gold through the alkanethiol linker, J. Phys. Chem. B 122 (2018) 10077–10085, https://doi.org/10.1021/acs.jpcb.8b07505.
[35] J.D. Slinker, N.B. Muren, S.E. Renfrew, J.K. Barton, DNA charge transport over 34 nm, Nature Chem. 3 (2011) 228–233, https://doi.org/10.1038/nchem.982.
[36] A.J. Bard, L.R. Faulkner, H.S. White, Electrochemical methods: Fundamentals and Applications, 3rd edition, Wiley, Hoboken, NJ, 2022.
[37] J.-M. Savéant, Molecular catalysis of electrochemical reactions. mechanistic aspects, Chem. Rev. 108 (2008) 2348–2378, https://doi.org/10.1021/cr068079z.
[38] E.E. Ferapontova, DNA electrochemistry and electrochemical sensors for nucleic acids, Annual Rev. Anal. Chem. 11 (2018) 197–218, https://doi.org/10.1146/annurev-anchem-061417-125811.
[39] J. Wang, G. Rivas, M. Jiang, X. Zhang, Electrochemically induced release of DNA from gold ultramicroelectrodes, Langmuir. 15 (1999) 6541–6545, https://doi.org/10.1021/la9905315.
[40] T. Snehalatha, K.C. Rajanna, P.K. Saiprakash, Methylene blue - ascorbic acid: an undergraduate experiment in kinetics, J. Chem. Educ. 74 (1997) 228, https://doi.org/10.1021/ed074p228.
[41] S. Mowry, P.J. Ogren, Kinetics of methylene blue reduction by ascorbic acid, J. Chem. Educ. 76 (1999) 970, https://doi.org/10.1021/ed076p970.
[42] U. Yogeswaran, S.-M. Chen, Multi-walled carbon nanotubes with poly(methylene blue) composite film for the enhancement and separation of electroanalytical responses of catecholamine and ascorbic acid, Sens. Actuators B: Chem. 130 (2008) 739–749, https://doi.org/10.1016/j.snb.2007.10.040.
[43] M. Arvand, Sh. Sohrabnezhad, M.F. Mousavi, M. Shamsipur, M.A. Zanjanchi, Electrochemical study of methylene blue incorporated into mordenite type zeolite and its application for amperometric determination of ascorbic acid in real samples, Anal. Chim. Acta 491 (2003) 193–201, https://doi.org/10.1016/S0003-2670(03)00790-6.
[44] A.A. Ensafi, Determination of ascorbic acid by electrocatalytic voltammetry with methylene blue, Anal. Lett. 36 (2003) 591–604, https://doi.org/10.1081/AL-120018250.
[45] X. Ma, K. Qian, O. Ejeromedoghene, M. Kandawa-Schulz, W. Song, Y. Wang, p-Co-BDC/AuNPs-based multiple signal amplification for ultra-sensitive electrochemical determination of miRNAs, Anal. Chim. Acta 1183 (2021) 338979, https://doi.org/10.1016/j.aca.2021.338979.
[46] E.L.S. Wong, J.J. Gooding, Electronic detection of target nucleic acids by a 2,6-disulfonic acid anthraquinone intercalator, Anal. Chem. 75 (2003) 3845–3852, https://doi.org/10.1021/ac034129d.
[47] Y.H. Zhao, X. Li, Q.Q. Du, L.C. Hou, X.J. Wang, Reduction kinetics and electrochemistry property of ascorbic acid, AMR 233–235 (2011) 1752–1755, https://doi.org/10.4028/www.scientific.net/AMR.233-235.1752.

3. Publication III

Žalnėravičius, R.; Talaikis, M.; Klimas, V.; **Serapinas, S**.; Butkevičius, M.; Vaičiūnienė, J.; Morkvėnas, A.; Karabanovas, V.; Niaura, G.; Jagminas, A.; Dagys, M.

Fabrication of Porous Black Gold Films by One-Step Anodic Treatment: Towards the Development of SERS-Active Nanosensors. *Materials Today Chemistry* **2025**, *47*, 102849. https://doi.org/10.1016/j.mtchem.2025.102849.

Materials Today Chemistry 47 (2025) 102849

Contents lists available at ScienceDirect

Materials Today Chemistry

journal homepage: www.journals.elsevier.com/materials-today-chemistry/

Fabrication of porous black gold films by one-step anodic treatment: towards the development of SERS-active nanosensors

Rokas Žalnėravičius [a,b,*], Martynas Talaikis [a,b], Vaclovas Klimas [b], Skomantas Serapinas [a], Marius Butkevičius [a], Jūratė Vaičiūnienė [b], Augustas Morkvėnas [c], Vitalijus Karabanovas [c], Gediminas Niaura [a,b], Arūnas Jagminas [b], Marius Dagys [a]

[a] Institute of Biochemistry, Life Sciences Center, Vilnius University, Saulėtekio av. 7, LT-10257, Vilnius, Lithuania
[b] Center for Physical Sciences and Technology (FTMC), Saulėtekio av. 3, LT-10257, Vilnius, Lithuania
[c] Laboratory of Biomedical Physics, National Cancer Institute, Baublio st. 3B, LT-08660, Vilnius, Lithuania

ARTICLE INFO

Keywords:
Nanoporous gold (NPG)
Gold anodization
Anodic treatment
SERS substrate
Doxorubicin (DOX)
Oxalic acid

ABSTRACT

Developing cost-effective, fast, and easy-to-scale fabrication of disposable gold-based SERS-active nanosensors may benefit surface-enhanced Raman scattering (SERS) technology. In our study, the nanoporous gold (NPG_{ox}) layer was synthesized by one-step anodic treatment of the 2D gold in oxalate-containing aqueous solutions. The obtained black-colored coatings are comprised of uniformly distributed, oval-shaped (*ca.* 38 ± 1 nm) metallic state (Au^0) gold nanoparticles (NPs) interconnected to each other via 45–70 nm length, chain-like fibers and forming a sponge-like 3D porous network. The insights into the mechanism of porous growth, as well as the comprehensive electrochemical characterization of NPG_{ox}, have been outlined herein. The NPG_{ox}-based SERS-active substrate possessed an enhancement factor of 1.4×10^7 for 4-mercaptobenzoic acid monolayer at 633 nm laser excitation. The proposed nanosensors rapidly and quantitatively detected an anticancer drug, doxorubicin (DOX), within the concentration range from 10^{-6} to 10^{-2} M. Moreover, it was found that the 3-month storage of nanosensors in an ambient environment leads to the reduction of SERS signal only by 6.4–7.4 %. Comparing their SERS performances with commercially available ones, we have evidenced that our proposed SERS nanosensors overcome their analogs and could be a promising tool for routine laboratory research to detect various drugs and other medically relevant molecules.

1. Introduction

Surface-enhanced Raman scattering (SERS) forecasted to commence a new era of non-destructive and sensitive detection technique that originated 50 years ago when Fleishmann's group accidently acquired the Raman signal of pyridine on an electrochemically roughened silver electrode [1]. The effect was confirmed by Van Duyne and Jeanmaire, and by Albrecht and Creighton in 1977 [2,3]. Significant advancements have been achieved in the field thanks to the substantial progress made in understanding the Raman signal amplification phenomenon. This amplification relies on (*i*) chemical enhancement arising due to charge-transfer interactions between nanostructured surfaces and target molecules [4] and (*ii*) electromagnetic enhancement associated with the formation of localized surface plasmon resonance on the corrugated noble metal surfaces (dominant mechanism) [5]. SERS benefits from "hot spots" – enormous electromagnetic field enhancement-localized near sharp edges, tips, or gaps between nanostructures, which leads to substantial Raman signal amplification of target molecule. When probe molecules are placed near or on the surface of nanomaterials serving as plasmonic nanosensors (i.e., SERS substrates), these substrates can amplify the Raman signal by factors ranging from hundreds to millions [6]. Therefore, the SERS substrates drive the detection limit of target molecules down to a trace level ranging between 10^{-3} and 10^{-11} M [7]. This ultrasensitive vibrational technique requires minimal sample preparation and provides highly specific molecular fingerprints [8].

Over the years, SERS has been extensively adopted for various analytical purposes, including pharmaceutical analysis [9], biomedicine [10], environmental monitoring [11], food safety [11], as well as chemical [12], biochemical [13], and microbiological sensing [14]. Despite the intense research efforts that have been made in SERS-based

* Corresponding author. Institute of Biochemistry, Life Sciences Center, Vilnius University, Saulėtekio av. 7, LT-10257, Vilnius, Lithuania.
E-mail address: rokas.zalneravicius@gmc.vu.lt (R. Žalnėravičius).

https://doi.org/10.1016/j.mtchem.2025.102849
Received 19 February 2025; Received in revised form 26 May 2025; Accepted 25 June 2025
Available online 28 June 2025

molecular detection, the method's popularity continues to grow [15]. However, its industrial applications, where the SERS would be used routinely, still face unresolved challenges, primarily related to the demand for the effective, stable, reproducible, scalable, and, importantly, inexpensive production of SERS nanosensors. These substrates should exhibit sufficient enhancement factor (EF), preferably no less than 10^5–10^6 [15–17]. Moreover, the real-world scenario requires a considerable reduction in cost, with a target of producing 10^5 to 10^6 substrates at $10 or $1 each [17]. Currently, the price of commercially available SERS nanosensors varies from $10 to $80 per unit [15]. Nevertheless, the market of SERS substrates has garnered some attention and, according to Market Reports, is projected to grow by up to 12 % between 2023 and 2030 [18], further stimulating efforts to reduce manufacturing costs.

The success of detecting target molecules relies on tailored nanosensors, which play a crucial role in SERS. Today, SERS substrates are conventionally based on carbon materials (i.e., MXene, graphene and carbon nanotubes), noble metals (Au, Ag, Pd, Pt), their alloys, and transition metals (Ni, Cu) [19,20,20]. Their production methods are typically classified into two categories. The SERS substrates comprising colloidal nanoparticles (NPs) are fabricated via bottom-up approaches. On the one hand, these methods offer high scalability and low production cost; however, they suffer from limited stability [21]. On the other hand, nanostructured surfaces formed directly through top-down approaches rely on lithography-patterned surfaces followed by subsequent metallization processes [13]. Recently, nanoporous films of noble metals and their alloys have gained considerable attention as promising candidates for Raman scattering amplification of target molecules adsorbed on their roughened surfaces [22]. Chemical or electrochemical dealloying is among the most accessible methods for fabricating porous layers. This process selectively dissolves more active elements from a precursor alloy, while the noble metal-based nano-objects reorganize along the electrode/electrolyte interface to forming 3D porous films [23]. However, this method requires aggressive acids, which often introduce impurities. Furthermore, in the case of dual-functional sensor systems, such as printed disposable electrodes, acids (i.e. commonly used HNO_3) can irreversibly damage other parts of the electrode (i.e., pseudo-reference Ag electrode), thus complicating the method's applicability.

In their pioneering research, Nisho et al. were the first to demonstrate the formation of black nanoporous gold (NPG) [24]. Lately, we have demonstrated that the morphology transitions of NPG can be controlled by applying different organic acids as supporting electrolytes during the anodization of gold [25]. This fabrication technique tends to be attractive due to its simplicity and applicability for any gold surfaces (including printed ones), thus, probably being more suitable for dual-functionalized nanoelectrodes production. Only a few proof-of-concept studies exist on fabricating SERS nanosensors using the anodic process in oxalic acid. Scaglione et al. reported the synthesis of NPG-based SERS substrate via a two-step fabrication approach [26]. Using 4,4'-bipyridine as a SERS probe molecule, the authors found the detection limit to be 10^{-16} M, which they attributed to the presence of nanometer-scale ligaments and crystals in the NPG matrix. Xu et al. demonstrated that NPG films exhibit significant SERS activity by detecting pyridine in aqueous solutions [27]. However, both studies provided limited information regarding the stability of SERS substrates, their accessibility to target molecules, and the homogeneity and variation of their properties across the surface. To address these limitations, we conducted extensive research to overcome these challenges.

In this paper, we report a one-step, low-cost, relatively fast, and scalable approach for fabricating effective NPG_{ox}-based ("ox" denotes oxalate) SERS nanosensors. We also present their critical characterization and practical application in detecting anticancer drug doxorubicin (DOX) in aqueous solutions. The black-colored NPG_{ox} layers were obtained by anodic polarization of printed gold surfaces in oxalate-containing aqueous solutions for 5–20 min. This manufacturing path provides a dual-functional sensor system that renders screen-printed gold electrodes suitable for electrochemical (Fig. S1) or SERS sensing. We then benchmarked the SERS performances of NPG_{ox} nanosensors against commercial analogs, proving their feasibility for practical application. By combining high Raman signal amplification, characterized by an enhancement factor (EF) of 1.4×10^7 at 633 nm laser excitation, and inexpensive production costs, the developed NPG_{ox} substrates could serve as a promising tool for therapeutic drug monitoring in various scientific laboratories.

2. Experimental section

2.1. Gold cleaning

Prior to the formation of the nanoporous layer, gold disc and gold-based SPE electrodes were cleaned following two different paths. Gold disc electrodes were mechanically polished by turns with 1.0 μm and 0.3 μm of alumina suspension. The mirror-like gold discs were re-cleaned using an ultrasonic bath in ethanol and water for 6 min to remove the abrasive residuals. Then, electrodes were subjected to electrochemical dissolution in the 0.5 M H_2SO_4 solutions by sweeping the potential from 50 to 2650 mV for 8 cycles at a scan rate of 100 mV s^{-1}. The prepared electrodes were stored in distilled water (DI) to minimize the adsorption of various extraneous molecules. The SPE electrodes were cleaned following a similar path except for mechanical polishing steps.

2.2. Anodization of gold

The nanoporous gold (NPG_{ox}) layer was formed by exploiting one-step anodization of 2D gold electrodes (i.e., GE and SPE) in three solutions containing pure organic acids: oxalic, tartaric and citric. Electrochemical oxidation of gold has occurred in a thermostated three-electrode configuration cell, composed of bare gold and platinum electrodes acting here as anode (working electrode) and cathode (counter electrode), respectively. The Hg/Hg_2SO_4 reference electrode (+651 mV vs SHE) has been chosen to prevent chloride anions. The anodic oxidation of gold was performed in a supporting electrolyte containing 0.3 or 0.6 M of organic acids, according to our previous work [25]. The reaction proceeds by applying the constant potential ranging from 2.8 to 3.8 V at 4 ± 1 °C under slow (100 rpm) magnetic mixing. When not used, the synthesized NPG electrodes were carefully rinsed with DI by immersion and kept in ultrapure DI when not in use.

2.3. Modification of NPG

Several alkane thiols with distinct terminal groups, including carboxylic, amine and alkane, were used to modify the NPG_{ox} electrode surface. The self-assembly monolayers (SAM) were formed to build up different functional groups on NPG_{ox} and determine its influence on the physicochemical interactions responsible for direct DOX adsorption on gold. To realize this, the NPG electrodes were incubated separately in an N_2-saturated methanol solution containing 1−5 mM of a single or mixed thiol molecule, which includes 4-MBA, MHA, MUA, DEA, 1-propanethiol, and 1-octanethiol. The SAM immobilization has taken place overnight. Prior to the DOX adsorption, NPG electrodes were carefully rinsed with pure methanol solution and stored in DI.

2.4. Electrochemical investigation of NPG_{ox}

To evaluate the NPG_{ox} electrodes' electrochemical surface area (ESA), the cyclic voltammetry (CV) analysis was performed in 0.1 M H_2SO_4 solution at a scan rate of 50 mV s^{-1}. The ESA was determined by integrating the current peak related to the reduction of oxygen-containing gold compounds ($E_{p,c} \sim 0.85$−0.9 V). Considering that the theoretical gold charge density is 390 ± 10 μC cm^{-2} [28], the relative

ESA (ɪESA) of NPG_{ox} electrodes were calculated by normalizing the determined ESA of NPG_{ox} electrodes with the ESA of the 2D gold. Prior to the modification with thiols, some of the NPG_{ox} electrodes were electrochemically reduced by sweeping the potential from the open circuit (usually 1.0–1.05 V) to the −60 mV in 0.1 M H_2SO_4 solution at a scan rate of 10 mV s^{-1}. The electrochemical investigations were performed using a Zennium electrochemical workstation equipped with CVB 120 probe Zahner-Elektrik (Germany). Unless otherwise stated, the electrode potentials presented in this research refer to the $Ag/AgCl_{3M\ KCl}$ standard electrode potential (+209 mV vs SHE).

2.5. Morphology and phase analysis of NPG

The changes in the chemical state of gold before and after electrochemical reduction were inspected by X-ray photoelectron spectroscopy (XPS). The phase analysis of recently prepared NPG_{ox} was performed by using Kratos AXIS Supra + spectrometer (UK) with monochromatic Al K_α radiation operated at 1486.6 eV and powered at 225 W. A low electron flood gun was used to neutralize the charge. During the spectral acquisition, the base pressure in the analysis chamber was less than 1×10^{-9} mbar. The XPS survey spectra were acquired for each NPG_{ox} electrode and recorded at pass energy of 160 eV with a resolution of 1 eV. High-resolution XPS (HR-XPS) spectra were collected using a reduced pass energy of 10 eV and a higher resolution of 0.1 eV. The binding energy scale was calibrated according to the C1s hydrocarbon peak at 284.8 eV.

The depth profile XPS analysis was performed to compare the chemical state of gold before and after electrochemical reduction. Both electrodes were subjected to 2 sputtering steps (30 s per circle) until the content of carbon and oxygen was utterly eliminated from the surface of NPG_{ox}. HR-XPS spectra were collected for Au, C, and O after each sputtering step, and the chemical composition was determined from the corresponding peak areas after subtraction of the inelastic background. The Avantage processing software ThermoScientific (UK) was used for data processing.

The morphology of the nanoporous films, as well as their thickness and porosity, were inspected by scanning electron microscope (SEM) Helios NanoLab 650 (Netherlands) equipped with a focused ion beam (FIB) technology. The 30 keV Ga^+ ions beam has been used for cross-section SEM imaging.

The concentration of gold (ionic species) in aged oxalic acid electrolyte was inspected by inductively coupled plasma optical emission spectroscope Optima7000DV (ICP-OES) PerkinElmer (USA) at the wavelength of λ_{Au} 267.6 nm.

A contact angle measuring system, EasyDrop (Germany), was used to determine the wetting properties of NPG_{ox}. To realize this, 10 μL DI water drop was placed on bare gold and recently synthesized NPG_{ox} nanoelectrodes. The side images of the drop were digitized and processed using the open-source software ImageJ (National Institute of Health).

2.6. Raman and SERS spectroscopy investigations

The Raman and SERS spectra were acquired using a multiwavelength inVia Raman spectrometer Renishaw (UK) equipped with a confocal microscope Leica (Germany) and a high-sensitivity, thermoelectrically cooled CCD detector operating at −70 °C. All Raman and SERS spectra were obtained by averaging 676 individual spectra recorded from the randomly selected surface of nanoporous gold. Laser light was focused on an NPG_{ox} substrate surface using a 50 × /0.75 NA objective lens on a spot of 1 μm in diameter. In most SERS measurements, the laser excitation was 633 nm (45 μW at the sample). To evaluate the effect of the laser excitation wavelength on the SERS performances, the additional laser sources were applied as follows: 532 nm (450 μW), 785 nm (450 μW), and 830 nm (16 mW). For initial SERS measurements, bare gold and porous gold fabricated in oxalic (NPG_{ox}), tartaric (NPG_{tar}) and citric (NPG_{cit}) acid, respectively, were incubated in 1 mM of 4-MBA solution for 2 h to form densely packed SAM on the surface. The mapping of 1590 cm^{-1} spectral mode was obtained by scanning an area of 50 × 50 μm on NPG_{ox} with the step of 2 μm and the spectral acquisition time of 2 s. The spectral intensities were estimated as counts per second (cps). Meanwhile, a simple baseline correction was performed for the graphical presentation.

To evaluate the efficiency of NPG_{ox} as a potential SERS-active substrate, the SERS enhancement factor (EF) was estimated by using the following equation [29]:

$$A = \frac{I_{NPG_{ox}}}{N_{NPG_{ox}}} \times \frac{N_{NR}}{I_{NR}} \quad (1)$$

where $I_{NPG_{ox}}$ and I_{NR} correspond to the measured intensities of ν(C–C) ring-breathing vibrational mode at 1590 cm^{-1} in the SERS and normal Raman (NR) spectrum. $N_{NPG_{ox}}$ and N_{NR} are the number of 4-MBA molecules adsorbed on NPG_{ox} (potential SERS nanosensors) and flat gold surface (bare gold) evaluated at the same laser power and accumulation time, respectively.

SERS measurements of doxorubicin were carried out using high throughput spectrometer Tornado HyperFlux (Tornado Spectral Systems, Mississauga, ON, Canada) equipped with fiber-optic cable for excitation and collection of the Raman spectra and 785 nm diode laser source. The laser power at the sample was set to 100 mW, and the beam was focused on a 100 μm diameter spot on the sample. Spectra were recorded for 100 s.

The information regarding materials and chemicals used in this research and a detailed description of the determination of the NPG-based electrode's active surface area is provided in the 'Supporting information' file.

3. Results and discussion

3.1. Surface characterization of NPG_{ox}-based SERS substrates

Although many commercially available SERS substrates exist today, their low-cost production on an industrial scale remains one of the major issues limiting the widespread practical application of SERS [30]. To address this issue, in this research, we propose a simple, fast, easy-to-scale, and low-cost fabrication method for SERS nanosensors with dual-functionalized properties, which can be customized directly on thin 2D leaf or printed gold surfaces without the need for external gold sources. Our previous research has shown the benefits of such three-dimensional networks for enzyme immobilization and efficient bioanode design [25]. Due to their 3D structure, these nanoporous architectures exhibit increased active surface areas suitable for molecule adsorption and ability to enhance Raman signal.

The fabrication of SERS-active nanosensors is based on the anodic polarization of 2D gold (i.e., planar or printed) in a cooled (~4 °C) oxalic acid electrolyte in a three-electrode configuration cell as presented in Fig. 1a. The different magnification top-side SEM images (Fig. 1b–d) reveal the arrangement of oval-shaped morphology of nanoparticles (NPs) uniformly distributed on the outermost surface of NPG_{ox}. These NPs are interconnected to each other via chain-like fibers forming sponge-like 3D porous networks. This 3D arrangement is hypothesized to facilitate the formation of plasmonic "hot spots" on the surface, although this has not been experimentally confirmed in the present study. The full-sized SEM images (Fig. S2 a–c) show a high degree of homogeneity in nanostructures, which are uniformly distributed across the entire surface of NPG_{ox}-based nanosensors formed during the anodization of gold. The diameter of the oval-shaped NPs varied from 28 to 50 nm, with an average value of 38 ± 1 nm (Fig. S3 a).

Top-side and cross-sectional SEM photographs (Fig. 1d–f insets) also revealed that black-colored NPG_{ox} films have numerous irregularly distributed pores with an average porous width of 56 nm. The NPG_{ox}

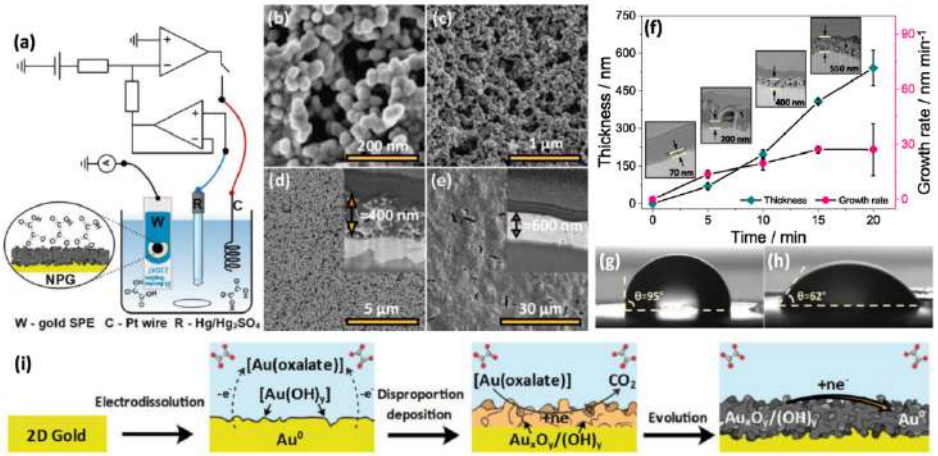

Fig. 1. Schematic illustration (a) of the fabrication of the nanoporous gold (NPG_{ox}) nanosensors. Top-side SEM images of the NPG_{ox} and bare SPE gold surfaces before (e) and after anodization (b–d) in 0.3 M oxalic acid for 20 min. NPG_{ox} film thickness and growth rate dependence on the anodic polarization time at an applied constant potential of 2.8 V. Photographs of a water droplet on the bare SPE gold surface (g) and NPG_{ox} (h), taken in air. Step-by-step schematic illustration of the mechanism underlying NPG_{ox} formation (i). *Insets*: time-dependent cross-sectional SEM images of NPG_{ox} (d, f) and bare SPE surface (e).

film thickness increases linearly from 5 to 20 min following the equation of porous growth rate: $v_g = 0.95t$ (min) + 9.98 with the correlation coefficient $R^2 = 0.89$ (Fig. 1f). These values were estimated from cross-sectional SEM images taken by focusing the ion beam at the center of the NPG_{ox} electrodes (Fig. 1f insets). The continuing growth of porous structures (more than 20 min) would lead to complete electrodissolution, especially at the electrode's edges, where the highest porous growth rate is expected. The surface morphology of the NPG_{ox} does not substantially depend on the applied potential or anodization time except for the first 5 s when individually distributed NPs appeared (Fig. S4 a). Additionally, the thicker structures (~1 µm or more) are prone to losing mechanical strength and may collapse under external pressure, such as finger contact. To minimize economic burdens and show that homogeneous NPG_{ox} layers can be formed even on the printed gold substrates which are easy to scale up in production, screen-printed (SPE) gold electrodes were chosen. Fig. 1e inset and Fig. S5 display the surface morphology and thickness of the bare SPE varied between 500 and 600 nm. Considering only the mass of gold (excluding production costs), the price of such an electrode (4 mm in diameter) is estimated to be approximately 0.01 €/electrode.

The formation of porous gold films on bare gold includes changes in their wetting properties. As shown in Fig. 1g, the water droplet on the bare gold exhibits intrinsic hydrophobicity with a contact angle (CA) of approximately 95°. In contrast, the NPG_{ox} displays a significantly reduced CA value of about 62° (Fig. 1h). The enhanced hydrophilicity of nanoporous gold suggests improved water penetration into 3D networks attributed to the development of numerous channels, sponge-like structures, and possible oxalate adsorption on the surface, thus facilitating the diffusion of molecules into the deeper layers of porous films.

The mechanism of porous gold formation during anodic treatment remains unclear. However, some insights can be drawn based on our previous research [25] and the current knowledge of electrochemical porous gold fabrication [31]. Fig. 1i illustrates the key stages of NPG formation, which include (*i*) electro-dissolution of gold, (*ii*) disproportion deposition, and (*iii*) evolution of NPG films. The formation of a passive film on the surface of anodically polarized metals is a continuation and consequence of active dissolution, occurring through the formation of an activated complex (i.e., gold-oxalate) localized on the metal surface and formed from the metal to be oxidized (i.e., gold) and active anions in the solution (i.e., oxalate) [32]. Increasing the anodic polarization enables the activated complex to remain adsorbed on the electrode surface after charge transfer, ultimately covering the entire surface due to diffusion limitations (a phenomenon known as a primary passivation). On the other hand, the dissolution product may be desorbed; however due to interaction with solution components in the pre-electrode layer, it may deposit on the dissolving metal surface upon reaching a critical solubility concentration (secondary passivation). In both cases, increasing the anodic polarization leads to a reduced metal dissolution rate and the formation of precipitates on the metal surfaces [33]. Since hydroxides and oxides have the lowest solubility product constants (K_{sp}) in non-complex solutions, metal passivation is usually considered as the transformation of [Me(OH)] into a particular metal oxide via anodic polarization. If the solution contains film-breaking anions, the dissolution rate increases again after approaching the critical passivation potential. This enhancement is related to pitting rather than extraneous reactions (i.e., oxygen evolution or oxidation of anion). This phenomenon appears in forming pores in passive films and changes in metal dissolution (in the porous layers) from a passive back to an active state. The main causes of pitting include the adsorption of aggressive anions that form metal complexes easily transferred into the solution, the penetration of the aggressive anions through the barrier layer, the formation of defects in the film that expose uncoated surface to the electrolyte, and localized acidification [34]. Usually, anodic films formed by the anodization of metal have a complex composition. For example, iron anodic films have been found to contain various hydroxides, oxides and oxyhydroxides and their interaction products with ionic species in solution [35].

Due to the intrinsic nobleness of gold ($\Delta G^0 = -434$ kJ mol^{-1}) and the reductive properties of oxalate anions, the outermost layers of gold oxides recover to metallic gold (Au^0) immediately after the anodization process. This behavior was described by Nishio and Masuda [24]. They found that thin gold oxides (Au^{+x}) can be distinguished by their orange

color, formed during gold anodization in other organic acid electrolytes (i.e., citric, tartaric, lactic, and others). The anodization of gold in oxalic acid seemed to follow different paths, whereas the black porous structures comprised metallic gold. A milder regime (2.2 V) and a shorter time (5 min) for SPE gold anodization have been applied to clarify this phenomenon more clearly. The time-dependent photographs show the blackening stages during the synthesis at 0, 20, 40, and 60 s (Fig. S6 c–g). After 0–20 s of exposure to air, the SPE gold electrode was orange (Fig. S6 d–e) with a black ring around the edges of gold, whereas the thicker film of NPG_{ox} was formed. However, after 40–60 s, the electrode turns to light black (Fig. S6 f–g), indicating the reduction of gold oxide (Au^{+z}) films. When sufficiently deep pores are formed, the top layers may be reduced to gold (Au^0) by oxalates (or their ionic species) with the assistance of O^{2-} (or other oxygen-containing species) and subsequently passivated by their carbonaceous species [24]. To highlight the reduction properties of oxalic acid (or its decomposed species), the aged reaction electrolyte was used to reduce the diluted (2 mM) gold acid. As shown in Fig. S6 a, the diluted gold acid remained stable for up to 1.0 h in deionized (DI) water, even after being heated at 70 °C. However, in the case of an aged electrolyte, the solution's color changed from slightly yellow to purple, indicating the reduction of gold acid and the formation of gold nanoparticles (Fig. S6 b). Since the blackening of gold was only achieved with oxalic acid, we predict these changes should be related to the oxalate molecule structure and its specific interactions with gold or other ionic species in solutions. However, further studies are needed to elucidate the NPG formation mechanism in oxalate solutions more comprehensively.

3.2. Electrochemical characterization of NPG_{ox} nanosensors

Since the surface morphology of NPG highly depends on the composition of supporting electrolytes, as shown in our previous work [25], the application of various porous gold electrodes formed in oxalic, tartaric, and citric acids for SERS has been inspected. First of all, the SERS spectra of 4-MBA molecules adsorbed on NPG_{ox} (Fig. S7 a), NPG_{tar} (Fig. S7 b), and NPG_{cit} (Fig. S7 c) were acquired. By comparing the dominant bands at 1077 and 1590 cm^{-1}, associated with the aromatic ring breathing mode (ν_{12}) and symmetric aromatic ring vibration (ν_{8a}), respectively, the NPG_{ox} tends to be 5–15 times more effective than other SERS substrates. Building on these results, the rest of the study aims to develop and characterize NPG_{ox} for SERS-based applications in greater depth.

Gold anodizing occurs above the Burshtein minimum, at approximately 1.8–2.0 V, whereas AuO and Au_2O_3-containing oxide layers are formed on all facets of the gold surface [36]. Within this potential range, the oxidation of oxalic acid and oxygen evolution take place simultaneously with the dissolution of gold. Three characteristic behaviors were observed in the current transient (Fig. 2a) recorded during anodizing of bare gold in 0.3 M oxalic acid at a constant potential of 2.8 V: (*i*) current density decreased immediately upon reaching the set potential (0–10 min), (*ii*) the current density stabilized at approximately 160 mA cm^{-2} with increased noise variation due to the evolution of oxygen (10–17 min), and (*iii*) the current density gradually decreased attributed to the edge effect on the electrode (17–30 min). As a result, the end of the O_2 evolution can be observed around the gold disc. Notably, apart from electrolyte composition, other factors, including applied voltage/-current, reaction time, electrolyte condition, and temperature, play an important role in managing the surface roughness and thickness of NPG_{ox} [25]. The NPG_{ox} growth proceeds at a potential 0.2–0.3 V lower in an aged oxalate solution (used for a couple of days to anodize gold) compared to a freshly prepared solution (Fig. S3 b) or when the oxalate solution's pH significantly increases (i.e., in sodium oxalate) [24]. However, the decreased onset potential resulted in approximately 3.2-fold lower current densities, suggesting that the anodization rate and the potential adsorption capability of carbonaceous species increase in the absence of protons. Additionally, the porosity of NPG_{ox} films increased significantly with a rise in the electrolyte temperature likely due to the more effective electro-dissolution of gold. As a result, the current densities increased more than threefold as the temperature rose from 4 to 20 °C (Fig. S3 c). Unfortunately, the fabrication of NPG_{ox} at room temperature results in insufficient mechanical strength, making it prone to collapse even when the electrode is removed from the anodization bath.

The formed NPG_{ox} films on a 2D gold electrode increased the cathodic and anodic peak currents that appeared at 0.85 and 1.1–1.5 V, respectively, indicating the electrochemically enhanced surface area

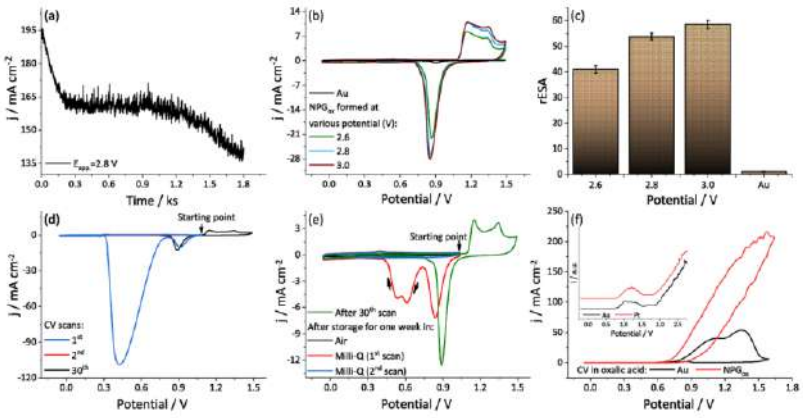

Fig. 2. Electrochemical characterization of NPG_{ox} formed in 0.3 M oxalic acid after anodic treatment of bare gold. Current transient (a) of NPG_{ox} formation at 2.8 V for 30 min. Cyclic voltammograms of NPG_{ox} nanosensors; (b) formed at various applied potentials for 20 min and their relative electrochemical surface area (rESA normalized with respect to bare gold); (c) CV scans of recently prepared (d) and aged in air or Milli-Q water for one week NPG_{ox}; (e) formed during the anodization at 2.8 V for 20 min; (f) CV scans of Au and NPG_{ox} in 0.3 M oxalic acid. Unless otherwise stated, all CV curves were registered in 0.1 M H_2SO_4 at 50 mV s^{-1}. *Inset*: linear sweep voltammetry (LSV) variables of Au and Pt electrodes recorded in 0.3 M oxalic acid solutions at 5 mV s^{-1}.

(ESA). Fig. 2b displays cyclic voltammograms (CVs) of recently fabricated NPG_{ox} nanosensors recorded in 0.1 M H_2SO_4 at the gold oxide/hydroxide formation and dissolution potential window as a function of the applied voltage.

To determine the ESA, the reduction current peak was integrated to evaluate the net charge density consumed to reduce oxygen-enriched gold to metallic gold, considering the conversion factor of 390 μC cm^{-2} [28]. The relative ESA (rESA) of the NPG_{ox} electrode was estimated by considering each electrode's charge density and normalizing it to the ESA of 2D gold. The rESA increased to 31.7 % and 41.5 % (from 41 to 54 and 58) by applying a higher anodization voltage with the step of 0.2 V (Fig. 2c). Since the rESA of NPG_{ox} formed at 2.8 V differs by only 7 % from those obtained at 3.0 V, we have chosen 2.8 V as an optimized voltage for producing NPG_{ox}-based SERS nanosensors.

Since the mechanism of the fabrication of NPG_{ox} in oxalate solutions is not well understood, the explanations proposed above can be further confirmed through the electrochemical characterization of recently prepared specimens. The presence of gold oxides/hydroxides on the NPG_{ox} films was verified using the CV analysis in 0.1 M H_2SO_4 solution. By sweeping the potential from 1.05 V into the cathodic direction, two reduction peaks, with $E_{p,c}$ values of 0.91 V and 0.42 V, were observed, indicating that the formed phases may correspond to gold oxides with varying levels of hydration complexity [37]. According to the Pourbaix diagram of gold (Fig. S8), only the Au(III) oxidation state is expected after the anodic treatment of gold [38]. Consequently, more than one reduction peak confirms the existence of different hydrous/anhydrous oxide phases on the NPG_{ox}. Typically, the peak corresponding to the reduction of bulk gold oxide appears at 0.85–0.9 V [30]. The negative shift of the peak implies that the reduction of these oxides is a highly irreversible process, as demonstrated by the second cathodic scan. In contrast, no redox peak was observed within the same potential window (Fig. 2d). Interestingly, the charge density associated with the irreversible process (calculated from the integrated peak area at $E_{p,c} = 0.42$ V) was over 30 times higher than that observed during the typical reduction of gold oxides. Considering that this difference was observed without any morphological changes, we speculate that some gold-oxalate complexes (or their decomposed fragments) may form during the electro-oxidation of gold, remaining adsorbed within the deep porous layer of NPG_{ox}. The ICP-OES analysis of an aged electrolyte revealed the presence of 0.3 μM of dissolved gold (most likely attributed to ionic gold species) that was found after a series of anodizations. According to the literature, the comparable broadening of the reduction peak was observed previously when the flat silver electrode was repeatedly oxidized and reduced in protein-containing solutions [40]. In this case, the broadening was caused by the interactions of silver ions with amino acids and their further complexation [41].

The formation and dissolution of gold oxides were observed when the anodic potential reached 1.5 V (Fig. 2e). As gold is a noble metal, its oxides and/or hydroxides are thermodynamically expected to spontaneously reduce to metallic gold (Au^0) even at room temperature without the needing an external energy source [42]. The NPG_{ox} electrodes were kept in DI water and air for one week to prove this assumption. As a result, no obvious redox peak attributed to gold oxide reduction was observed in the case of the NPG_{ox} aged in the air (at the potential window from −0.1 to +1.05 V). In contrast, when the electrode was stored in Milli-Q, the two reduction peaks appeared in the first cathodic scan (Fig. 2e). However, the peak current ($i_{p,c}$) was at least 20 times lower, suggesting that the reduction of gold in air proceeds more rapidly than in aqueous solutions.

As reported previously, the anodization of porous gold in oxalic acid completely differs from that in other carboxylic acids [25,42]. The anodic current started to increase at the onset potential of 0.7 V, then decreased steeply and recovered during the potential sweep (Fig. 2f inset). A Pt disc electrode was used as a control to show that this phenomenon is attributable to oxalic acid and unrelated to gold. As can be seen, in both cases, the oxalic acid decomposition (oxidation) started almost at the same potential window, evidencing that the process is rather oxalate-specific. Besides, in the case of NPG_{ox}, the oxidation of oxalic acid proceeds at a lower onset potential than in the case of bare gold, constituting that during the porous growth, the effective oxidation of oxalates occurs. However, the oxidation of oxalate ions does not initiate the porous gold formation, which starts only when the onset potential of oxygen evolution reaction (OER) is achieved (ca. 1.8 V).

3.3. Phase analysis of NPG_{ox}

The adsorption strength of target molecules on gold is governed by several factors, such as follows: chemical structure of the analyte, the nanosurface's composition, and the environment in which adsorption occurs [6]. Since the outermost surface of NPG_{ox} is most likely composed of (*i*) an oxide/hydroxide layer or (*ii*) adsorbed oxalate-gold ionic species, as revealed by electrochemical studies, the interactions between gold (Au^0) and its compounds (Au^{+x}) with target or modifier molecules may vary, and potentially affecting SERS activity. For example, Xue et al. have shown that the rupture force of Au–S bonds is higher when gold is oxidized [43].

To determine the surface composition and reveal the chemical state of gold in NPG_{ox}, X-ray photoelectron spectroscopy (XPS) was performed. The survey spectra of NPG_{ox} films reflected the presence of gold and carbon in the samples (Fig. 3a). The XPS spectra in the O1*s* region and its depth profiles revealed the presence of oxygen in recently fabricated NPG_{ox} (Fig. 3e and f).

However, this quantity reached only the trace level of 4.1 % (at.). The oxygen-containing gold phases disappeared after sputtering with Ar^+ ions for 30 s (Table S1). This implies the presence of oxidization states of gold only in the outermost layers of NPG_{ox}. The oxygen-comprised gold tends to spontaneously reduce, as confirmed by CV inspection with an aged NPG_{ox}. However, this transformation takes almost one week (in the air). Since the Au^0 is thermodynamically the most stable phase, we have thought that in the case of recently prepared NPG_{ox} nanosensors, the electrochemical reduction has to be accomplished by the shortened time required for this transduction. The XPS analysis was conducted to inspect the success of phase transformation in NPG_{ox} before and after electro-reduction. The narrow scans in the regions of Au 4*f* (recently prepared NPG_{ox}) shifted to higher binding energy compared with the electrochemically reduced specimens, implying a slight energy difference ($\Delta = 0.3$ eV) between each doublet (Fig. 3d). As for reduced NPG_{ox}, the deconvolution of Au 4*f* results in three $4f_{7/2}$ and $4f_{5/2}$ peaks at binding energy (BE) of 83.8, 84.3, and 85.0 eV. The two lower binding energies can be attributed to the photoelectrons emitted from metallic gold (Au^0). However, some traces of Au^{+3}, most likely related to the presence of Au_2O_3 and $Au(OH)_3$ [39,44], respectively, remain even after the electro-reduction (Fig. 3c). In the case of recently fabricated NPG_{ox}, the binding energy increases by 0.6 eV compared with pure gold (BE = 84 eV). This implies that the chemical state of gold is possibly affected by the nature of oxalates or their decomposed species originating during the NPG_{ox} fabrication process (Fig. 3b). These findings agree with those presented by Pramanik et al., where the shift of BE toward higher values appeared due to the charge transfer from Au core to phosphonium cations by forming gold nanoclusters. Authors assumed that the charge transfer makes Au atoms in gold clusters positively charged thus heightening their binding energy [45]. Following this logical sequence and considering the high charge density associated for NPG_{ox} reduction, along with the presence of ionic forms of gold in an aged electrolyte, we predict that a gold-carboxylate complex may be formed during the anodization of gold. Furthermore, the fitting of O1 *s* orbital reveals two low-intensity peaks at 532.0 and 533.4 eV that can be attributed to water molecules and surface-adsorbed species, most likely, gold-oxalates (or the products of their decomposition) complex (Fig. 3e). Besides, no apparent peaks in the 530–532 eV region were observed, revealing that black-colored NPG_{ox} nanosensors (Fig. 3 insets) mainly contain metallic gold (Au^0).

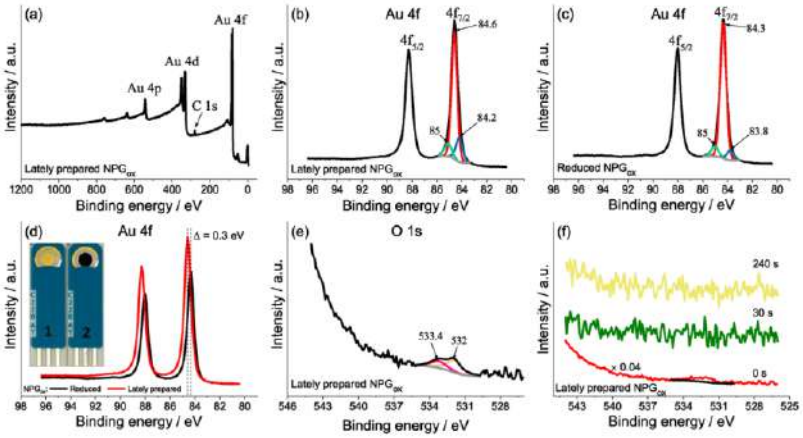

Fig. 3. XPS study of recently prepared and electrochemically reduced NPG$_{ox}$ nanosensors produced by anodic polarization of gold in a 0.3 M oxalic acid at 2.8 V for 30 min. XPS survey (a) and deconvoluted spectra of Au 4*f* (b, c, d), O1*s* (e), and depth profiles of O1*s* (f) after Ar^+ ion sputtering for 0 (bottom) to 240 s (top). Insets: photographs of gold-based SPE before (1) and after (2) anodic treatment.

3.4. SERS performances of 4-MBA on NPG$_{ox}$ nanosensors

The formation of nanoporous gold films is linked to the chemical or electrochemical dealloying of its alloys [36,46]. However, both techniques are limited by surface contamination caused by dissolving metal and the need for aggressive acids, which can damage the other electrode parts [47]. The anodic polarization of gold in nonaggressive organic acid solutions could benefit these circumstances and may be advantageous for producing NPG-based SERS nanosensors. Since each method has pros and cons, this research has critically inspected NPG nanosensors as potential SERS substrates. Notably, all SERS performances were examined using classic 4-mercaptobenzoic acid (4-MBA, 1 mM) dissolved in ethanol. All spectra were acquired at the excitation wavelength of 633 nm since it has shown the most significant enhancement of 4-MBA vibrational modes when the SERS intensity is compared to Raman intensity of 1590–1595 cm^{-1} modes (Fig. S9 a,b), and 4-MBA does not exhibit a resonance effect at these wavelengths [48].

Since the surface morphology of NPG strongly depends on the composition of the supporting electrolyte, as demonstrated in our recent work [25], the application of various porous gold electrodes formed in oxalic, tartaric, and citric acid for SERS was first investigated (Fig. S3 a–c). By comparing the most enhanced bands at 1077 and 1590 cm^{-1}, the NPG$_{ox}$ tends to be 5–15 times more effective than other SERS substrates. Based on these results, the remainder of the study aims to further develop and characterize NPG$_{ox}$ for SERS-based applications.

The NPG$_{ox}$ nanosensors exhibited a significant increase in Raman intensity compared with 2D gold (Fig. 4a curve #2 and #5). As a result, the two most prominent vibration bands assigned to the aromatic ring breathing (ν_{12}) and ring motion (ν_{8a}) of 4-MBA were found to be significantly amplified and appeared at 1077 and 1590 cm^{-1},

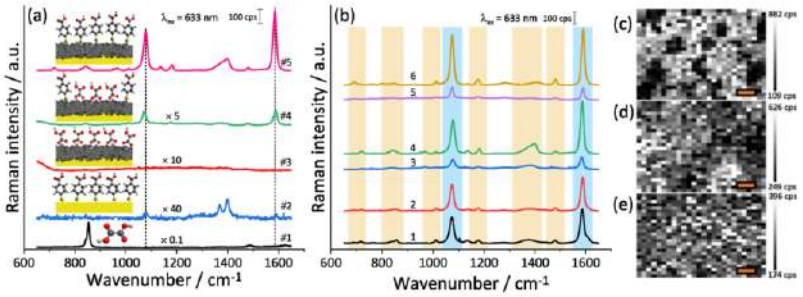

Fig. 4. Raman spectra (a) of oxalic acid (#1) and recently prepared NPG$_{ox}$ (#3) formed by anodic treatment of gold-based SPE in a 0.3 M oxalic acid. SERS spectra of 4-MBA on bare gold (#2) and NPG$_{ox}$ substrates after 2 h (#4) and 16 h (#5) of immobilization. SERS spectra (b) of 4-MBA on NPG$_{ox}$ produced on SPE gold (1–4) and gold disc (5, 6) electrodes after 2 h (1,3,5) and 16 h (2,4,6) of immobilization. Curves (1,2) correspond to SPE specimens aged in the air for 21 days. Curves (3–6) represent SPE and gold disc electrodes after electro-reduction. The photographs (c–e) correspond to the mapping of 1590 cm^{-1} spectral mode intensity obtained with NPG$_{ox}$ substrates formed on SPE (c, e) and gold disc (d) electrodes. The air-aged (c) and electro-reduced NPG$_{ox}$ on SPE (e) were examined. *Insets*: schematic illustrations of each particular specimen. Scale bar – 20 μm.

respectively. To estimate the surface potential of NPG_{ox} nanosensors for Raman scattering amplification, the enhancement factor (EF) was evaluated. The established EF for 4-MBA was 1.4×10^7 for 633 nm laser excitation, originating from mainly electromagnetic enhancement mechanism. This phenomenon occurs when the frequency of exiting laser radiation accompanies the frequency of collective oscillations of surface plasmons thus creating the electromagnetic field on NPG_{ox} surfaces [7]. Besides, the obtained EFs agree with those reported on nanoporous gold, silver, copper, and other composite nanomaterials (Table S2).

However, the high EF does not guarantee that it will be considered a promising SERS substrate. The surface chemistry in the context of "surface accessibility" to target molecules plays an important role [6]. An additional Raman analysis has been performed to study the NPG_{ox}'s surface nature. The intensive doublet band in the Raman spectrum of bulk oxalic acid (curve #1) appeared at 850 cm^{-1} and can be attributed to stretching vibrations of C–C bond coupled with C–O [20]. In contrast, the recently prepared NPG_{ox} substrate did not possess intense Raman bands in the tested window, as shown in Fig. 4a (curve #3). Interestingly, the SERS signal of 4-MBA molecules was nearly 20 times stronger after being immobilized for an extended period of 16 h. A similar behavior was reported in our previous study [25], in which the most efficient bioanode was developed by immobilizing a self-assembly monolayer (SAM) on NPG overnight. Given that S–Au bond formation is a rapid process, typically occurring within 1–2 h [49], we assume that the surface of NPG_{ox} is influenced by an unknown adsorbate, possibly carbonaceous species, which, as suggested by Nishio et al., may exist as a very thin layer [42]. This porous layer may compete further with 4-MBA molecules, as schematically presented in Fig. 4 insets. To prove this assumption, we have tested the SERS activity using air-aged NPG_{ox} nanosensors. In this case, the immersion time-dependent SERS activity disappeared, as displayed in Fig. 4b (curves 1 and 2). Furthermore, the prolonged immersion (more than 16 h) has no impact on the SERS activity. The thiol-gold interaction seems to be a favorable process that only requires an extended time for thiol chemisorption. Considering these results, we have thought that the electro-reduction of NPG_{ox} would lead to more rapid SAM development. However, NPG_{ox} formed on both types of gold electrodes (planar and SPE) exhibited similar behavior even after electro-reduction (Fig. 4 curves 3–6). Furthermore, this tendency is reflected in the mappings of 1590 cm^{-1} spectral mode obtained from the randomly selected scan over 180 × 180 μm areas on NPG_{ox} with the resolution of 2 μm (Fig. 4c–e). Air-aged NPG_{ox} substrates exhibited more than double the SERS intensities. However, the nonuniform SERS signal intensities across the scanned substrates indicate a lack of uniformity in the NPG_{ox}-based nanosensors. We estimated the relative standard deviations as follows: 49 % for air-aged NPG_{ox} on SPE (c), 28 % for electro-reduced NPG_{ox} on SPE (e), 31 % for NPG_{ox} on the gold disc electrode (d) and 53.5 % for commercial gold NPs-based SERS substrates.

To be more critical, we have further examined our fabricated NPG_{ox}-based SERS nanosensors and benchmarked them against commercial analogs. First, we collected SERS spectra across the NPG_{ox} surface (Fig. 5b) and compared them with commercially available gold-based SERS substrates (Fig. 5d), as presented schematically in Fig. 5a. Since the electro-dissolution occurs faster at the edges of the electrode due to the more rapid diffusion of ionic species [50], we expected slightly higher SERS performances at the edges of NPG_{ox}, especially in the case of prolonged anodic treatment. To examine the impact of anodic polarization time on SERS intensity, we investigated the series of NPG_{ox} substrates fabricated by anodization of gold with a stepwise increment of 5 min. Fig. 5f depicts the anodization time-dependent SERS performance of NPG_{ox} nanosensors.

The average intensity of the 1590 cm^{-1} band increased from 5 to 20 min, suggesting that during the prolonged anodic treatment of gold, the outermost 3D porous networks are formed by larger NPs with more effective electric field enhancement at 633 nm laser excitation. This statement was verified by comparing SEM images of NPG_{ox} films obtained after 5 s and 20 min anodization. At the initial stage of NPG_{ox} development (5 s), the average diameter of NPs was 6.5 times smaller ($Ø_{avg}$ ~ 5.8 nm) than after 20 min (Fig. S4 a–d, S10). Besides, the variation of normalized SERS intensity at 1590 cm^{-1} spectral mode was 25–30 % higher at the edge of electrodes, thus supporting our hypothesis (Fig. 5b). On the one hand, the SERS spectra uniformity increases significantly if the anodization of gold is carried out for a shorter time

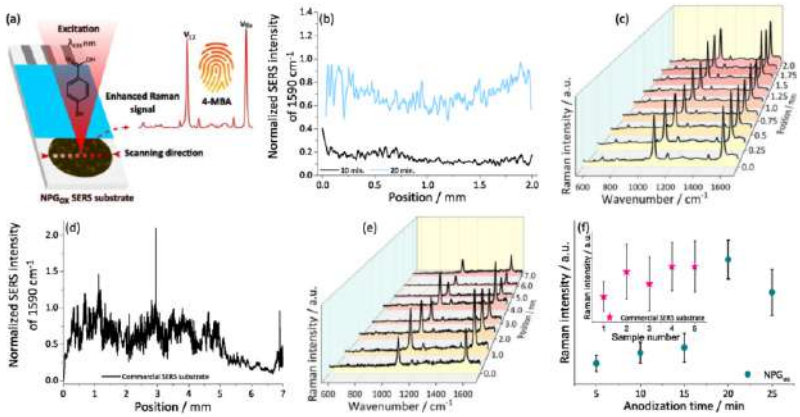

Fig. 5. Benchmarking of NPG_{ox}-based SERS nanosensors against commercial analogs. The schematic illustration (a) of Raman signal intensity (for 4-MBA) and detected points across the scanned SERS substrates. The normalized SERS intensities of 1590 cm^{-1} spectral mode were collected on NPG_{ox} fabricated by anodic treatment of gold for 10 and 20 min (b) and commercial SERS substrates (d). Their randomly selected SERS spectra distributions at different electrode positions are presented in (c) and (e). In (f), the anodic polarization time-dependent Raman intensity variations of 1590 cm^{-1} vibrational mode. *Inset*: SERS intensity distribution of 1590 cm^{-1} mode collected on randomly selected commercial substrates.

(10 min). On the other hand, the SERS intensity increased over 4 times when the 20-min anodization regime was selected. However, compared with the commercial analogs (Fig. 5d), the observed fluctuations of the SERS intensities were approximately 35–40 % lower. These values can be enhanced if we exclude up to 10–15 % of the NPG_{ox} films starting from the edge of the circuit, whereas the control of the NPG_{ox} formation process is complicated due to the edge effect [50]. Consequently, the nanoporous growth occurs faster over there, as revealed by SEM analysis of bare gold after the anodic treatment for 15 s (Fig. S4 b–c). The potential between commercially available and NPG_{ox} as SERS substrates can be seen in position-dependent 3D SERS spectra distributions (Fig. 5c–e). The imperfect SERS performances of commercial analogs are also verified by examination of repeatability with randomly selected specimens (Fig. 5 inset).

In summary, we have to conclude that none of the tested SERS substrates are ideal and match all requirements to be fulfilled as excellent SERS substrates. However, from a critical point of view, NPG_{ox}-based SERS substrates can advance commercial analogs, thus being suitable for SERS-based applications. Besides, their inexpensive fabrication may benefit the current production techniques. Considering the current prices of gold (2750 $/oz), thickness and diameter of printed gold layers on SPE (~600 nm and 4 mm), we have estimated that the cost of dual-functionalized NPG_{ox}-based SERS nanosensors (excluding the printing expense) would be ca. 0.015 $/item proving its cost-effective and sustainable manner.

3.5. Detection of DOX on NPG_{ox} nanosensors

To investigate the NPG_{ox}-based SERS nanosensor's suitability for the detection of practical-relevant molecules that do not form covalent bonds with gold, the anticancer drug doxorubicin (DOX) has been chosen. DOX is an excellent candidate for SERS detection since it contains a conjugated ring system, allowing it to possess relatively high Raman scattering cross-sections [9]. To date, DOX remains one of the forefront chemotherapeutic drugs for leukemic, sarcoma and malignant breast treatment [51]. However, it causes harmful side effects, including cardiotoxicity, which leads to cardiomyopathy and congestive heart failure [52], thus limiting its clinical applications. Monitoring DOX concentration in human blood during treatment will be advantageous and could minimize the potential harm to the patient during chemotherapy [7].

To avoid resonance effects due to DOX's electronic absorption in the visible region, we employed the 785 nm laser for the following SERS measurements [53]. DOX has a characteristic Raman spectrum with skeletal deformations and ring stretch-associated vibrations. However, detecting DOX in aqueous solutions by Raman spectroscopy is challenging even at millimolar level concentrations (Fig. 6a). At this point, the surfaces with highly dense aggregated NPs (i.e., SERS substrates) have been used to amplify the weak Raman signals and increase the sensitivity. DOX detection on NPG_{ox} nanosensors (recently fabricated or after electro-reduction) enhanced its limit of detection (LOD), but only up to 1 mM (data not shown). This suggests that DOX adsorption on NPG_{ox} competes with other interactions, possibly related to oxalate-gold conjugate. Recently, Curry et al. have extensively studied the gold-DOX interactions by measuring fluorescence and experimentally proved that DOX adsorption on citrate-capped Au NPs is driven by cation-π-interactions with the adsorbed Au^{+} on gold surfaces [54]. Considering these findings, we assumed that electrostatic forces of negatively charged oxalate (or its decomposed species) and Au^{+} on NPG_{ox} may favor the oxalate-gold interaction against DOX adsorption, especially in diluted solutions (less than 1 mM). To improve DOX's LOD, we have modified NPG_{ox} nanosensors by covalently bound MHA and TGA thiol molecules. The prepared substrates exhibited higher SERS activity, allowing the detection of DOX at concentrations from 10 μM to 10 mM (Fig. 6b and c). The linear fit was implemented on the logarithmic coordinates of the averaged peak intensities at 1082 and 1210 cm^{-1} (assigned to skeletal deformations and ring stretching symmetric vibrations, respectively) as a function of the DOX molar concentration.

In order to benchmark the performances of NPG_{ox}-based SERS nanosensors, we compared their SERS detection capability for DOX with commercially available SERS substrates.

Fig. 6d and e depict the concentration-dependent SERS spectra of DOX adsorbed at commercial gold-based substrates (Fig. S6 h) and the calibration curves of their most intense vibration bands, which follow

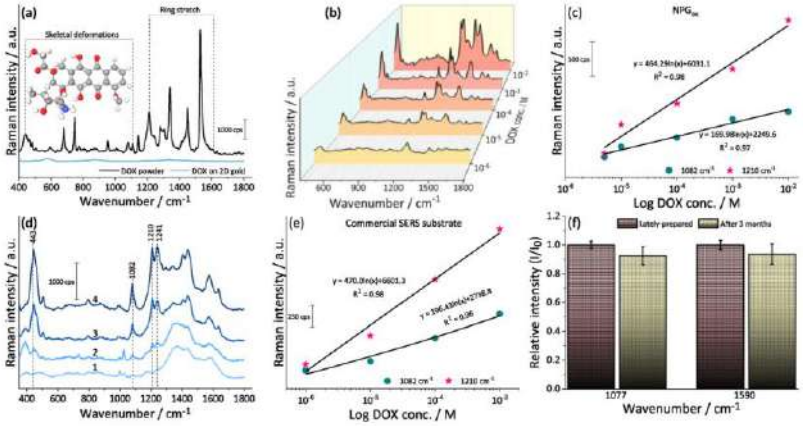

Fig. 6. Detection of DOX on NPG_{ox} and commercial SERS substrates. Raman spectra of DOX powder and SERS spectrum of 1 mM of DOX on 2D gold electrode (a). Series of SERS spectra of DOX adsorbed on MHA and TGA (2.5 mM of each) modified NPG_{ox} (b) and commercial (d) substrates at different concentrations. Plots 1–4 correspond to the DOX concentration of 10^{-6} to 10^{-3} M, respectively. The calibration curves for DOX detection on NPG_{ox} (c) and commercial (e) SERS substrates. In (f), the stability of recently prepared and stored in ambient conditions for 3 months 4-MBA modified NPG_{ox} nanosensors. Measurements were carried out using hight throughput Tornado HyperFlux spectrometer equipped with 785 nm laser excitation.

the linear regression within the concentration ranging between 10^{-3} and 10^{-6} M. Comparing the SERS performances of both substrates showed that our NPG_{ox} nanosensors exhibited SERS activity comparable to their commercial analogs. Since the proposed NPG_{ox} nanosensors were modified with SAM, their chemical stability affects the lifetime of the SERS substrate as a whole. The control experiments with 4-MBA provide the experimental evidence that after storage them for 3 months under ambient conditions, the Raman intensities at 1077 and 1590 cm^{-1} decreased only by 6.4–7.4 %, indicating an acceptable long-term stability (Fig. 6f). Regarding excellent stability, gold-based SERS substrates are preferred compared to others (i.e., Ag), whereas the SERS nanosensors must be stored at inert conditions [11].

By summarising the results, we can conclude that our proposed NPG_{ox} nanosensors exhibited equivalent (compared to the commercial analogs) SERS performances toward DOX detection. We believe that the inexpensive and easy-to-scale fabrication of NPG_{ox} nanosensors renders them suitable for dual-functionalized nanostructured electrode production for electrochemical and SERS-based applications.

4. Conclusions

This research presents an inexpensive, relatively fast, one-step, and easy-to-scale path for producing gold-based (NPG_{ox}) SERS-active nanosensors. The proposed method relies on 2D gold anodic treatment in an oxalate-containing solution. This results in uniformly distributed, 38 nm diameter, interconnected oval-shaped nanostructures, ensuring 3D porous film development. The phase analysis confirms that NPG_{ox} nanosensors comprise metallic gold (Au^0). The SERS performances of NPG_{ox} substrates were critically investigated using traditional 4-MBA molecules and compared with the commercially available analogs. The designed NPG_{ox} substrates demonstrated high Raman signal enhancement with an EF of 1.4×10^7 at 633 nm laser excitation. The rapid and quantitative detection of the anticancer drug doxorubicin was performed using fabricated NPG_{ox} nanosensors, thus evidencing their practical applicability to assess the concentration of pharmaceutical drugs in aqueous media. The additional modification of NPG_{ox} with self-assembly monolayers allows to extend the LOD by two orders of magnitude, thus enabling the detection of DOX at the concentration from 10 μM to 10 mM. Besides, the fabricated SERS nanosensors exhibited prominent long-term stability of at least 3 months, losing the intensity of 4-MBA by up to 6.4–7.4 %. Furthermore, it was demonstrated that NPG_{ox} outperformed commercial SERS substrates by offering lower fabrication costs and greater SERS amplification stability across the sensing electrode, making it a promising candidate for practical applications.

CRediT authorship contribution statement

Rokas Žalneravicius: Writing – original draft, Validation, Methodology, Writing – review & editing, Visualization, Supervision, Conceptualization. **Martynas Talaikis:** Writing – review & editing, Investigation, Data curation, Supervision, Formal analysis. **Vaclovas Klimas:** Writing – review & editing, Conceptualization. **Skomantas Serapinas:** Visualization, Writing – review & editing, Formal analysis. **Marius Butkevičius:** Writing – review & editing, Formal analysis, Visualization. **Jūratė Vaičiūnienė:** Writing – review & editing, Formal analysis. **Augustas Morkvėnas:** Formal analysis. **Vitalijus Karabanovas:** Conceptualization, Writing – review & editing. **Gediminas Niaura:** Conceptualization, Writing – review & editing. **Arūnas Jagminas:** Writing – review & editing, Conceptualization, Resources. **Marius Dagys:** Writing – review & editing, Funding acquisition, Resources, Conceptualization.

Declaration of competing interest

The authors declare that they have no known competing financial interests or personal relationships that could have appeared to influence the work reported in this paper.

Acknowledgements

This project has received funding from the Research Council of Lithuania (LMTLT), agreement No P-PD-22-079. We are grateful to dr. Vitalija Jasulaitienė and dr. Arnas Naujokaitis for the XPS and SEM inspection, respectively.

Appendix A. Supplementary data

Supplementary data to this article can be found online at https://doi.org/10.1016/j.mtchem.2025.102849.

Data availability

Data will be made available on request.

References

[1] M. Fleischmann, P.J. Hendra, A.J. McQuillan, Raman spectra of pyridine adsorbed at a silver electrode, Chem. Phys. Lett. 26 (1974) 163–166, https://doi.org/10.1016/0009-2614(74)85388-1.

[2] D.L. Jeanmaire, R.P. van Duyne, Surface Raman spectroelectrochemistry. Part I. Heterocyclic, aromatic, and aliphatic amines adsorbed on the anodized silver electrode, J. Electroanal. Chem. 84 (1977) 1–20, https://doi.org/10.1016/S0022-0728(77)80224-6.

[3] M.G. Albrecht, J.A. Creighton, Anomalously intense Raman spectra of pyridine at a silver electrode, J. Am. Chem. Soc. 99 (1977) 5215–5217, https://doi.org/10.1021/ja00457a071.

[4] N. Khinevich, M. Juodėnas, A. Tamulevičienė, T. Tamulevičius, M. Talaikis, G. Niaura, S. Tamulevicius, Wavelength-tailored enhancement of Raman scattering on a resonant plasmonic lattice, Sensor. Actuator. B Chem. 394 (2023) 134418, https://doi.org/10.1016/j.snb.2023.134418.

[5] S.S. Sinha, S. Jones, A. Pramanik, P.C. Ray, Nanoarchitecture based SERS for biomolecular fingerprinting and label-free disease markers diagnosis, Acc. Chem. Res. 49 (2016) 2725–2735, https://doi.org/10.1021/acs.accounts.6b00384.

[6] Y. Xu, Y. Zhang, C. Li, Z. Ye, S.E.J. Bell, SERS as a probe of surface chemistry enabled by surface-accessible plasmonic nanomaterials, Acc. Chem. Res. 56 (2023) 2072–2083, https://doi.org/10.1021/acs.accounts.3c00207.

[7] L. Golubewa, A. Klimovich, I. Timoshchenko, Y. Padrez, M. Fetisova, H. Rehman, P. Karvinen, A. Selskis, S. Adomavičiūtė-Grabusovė, I. Manulaitienė, A. Ramanavicius, R. Karpicz, T. Kulahava, Y. Svirko, P. Kuzhir, Stable and reusable lace-like black silicon nanostructures coated with nanometer-thick gold films for SERS-based sensing, ACS Appl. Nano Mater. 6 (2023) 4770–4781, https://doi.org/10.1021/acsanm.3c00281.

[8] Z. Ye, C. Li, Y. Xu, S.E.J. Bell, Exploiting the chemical differences between Ag and Au colloids allows dramatically improved SERS detection of 'non-adsorbing' molecules, Analyst 144 (2019) 448–453, https://doi.org/10.1039/C8AN01927D.

[9] F. Sun, H.C. Hung, A. Sinclair, P. Zhang, T. Bai, D.D. Galvan, P. Jain, B. Li, S. Jiang, Q. Yu, Hierarchical zwitterionic modification of a SERS substrate enables real-time drug monitoring in blood plasma, Nat. Commun. 7 (2016) 1–9, https://doi.org/10.1038/ncomms13437.

[10] T.D. Payne, S.J. Klawa, T. Jian, S.H. Kim, M.J. Papanikolas, R. Freeman, Z. D. Schultz, Catching COVID: engineering peptide-modified surface-enhanced Raman spectroscopy sensors for SARS-CoV-2, ACS Sens. 6 (2021) 3436–3444, https://doi.org/10.1021/acssensors.1c01344.

[11] H. Li, E. Dumont, R. Slipets, T. Therkleff, A. Boisen, G.A. Sotiriou, Democratizing robust SERS nano-sensors for food safety diagnostics, Chem. Eng. J. 470 (2023) 144023, https://doi.org/10.1016/j.cej.2023.144023.

[12] K. Chang, Y. Zhao, M. Wang, Z. Xu, L. Zhu, L. Xu, Q. Wang, Advances in metal-organic framework-plasmonic metal composites based SERS platforms: engineering strategies in chemical sensing, practical applications and future perspectives in food safety, Chem. Eng. J. 459 (2023) 141539, https://doi.org/10.1016/j.cej.2023.141539.

[13] K. Sanger, O. Durucan, K. Wu, A.H. Thilsted, A. Heiskanen, T. Rindzevicius, M. S. Schmidt, K. Zór, A. Boisen, Large-scale, lithography-free production of transparent nanostructured surface for dual-functional electrochemical and SERS sensing, ACS Sens. 2 (2017), https://doi.org/10.1021/acssensors.7b00783, 1869–187.

[14] T. Dai, Z. Xiao, D. Shan, A. Moreno, H. Li, M. Prakash, N. Banaei, J. Rao, Culture-independent multiplexed detection of drug-resistant bacteria using surface-enhanced Raman scattering, ACS Sens. 8 (2023) 3264–3271, https://doi.org/10.1021/acssensors.3c01345.

[15] I. Aleknavičienė, E. Pabreža, M. Talaikis, M. Jankunec, G. Račiukaitis, Low-cost SERS substrate featuring laser-ablated amorphous nanostructure, Appl. Surf. Sci. 571 (2022) 151248, https://doi.org/10.1016/j.apsusc.2021.151248.

[16] T. Itoh, M. Procházka, Z.C. Dong, W. Ji, Y.S. Yamamoto, Y. Zhang, Y. Ozaki, Toward a new era of SERS and TERS at the nanometer scale: from fundamentals to

innovative applications, Chem. Rev. 123 (2023) 1552–1634, https://doi.org/10.1021/acs.chemrev.2c00316.
[17] M.J. Natan, Concluding remarks: surface enhanced Raman scattering, Faraday Discuss 132 (2006) 321–328, https://doi.org/10.1039/B601494C.
[18] Research and Markets USA, Surface-enhanced Raman spectroscopy (SERS) substrate market report: trends, forecast and competitive analysis to 2030. https://www.researchandmarkets.com, 2024. (Accessed 13 January 2025).
[19] V. Amendola, S. Scaramuzza, L. Litti, M. Meneghetti, G. Zuccolotto, A. Rosato, E. Nicolato, P. Marzola, G. Fracasso, C. Anselmi, M. Pinto, M. Colombatti, Magneto-plasmonic Au-Fe alloy nanoparticles designed for multimodal SERS-MRI-CT imaging, Small 10 (2014) 2476–2486, https://doi.org/10.1002/smll.201303772.
[20] V. Mohaček-Grošev, J. Grdadolnik, J. Stare, D. Hadži, Identification of hydrogen bond modes in polarized Raman spectra of single crystals of α-oxalic acid dihydrate, J. Raman Spectrosc. 40 (2009) 1605–1614, https://doi.org/10.1002/jrs.2308.
[21] J. Plou, P.S. Valera, I. García, C.D.L. De Albuquerque, A. Carracedo, L.M. Liz-Marzán, Prospects of surface-enhanced Raman spectroscopy for biomarker monitoring toward precision medicine, ACS Photonics 9 (2022) 333–350, https://doi.org/10.1021/acsphotonics.1c01934.
[22] D. Raj, M. Pulumbo, G. Fiore, F. Celegato, F. Scaglione, P. Rizzi, Sustainable nanoporous gold with excellent SERS performances, Mater. Chem. Phys. 293 (2022) 126883, https://doi.org/10.1016/j.matchemphys.2022.126883.
[23] Z. Xu, A.M. Erinomo, Z. Dan, F. Qin, H. Chang, Flexible SERS substrates with gradient porous Cu structure dealloying from the thermal diffusion couples of Al/Cu stacking foils, Chem. Eng. J. 490 (2024) 151871, https://doi.org/10.1016/j.cej.2024.151871.
[24] K. Nishio, H. Masuda, Anodization of gold in oxalate solution to form a nanoporous black film, Angew. Chem. Int. Ed. 50 (2011) 1603–1607, https://doi.org/10.1002/anie.201005706.
[25] R. Žalnėravičius, A. Naujokaitis, V. Jasulaitienė, R. Rutkienė, R. Meškys, M. Dagys, A 2D-to-3D morphology transitions of gold in organic acid electrolytes: characterization and application in bioanode design, Appl. Surf. Sci. 642 (2024) 158654, https://doi.org/10.1016/j.apsusc.2023.158654.
[26] F. Scaglione, L. Battezzati, P. Rizzi, Breaking down SERS detection limit: engineering of a nanoporous platform for high sensing and technology, Nanomaterials 12 (2022) 1737, https://doi.org/10.3390/nano12101737.
[27] Y. Yang, Y. Xia, W. Huang, J. Zheng, Z. Li, Fabrication of nano-network gold films via anodization of gold electrode and their application in SERS, J. Solid State Electrochem. 16 (2012) 1733–1739, https://doi.org/10.1007/s10008-011-1600-8.
[28] S. Trasatti, O.A. Petrii, Real surface area measurements in electrochemistry, Pure Appl. Chem. 63 (1991) 711–734, https://doi.org/10.1351/pac199163050711.
[29] C.J. Orendorff, A. Gole, T.K. Sau, C.J. Murphy, Surface-enhanced Raman spectroscopy of self-assembled monolayers: sandwich architecture and nanoparticle shape dependence, Anal. Chem. 77 (2005) 3261–3266, https://doi.org/10.1021/ac048176x.
[30] S.E.J. Bell, G. Charron, E. Cortés, J. Kneipp, M.L. de la Chapelle, J. Langer, M. Procházka, V. Tran, S. Schlücker, Towards reliable and quantitative surface-enhanced Raman scattering (SERS): from key parameters to good analytical practice, Angew. Chem. Int. Ed. 59 (2020) 5454–5462, https://doi.org/10.1002/anie.201908154.
[31] Y. Deng, W. Huang, X. Chen, Z. Li, Facile fabrication of nanoporous gold film electrodes, Electrochem. Commun. 10 (2008) 810–813, https://doi.org/10.1016/j.elecom.2008.03.003.
[32] V. Maurice, P. Marcus, Structure, passivation and localised corrosion of metal surfaces, in: S.I. Pyun, J.W. Lee (Eds.), Progress in Corrosion Science and Engineering I. Modern Aspects of Electrochemistry, Springer., New York, 2009, pp. 1–58, https://doi.org/10.1007/978-0-387-92263-8_1.
[33] D. Sazou, M. Pagitsas, On the onset of current oscillations at the limiting current region emerged during iron electrodissolution in sulfuric acid solutions, Electrochim. Acta 51 (2006) 6281–6296, https://doi.org/10.1016/j.electacta.2006.04.010.
[34] P. Marcus, V. Maurice, H.H. Strehblow, Localized corrosion (pitting): a model of passivity breakdown including the role of the oxide layer nanostructure, Corros. Sci. 50 (2008) 2698–2704, https://doi.org/10.1016/j.corsci.2008.06.047.
[35] V. Klimas, V. Pukštas, I. Vrublevsky, K. Chernyakova, A. Jagminas, Fabrication and characterization of anodic films onto the type-304 stainless steel in glycerol electrolyte, J. Phys. Chem. C 117 (2013) 20730–20737, https://doi.org/10.1021/jp407028n.
[36] G. Wittstock, M. Bäumer, W. Dononelli, T. Klüner, L. Lührs, C. Mahr, L. V. Moskaleva, M. Oezaslan, T. Risse, A. Rosenauer, A. Staubitz, J. Weissmüller, A. Wittstock, Nanoporous gold: from structure evolution to functional properties in catalysis and electrochemistry, Chem. Rev. 123 (2023) 6716–6792, https://doi.org/10.1021/acs.chemrev.2c00751.
[37] S. Yang, D.G.H. Hetterscheid, Redefinition of the active species and the mechanism of the oxygen evolution reaction on gold oxide, ACS Catal. 10 (2020) 12582–12589, https://doi.org/10.1021/acscatal.0c03548.
[38] M. Pourbaix, H. Zhang, A. Pourbaix, Presentation of an Atlas of chemical and electrochemical equilibria in the presence of a gaseous phase, Mater. Sci. Forum 251 (1997) 143–148, https://doi.org/10.4028/www.scientific.net/MSF.251-254.143.
[39] K. Juodkazis, J. Juodkazytė, B. Sebeka, A. Lukinskas, Cyclic voltammetric studies on the reduction of a gold oxide surface layer, Electrochem. Commun. 1 (1999) 315–318, https://doi.org/10.1016/S1388-2481(99)00062-4.
[40] P.M.S. Tchekwagep, R. Žalneravičius, C.P. Nansen-Njiki, E. Ngameni, T. Arnebrant, T. Ruzgas, Electrochemical insights into layered assemblies of silver nanoparticles, poly-L-lysine, and bovine serum albumin, Electroanalysis 36 (2024) 1–12, https://doi.org/10.1002/elan.202400031.
[41] G.J.A. Vidugiris, V.J. Razumas, A.A. Drungilienė, J.J. Kulys, Complex formation of amino acids and proteins with silver ions, Bioelectrochem. Bioenerg. 19 (1988) 513–520, https://doi.org/10.1016/0022-0728(88)87086-4.
[42] K. Nishio, H. Masuda, Formation of nanoporous anodic gold oxide films in carboxylic acids and spontaneous reduction to nanoporous gold, Bull. Chem. Soc. Jpn. 86 (2013) 1144–1150, https://doi.org/10.1246/bcsj.20130142.
[43] Y. Xue, X. Li, H. Li, W. Zhang, Quantifying thiol-gold interactions towards the efficient strength control, Nat. Commun. 5 (2014) 4348, https://doi.org/10.1038/ncomms5348.
[44] B.V. Crist, Handbook of Monochromatic XPS Spectra, John Wiley, Chichester, 2000.
[45] G. Pramanik, J. Humpolíčková, J. Valenta, P. Kundu, S. Bals, P. Bour, M. Dračínský, P. Cígler, Gold nanoclusters with bright near-infrared photoluminescence, Nanoscale 10 (2018) 3792–3798, https://doi.org/10.1039/C7NR06050E.
[46] P. Bollella, Porous gold: a new frontier for enzyme-based electrodes, Nanomaterials 10 (2020) 722, https://doi.org/10.3390/nano10040722.
[47] D. Zhang, T. Wang, M. Zhang, Y. Miao, Q. Feng, X. Chen, Z. Hu, L. Ma, J. Qi, F. Wei, F. Dang, P. Cao, W. Zhang, Y. Sui, Application of morphology and phase design of dealloying method in supercapacitor, J. Alloys Compd. 927 (2022) 166974, https://doi.org/10.1016/j.jallcom.2022.166974.
[48] R. Chen, S. Li, Y. Sun, B. Huo, Y. Xia, Y. Qin, S. Li, B. Shi, D. He, J. Liang, Z. Gao, Surface-enhanced Raman spectroscopy aptasensor for simultaneous determination of ochratoxin A and zearalenone using Au@Ag core-shell nanoparticles and gold nanorods, Microchim. Acta 188 (2021), https://doi.org/10.1007/s00604-021-04919-6.
[49] A. Bard, R. Rondon, D.T. Marquez, A.E. Lanterna, J.C. Scaiano, How fast can thiols bind to the gold nanoparticle surface? Photochem. Photobiol. 94 (2018) 1109–1115, https://doi.org/10.1111/php.13010.
[50] D.K. Cope, The edge effect for planar electrodes, J. Electroanal. Chem. 439 (1997) 7–27, https://doi.org/10.1016/S0022-0728(97)00367-7.
[51] S. Sritharan, N. Sivalingam, A comprehensive review on time-tested anticancer drug doxorubicin, Life Sci. 278 (2020) 119527, https://doi.org/10.1016/j.lfs.2021.119527.
[52] Y. Chen, Y. Wan, Y. Wang, H. Zhang, Z. Jiao, Anticancer efficacy enhancement and attenuation of side effects of doxorubicin with titanium dioxide nanoparticles, Int. J. Nanomed. 6 (2011) 2321–2326, https://doi.org/10.2147/IJN.S25460.
[53] N. Andhariya, B. Chudasama, R.V. Mehta, R.V. Upadhyay, Biodegradable thermoresponsive polymeric magnetic nanoparticles: a new drug delivery platform for doxorubicin, J. Nanoparticle Res. 13 (2011) 1677–1688, https://doi.org/10.1007/s11051-010-9921-6.
[54] D. Curry, A. Cameron, B. MacDonald, C. Nganou, H. Scheller, J. Marsh, S. Beale, M. Lu, Z. Shan, R. Kaliaperumal, H. Xu, M. Servos, C. Bennett, S. MacQuarrie, K. D. Oakes, M. Mkandawire, X. Zhang, Adsorption of doxorubicin on citrate-capped gold nanoparticles: insights into engineering potent chemotherapeutic delivery systems, Nanoscale 7 (2015) 19611–19619, https://doi.org/10.1039/C5NR05856K.

4. Publication IV

Serapinas, S.; Stakelytė, D.; Tučinskytė, K.; Tomkuvienė, M.; Dagys, M.; Ratautas, D. Constant Temperature Electrochemical Biosensor for SNP Detection in Human Genomic DNA Based on DNA Melting Analysis. *ACS Sens.* **2025**, *10* (9), 6819–6827. https://doi.org/10.1021/acssensors.5c01577.

ACS SENSORS

pubs.acs.org/acssensors

Article

Constant Temperature Electrochemical Biosensor for SNP Detection in Human Genomic DNA Based on DNA Melting Analysis

Skomantas Serapinas,* Deimantė Stakelytė, Kornelija Tučinskytė, Miglė Tomkuvienė, Marius Dagys, and Dalius Ratautas*

Cite This: https://doi.org/10.1021/acssensors.5c01577

Read Online

ACCESS | Metrics & More | Article Recommendations | Supporting Information

ABSTRACT: Detection of single-nucleotide polymorphisms (SNPs) is critical in both bioanalytical science and clinical diagnostics. We present an electrochemical biosensor capable of SNP detection in human genomic DNA immediately following a polymerase chain reaction, eliminating the need for temperature gradients. The biosensor employs a "sandwich" hybridization format in which a target DNA strand binds to an electrode-anchored probe and is interrogated by two allele-specific reporters. By analyzing the kinetic differences in melting rates (k_d) between perfect match (PM) and mismatch (MM) duplexes at constant temperature, we achieved statistically significant differentiation of homozygous and heterozygous alleles ($>2\sigma$, $n = 7$). As proof of concept, the biosensor was applied to detect the *CYP2C19*17* allele in human saliva samples ($n = 6$), with results confirmed using sequencing. Additionally, melting-rate-derived Gibbs free energy differences allowed for the identification of previously undetected mismatches, suggesting a novel pathway for electrochemical sequencing.

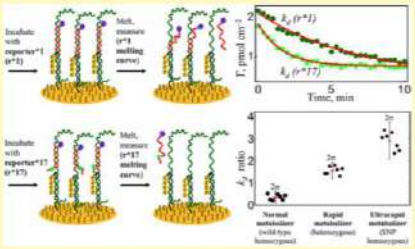

KEYWORDS: *single-nucleotide polymorphism, gold, biosensor, melting, CYP2C19*

Single-nucleotide polymorphisms (SNPs) are the most common form of genetic variation in the human genome, typically occurring once every ~300 base pairs and having a minor allele frequency greater than 1%.[1] Over 84 million SNPs have been identified to date,[2] and while most are harmless, certain variants are linked to diseases,[3] aging[4] and drug metabolism.[5,6]

One clinically significant example is the *CYP2C19* gene, located on chromosome 10, which encodes the cytochrome P450 2C19 enzyme responsible for metabolizing a wide range of xenobiotics. This enzyme is predominantly expressed in the liver, stomach, small intestine, and duodenum.[7] Clinically relevant variants of *CYP2C19* include loss-of-function (*2–*8), wild-type (WT) (*1), and gain-of-function (*17) alleles. The *17 allele, with a global frequency ranging between 3 and 21%,[8] affects the metabolism of drugs such as clopidogrel,[9,10] esomeprazole,[11,12] and voriconazole,[13,14] potentially leading to reduced drug efficiencies, treatment unpredictability, and increased toxicity.[15] Individuals with a heterozygous (*1/*17) or homozygous (*17/*17) genotype are considered rapid or ultrarapid metabolizers, respectively. While research have varied in their stance on *CYP2C19* genotyping,[16] recent 2024 American Heart Association guidelines recommendations endorse genetic testing for patients undergoing percutaneous coronary intervention or with coronary artery disease.[17]

Electrochemical biosensors are attractive devices for point-of-care determination of analytes of interest. Traditionally, electrochemical biosensors were created for the detection of metabolites such as glucose,[18] alcohols,[19] and L-amino acids[20] usually involving enzymatic catalysts for recognition. Later, biosensors for DNA and RNA detection were also designed and were typically based on DNA or RNA hybridization. For example, Sebuyoya et al. demonstrated an electrochemical biosensor that takes advantage of isothermal LAMP amplification and room temperature hybridization (~200 bp fragments) for HPV16/18 detection in cervical samples.[21] Although methods such as TaqMan assays, ddPCR, and SNP microarrays are cost-effective for SNP detection, there remains a strong demand for rapid, low-cost, point-of-care technologies.

SNP detection poses a particular challenge due to the minimal difference between wild-type and variant sequences.[22] Nevertheless, electrochemical biosensors have been developed for SNP detection. Xu et al. reported an electrochemical biosensor for the detection of epidermal growth factor receptor

Received: May 8, 2025
Revised: June 23, 2025
Accepted: June 25, 2025

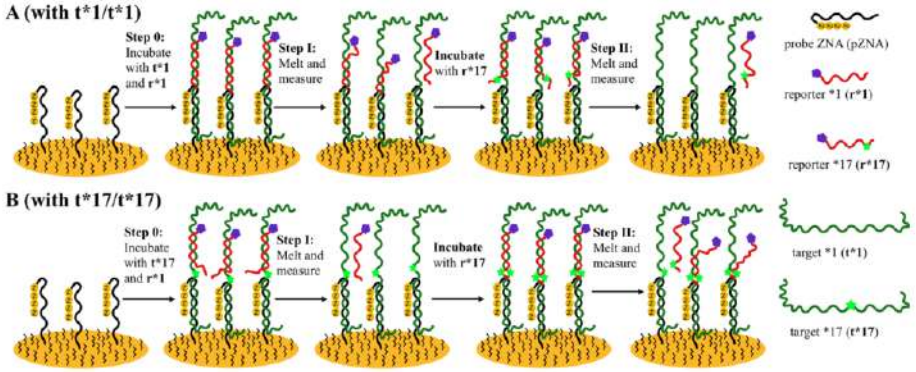

Figure 1. Principle of SNP sensor operation. (A) For the wild-type target (t*1/t*1). At Step 0, the ZNA probe-modified gold electrode is incubated with t*1 and r*1. At Step I, the electrode is placed at an increased fixed temperature, inducing the melting of the r*1−t*1 duplex. Melting kinetics are registered using linear sweep voltammetry (LSV), observing a decrease in the r*1 methylene blue redox signal. Afterward, the r*1-free electrode is incubated with r*17 and at Step II again placed at an increased fixed temperature to observe and record the melting kinetic curve. (B) For SNP target (t*17/t*17). The procedure is the same as in panel (A). After step I and step II, the melting-rate constants k_d (r*1) and k_d (r*17) and their ratios k_d (r*1)/ k_d (r*17) are determined.

exon 19 SNP.[23] They tackled the problem of amplicon (dsDNA) renaturation with phosphorylated primers and lambda exonuclease digestion. Ortiz et al. demonstrated a biosensor for the detection of SNPs associated with rifampicin resistance in *Mycobacterium tuberculosis* using solid-phase primer elongation with ferrocene-labeled nucleotides.[24] This measurement is "monoploid", where an electrode array simultaneously measures all 4 possible variants of the point-mutation and compares them. The authors develop their own ferrocenylated master mix, and the discrimination between genes is performed by Klenow polymerase, isothermally on solid phase. Liu et al. showed an SNP analysis platform using multiplexed electrochemical biosensors, highlighting the need to detect several SNPs at once (e.g., *CYP2C19* C680T and G681A).[25] Han et al. demonstrated a biosensor applicable also to SNP detection. Upon target recognition, dual-DNA–functionalized AuNPs hybridized and bound to SWCNT-DNA via linker strands, forming 3D nanoclusters with apparent electrochemical signals.[26] Xiao et al. reported a system where an electrochemical sensor was designed for SNP detection based on a triple-stem hairpin DNA probe.[27] Among these approaches, melting curve analysis remains one of the most widely adopted approaches for distinguishing SNPs. Several notable electrochemical sensors for SNP detection were designed by using this approach. Yang et al. developed a sensor for SNPs in the apolipoprotein E gene, related to Alzheimer's disease.[28] The sensor detected SNPs by measuring differences in redox current changes caused by gradually increasing the temperature of WT- and SNP-containing target sequences hybridized to a redox-labeled probe. In this case, a 61-bp target sequence quenches the probe-connected methylene blue (MB) signal. To circumvent the thermal liability of the Au−S bond, the authors employ a trithiolated DNA probe. Chahin et al. showed a similar biosensing platform.[29] Biosensor utilized ferrocene (Fc)-labeled primer to produce Fc-labeled PCR amplicon. After hybridization with the probe on the electrode surface, the electrode array was subjected to a gradual temperature increase during which the Fc electrochemical signal was measured. The same group also recently demonstrated a biosensing platform, focusing on automation capable to detect several SNPs from human blood.[30]

In this study, we present an improved electrochemical biosensor that eliminates the need for temperature gradients, a major limitation in previous systems. Instead, we optimized the electrode and assay conditions to operate at a constant temperature, enabling SNP detection directly after PCR without additional processing. The biosensor discriminates between wild-type and variant sequences based on differences in melting kinetics. Furthermore, we introduced ZNA-modified probes to enhance electrochemical signal quality. Finally, we show that kinetic melting profiles and derived Gibbs free energy values correlate with the theoretical predictions based on mismatch (MM) position, indicating a potential for broader applications, including the identification of unexpected SNPs within target sequences.

RESULTS AND DISCUSSION

Principle of Operation of the SNP Sensor. For SNP sensing, we used planar gold electrodes with their surface modified using a ZNA-modified probe (pZNA, nt 21) chemisorbed to the gold surface via thiol chemistry, together with mercaptohexanol for surface blocking. The first iteration sensors were designed using standard DNA probes and performed well with shorter synthetic DNA targets (0−1 nt 5′ overhangs). However, signal transduction was significantly deteriorated when using longer PCR-amplified targets with 14−15 nt 5′ and 4 nt 3′ overhangs resulting from primer design. To overcome this, we have replaced the DNA probe with a 4-spermine unit-containing zip nucleic acid (ZNA-4) probe (formal charge is −10) (see Supporting Information (SI), Probe selection, Figure S1). The ZNA modification was expected to neutralize excess negative charge on the electrode surface, facilitating access of the negatively charged Atto-MB-labeled reporter strand. Previous studies have reported that

https://doi.org/10.1021/acssensors.5c01577
ACS Sens. XXXX, XXX, XXX−XXX

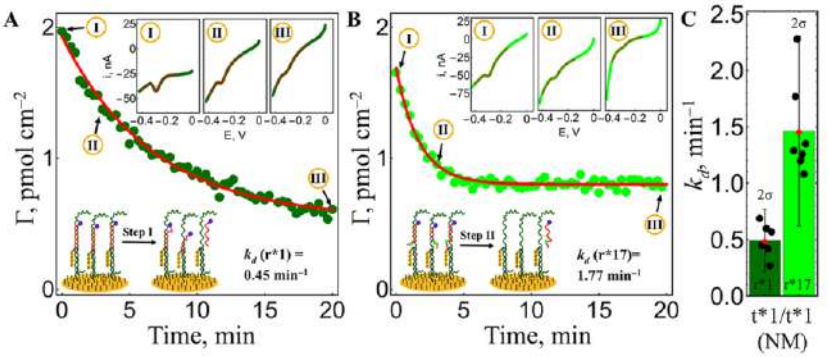

Figure 2. Analysis of the SNP sensor electrode incubated with the NM target. (A) Melting kinetics measured during step I from redox peaks of MB-labeled reporter r*1 using LSV (50 mV s^{-1}). Inset: LSV curves at t = 0 (I), t = 3 min (II), and t = 20 min (III). Fitting of the melting kinetics curve to a model to determine the k_d value for r*1. (B) Melting kinetics were measured during step II from redox peaks of MB-labeled reporter r*17 using LSV. The inset shows LSV curves at t = 0 (I), t = 3 min (II), and t = 20 min (III). Fitting of the melting kinetics curve to a model to determine the k_d value for r*17. (C) k_d values for reporters r*1 (dark green) and r*17 (light green) obtained from 7 independent electrodes. Error bars show confidence intervals (±2 standard deviations (SD), 2σ).

such charge neutralization reduces ZNA oligonucleotide solubility[31] and increases duplex melting temperatures.[32] In terms of surface-bound DNA this effect is referred to as cation-induced nucleic acid collapse and has been demonstrated via addition of Mg(II),[33] organic solvents (ethanol)[34] and freely diffusing polycations.[35] In our case, probe-bound polycations offer precise, partial charge neutralization localized on the probe molecule.

The assay was designed in the sandwich configuration for compatibility with a large variety of targets. The sensing principle is based on a key property of DNA duplexes: different melting kinetics of perfect match (PM) (r*1-t*1 or r*17-t*17) vs mismatch (r*17-t*1 or r*1-t*17) (Table 3). The melting kinetics of the target-reporter duplex can be observed by using a labeled reporter. In this case, the reporter redox signal is observed via an Atto-MB label (Figure 1). As the target remains captured by the electrode-bound probe, it can be interrogated sequentially with two allele-specific reporters. At least one of the target-reporter duplexes has a mismatch, and it is expected that melting kinetics will differ significantly; the process will be faster. The workflow takes advantage of *ex situ* hybridization (see SI, Figure S2), where the measurement is performed in a separate vessel, while the sample is preserved uncompromised and undiluted by the measurement buffer (Figure 1, Step 0). The sandwich-hybridization stage can be done in two steps to preserve the sample; however, for more rapid one-step hybridization, an excess of reporter was introduced into the sample solution. This approach allows for measurement with a tailored melting solution composition, which may be unsuitable for the hybridization reaction.

To ensure proper assay performance, NaCl concentration and temperature were optimized (SI, Optimization, Figures S3 and S4). Gold–thiol bonds are temperature-sensitive, so the operating temperature was limited to 42 °C to avoid destabilizing the surface.[36] Also, from previous work, we were aware that maintaining a higher temperature (i.e., 45 °C) over a reasonable amount of time could cause electrode instability.[37] High NaCl (>500 mM) slows melting but stabilizes duplex formation and provides better electrostatic screening at the electrode,[38] while low NaCl (<100 mM) causes a rapid dissociation even of perfect-match duplexes, which compromises detection (SI, Figure S3). Moreover, low NaCl could increase the impact of electrode potential on duplex melting, which is undesirable in our case.[39,40] By screening a narrow NaCl concentration range (SI, Figure S4), a balance was found and 280 mM NaCl was selected as the most suitable concentration. Additionally, formamide was used as the denaturing agent due to its compatibility with electrochemical detection and its ability to speed up the assay while permitting the use of higher NaCl concentrations.

Electrochemical Differentiation between Three Possible Diplotypes. The differentiation between the three possible diplotypes, normal metabolizer (NM, t*1/t*1), rapid metabolizer (RM, t*1/t*17), and ultrarapid metabolizer (UM, t*17/t*17)—is essential for genotyping individuals carrying two allele variants. At first, synthetic DNA targets were used to simulate each diplotype. Linear sweep voltammetry (LSV) was selected as the detection method due to its short scan duration and minimal impact on electrode integrity compared to cyclic voltammetry. During melting, LSV curves showed a progressive loss of the Atto-MB redox signal, corresponding to the dissociation of the reporter strand (Figure 2A,B). These curves were fitted using a potential–current function for irreversibly adsorbed species (red lines (inset), Figure 2; SI, eq S1), which enabled the calculation of surface coverage (pmol cm^{-2}), while an exponential decay function (eq 1) was then used to fit the determined values to calculate dissociation rate constants (k_d, min^{-1}).

Since both reporters, r*1 and r*17, were applied sequentially to the same electrode, their k_d values are directly comparable. In the example shown (Figure 2), r*1 displays a lower k_d (higher affinity), while r*17 shows a greater k_d (lower affinity), consistent with a t*1/t*1 diplotype. This approach was extended to all three diplotypes to calculate the k_d values for both reporters (Figure 3A). While the k_d values for the first hybridization (r*1, dark green, Figure 3A) demonstrated an

https://doi.org/10.1021/acssensors.5c01577
ACS Sens. XXXX, XXX, XXX−XXX

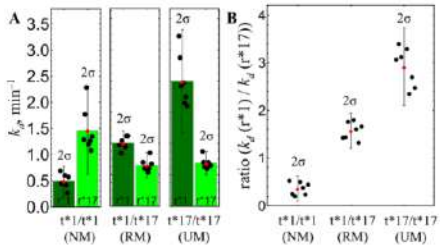

Figure 3. SNP sensor electrode precalibration. (A) k_d values for reporters r*1 and r*17 for different targets (p values between diplotypes: RM/UM pair with r*17 – n. s.; otherwise all $p < 0.001$). (B) Ratio k_d (r*1)/ k_d (r*17) for different targets ($p < 0.0000005$). The values were obtained from 7 independent electrodes. Error bars show confidence interval (±2 standard deviations, 2σ).

increasing trend (0.48 → 1.2 → 2.4), subsequent hybridization (r*17, light green, Figure 3A) did not provide a clear separation (1.47 → 0.78 → 0.81). To improve the resolution, the ratio of the dissociation rate constants k_d (r*1)/ k_d (r*17) was calculated for each electrode (Figure 3B), allowing for robust intraelectrode comparison. The resulting k_d ratios enabled clear differentiation between diplotypes, with statistically significant separation: 0.35 ± 0.24, 1.56 ± 0.34, and 2.9 ± 0.76 for NM, RM, and UM, respectively (Figure 3B). These ratio intervals were used to precalibrate sensors and define the analysis thresholds (Table 1).

Because the sensors are calibration-free and the k_d ratio is dimensionless (although no outliers have been observed), it is important to have a sensor quality control (QC) method for future analysis of real clinical samples. We applied a two-tier QC system by combining acceptable surface coverage (Γ_0) and the k_d ranges. For Γ_0, the range was determined using a 3 interquartile range (IQR) fence method,[41] while the k_d values were determined during the precalibration (Table 1). In a case where electrode performance values are observed outside of those ranges, the sensor result cannot be trusted, and such measurement should be discarded as a QC-fail.

Analysis of *CYP2C19* Allele Variants in Human Saliva Genomic DNA. Saliva is an attractive matrix for point-of-care pharmacogenomic testing because it is noninvasive and requires minimal processing. Six anonymized saliva samples (BioIVT) were examined. For each, a 55-bp single-stranded PCR amplicon containing the rs12248560 SNP (*CYP2C19**1/*17) locus was generated and applied directly, without purification and any additional pretreatment, to the electrochemical SNP sensor. Of note, asymmetric PCR generating the single-stranded DNA fragment of interest eliminated the need for amplicon denaturation prior to measurements. Parallel sequencing served as the reference. Three samples carried the *1/*1 diplotype (NM), one was *1/*17 (RM), and one was found *17/*17 (UM), covering all possible cases (Table 2). One sample yielded k_d ratio of 0.79, falling between the NM and RM precalibration ranges (Table 1), and thus was flagged as QC-fail. We suspect that PCR carried contamination, although this was not confirmed. Excluding the QC-fail, sensor genotypes were concordant with sequencing in all samples, demonstrating accuracy and robustness when applied directly to saliva-derived amplicons. Notably, the flagged sample should not be considered a failure *per se*; in real-world settings, variability in sample or electrode preparation is expected, and a well-designed sensor should be capable of detecting such discrepancies via internal QC.

Using Free Energy Differences to Detect Multiple SNPs and Unknown Mutations. While the specific *CYP2C19* sequence used in this study has only one known SNP (1900C > T), many genomic regions contain multiple nearby SNPs, e.g., rs7802307 and rs7802308.[42] Detecting these with traditional methods can be time-consuming, especially when the variants are unknown or rare. In fluorescence-based DNA microarrays, it is well established that the location of a mismatch has the greatest impact on hybridization signal intensity.[43−46] Similarly, we found that melting-rate constants (k_d) in our system reflect mismatch affinity and can be used to predict sequence differences.

To extract sequence-specific thermodynamic values, we calculated relative free energy differences ($\Delta\Delta G_{MM}$) by comparing the k_d values of sample targets to synthetic, perfect-match references (two-target, one-reporter system) (eq 2; SI, Table S3). This isolates the energetic difference introduced by a mismatch. When these experimentally derived $\Delta\Delta G_{MM}$ values are compared to predicted values from thermodynamic models (i.e., DINAmelt), they can be used to estimate the position and potentially the identity of the mismatch. As a proof of concept, we examined a series of synthetic targets: expected SNP (1900C > T) with unexpected mutation (1888C > G) (S1), expected WT only (1900C) (S2), double mismatch (1888C > G; 1900C) (S3), with the perfect match (1900C > T), used as a reference ($\Delta\Delta G_{MM} = 0$) (S0). In these experiments, we used r*17 as the reporter, forming a perfect match duplex with t*17. The S3 target, containing two mismatches, produced a distinct and significantly elevated $\Delta\Delta G_{MM}$ relative to the single-mismatch targets, demonstrating that multiple deviations from the reference sequence can be determined thermodynamically (Figure 4A). Although the absolute (kcal mol^{-1}) values were offset from theoretical predictions by a relative factor of ~0.55, this discrepancy could be attributed to the heterogeneous nature of the electrode-bound species and the presence of formamide, which is known to alter duplex Gibbs energy by 1.73−5.28 kcal mol^{-1} at 10% on high density microarrays.[46] Despite this offset, the relative differences between the model targets aligned well with calculated values, enabling discrimination of sequences with single vs double mismatches.

Having obtained these exciting results, we decided to push this approach further and test if it is suitable for the detection of unknown mutations. Additional "unusual" sequences were

Table 1. Precalibration and Quality Control Data of the SNP Sensor

target	k_d ratio range (2σ)	Γ_0 range	k_d (r*1) range	k_d (r*17) range
normal metabolizer (t*1/t*1, wild-type homozygous)	0.1−0.62	0.36−3.16 pmol cm^{-2}	0.3−3.6 min^{-1}	0.6−3.6 min^{-1}
rapid metabolizer (t*1/t*17, heterozygous)	1.21−1.93			
ultrarapid metabolizer (t*17/t*17, SNP-type homozygous)	2.09−3.71			

https://doi.org/10.1021/acssensors.5c01527
ACS Sens. XXXX, XXX, XXX−XXX

Table 2. Direct Human Saliva Sample Amplicon Analysis Using an SNP Sensor

Sample	Sensor							Sequencing
	Γ_0 r*1 pmol cm^{-2}	Γ_0 r*17 pmol cm^{-2}	k_d (r*1) min^{-1}	k_d (r*17) min^{-1}	k_d ratio	QC	Genotype	
1	0.73	0.47	1.19	2.52	0.47	PASS	NM	NM
2	1.21	0.48	0.52	2.28	0.23	PASS	NM	NM
3	0.61	0.39	1.27	0.96	1.32	PASS	RM	RM
4	0.87	0.40	1.66	0.76	2.20	PASS	UM	UM
5	0.90	0.56	0.52	2.66	0.20	PASS	NM	NM
6	0.68	0.38	1.91	2.42	0.79	FAIL	-	RM

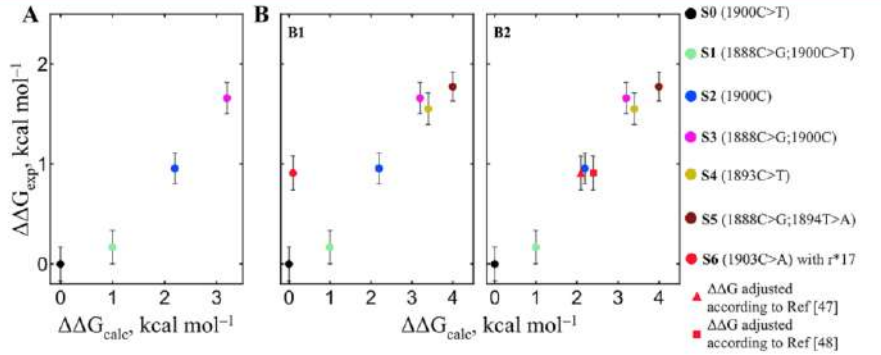

Figure 4. Correlation of measured $\Delta\Delta G_{MM}$ values ($\Delta\Delta G_{exp}$) versus calculated values ($\Delta\Delta G_{calc}$) for the targets having a single mismatch (S1, S2, S4, and S6) and double mismatch (S3, S5). Values are relative to t*17-s-r*17 duplex, which is a perfect match ($\Delta\Delta G = 0$). (A) $\Delta\Delta G_{MM}$ values for targets tested with/without expected mismatch position 1900C > T. (B) Targets testing with unknown mismatches. Mean ± propagated error; n = 3. (Pairs: S0|S1, S2|S6, S3|S4, S3|S5, S4|S5 − n. s., else − $p < 0.01$).

tested, having a single mismatch: 1893C > T (S4), 1903C > A (S6), and a double mismatch 1888C > G; 1894T > A (S5). The measured $\Delta\Delta G_{MM}$ values were in good agreement with theoretical predictions (Figure 4B1), except for that of S6. We predict that the S6 sequence was behaving unusually. The main difference in S6 was a mismatch at the 3′-terminal position, where the loss of base stacking between the probe and reporter likely caused an underestimation of Gibbs energy. Since DINAmelt does not account for stacking losses (the probe molecule is not included in the calculation at all), the S6 value appeared as an outlier. After applying a correction for *G|A* base stacking loss ($\Delta G_{stack} \approx +2.1 \pm 0.3$ kcal mol^{-1}),[47,48] the adjusted data point aligned well with model predictions (Figure 4B2).

While the presented approach is promising, several limitations remain. Terminal mismatches, particularly at the 3′ end, can introduce deviations due to base stacking effects, which are not taken into account in standard thermodynamic predictions. Additionally, the presence of formamide in the melting buffer leads to systematic offsets in absolute $\Delta\Delta G$ values, requiring normalization for direct comparison with theoretical models. Variability in the mismatch position relative to the reporter and label may also affect the melting behavior. These limitations can be solved by applying stacking energy corrections, leaving an abasic or similar site in the distal end of the probe or shortening the proximal end of the reporter, and constraining measurements to a single reporter system.

Future Directions. For clinical applications, we believe two major challenges must be addressed: eliminating the need for thermal cycling (by adopting isothermal amplification methods) and enabling multiplex detection of multiple SNPs simultaneously. Among isothermal approaches, recombinase polymerase amplification has been successfully integrated into a biosensor platform.[30] For whole-genome amplification, multiple displacement amplification has also proven effective in comparative genomic studies.[49] Ideally, the hybridization step should be performed at the same assay temperature. In our study, this could not be done due to excessive heating of the electrode. However, replacing standard thiolated probes with trithiolated analogues could improve electrode thermal stability sufficiently to allow sustained exposure at 42 °C.[28] As for multiplexing, a promising example involves the use of a 16-electrode array to detect multiple SNPs in parallel.[25] This highlights the potential for electrochemical platforms to eventually achieve high-throughput capabilities comparable to those of spectrophotometric 96-well plate assays for practical clinical use.

CONCLUSIONS

Detection of single-nucleotide polymorphisms was achieved by monitoring the isothermal melting kinetics of DNA duplexes. The biosensor assay was based on a sandwich-hybridization principle: the target DNA was captured by an electrode-bound probe, and the melting-rate constants (k_d) of two allele-specific

https://doi.org/10.1021/acssensors.5c01577
ACS Sens. XXXX, XXX, XXX−XXX

Table 3. Sequences Used for *CYP2C19*1/*17* Genotyping[a]

Name	Comment	Sequence 5'-3'
pDNA	Probe DNA	(SH-C6)-CGC ATT ATC TCT TAC ATC AGA
pZNA	Probe ZNA	(SH-C6)-CGC ATT ATC TCT TAC ATC AGA-(ZNA-4)
t*1	Target CYP2C19*1 (normal metabolizer)	CAAATTTGTGTCTT CTGTTCTCAAAGCATC TCTGATGTAAGAGATAATGCG CCAC
t*17	Target CYP2C19*17 (rapid metabolizer)	CAAATTTGTGTCTT CTGTTCTCAAAGTATC TCTGATGTAAGAGATAATGCG CCAC
r*1	Reporter CYP2C19*1	GAT GCT TTG AGA ACA-(Atto MB2)
r*17	Reporter CYP2C19*17	GAT ACT TTG AGA ACA G-(Atto MB2)

[a]Nucleotide substitution position (1900C > T) and related reporter nucleotide position (G > A) are highlighted in red.

reporters were measured sequentially. The assay took advantage of the inherent difference in melting rates between perfect match (PM) and mismatch (MM) duplexes, with PM duplexes showing lower k_d, and MM duplexes exhibiting faster dissociation. As a proof of concept, this study focused on a clinically relevant pharmacogenomic variant in the cytochrome P450 family − *CYP2C19*. By employing external sample capture, we enabled the reuse of a single sample amplicon across multiple electrodes, either in parallel or sequentially. The assay is performed entirely at a constant temperature, allowing for simplified instrumentation and uninterrupted melting measurements. Validation was performed using six human saliva genomic samples, successfully distinguishing between CYP2C19 t*1/t*1, t*1/t*17, and t*17/t*17 genotypes. Both allele-specific k_d values were determined in under 80 min per sample. Unlike traditional SPR-based kinetic systems, our assay focuses solely on dissociation, eliminating the influence of sample concentration and microfluidic variability. Compared to fluorescence-based assays, the required instrumentation is less complex, more cost-effective, and suitable for miniaturization—offering potential for multiplexing via parallel electrodes, particularly for high-value pharmacogenetic targets. Additionally, this study also uncovered a new application of the method: the prediction of one or more nucleotide substitutions based on target affinity. We demonstrated that differences in the Gibbs free energy, derived directly from k_d values, can be used to detect and characterize additional mismatches. This insight opens a promising path toward electrochemical pseudosequencing, where unknown point mutations could be identified through dissociation-based Gibbs energy profiling.

■ EXPERIMENTAL SECTION

Instrumentation. SensoQuest Labcycler was used for PCR. A Gamry Reference 600+ potentiostat for electrochemical measurements was used with a Pt wire counter electrode and Ag/AgCl (3 M KCl) reference electrode.

Reagents, Solutions, Materials, and Electrodes. Felt pads and 0.3 μm alumina suspension were purchased from Buehler. The gold disc (d = 2 mm) working electrodes were purchased from BASi. Nuclease-free water, Sodium chloride, tris(2-carboxyethyl)phosphine hydrochloride (TCEP), and 6-mercapto-1-hexanol were purchased from Sigma. Disodium hydrogen phosphate was purchased from Alfa Aesar. Formamide, magnesium chloride hexahydrate, and sulfuric acid were purchased from Merck. Tris was obtained from Roth. Tween-20 was purchased from Ferak Berlin. Yeast RNA was purchased from Roche. All reagents were analytical grade. All synthetic oligonucleotides used in this work were purchased from Metabion AG. The sequences are given in Tables 3, S1, and S2. The obtained freeze-dried oligonucleotides were dissolved in 10 mM Tris buffer, pH 8.00. The storage concentration of the target sequences was 400 μM and of the reporter sequences, 100 μM. The ZNA probes were obtained as a 100 μM solution in water, which was aliquoted prior to freezing and used as is. These solutions were kept at −20 °C. Human saliva samples were purchased from BioIVT (Human Head and Neck-Related Other Biofluids).

Electrode Preparation. The electrodes were polished on a felt pad wetted with deionized water and a 0.3 μm alumina suspension and sonicated in water for 5 min in an ultrasound bath. The electrochemical cleaning was performed by running 20 CV scans from − 0.2 to 1.75 V at a scan rate of 0.3 V s^{-1} in 500 mM H_2SO_4 solution. The electrodes were kept in H_2SO_4 and thoroughly rinsed with deionized water prior to modification. The probe oligo (pZNA or pDNA) solution was prepared using TCEP (33.3 μM thiolated oligo, 20 mM TCEP, 10 mM Tris, and 100 mM $MgCl_2$, pH 7.2). This mixture was kept at room temperature for 30 min. The probe oligomers were diluted to a final concentration of 0.125 μM (10 mM Tris, 100 mM $MgCl_2$, pH 7.2). Gold electrodes were immersed and kept in the probe oligo solution ([pZNA] = 0.125 μM; [pDNA] = 0.25 μM) for 40 min at room temperature. Afterward, the electrodes were submerged in 7.3 mM aqueous 6-mercapto-1-hexanol solution for 30 min for surface blocking, at RT. Subsequently, the electrodes were washed with 20 mM PBS, 3 M NaCl, pH 7 buffer solution, and left overnight in the same solution.

Hybridization. The electrodes were briefly washed using a solution containing 20 mM PBS and 200 mM NaCl, pH 7. The hybridization of Target and Reporter sequences with the immobilized probe on the gold disc electrode were performed as one step in a single test tube in 5XSSC/0.1% SDS solution containing 100 nM Target ssDNA or at least 0.1 v/v PCR product and 170 nM Reporter ssDNA (the first hybridization performed with r*1 and the second with r*17) sequences and 0.2 mg/mL yeast RNA at 39 °C for at least 20 min. The final volume of the hybridization solution was at least 100 μL. No additional purification or denaturation steps were performed for the PCR product. The electrodes were briefly rinsed in the melting buffer prior to a second measurement with r*17 to ensure only minuscule previous reporter (r*1) presence.

Melting Measurements. The melting experiments were carried out in a jacketed cell in 20 mM PBS, 280 mM NaCl, 10% Formamide, and 0.05% Tween-20, pH 7 (Melting buffer) at 42 °C, unless stated otherwise. The solution was stirred constantly (200 rpm). LSVs were recorded from 0 to −0.42 V at a scan rate of 0.05 V s^{-1}. For every melting measurement, a total of 60 LSVs were recorded at intervals of 20s. The melting curves were fitted according to an exponential dissociation model, ignoring reassociation based on the Polanyi–Wigner equation[50,51]

$$\Gamma(t) = (\Gamma_0 - \Gamma_\infty)e^{-k_d \times t} + \Gamma_\infty \quad (1)$$

Here, Γ_0 − starting surface coverage of reporter (pmol cm^{-2}), Γ_∞ − final surface coverage of reporter which is left hybridized (pmol cm^{-2}), k_d − dissociation rate constant (min^{-1}), t − time (min).

After the first measurement, the electrode was submerged in the second hybridization solution (as above) and measured again to obtain the dissociation rate constant for the second reporter. The

https://doi.org/10.1021/acssensors.5c01527
ACS Sens. XXXX, XXX, XXX−XXX

melting buffer (at least 8.0 mL was used for measurements) was not replaced between the electrodes or measurements.

Measurement of Mismatch Free Energy. Since the hybridization during the experiment is negligible (only melting occurs), then $k_d \propto e^{-E_a/RT}$. $\Delta\Delta G_{MM}$ can be calculated from existing k_d (s^{-1}) rate constants using the formula[48]

$$\Delta\Delta G_{MM} = \Delta E_a = RT \ln(k_{d(MM)}/k_{d(PM)}) \quad (2)$$

Here, R – gas constant (1.9872 cal·K^{-1} mol^{-1}), T – temperature (315.15 K).

The $\Delta\Delta G_{calc}$ values were obtained using UnaFold Two State Melting-hybridization,[52] which could be freely calculated using The UNAFold Web Server. Using T = 42 °C, 280 mM Na^+, and 0.01 mM C_T in Oligo Mode. Only the reporter-complementary portion of the target was taken into account for calculations. By subtracting $\Delta G_{MM\,calc} - \Delta G_{PM\,calc} = \Delta\Delta G_{MM\,calc}$, the calculated $\Delta\Delta G_{calc}$ values were obtained. The experimental values were obtained from t*17-s and S1–S6 targets.

Human Saliva Genomic DNA Asymmetric PCR Amplification to Generate Single-Stranded DNA Fragments of Interest. PCR was performed directly on human saliva samples, using DreamTaq DNA Polymerase in its reaction buffer (as recommended by the manufacturer Thermo Scientific), 0.25 μM primers (Table S1), and 0.2 μL of saliva sample to generate a 55 bp PCR product spanning the SNP of interest (rs12248560). PCR was carried out in thin-walled test tubes in a thermocycler under the following conditions: initial denaturation at 95 °C for 2 min, followed by 35 cycles of denaturation at 95 °C for 30 s, annealing at 57.8 °C for 30 s, and extension at 72 °C for 1 s. Further, ssDNA copies of the strand of interest were generated by asymmetric amplification by adding 0.5 μM forward primer and 1.25U DreamTaq polymerase directly into the reaction mixture and applying the second round of thermocycling conditions as described above, up to 35–50 additional cycles. In parallel, 462 bp long dsDNA PCR products,[53] spanning the site of interest, were produced, followed by nanopore-sequencing by SeqVision.

Statistics. For reliable diplotype determination, a minimum separation of 2σ was targeted to ensure high-confidence discrimination. To aid data interpretation, additional multiple comparisons were performed using one-way ANOVA followed by Tukey's HSD test, with $p < 0.01$ being considered statistically significant. In Figure 3, only target sequences were compared as the reporter sequence is known and does not require measurement. In Figure 4, the mean, propagated standard deviation (SD), and number of measurements and groups were used instead of experimental replicates, as only the mean experimental free energy values (kcal mol^{-1}) were available.

■ ASSOCIATED CONTENT

Supporting Information

The Supporting Information is available free of charge at https://pubs.acs.org/doi/10.1021/acssensors.5c01577.

Tables of all used nucleotide sequences (including those for $\Delta\Delta G$ measurements); *ex situ* hybridization workflow figure; supporting figures for probe selection and optimization; and supporting equation (PDF)

■ AUTHOR INFORMATION

Corresponding Authors

Skomantas Serapinas – *Institute of Biochemistry, Life Science Center, Vilnius University, LT-10224 Vilnius, Lithuania*; Email: skomantas.serapinas@gmc.vu.lt

Dalius Ratautas – *Institute of Biochemistry, Life Science Center, Vilnius University, LT-10224 Vilnius, Lithuania*; orcid.org/0000-0003-3938-3574; Email: dalius.ratautas@gmc.vu.lt

Authors

Deimantė Stakelytė – *Institute of Biochemistry, Life Science Center, Vilnius University, LT-10224 Vilnius, Lithuania*

Kornelija Tučinskytė – *Institute of Biotechnology, Life Science Center, Vilnius University, LT-10224 Vilnius, Lithuania*

Miglė Tomkuvienė – *Institute of Biotechnology, Life Science Center, Vilnius University, LT-10224 Vilnius, Lithuania*

Marius Dagys – *Institute of Biochemistry, Life Science Center, Vilnius University, LT-10224 Vilnius, Lithuania*

Complete contact information is available at: https://pubs.acs.org/10.1021/acssensors.5c01577

Funding

This project has received funding from the Research Council of Lithuania (LMTLT), agreement No. S-MIP-23-127.

Notes

The authors declare no competing financial interest.

■ REFERENCES

(1) Nelson, M. R.; Marnellos, G.; Kammerer, S.; Hoyal, C. R.; Shi, M. M.; Cantor, C. R.; Braun, A. Large-Scale Validation of Single Nucleotide Polymorphisms in Gene Regions. *Genome Res.* **2004**, *14* (8), 1664–1668.

(2) The 1000 Genomes Project Consortium; Abecasis, G. R.; Altshuler, D. M.; et al. A Global Reference for Human Genetic Variation. *Nature* **2015**, *526* (7571), 68–74.

(3) Wang, Z.; Moult, J. SNPs, Protein Structure, and Disease. *Hum. Mutat.* **2001**, *17* (4), 263–270.

(4) Zhu, Z.; Xia, W.; Cui, Y.; Zeng, F.; Li, Y.; Yang, Z.; Hequn, C. Klotho Gene Polymorphisms Are Associated with Healthy Aging and Longevity: Evidence from a Meta-Analysis. *Mech. Ageing Dev.* **2019**, *178*, 33–40.

(5) Ma, M. K.; Woo, M. H.; McLeod, H. L. Genetic Basis of Drug Metabolism. *Am. J. Health-Syst. Pharm.* **2002**, *59* (21), 2061–2069.

(6) Cascorbi, I. Role of Pharmacogenetics of ATP-Binding Cassette Transporters in the Pharmacokinetics of Drugs. *Pharmacol. Ther.* **2006**, *112* (2), 457–473.

(7) Fagerberg, L.; Hallström, B. M.; Oksvold, P.; Kampf, C.; Djureinovic, D.; Odeberg, J.; Habuka, M.; Tahmasebpoor, S.; Danielsson, A.; Edlund, K.; et al. Analysis of the Human Tissue-Specific Expression by Genome-Wide Integration of Transcriptomics and Antibody-Based Proteomics. *Mol. Cell. Proteomics* **2014**, *13* (2), 397–406.

(8) Scott, S. A.; Sangkuhl, K.; Stein, C. M.; Hulot, J.-S.; Mega, J. L.; Roden, D. M.; Klein, T. E.; Sabatine, M. S.; Johnson, J. A.; Shuldiner, A. R. Clinical Pharmacogenetics Implementation Consortium. Clinical Pharmacogenetics Implementation Consortium Guidelines for CYP2C19 Genotype and Clopidogrel Therapy: 2013 Update. *Clin Pharmacol. Ther.* **2013**, *94* (3), 317–323.

(9) Clifford, C.; Knoll, W.; Boudreau, R.; Barry, Q.; Visintini, S.; Alhassani, S.; Laverdure, M.; So, D. TCT-507 Association of CYP2C19*17 Carrier Status to Ischemic and Bleeding Outcomes Among Patients With Coronary Artery Disease Treated With Clopidogrel: A Meta-Analysis. *J. Am. Coll. Cardiol.* **2023**, *82* (17), B204.

(10) Lee, C. R.; Luzum, J. A.; Sangkuhl, K.; Gammal, R. S.; Sabatine, M. S.; Stein, C. M.; Kisor, D. F.; Limdi, N. A.; Lee, Y. M.; Scott, S. A.; et al. Clinical Pharmacogenetics Implementation Consortium Guideline for *CYP2C19* Genotype and Clopidogrel Therapy: 2022 Update. *Clin. Pharmacol. Ther.* **2022**, *112* (5), 959–967.

(11) Deshpande, N.; V, S.; V V, R. K.; H V V, M.; M, S.; Banerjee, R.; Tandan, M.; D, N. R. Rapid and Ultra-Rapid Metabolizers with CYP2C19*17 Polymorphism Do Not Respond to Standard Therapy with Proton Pump Inhibitors. *Meta Gene* **2016**, *9*, 159–164.

(12) Lima, J. J.; Thomas, C. D.; Barbarino, J.; Desta, Z.; Van Driest, S. L.; El Rouby, N.; Johnson, J. A.; Cavallari, L. H.; Shakhnovich, V.; Thacker, J.; et al. Clinical Pharmacogenetics Implementation Con-

sortium (CPIC) Guideline for *CYP2C19* and Proton Pump Inhibitor Dosing. *Clin. Pharmacol. Ther.* **2021**, *109* (6), 1417−1423.
(13) Lamoureux, F.; Duflot, T.; Woillard, J.-B.; Metsu, D.; Pereira, T.; Compagnon, P.; Morisse-Pradier, H.; El Kholy, M.; Thiberville, L.; Stojanova, J.; Thuillez, C. Impact of CYP2C19 Genetic Polymorphisms on Voriconazole Dosing and Exposure in Adult Patients with Invasive Fungal Infections. *Int. J. Antimicrob. Agents* **2016**, *47* (2), 124−131.
(14) Moriyama, B.; Obeng, A. O.; Barbarino, J.; Penzak, S.; Henning, S.; Scott, S.; Agúndez, J.; Wingard, J.; McLeod, H.; Klein, T.; Cross, S.; Caudle, K.; Walsh, T. Clinical Pharmacogenetics Implementation Consortium (CPIC) Guidelines for *CYP2C19* and Voriconazole Therapy. *Clin. Pharmacol. Ther.* **2017**, *102* (1), 45−51.
(15) Sibbing, D.; Koch, W.; Gebhard, D.; Schuster, T.; Braun, S.; Stegherr, J.; Morath, T.; Schömig, A.; Von Beckerath, N.; Kastrati, A. Cytochrome 2C19*17 Allelic Variant, Platelet Aggregation, Bleeding Events, and Stent Thrombosis in Clopidogrel-Treated Patients With Coronary Stent Placement. *Circulation* **2010**, *121* (4), 512−518.
(16) Li-Wan-Po, A.; Girard, T.; Farndon, P.; Cooley, C.; Lithgow, J. Pharmacogenetics of CYP2C19: Functional and Clinical Implications of a New Variant CYP2C19*17. *Br. J. Clin. Pharmacol.* **2010**, *69* (3), 222−230.
(17) Pereira, N. L.; Cresci, S.; Angiolillo, D. J.; Batchelor, W.; Capers, Q.; Cavallari, L. H.; Leifer, D.; Luzum, J. A.; Roden, D. M.; Stellos, K.; et al. *CYP2C19* Genetic Testing for Oral P2Y12 Inhibitor Therapy: A Scientific Statement From the American Heart Association. *Circulation* **2024**, *150* (6), e129−e150, DOI: 10.1161/CIR.0000000000001257.
(18) Ramašauskas, L.; Meškys, R.; Ratautas, D. Real-Time Glucose Monitoring System Containing Enzymatic Sensor and Enzymatic Reference Electrodes. *Biosens. Bioelectron.* **2020**, *164*, No. 112338.
(19) Ramonas, E.; Ratautas, D.; Dagys, M.; Meškys, R.; Kulys, J. Highly Sensitive Amperometric Biosensor Based on Alcohol Dehydrogenase for Determination of Glycerol in Human Urine. *Talanta* **2019**, *200*, 333−339.
(20) Miškinis, J.; Ramonas, E.; Gurevičienė, V.; Razumienė, J.; Dagys, M.; Ratautas, D. Capacitance-Based Biosensor for the Measurement of Total Loss of L-Amino Acids in Human Serum during Hemodialysis. *ACS Sens.* **2022**, *7* (11), 3352−3359.
(21) Sebuyoya, R.; Moranova, L.; Izadi, N.; Moran, L.; Hrstka, R.; Anton, M.; Bartosik, M. Electrochemical DNA Biosensor Coupled to LAMP Reaction for Early Diagnostics of Cervical Precancerous Lesions. *Biosens. Bioelectron.: X* **2022**, *12*, No. 100224.
(22) Wu, K.; Kong, F.; Zhang, J.; Tang, Y.; Chen, Y.; Chao, L.; Nie, L.; Huang, Z. Recent Progress in Single-Nucleotide Polymorphism Biosensors. *Biosensors* **2023**, *13* (9), 864.
(23) Xu, X.-W.; Weng, X.-H.; Wang, C.-L.; Lin, W.-W.; Liu, A.-L.; Chen, W.; Lin, X.-H. Detection EGFR Exon 19 Status of Lung Cancer Patients by DNA Electrochemical Biosensor. *Biosens. Bioelectron.* **2016**, *80*, 411−417.
(24) Ortiz, M.; Jauset-Rubio, M.; Skouridou, V.; Machado, D.; Viveiros, M.; Clark, T. G.; Simonova, A.; Kodr, D.; Hocek, M.; O'Sullivan, C. K. Electrochemical Detection of Single-Nucleotide Polymorphism Associated with Rifampicin Resistance in *Mycobacterium tuberculosis* Using Solid-Phase Primer Elongation with Ferrocene-Linked Redox-Labeled Nucleotides. *ACS Sens.* **2021**, *6* (12), 4398−4407.
(25) Liu, G.; Lao, R.; Xu, L.; Xu, Q.; Li, L.; Zhang, M.; Song, S.; Fan, C. Single-Nucleotide Polymorphism Genotyping Using a Novel Multiplexed Electrochemical Biosensor with Nonfoulingsurface. *Biosens. Bioelectron.* **2013**, *42*, 516−521.
(26) Han, S.; Liu, W.; Zheng, M.; Wang, R. Label-Free and Ultrasensitive Electrochemical DNA Biosensor Based on Urchinlike Carbon Nanotube-Gold Nanoparticle Nanoclusters. *Anal. Chem.* **2020**, *92* (7), 4780−4787.
(27) Xiao, Y.; Lou, X.; Uzawa, T.; Plakos, K. J. I.; Plaxco, K. W.; Soh, H. T. An Electrochemical Sensor for Single Nucleotide Polymorphism Detection in Serum Based on a Triple-Stem DNA Probe. *J. Am. Chem. Soc.* **2009**, *131* (42), 15311−15316.
(28) Yang, A. H. J.; Hsieh, K.; Patterson, A. S.; Ferguson, B. S.; Eisenstein, M.; Plaxco, K. W.; Soh, H. T. Accurate Zygote-Specific Discrimination of Single-Nucleotide Polymorphisms Using Microfluidic Electrochemical DNA Melting Curves. *Angew. Chem., Int. Ed.* **2014**, *53* (12), 3163−3167.
(29) Chahin, N.; Escobar-Nassar, S.; Osma, J.; Bashammakh, A. S.; AlYoubi, A. O.; Ortiz, M.; O'Sullivan, C. K. Low-Cost Platform for Multiplexed Electrochemical Melting Curve Analysis. *ACS Meas. Sci. Au* **2022**, *2* (2), 147−156.
(30) Yenice, C. P.; Chahin, N.; Jauset-Rubio, M.; Hall, M.; Biggs, P.; Dimai, H.-P.; Obermayer-Pietsch, B.; Ortiz, M.; O'Sullivan, C. K. Semiautomated Electrochemical Melting Curve Analysis Device for the Detection of an Osteoporosis Associated Single Nucleotide Polymorphism in Blood. *Anal. Chem.* **2023**, *95* (38), 14192−14202.
(31) Gagnon, K. T.; Watts, J. K.; Pendergraff, H. M.; Montaillier, C.; Thai, D.; Potier, P.; Corey, D. R. Antisense and Antigene Inhibition of Gene Expression by Cell-Permeable Oligonucleotide−Oligospermine Conjugates. *J. Am. Chem. Soc.* **2011**, *133* (22), 8404−8407.
(32) Noir, R.; Kotera, M.; Pons, B.; Remy, J.-S.; Behr, J.-P. Oligonucleotide−Oligospermine Conjugates (Zip Nucleic Acids): A Convenient Means of Finely Tuning Hybridization Temperatures. *J. Am. Chem. Soc.* **2008**, *130* (40), 13500−13505.
(33) Sykes, K. S.; Oliveira, L. F. L.; Stan, G.; White, R. J. Electrochemical Studies of Cation Condensation-Induced Collapse of Surface-Bound DNA. *Langmuir* **2019**, *35* (40), 12962−12970.
(34) Sykes, K. S.; White, R. J. Effects of Nucleic Acid Structural Heterogeneity on the Electrochemistry of Tethered Redox Molecules. *Langmuir* **2022**, *38* (23), 7322−7330.
(35) Sykes, K. S.; White, R. J. Nucleic Acid Identity, Structure, and Flexibility Affect the Electrochemical Signal of Tethered Redox Molecules upon Biopolymer Collapse. *Langmuir* **2021**, *37* (42), 12466−12475.
(36) Civit, L.; Fragoso, A.; O'Sullivan, C. K. Thermal Stability of Diazonium Derived and Thiol-Derived Layers on Gold for Application in Genosensors. *Electrochem. Commun.* **2010**, *12* (8), 1045−1048.
(37) Gineitytė, J.; Serapinas, S.; Ratautas, D. Electrochemical DNA Hybridization Signal Amplification System Using Methylene Blue and Ascorbic Acid. *Electrochim. Acta* **2024**, *507*, No. 145146.
(38) Gong, P.; Levicky, R. DNA Surface Hybridization Regimes. *Proc. Natl. Acad. Sci. U.S.A.* **2008**, *105* (14), 5301−5306.
(39) Wong, I. Y.; Melosh, N. A. An Electrostatic Model for DNA Surface Hybridization. *Biophys. J.* **2010**, *98* (12), 2954−2963.
(40) Ho, D.; Hetrick, W.; Le, N.; Chin, A.; West, R. M. Electric Field-Induced DNA Melting with Detection by Square Wave Voltammetry. *J. Electrochem. Soc.* **2019**, *166* (4), B236−B242.
(41) Beyer, H. Tukey, John W.: Exploratory Data Analysis. Addison-Wesley Publishing Company Reading, Mass. — Menlo Park, Cal., London, Amsterdam, Don Mills, Ontario, Sydney 1977, XVI, 688 S. *Biom. J.* **1981**, *23* (4), 413−414.
(42) Maitra, A.; Shanker, J.; Dash, D.; John, S.; Sannappa, P.; Rao, V.; Ramanna, J.; Kakkar, V. Polymorphisms in the IL6 Gene in Asian Indian Families with Premature Coronary Artery Disease − The Indian Atherosclerosis Research Study. *Thromb. Haemostasis* **2008**, *99* (11), 944−950.
(43) Naiser, T.; Ehler, O.; Kayser, J.; Mai, T.; Michel, W.; Ott, A. Impact of Point-Mutations on the Hybridization Affinity of Surface-Bound DNA/DNA and RNA/DNA Oligonucleotide-Duplexes: Comparison of Single Base Mismatches and Base Bulges. *BMC Biotechnol.* **2008**, *8* (1), 48.
(44) Naiser, T.; Kayser, J.; Mai, T.; Michel, W.; Ott, A. Position Dependent Mismatch Discrimination on DNA Microarrays − Experiments and Model. *BMC Bioinf.* **2008**, *9* (1), 509.
(45) Fish, D. J.; Horne, M. T.; Brewood, G. P.; Goodarzi, J. P.; Alemayehu, S.; Bhandiwad, A.; Searles, R. P.; Benight, A. S. DNA Multiplex Hybridization on Microarrays and Thermodynamic Stability in Solution: A Direct Comparison. *Nucleic Acids Res.* **2007**, *35* (21), 7197−7208.

(46) Yilmaz, L. S.; Loy, A.; Wright, E. S.; Wagner, M.; Noguera, D. R. Modeling Formamide Denaturation of Probe-Target Hybrids for Improved Microarray Probe Design in Microbial Diagnostics. *PLoS One* **2012**, 7 (8), No. e43862.
(47) Rieu, M.; Vieille, T.; Radou, G.; Jeanneret, R.; Ruiz-Gutierrez, N.; Ducos, B.; Allemand, J.-F.; Croquette, V. Parallel, Linear, and Subnanometric 3D Tracking of Microparticles with Stereo Darkfield Interferometry. *Sci. Adv.* **2021**, 7 (6), No. eabe3902.
(48) Abraham Punnoose, J.; Thomas, K. J.; Chandrasekaran, A. R.; Vilcapoma, J.; Hayden, A.; Kilpatrick, K.; Vangaveti, S.; Chen, A.; Banco, T.; Halvorsen, K. High-Throughput Single-Molecule Quantification of Individual Base Stacking Energies in Nucleic Acids. *Nat. Commun.* **2023**, *14* (1), No. 631.
(49) Arriola, E.; Lambros, M. B. K.; Jones, C.; Dexter, T.; Mackay, A.; Tan, D. S. P.; Tamber, N.; Fenwick, K.; Ashworth, A.; Dowsett, M.; Reis-Filho, J. S. Evaluation of Phi29-Based Whole-Genome Amplification for Microarray-Based Comparative Genomic Hybridisation. *Lab. Invest.* **2007**, *87* (1), 75−83.
(50) Schuhfried, E.; Aprea, E.; Cappellin, L.; Soukoulis, C.; Viola, R.; Märk, T. D.; Gasperi, F.; Biasioli, F. Desorption Kinetics with PTR-MS: Isothermal Differential Desorption Kinetics from a Heterogeneous Inlet Surface at Ambient Pressure and a New Concept for Compound Identification. *Int. J. Mass Spectrom.* **2012**, *314*, 33−41.
(51) Cheng, F.; Gamble, L. J.; Castner, D. G. XPS, TOF-SIMS, NEXAFS, and SPR Characterization of Nitrilotriacetic Acid-Terminated Self-Assembled Monolayers for Controllable Immobilization of Proteins. *Anal. Chem.* **2008**, *80* (7), 2564−2573.
(52) Markham, N. R.; Zuker, M. DINAMelt Web Server for Nucleic Acid Melting Prediction. *Nucleic Acids Res.* **2005**, 33 (Web Server), W577−W581.
(53) Jin, C.; Li, Z.; Zheng, X.; Shen, K.; Chao, J.; Dong, Y.; Huang, Q.; Yin, Q.; Deng, Y.; Zhu, W. Development and Validation of T-ARMS-PCR to Detect CYP2C19*17 Allele. *J. Clin. Lab. Anal.* **2020**, *34* (1), No. e23005.

https://doi.org/10.1021/acssensors.5c01577
ACS Sens. XXXX, XXX, XXX−XXX

ACKNOWLEDGEMENTS

I would like to express my thanks to a number of people who have helped me complete these tasks. First and foremost, Dr. Marius Dagys for the supervision and for the push to develop these sensors while giving me the freedom to create my own designs.

I am very grateful to Dr. Dalius Ratautas for overseeing many of my experiments, for the innumerable consultations and the support in writing and publishing. My gratitude also goes out to the current and former members of the Department of Bioanalysis for a broad scope of expertise and assistance.

I would like to personally thank:

Dr. Jonas Šarlauskas for the countless brilliant discussions.

Dr. Miglė Tomkuvienė and Kornelija Tučinskytė for their expertise, support and positivity and the DNA amplification reactions at the Department of Biological DNA Modification.

Dr. Laurynas Dagys for the NMR spectroscopy at The Institute of Chemical Physics and the fruitful conversations.

Dr. Ilja Ignatjev for the much needed help with Raman measurements at The Center for Physical Sciences and Technology.

Dr. Mantas Jonušis, from The Laboratory of Bioorganic Compounds Chemistry for the GCMS measurements.

Dr. Tadas Ragaliauskas for the atomic gold deposition at the Institute of Biochemistry.

Dr. Rasa Petraitytė-Burneikienė and The Department of Eukaryote Gene Engineering for the help with gel imaging.

Zdislav Staševskij for the ^{32}P DNA postlabelling and autoradiographic imaging.

Dr. Marija Jankunec for the help with atomic force microscopy at the Department of Bioelectrochemistry and Biospectroscopy.

Jonas Špečkauskas from Protogama, for the CNC-machined parts.

I am also grateful to my family and relatives for personal support.

UŽRAŠAMS

Vilniaus universiteto leidykla
Saulėtekio al. 9, III rūmai, LT-10222 Vilnius
El. p. info@leidykla.vu.lt, www.leidykla.vu.lt
bookshop.vu.lt, journals.vu.lt
Tiražas 15 egz.